A search for particle showers at the edge of IceCube's instrumental volume

DISSERTATION

zur Erlangung des akademischen Grades

doctor rerum naturalium
(Dr. rer. nat)
im Fach Physik

eingereicht an der
Mathematisch-Naturwissenschaftlichen Fakultät
der Humboldt-Universität zu Berlin
von
Herrn Dipl. Phys. Johannes Achim Stößl

Präsident der Humboldt-Universität zu Berlin:
Prof. Dr. Jan-Hendrik Olbertz
Dekan der Humboldt-Universität zu Berlin:
Prof. Dr. Elmar Kulke

Gutachter:
1. Prof. Dr. Alexander Kappes
2. Prof. Dr. Marek Kowalski
3. Prof. Dr. Joanna Kiryluk

eingereicht am: 4.8.2015
Tag der mündlichen Prüfung: 29.6.2016

für Tini

Abstract

Among the analysis strategies used in IceCube, searches for neutrino-induced particle showers, so called cascades, provide good energy resolution and a relative low atmospheric background. Therefore, they provide large sensitivity to the extraterrestrial neutrino flux. Previously, these searches have been constrained to neutrino interactions in a center region of the instrumented volume. The volume at the border and surrounding the detector was needed to veto the incident atmospheric muon background. This dissertation presents an analysis of two years of IceCube data and demonstrates the feasibility of using the veto region for cascade searches. This increases the usable detector volume by $\approx$ 80% and improves the statistic in the high-energy tail of the neutrino spectrum by adding 18 neutrino candidates in the energy range from 34 to 576 TeV. The result is supports the established evidence for the extraterrestrial neutrino flux by rejecting the pure atmospheric background hypothesis at the 2.7 sigma level, the data prefers an extraterrestrial neutrino flux with a featureless power law with an index of $\gamma = 2.50^{+0.28}_{-0.28}$ well in agreement with previous IceCube results.

Zusammenfassung

Unter den Methoden zur Suche nach Neutrino Ereignissen in IceCube versprechen Suchen nach Teilchenschauern, sogenannten Kaskaden eine gute Energieauflösung und einen verhätlnismässig geringen atmosphärischen Untergrund. Dadurch erreichen solche Suchen eine hohe Sensitivität für einen extraterrestrischen Neutrino Fluss. Bisher beschränkte sich die Suche nach solchen Ereignissen auf solche in einer inneren Region des IceCube Detektors. Das Detektorvolumen am Rand wurde bisher benutzt um den Untergrund von einfallenden atmosphärischen Muonen zu Unterdrücken. Diese Dissertation präsentiert eine Analyse von 2 Jahren IceCube Daten und demonstriert die Möglichkeit, diese Veto Region für die Suche nach kaskadenartigen Ereignissen zu nutzen. Dadurch wird das nutzbare Detektorvolumen um ungefähr 80% vergrößert und die Statistik im hochenergetischen Bereich des Neutrino Spektrums durch das Hinzufügen von 18 Neutrino Kandidaten im Energiebereich von 34 - 578 TeV erhöht. Das Ergebnis ist in Übereinstimmung mit dem etablierten Nachweis eines extraterrestrischen Neutrino Flusses, eine reine Untergrund Hypothese kan mit 2.7 sigma verworfen werden und die Daten favorisieren einen extraterrestrischen Neutrino Fluss mit einem ungebrochen Potenzgesetz mit einem Index von $\gamma = 2.50^{+0.28}_{-0.28}$ in guter Übereinstimmung mit bisherigen Ergebnissen von IceCube.

CONTENTS

1

Introduction

Since the beginning of civilization, mankind has undertaken great endeavors to observe and understand the night sky. Examples can be found all over the world for different cultures and epochs[1, 2]. In many ways, these endeavors and the resulting scientific progresses had influenced or even triggered cultural development and might thus be considered as major milestones in the development of societies[3–5].

Since the beginning of the last century, the research field of astrophysics has benefited from the rapid development of optical instruments and newly available techniques to observe light in wavelengths not accessible by the astronomers before and thus it was possible to push the frontier of observation even further. In parallel, following the discovery of radioactivity[6] and with the development of quantum mechanics a whole new field of physics - particle physics - has evolved.

Already at the dawn of the new field in the early 20th century, the discovery of an increasing ionization of the air with increasing altitude revealed a component of ionizing radiation which originated from outer space[7]. Unknowingly about its nature as a particle radiation, the term “cosmic rays” was assigned to the new discovery. Cosmic rays are highly energetic ionized nuclei and leptons which hit the Earth’s atmosphere with energies and fluxes spread over many

orders of magnitude, their energies reaching up to $\approx 10^{20}$ eV. They hold the record of the highest ever observed energy of a single particles of about 320 EeV[8], which would be a typical kinematic energy of a macroscopic object.
The discovery of a particle radiation originating from outer space indicated already that merging the efforts of the fields of astrophysics and particle physics might be needed to unveil its nature and origin. Despite the efforts made, at present time the origin - and also the composition - of the high energy part of the cosmic ray spectrum remains unknown. The question is of importance for several reasons: As the energies up to which particles are accelerated in the sources can not be reached in accelerators on Earth, one would like to know about the conditions which allow to reach these energies. Revealing the acceleration mechanism allows also to probe the source and its ambient medium itself. Observing the particles itself allows to measure cross sections in an energy regime which can not be reached on Earth. Of special interest is also the fact that the observed particles created in the collisions of the primary cosmic rays with the nuclei of the atmosphere are strongly boosted in the direction of the incoming particle. This is called the forward region, and it is difficult to asses with particle detectors due to their toroid design around the beam line.
Due to the importance of the answer to this question, also known as the "cosmic ray puzzle" many different approaches to solve it are followed in parallel, leading to many different types of detectors, among these the currently largest particle detector in the world, IceCube [9]. The IceCube neutrino observatory is dedicated to measure a neutrino component which is produced in association with cosmic rays for a large class of models. Other detectors are dedicated to observe either the charged component of cosmic rays directly[10, 11] or to observe γ rays[12, 13] which are predicted to be produced associatively by also a large class of models. Each technique has to face different challenges, only the highest energetic charged cosmic rays at EeV energies are able to keep their direction information and are not significantly deflected on their way to the Earth. However, at this energies, the flux is suppressed by the GZK-effect[14], the interaction of cosmic ray primaries with the cosmic microwave background (CMB). Gamma ray astronomy has been very successful in the last decades and discovered thousands of sources in the GeV - 100 TeV regime. Supernova remnants (SNR) have been identified as sources for a galactic cosmic ray component by the Fermi collaboration[15], however it can be deduced already from

simple arguments as further described in subsection 1.1.3, that for the ultra high component of charged cosmic rays, accelerators with either stronger magnetic fields or of larger dimension than SNR are needed. Unfortunately, the cosmic horizon of high energy γ ray astronomy is limited due to the interaction of γ rays with intergalactic radiation fields[16, 17]. The cosmic horizon for γ astronomy is illustrated in Figure 1.1. Utilizing neutrinos as messenger particles overcomes this limitation as neutrinos interact only weakly and thus the likelihood that they are absorbed or deflected is small. Thus they can be used to pinpoint the sources of cosmic rays in our universe, complementing the γ ray measurements.

In the past, the observation of extraterrestrial neutrinos was limited to observations of the sun[19] and a supernova in the large Magellanic cloud, SN1987A [20–22]. The observation of the sun was proving the concept of neutrino astronomy, however only for the MeV neutrino energy region and for a close-by object.

Modern neutrino detectors of the 1 GTon size of interaction target are capable to observe high energetic neutrinos of TeV - EeV and recently an astrophysical neutrino flux in the TeV - PeV region has been discovered by the IceCube collaboration[23], marking a major step in neutrino astronomy. Early analysis performed were sensitive to ν_μ charge current only, as this interaction leads to a track-like signature, which allowed for a good angular resolution and thus reducing the background by only selecting upward going events. The concepts and techniques of neutrino observatories are elaborated further on in section 2.3. Current advanced analysis methods comprise the inclusion of shower-type events. For deep-inelastic neutrino nucleon scattering (DIS), as described in subsection 2.1.1, the fragments of the target nuclei will emerge as a particle shower in the ice. At the energies observable with IceCube, the shower is boosted in the forward direction and charged components might emit Cherenkov light. The dimensions of the shower are of several meters, and as the instrumentation of IceCube is sparse, the shower appears as a point-like light source to the instrument. Such showers are also created by charge current interactions of ν_e and ν_τ, where the correspondent partner lepton leads to a secondary shower. Especially ν_e will only leave a shower-type signature in the detector. The first indications of the presence of an astrophysical neutrino flux measurable by IceCube came from the observation of two PeV shower-

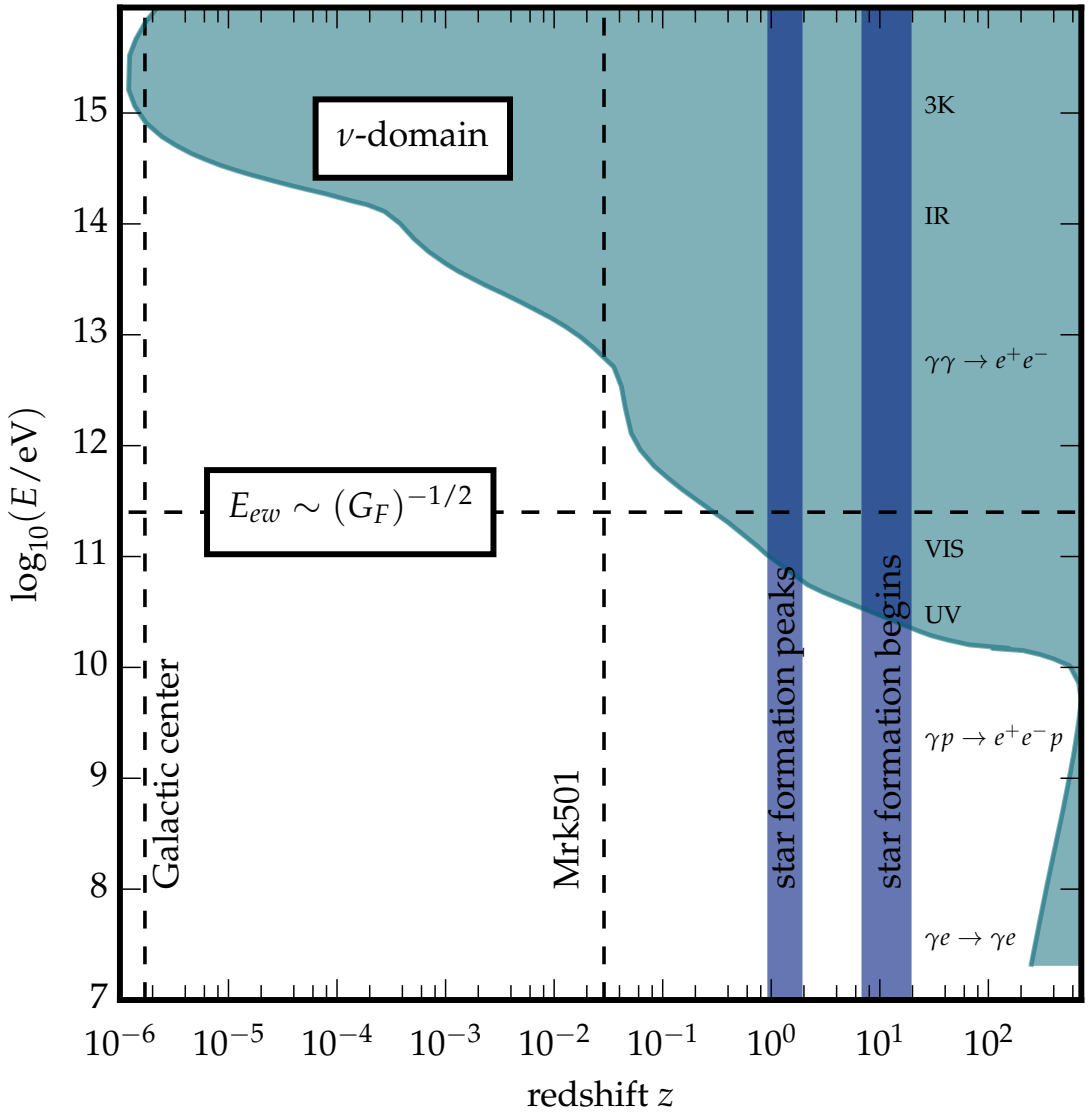

Figure 1.1 – The cosmic horizon for γ ray astronomy. The object Markarian 501, one of the brightest objects in the TeV γ ray sky is labeled in the plot. On the right edge, the dominant photon interaction processes are indicated. Figure adapted from [18].

type events[24]. The possibility to measure all neutrino flavors increases the collected statistics for an astrophysical neutrino flux significantly, if the equal flavor ratio of this flux is assumed. Measuring shower-type events allows also for a reasonable energy resolution, especially in the case of contained ν_e interactions, where none of the primary neutrino energy leaves the detector. As described in section 1.2, the atmospheric ν_e flux is lower than the atmospheric ν_μ flux[25], and the atmospheric ν_τ flux is basically non existent, which is also a benefit of an analysis sensitive to shower-type events. However, as the directional resolution for these event class is low, background reduction of atmospheric muons can not rely on selecting upward going events anymore, established techniques define a fiducial volume in the center part of the detector, accompanied by a veto region consisting of the outer layers of the instrumentation. This veto region typically consumes about half of the instrumented volume.

To gain further sensitivity for all-flavor, all-sky astrophysical neutrino searches, the here presented analysis investigates the physics capability of this veto region. It is the first time since the IceCube collaboration published the discovery of an extraterrestrial neutrino flux that the physics capability of this veto region is explicitly studied.

In this analysis it is demonstrated that using the veto region is feasible and that the effective volume of IceCube can be increased from $\approx$ 450 MTon to $\approx$ 850 MTon. The analysis adds 16[1] events with energies from 34 to 660 TeV in the regions formerly used as veto analyzing 2 years of IceCube data. This is a significant increase in high energy neutrino induced showers, comparing to the 27 events which were found in the same time period and energy range inside the fiducial volume.

The following chapter will give an introduction to cosmic rays and the connection to neutrinos. Chapter 2 discusses the principle of neutrino detection via charged secondaries in more detail, and introduces IceCube, the current largest particle detector in the world. Chapter 3 describes the methods used to reconstruct and simulate the observed events. Finally in chapter 5 the event selection and the search for high energy neutrinos are discussed, and a statistical interpretation of the found events is given. At last this work is reviewed in the context of present science in the conclusion.

[1] or 18, if including 2 which were found in the 10% sample used to develop the event selection

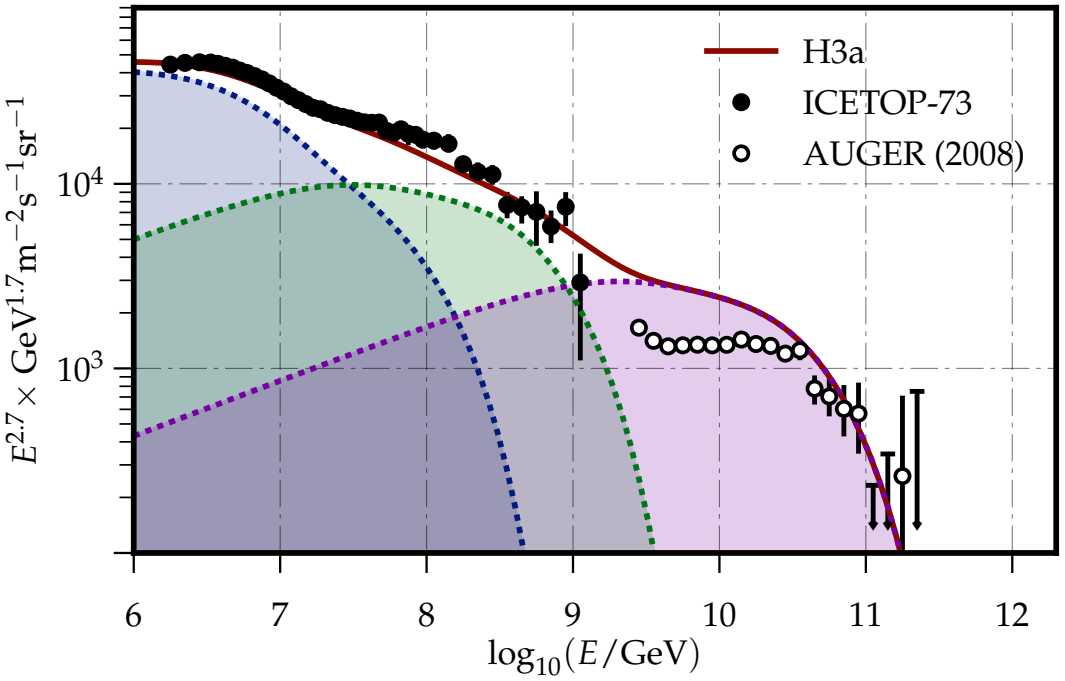

Figure 1.2 – The high energy tail of the primary cosmic ray spectrum, data taken from selected measurements[26, 27]. A phenomenological 3 component model as described in subsection 1.1.1 is indicated by the color filled areas.

1.1 Cosmic rays

Investigating the nature of ambient ionizing radiation, the term "cosmic radiation" was first used by A. Gockel in 1908 when describing ionization measurements at different altitudes[28]. Following measurements showed conclusively the increase of the level of radiation with altitude[29], which justified the term to emphasize the contrast to the radiation emitted from the ground.
The study of cosmic rays further revealed their nature as a particle radiation. Incident charged particles - mainly ionized nuclei - hit the upper atmosphere, eventually creating a cascade of secondaries. Very often and in this work as well, the term "cosmic rays" refers only to the hadronic component of the incident particles, however there is also a small contribution of leptons and γ-rays hitting the Earth from outer space. The composition of the primary cosmic rays follows mostly the abundances of elements in the universe, thus protons are the dominant component at GeV and TeV energies[30]. However, the composition changes with energy. Measurements indicate the dominance of heavier

elements at EeV energies[31], however there are also measurements favoring a more lighter composition[32]. The cosmic ray flux spans from one particle per $cm^2 s^{-1}$ to lower than one particle per square kilometer per century at the highest energies in the cut-off region of 10^{20} eV of the spectrum. High energy cosmic rays will create an air shower of particles in the atmosphere, among the muons and atmospheric neutrinos, as it is described in subsection 1.2.1. Above about a TeV of primary energy, a non-negligible fraction of muons with energies of several ten GeV and larger will reach the surface of the Earth and might even propagate further to the IceCube neutrino observatory[33]. Muons and atmospheric neutrinos form the main component of background for the search of astrophysical neutrinos. Though both are products of cosmic ray interaction, the muons and atmospheric neutrinos created at Earth lost their direct connection to the cosmic ray sources, since the cosmic rays get deflected at magnetic field inhomogeneities while traveling the cosmos. Astrophysical neutrinos though will travel the cosmos mostly undisturbed, carrying the full information about their production. Since as discussed, the knowledge of the high energy part of the cosmic ray spectrum as measured on Earth is important to astrophysical neutrino searches as presented here, we will further discuss the high energy part beyond 1 PeV as shown in Figure 1.2. The flux follows an energy dependent power law with a varying spectral index over different energy intervals. Recent measurements fit 4 different spectral indexes over an energy range from PeV to EeV, and reject the single power-law hypothesis with high confidence[26]. The most prominent features in the transition region of the power law are commonly referred in increasing order of energy as "knee" at about 3-4 PeV, "second knee" at 100 PeV and "ankle" at about 1 EeV. The different spectral indexes can be attributed to the existence of different populations of cosmic ray sources. Such a model is indicated in Figure 1.2 and further described in subsection 1.1.1. A power law indicates a non-thermal production of cosmic rays. The observable cut-off of the energy spectrum in the region above few 10 EeV can be described by the increased probability for ultra-high-energetic nuclei to interact with the cosmic microwave background (CMB)[34]. At these energies, Δ^+ resonances are produced in the interactions of protons with the CMB photons[14, 35].
Searches for neutrinos associated with this process[36] can further help to test models predicting a cutoff. IceCube has set limits on the observation of such

cosmogenic neutrinos[36]. Alternatively, the cutoff can be also interpreted by a change to a heavier composition as the accelerators are not capable to accelerate light elements to these energies any more. The measured flux of cosmic rays at Earth is mostly isotropic, with a measured anisotropy on the level of $10^{-4} - 10^{-3}$ in the TeV regime in the Northern[37] and Southern hemisphere[38]. The anisotropy might be caused by variations in the galactic magnetic field or by close-by sources, however a conclusive statement has not been made yet[38].

1.1.1 Cosmic ray flux models

Suggested by Hillas[39], a phenomenological model with three cosmic ray populations was developed[40]. The three populations of cosmic ray sources can be interpreted as a low-energy galactic component, mainly ejected by supernova remnants, a higher energetic galactic component and an extragalactic component, both of yet unknown origin. The model was derived from fits to data gathered by the balloon-born cosmic ray experiments CREAM and ATIC2[41, 42]. The direct measurements reach only up to energies of about 100 TeV, thus the data had to be extrapolated to higher energies while being consistent with data from air shower experiments. In this model, the cosmic ray composition is described by 5 components, which represent the five groups of most abundant nuclei in the universe[43]: H, He, CNO, Mg-Si, Mn-Fe.
A basic assumption of this model is that the features in the cosmic ray spectrum can be described by the magnetic rigidity R of a nucleus with energy E_0 and charge Ze:

$$R = \frac{E_0}{Ze} \tag{1.1}$$

Each rigidity corresponds to a gyro radius $r_g = R/B$ of a particle in an external magnetic field of strength B. This can be used for the formulation of a criterion for the size a cosmic ray accelerator must have to accelerate particles to that rigidity, this is further discussed in subsection 1.1.3. The proposed flux Φ_i per element i with atomic number Z_i is then described by the summation over the fluxes of the three populations, where each flux is modeled by a power law with an exponential cutoff:

$$\Phi_i(E) = \sum_{j=1}^{3} \alpha_{i,j} E^{-\gamma_{i,j}} \cdot \exp\left(\frac{E}{Z_i R_{C,j}}\right) \tag{1.2}$$

$R_{C,j}$	γ	p	He	CNO	Mg-Si	Fe
γ for Pop. 1	-	1.66	1.58	1.63	1.67	1.63
Pop. 1: 4 PeV	See line 1	7860	3550	2200	1430	2120
Pop. 2: 30 PeV	1.4	20	20	13.4	13.4	13.4
Pop. 3 (mixed): 2 EeV	1.4	1.7	1.7	1.14	1.14	1.14
Pop. 3 (p only): 60 EeV	1.6	200	0	0	0	0

Table 1.1 – Spectral indices γ_j, normalization constants α_j and cutoff rigidities $R_{C,j}$ for the three populations. Values taken from [40].

with the values for $\alpha_{i,j}$,$\gamma_{i,j}$ and the cutoff rigidity $R_{C,j}$ as given in Table 1.1. Per se, the model does not include effects of cosmic ray propagation through the Galaxy or interactions with the CMB, but they are parametrized through γ and R_C. Two variants of this model exist: The difference is the assumed composition of the extra-galactic component, which can also be assumed as protons only instead of a mixed composition including heavier elements. The model is further on referred to as H3a/H4a, where H3a stands for the mixed composition extra-galactic population and H4a for the proton only variant. However, in this work only the H3a model is used, as the difference between these models has been found irrelevant for the here presented analysis.

1.1.2 Acceleration of cosmic rays

The observed power law of the cosmic-ray spectrum and the large energy content carried by cosmic rays in the Galaxy, lead E. Fermi to propose an efficient acceleration mechanism: In his scenario, particles are scattered on moving magnetic inhomogeneities in the interstellar space[44] and thus gain energy. Magnetic inhomogeneities can be realized by wandering clouds of partly ionized material, which carry their own magnetic field, slightly different from the ambient interstellar medium (ISM). A particle in the ISM might gain or lose energy by elastic collision with these inhomogeneities through the transfer of momentum. However collisions where the particle gains energy are more frequent than those where it loses energy and in the average a net energy gain will remain. In the context of the theory colliding means collision-less scattering of the particles on the magnetic fields, as particle collisions would thermalize the

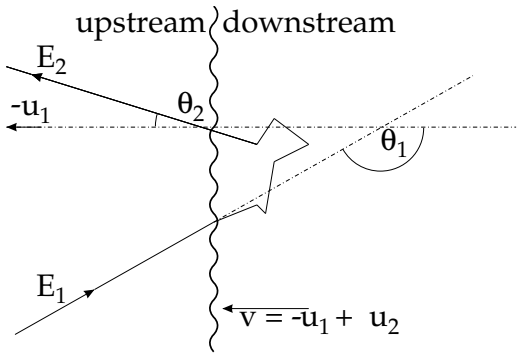

Figure 1.3 – Shock front acceleration mechanism with upstream and downstream region indicated, moving respectively with speeds u_1 and u_2 in the comoving coordinate system of the shock. A particle which enters with the energy E_1 under the angle θ_1, is scattered multiple times and leaves the shock front under the angle θ_2 with a net gain in energy $E_2 = E_0(1+\xi)^n$. Figure adapted from[33]

spectrum, and not lead to an acceleration.
The basic concept behind the theory is that each time, when a particle enters a cloud, its direction is isotropized in the rest frame of the cloud, and momentum is transferred from the cloud to the particle. After leaving the rest frame of the cloud an average net gain in energy remains. The originally proposed mechanism is called second order Fermi acceleration, as the energy gain is proportional to the square of the plasma cloud velocity.
The process becomes more effective for plane shock acceleration, by considering infinite, plane shock fronts instead of localized clouds. In this scenario, the energy gain is proportional to the plasma flow velocity. A shock is formed by particles in a plasma which move with speeds larger than the speed of sound. Such shock fronts are e.g. observed in supernova remnants (SNR)[45]. Instead of the second order process, shock front acceleration is more efficient and thus able to accelerate particles to higher energies. The geometry of the shock front acceleration mechanism is displayed in Figure 1.3, where the shock moves with the velocity v in the laboratory frame. For the shock acceleration model to work, the particle has to be confined in the shock front region for a certain time. The basic idea of the proposed acceleration mechanism is that a particle with energy E_0 acquires energy ξE_0 in a number of subsequent encounters n, and is able to escape the acceleration region with the probability P_{esc} per each encounter. The energy E_n of the particle after n encounters is then given by Equation 1.3:

$$E_n = E_0(1+\xi)^n \tag{1.3}$$

With the probability $(1 - P_{esc})^n$ to stay confined in the acceleration region, it is possible to express the number of particles $N(E \geqslant E_n)$ which have reached at least the energy E_n during the acceleration process with the geometrical series:

$$N(E \geqslant E_n) \propto \sum_{m=n}^{\infty} (1 - P_{esc})^m = \frac{(1 - P_{esc})^n}{P_{esc}} \tag{1.4}$$

Solving Equation 1.3 for n and substituting it into Equation 1.4 leads to a power law spectrum:

$$N(E \geqslant E_n) \propto \frac{1}{P_{esc}} \left(\frac{E}{E_0} \right)^{-\gamma} ; \; \gamma = \ln \left(\frac{1}{1 - P_{esc}} \right) / \ln(1 + \xi) \approx \frac{P_{esc}}{\xi} \tag{1.5}$$

In the case of shock front acceleration, it can be shown that the index γ in Equation 1.5 is close to -1, or -2 in dN/dE which is a reasonable precondition for the observed power law close to $\gamma = -2.7$ in dN/dE, as no effects of cosmic ray propagation are included in the model, that will soften the spectrum[33].
The escape probability P_{esc} from Equation 1.5 can be calculated by the ratio between the cosmic rays which escape the shock to the total amount of cosmic rays which entered the shock. The rate of encounters of cosmic rays with the shock front can be calculated by projecting the isotropic flux of cosmic rays $c\rho_{cr}$ on the plane of the shock where the velocity of cosmic rays is assumed to be close to the speed of light:

$$\int_0^1 d \cos\theta \int_0^{2\pi} d\phi \frac{c\rho_{cr}}{4\pi} \cos\theta = \frac{c\rho_{cr}}{4} \tag{1.6}$$

The rate of cosmic rays which escape in the downstream region with velocity u_2 is given by $\rho_{cr} u_2$. Thus the escape probability can be written as:

$$P_{esc} = \frac{\rho_{cr} u_2}{c\rho_{cr}/4} \tag{1.7}$$

Calculating the average energy gain $\hat{\xi}$ involves a consideration of the angles under which the particle enters the shock region as well as a back and forth transformation of the coordinate system which is moving with the shock. The

following is found for the individual energy gain ξ per encounter[33]:

$$\xi = \frac{1 - \beta\cos\theta_1 + \beta\cos\theta_2' - \beta^2\cos\theta_1\cos\theta_2'}{1-\beta^2} - 1 \tag{1.8}$$

In Equation 1.8 the angles θ_1 and θ_2' describe the entering and exit angles of the particle into or from the shock in the laboratory frame, β is the velocity of the gas moving away from the shock. Averaging over all angles θ_1 and θ_2' will yield the above stated first order dependence:

$$\hat{\xi} \sim \frac{4}{3}\beta = \frac{4}{3}\frac{u_1 - u_2}{c} \tag{1.9}$$

with the upstream velocity u_1 and downstream velocity u_2 as the velocity of the unshocked and shocked gas respectively in the rest frame of the shock front.

$$\gamma = \frac{3}{u_1/u_2 - 1} \tag{1.10}$$

For a strong shock, for which the Mach number $M = u_1/c_s$, the relative velocity of the gas with respect to the velocity of sound c_s, is much larger than 1, it can be shown that:

$$\gamma \approx 1 + \frac{4}{M^2} \tag{1.11}$$

and indeed a value of γ close to 1 is found[33]. Considering the above described conditions including cosmic ray propagation this yields an ≈ -2.4 power law, which is reasonably close to the observation of $\gamma \approx -2.7$

It has to be noted however, that in the original theory an injection mechanism is needed, which pre-accelerates the cosmic-ray particles to a mass-dependent threshold energy. In Fermi's original publication, the nature of this mechanism remains unclear. The existence of the threshold energy explains the lack of electrons in the cosmic ray spectrum, as they lose their energy too quickly by radiative processes to be picked up by the accelerator mechanism. However, this threshold energy prohibits the original theory to model the abundance of heavy nuclei in the high energy part of the spectrum. It is not clear how particles with high masses should be able to reach the high threshold energy before entering the acceleration mechanism.

1.1.3 Cosmic accelerators

Independent of the particular characteristics of a possible source of cosmic rays, it must fulfill a general criterion to allow it to accelerate particles to the observed energies. As charged particles will escape after being accelerated in the source, magnetic fields must provide confinement of the particles in the acceleration region for further energy transfer. This assumption allows to correlate the size of source candidates with the strength of their magnetic fields B by the gyro radius r_g of the particle with energy E_0 and charge Ze in the high energy approximation[46].

$$r_g = \frac{E_0}{|ze| \cdot B} \tag{1.12}$$

The relation is illustrated in the Hillas plot, shown in Figure 1.4. The maximum particle energy which can be reached by several objects can be indicated by diagonal lines in this plot. In the following some exemplary Galactic and extragalactic sources will be briefly described.

Galactic sources

Supernova remnants (SNR): Models describing core-collapse supernovae, predict about 99% of the dissipated energy to be emitted in MeV neutrinos [48]. Due to the high density of the material, the neutrinos will heat up the material and drive outward shocks of ejecta[49]. These shock fronts provide an environment suitable to accelerate cosmic rays. Calculations of the released energy by supernovae and the observed energy density in cosmic rays at Earth indicate that SNR contribute largely to the observed cosmic- ray flux, and γ-ray observations with the FERMI -LAT instrument fortify this assumption for the low TeV regime[15].

Extragalactic sources

Starburst galaxies: Likely created by soft collisions of galaxies or close flybys, starbursts contain large fractions of warm interstellar gas. These galaxies are typically of the spiral type and are among the brightest ob-

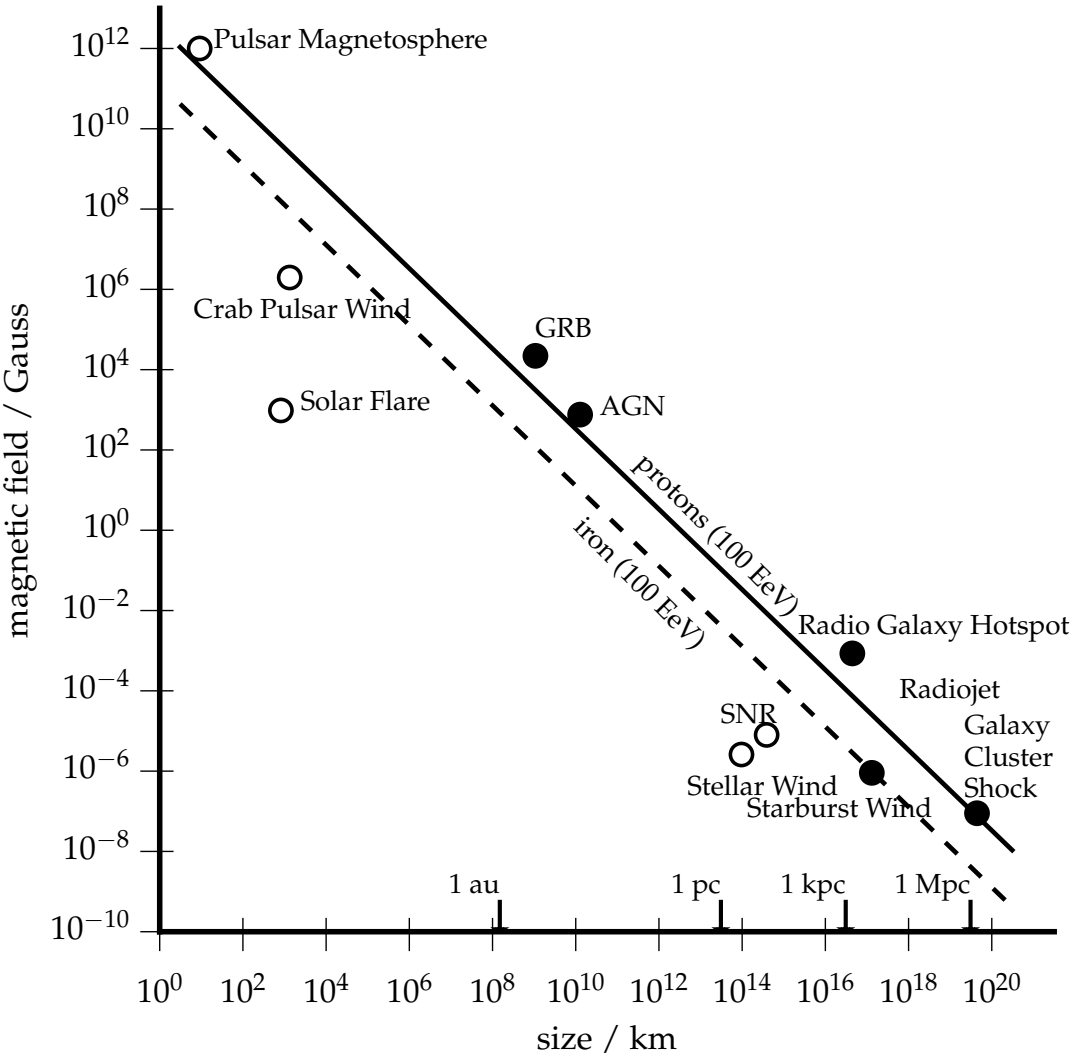

Figure 1.4 – The "Hillas plot": Magnetic field strength of objects and their extension. The maximum gyro radius of a particle accelerated in this object is its size, therefore a maximum energy which can be reached by particles being accelerated in these objects can be defined. These energies are indicated with the two lines for proton and iron. Galactic objects are marked with the white markers. The points in the plot are centered at an average value for the individual objects classes, its extension not related to the extension of the data in the parameter space. Data taken from [47].

jects in the infrared. The warm interstellar gas contained in these galaxies provides a perfect cradle for young, massive, hot stars, which have a lifespan of typically several 100 million years, before they explode in supernovae[30].
Observations of high energy γ rays from such objects[50] indicate cosmic-ray densities which are three orders of magnitudes higher than in the center of the Milky way. Though not expected to be high in neutrino luminosity[51], these objects are abundant in the universe and might be a relevant population to contribute noticeably to the observed diffuse neutrino flux[52] as shown in Figure 1.5. This seems to be fortified by γ-ray observations as well[53].

Exotic neutrino sources

Another speculative source of high energetic neutrinos which are not related to acceleration and thus do not follow the criterion depicted in subsection 1.1.3 consider a dark matter candidate *weakly interacting massive particle (WIMP)* χ to decay to high energy neutrinos:

$$\chi \rightarrow \nu_\ell + \bar{\nu}_\ell \tag{1.13}$$

The models predict WIMP accumulation in gravity confined environments e.g. Galaxy clusters[54], or also smaller environments such as the sun[55]. Calculations exist, which attribute the measured diffuse neutrino flux to a decaying dark matter component[56]. The latter model is interesting to the analysis as the calculations fit also a suspected gap in the energy spectrum published by IceCube [23]. Data presented here can further constrain such models, as it eliminates the suspected gap in the spectrum.

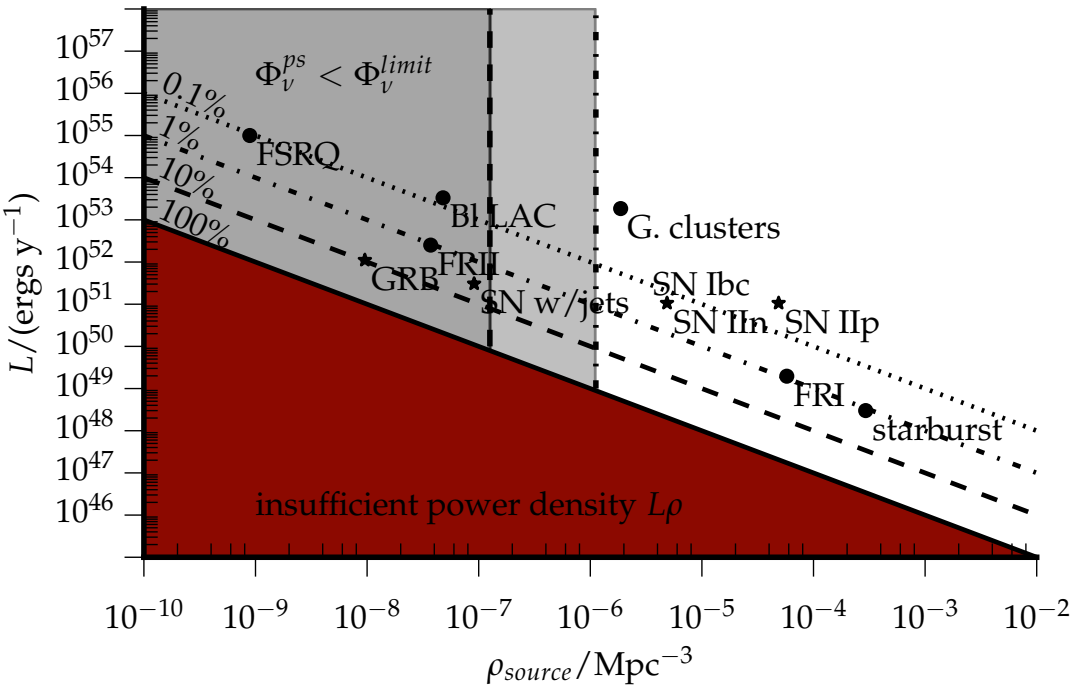

Figure 1.5 – The measured extraterrestrial diffuse neutrino flux can be accounted for by different classes of objects. If their luminosity is plotted against their source population, it is possible to constrain the contribution of several source populations to the flux. In this plot, luminosity is the luminosity in a characteristic wavelength band. Transient sources are marked with a star. The luminosity of transients in this plot refers to the energy released by a transient in a given year and the population density refers to the number density in this given year. Source populations which are in the reddish region generate not enough power to produce the measured flux. Those in the grayish area are producing per object such a high flux, that their existence is constraint by the IceCube point source limits for time-integrated and variable searches. The other lines indicate the fraction of the measured extraterrestrial flux. Figure adapted from [52].

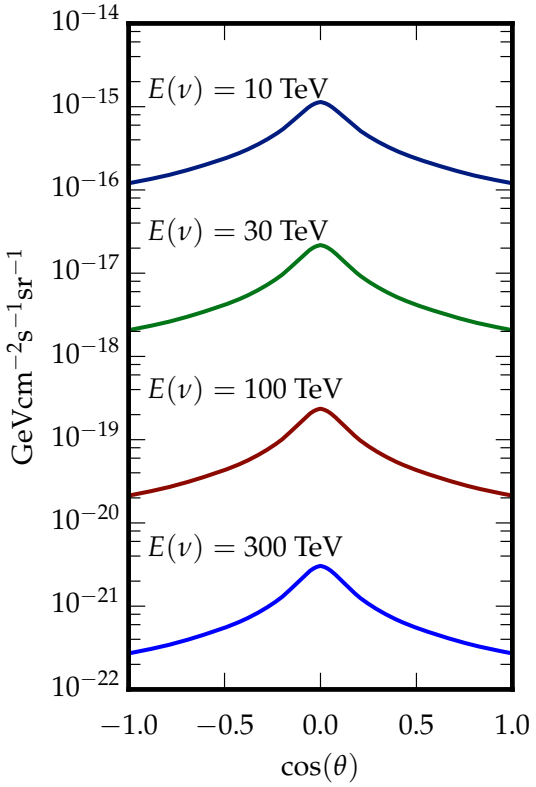

Figure 1.6 – Zenith distribution of conventional atmospheric fluxes for different energies. Plotted is the model from Honda et al.[57] where the cosmic ray model in the calculation has been updated to the model described in subsection 1.1.1. Figure adapted from [58].

1.2 Neutrinos

1.2.1 Atmospheric neutrino production

The interaction of primary cosmic rays in the atmosphere is of special interest to this work, as the muons and neutrinos created will be considered background for the extraterrestrial neutrino search presented.
Entering the atmosphere, an incident nucleus with sufficient enough energy will interact with the ambient nuclei, producing an extended air shower of secondary particles. As a process of strong interaction, hadronic fragments are emitted from the interaction vertex, at high primary energies strongly boosted in the forward region, which is in the direction of the primary shower axis. In this process pions and kaons are created, the dominant production channels are shown in Table 1.2. Subsequent interactions and decays of the hadronic fragments will feed a hadronic shower core. This core is accompanied by a muonic component, mainly fed by the decays of charged π and K mesons which are abundantly created in the hadronic interactions, and an electromagnetic

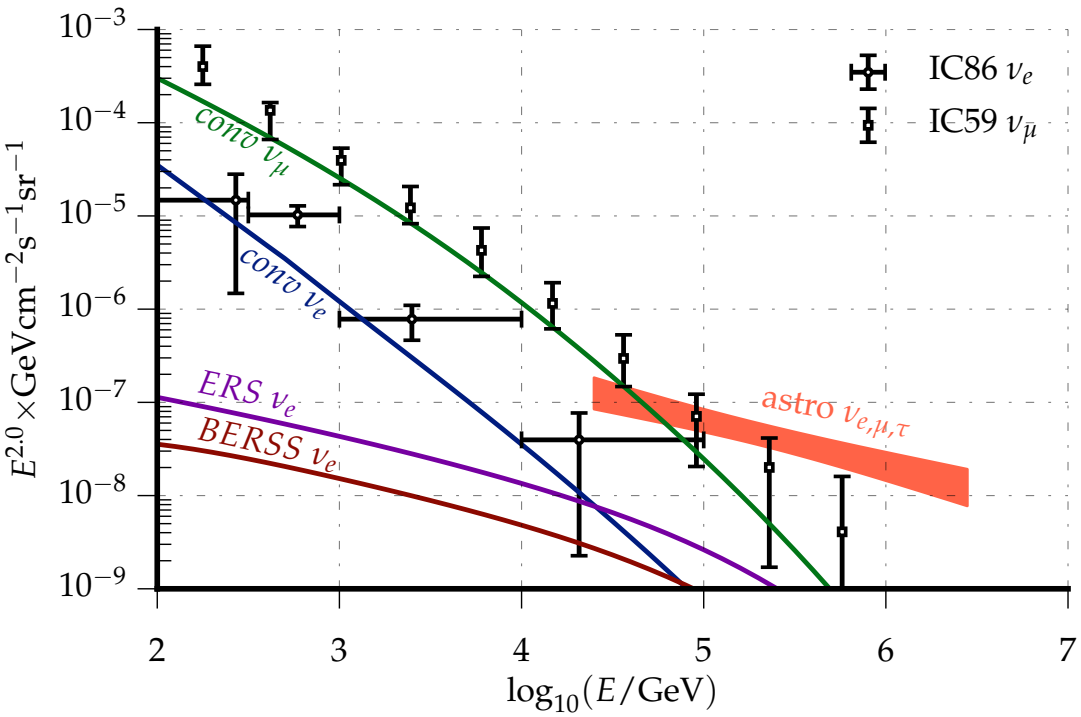

Figure 1.7 – Fluxes of neutrinos: Shown are the conventional atmospheric contributions predicted by the HKKMS07/H3a model for ν_e and ν_μ, as well as two predictions for the prompt ν_e component. The newer BERSS model is not used for the analysis. The fitted power law for the extraterrestrial ν_ℓ component obtained by a combined measurement of multiple IceCube analysis is indicated with the reddish butterfly[59]. Two measurements performed by IceCube are shown, sensitive to either the ν_e or ν_μ contribution to the conventional atmospheric spectrum [60, 61].

p + X	$\rightarrow \pi^0 + p + X$	(1.14)
p + X	$\rightarrow \pi^+ + \pi^- + p + X$	(1.15)
p + X	$\rightarrow \Lambda^0 + K^+ + p + X$	(1.16)
p + X	$\rightarrow K^+ + K^- + p + X$	(1.17)

Table 1.2 – Relevant π/K production channels. X is a placeholder for any other hadrons involved.

$\pi^{\pm}$	$\rightarrow \mu^{\pm} + \overset{(-)}{\nu}_{\mu}$	(99.9%)	(1.18)
$K^{\pm}$	$\rightarrow \mu^{\pm} + \overset{(-)}{\nu}_{\mu}$	(63.4%)	(1.19)
$K^{\pm}$	$\rightarrow \pi^{\pm} + \pi^{0}$	(20.7%)	(1.20)
K^{0}	$\rightarrow \pi^{+} + \pi^{-}$	(30.7%)	(1.21)
K^{0}	$\rightarrow \pi^{0} + \pi^{0}$	(69.2%)	(1.22)

Table 1.3 – Dominant decay channels of π and K mesons. As written, the equations for the K^0 decay channels apply only to K^0_S, K^0_L has a 67.5% probability for a semileptonic decay.

component, mostly fed by π^0 decays in the core. The electromagnetic part is fully described by the interplay of e^-e^+ pair production and the emission of bremsstrahlungs photons as further described in subsection 2.2.4. A forth component, the ν component, is formed by the decays of charged mesons from the hadronic component and the decaying μ fraction of the muonic component. For primary energies above 100 TeV the shower core reaches the ground at a high-altitude location, for lower energies or at sea level only the muonic component is measurable in addition to the always present neutrino component.
The hadronic and electromagnetic component of air showers can be measured by surface detectors, such as IceTop [62] or AUGER [10]. The μ and ν component will reach underground facilities such as IceCube. The muons and neutrinos are for the most part created in the decays of π and K, Table 1.3 gives an overview. Depending on their energy and depth in the atmosphere the mesons will propagate and might interact with the atmosphere before they decay. The main decay channels can be found in Table 1.3. The hyperon Λ^0 in Equation 1.16 will decay almost entirely to $\pi^- + p$, albeit other hyperons might be created as well instead of the Λ^0. Decaying muons will further feed the neutrino component:

$$\mu^{\pm} \rightarrow e^{\pm} + \overset{(-)}{\nu}_{\mu} + \overset{(-)}{\nu}_{e} \tag{1.23}$$

The neutrinos created in the above reactions carry about the same energy due to kinematic reasons[33] and a fraction of $\nu_\mu : \nu_e \approx 2 : 1$ is produced at energies $\lesssim 2$ GeV. Almost no ν_τ are created in the interactions and the chance other flavors oscillate to ν_τ is negligible for the here discussed oscillation lengths. The fraction however decreases with muon energy, as the fraction of muons which reach the ground increases where they quickly lose their kinetic energy before decaying into ν_e. Muons with an energy larger than $E_\mu \approx 2.5$ GeV have a typical decay length of 15 km and will reach the ground. For the muons reaching the surface of Earth, a mean energy of ≈ 4 GeV is observed[43]. For the calculation of the atmospheric neutrino fluxes in the energy region of interest for high energy extraterrestrial ν searches, the relevant muons have energies of at least 1 TeV, and thus muon decay and energy loss can be neglected. The neutrino antineutrino ratio will approximately follow the muon charge ratio. The ratio of μ^+/μ^- is not only sensitive to the net positive charge ratio in primary cosmic rays but also to the π/K ratio, due to the different contributions for π and K. The π/K ratio is dependent on the slant depth, a density weighted measure of the atmosphere traversed and thus affected by seasonal variations of the atmosphere. Measuring seasonal variations in neutrino and muon fluxes thus allows correlation studies to temperature variations in the upper atmosphere[63]. Calculations have yielded an energy, slant depth integrated value of 0.135 for the ratio K/π[40]. The result is to a certain degree supported by accelerator measurements as e.g. by ALICE[64], however the energy range and scattering angle are different. The total neutrino flux from the decays of π, K, μ and following decays is commonly referred to as "conventional" atmospheric neutrino flux and is strongly correlated to the muon flux. The total neutrino flux can be written approximately in the form[40]:

$$\Phi_\nu(E_\nu) = \Phi_N(E_\nu) \cdot \left(\frac{A_{\pi\nu}}{1 + B_{\pi\nu}\cos(\theta^*) \cdot E_\nu/\epsilon_\pi} + \frac{A_{K\nu}}{1 + B_{K\nu}\cos(\theta^*) \cdot E_\nu/\epsilon_K} \right) \quad (1.24)$$

The flux depends on the initial cosmic ray spectrum $\Phi_N(E_\nu) \sim E_\nu^\gamma$ with index γ at the neutrino energy E_ν. The parameters $A_{\pi\nu}, B_{\pi\nu}, A_{K\nu}, B_{K\nu}$ incorporate cross sections and branching ratios for the different processes. The inclination angle θ^* is the observed zenith angle on the Earth's surface, corrected for its curvature. The curvature correction is depicted in Figure 1.8. The parameters $\epsilon_\pi \approx 115$ GeV and $\epsilon_K \approx 850$ GeV are cut-off energies, above which the mesons will

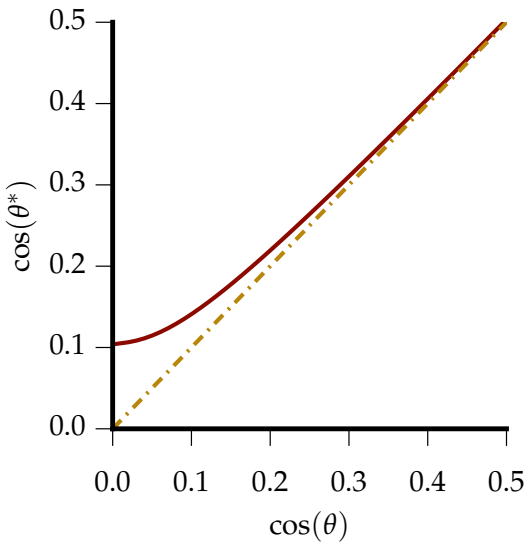

Figure 1.8 – Curvature correction. Incoming neutrinos from the zenith angle θ are observed under the angle θ^* at the Earth's surface due to its curvature. The effect is mainly noticeable at the horizon. Data taken from [65].

interact more likely than decay, resulting in a reduced neutrino production. As $\epsilon_\pi < \epsilon_K$ the contribution of neutrinos from K decays will increase with energy. For energies larger than $\epsilon_{\pi,K}$, the steepening of the ν-spectrum by about $1/E_\nu$ follows directly from Equation 1.24. In this energy regime, the decay probability increases with the length of the mean free path between interactions, imprinting a zenith dependency on the measured neutrino spectrum at the surface: Due to the less dense atmosphere column and thus increased mean free path for the mesons produced at the horizon, an increased neutrino yield compared to less inclined meson trajectories is expected.
Precise calculations of the fluxes are non trivial[57]. Main uncertainties in the calculation arise due to the uncertainty in the composition of the primary cosmic ray spectrum as well as due to the uncertainty on the relative π/K production yields. The latter is known at the level of 10%[66], recent measurements predict a slightly higher value, however compatible with the original prediction[67]. Since more accurate cosmic ray models have become available since 2006, the original calculation by Honda et al.[57] which included only a single power law was updated with the model described in subsection 1.1.1.

High energetic neutrinos from prompt decays of charmed mesons

Beyond neutrino energies of about 100 TeV, a third yet unmentioned component of the atmospheric neutrino flux becomes dominant. The energy of incident cosmic rays is high enough to produce charmed mesons in the atmo-

Table 1.4 – Entities of the standard model, grouped as left handed weak isospin doublets. The symbols d', s', b' describe the eigenstates of the weak interaction, which are superpositions of the quark flavor eigenstates of the strong interaction.

FERMIONS			
QUARKS	$\begin{pmatrix} u \\ d' \end{pmatrix}_L$	$\begin{pmatrix} c \\ s' \end{pmatrix}_L$	$\begin{pmatrix} t \\ b' \end{pmatrix}_L$
LEPTONS	$\begin{pmatrix} e \\ \nu_e \end{pmatrix}_L$	$\begin{pmatrix} \mu \\ \nu_\mu \end{pmatrix}_L$	$\begin{pmatrix} \tau \\ \nu_\tau \end{pmatrix}_L$
BOSONS			
g	$W^\pm$	Z^0	H

sphere, which will decay promptly without further interactions and provide a source for high energy atmospheric neutrinos with a harder spectrum than conventional neutrinos. This component is commonly referred to as "prompt" atmospheric neutrinos. The primary interactions which contribute dominantly to the prompt ν flux are the production of $D^\pm, D^0, D_S^\pm$ mesons and their antiparticles as well as the hyperon Λ_C^+. The reactions can be seen in some sense as the charmed counterpart to Equation 1.16 and Equation 1.17, and decay modes of these particles include often K and ν in their final states. In these decays ν_μ and ν_e are produced in equal numbers, and there is also a small ν_τ contribution of about 1/20 of the ν_μ/ν_e flux, as $D_S^\pm$ has about a 5.4% chance to decay to $\tau^\pm + \nu_\tau$[43]. The precise calculation needs the knowledge of the cross section for gluon and quark fusion in the forward region at small values of Bjorken x, which are difficult to obtain from collider experiments. A calculation of the neutrino fluxes using pertubative QCD is presented in[68]. Since new measurements of the cross section became available, the calculation was updated[69], also switching from a broken power law cosmic ray model to the model described in subsection 1.1.1

1.2.2 Neutrinos in and beyond the standard model of particle physics

The standard model of particle physics is a compilation of quantum field theories, which comprises the description of elementary particles and interactions, where elementary means without further internal structure and thus assumed

as point-like[70, 71]. The elementary particles which build up all baryonic matter[1] are listed in Table 1.4 together with the gauge bosons of the two forces *electro-weak* and *strong* - or three if one considers electro-magnetism and the weak force separately. In the standard model, the neutrino is a only weakly interacting, massless, uncharged fermion with a spin of 1/2. Three different flavors of neutrinos are present in the standard model, that is electron (e), muon (μ) and tau (τ) flavor. During creation, neutrinos are produced with a fixed flavor. The standard model is well accepted to describe and predict particle interactions at high precision, and the recent discovery of a standard model predicted Higgs boson at the *Large Hadron Collider* experiments[72] further increased trust in the model's predictions.
Despite its predictions being well fortified by experiments, the standard model falls short to explain all observed phenomena in recent particle physics, e.g. it seems not to be able to provide a candidate particle which to explain dark matter and fits in the current most promising models[73]. More related to this work and thus further discussed in subsection 1.2.3 is the discovery of neutrino oscillations. Neutrino oscillations refer to a change of flavor for neutrinos while traveling. This mechanism was identified to solve the puzzle of the lack of solar neutrinos in early neutrino experiments[74]. The discovery of neutrino oscillations has not been predicted by the standard model, where the neutrinos are considered massless and thus fail a necessary requirement for oscillations.
A particle property important in the context of neutrinos is the helicity, which is the projection of the spin on the particle momentum. Spin 1/2 particles thus can have two helicity eigenstates, which are figuratively denoted as left and right handed. Switching between these eigenstates requires a mass term. As in the standard model neutrinos are considered massless, and due to the maximum parity violation of the weak interaction they are always produced with the same helicity. This means that only left handed neutrinos and right handed anti-neutrinos exist. Due to CPT invariance, which is the transformation under the charge, parity and time operators, anti neutrinos are always produced right handed. The prediction of this is seconded by experiment where the absence of right-handed neutrinos has been measured beyond doubt[75]. Such neutrinos might exist, however it will be a challenge to detect them, since they can

[1] which in this context means everything which does not consist out of dark matter. Dark matter is not described in the current version of the standard model

only interact via Z boson exchange in comparison to standard model neutrinos which interact via Z and W boson exchange. In consequence, these *sterile* neutrinos provide dark matter candidates. Searches have been ongoing and limits have been set[76].
At present day it is unclear if the neutrino is its own antiparticle - then only left and right handed neutrinos would exist, or if it is not in which case four neutrinos would be possible, two of them either *sterile* or non-existent. Promising experiments to solve the issue are currently performed[77].

1.2.3 Neutrino oscillations

The discovery of flavor mixing in the quark sector raises the question if flavor mixing can also happen in the lepton sector. The idea was first formulated by Gribov and Pontecorvo[78], however for oscillations between neutrino and antineutrino. Neutrino flavor oscillation models then became popular as a possible solution to solve the solar neutrino puzzle, a discrepancy in expected and observed solar neutrino fluxes in early experiments[79].
The proposed flavor mixing will allow a neutrino to change its flavor during propagation. To generate such a mechanism the eigenvectors of the propagator operator $\hat{H}$ must not be degenerated which means that the Hamilton operator $\hat{H}$ requires a mass term[1]. To observe the effect, the wave packets for the different mass eigenstates need to overlap coherently. This is the case if the uncertainty on the mass at production of the neutrino is in the order of the differences of the values for the different masses. The suspected masses for neutrinos are small enough that due to the smearing of energy and momentum caused by the uncertainty principle the uncertainty on the mass at production is high enough.
To elaborate on the idea of neutrino mixing, we will first look at the time development $|\nu_i(t)\rangle$ of the neutrino $|\nu_i(t_0\rangle$:

$$|\nu_i(t)\rangle = \exp\left(\frac{-i}{\hbar}Et - \vec{p}\vec{x}\right)|\nu_i(t_0)\rangle \tag{1.25}$$

[1] Two different scenarios which allow a neutrino mass term exist: *Dirac* or *Majorana* type neutrinos. In both cases, the mass term occurs due to the coupling of the left-handed neutrino to its non-standard model right-handed partner. In the *Dirac* scenario 4 different neutrinos per flavor exist, $\nu_L, \nu_R, \bar{\nu_L}, \bar{\nu_R}$. In the *Majorana* scenario there are only two, due to the equality of ν and $\bar{\nu}$.

Assuming a small neutrino mass m and a highly relativistic neutrino $m \ll E$, the absolute value of the momentum $\vec{p}$ can be approximated:

$$p \approx \frac{1}{c}\left(E - \frac{m^2c^4}{2E}\right) \tag{1.26}$$

The neutrino itself is created in a weak interaction, and thus created as an eigenstate of the operator of the weak isospin, which assigns a flavor α to the neutrino. This flavor eigenstate $|\nu_\alpha\rangle$ is propagated after its creation:

$$|\nu_\alpha\rangle = \sum_i |\nu_i\rangle\langle\nu_i|\nu_\alpha\rangle = \langle\nu_i|\nu_\alpha\rangle \exp\left(\frac{-i}{\hbar}\frac{m_i^2c^4}{2E}\frac{L}{c}\right)|\nu_i\rangle \tag{1.27}$$

where the high energy approximation Equation 1.26 and the substitution of $t = L/c$ is used, with L being the distance traveled by the neutrino. Constraints on the matrix elements $\langle\nu_i|\nu_\alpha\rangle = U_{\alpha i}$ are given as the time evolution operator is self-adjoint and thus the matrix U must be unitary. In consequence the amount of free parameters of U is reduced from 18 to 9, and 5 of the remaining parameters can be absorbed by the neutrino fields if Dirac type neutrinos are assumed.
The 4 free parameters of U are typically written as three rotation angles and a CP violating phase. Thus the matrix U can be written as:

$$U = \begin{pmatrix} 1 & 0 & 0 \\ 0 & c_2 & s_2 \\ 0 & -s_2 & c_2 \end{pmatrix} \cdot \begin{pmatrix} c_1 & s_1 & 0 \\ -s_1 & c_1 & 0 \\ 0 & 0 & 1 \end{pmatrix} \cdot \begin{pmatrix} 1 & 0 & 0 \\ 0 & 1 & 0 \\ 0 & 0 & e^{i\delta} \end{pmatrix} \cdot \begin{pmatrix} 1 & 0 & 0 \\ 0 & c_3 & s_3 \\ 0 & -s_3 & c_3 \end{pmatrix} \tag{1.28}$$

with the abbreviations $c_i = \cos(\theta_i)$, $s_i = \sin(\theta_i)$. The transition amplitude $A(\alpha \to \beta)$ follows from Equation 1.27

$$A(\alpha \to \beta) = \langle\nu_\beta|\,|\nu_\alpha\rangle = \sum_i U_{\alpha i}U^*_{\beta i} \exp\left(\frac{-i}{\hbar}\frac{m_i^2c^4}{2E}\frac{L}{c}\right)|\nu_i(t_0)\rangle \tag{1.29}$$

A non-zero CP violating phase in the matrix U results in different transition amplitudes $A(\alpha \to \beta) \neq A(\beta \to \alpha)$. The transition or survival probabilities

respectively are the absolute value of the square of the amplitudes, e.g.:

$$P(\nu_\alpha \to \nu_\beta) = \left|\langle \nu_\alpha | \nu_\beta \rangle\right|^2 \tag{1.30}$$

$$= \underbrace{\sum_i |U_{i,\alpha} U^*_{\beta_i}|}_{\text{(I)}} + \underbrace{2Re \sum_{j>i} U_{\alpha i} U^*_{\alpha j} U^*_{\beta i} U_{\beta j} \exp\left(\frac{-i}{\hbar}\Delta_{ij}\right)}_{\text{(II)}} \tag{1.31}$$

The term (I) in Equation 1.31 describes an average transition probability for all energies or distances respectively. The measurement of the average transition probability allows to infer the mixing angles, however not the relative mass differences.
The term (II) in Equation 1.31 is the oscillatory term, with the phase difference $\frac{\delta m^2_{ij}}{2} \cdot \frac{L}{E}$ and describes the time or respectively distant dependent oscillations. Measuring this term allows to infer the relative mass differences. For the 2 flavor case where no CP violating term exist, Equation 1.31 can be simplified to:

$$\approx \sin^2(\theta_{12}) \sin^2 \frac{\Delta}{2} \tag{1.32}$$

where Δ can be written as $\Delta = 2\pi \frac{L}{L_0}$ with the oscillation length L_0:

$$L_0 = 4\pi\hbar c \frac{E}{|\delta m^2|} \tag{1.33}$$

The 4 parameters of U are not constrained by the standard model and have to be measured. Measuring the values for δm_{ij}, it is found that one is much larger than the other. This leads to two scenarios for the individual neutrino masses, with two neutrino mass states being relatively lightweight - this is called *normal hierarchy* - or both relatively heavy compared to the third state. The latter scenario is denoted as *inverted hierarchy*. In both scenarios effectively a two flavor mixing is observed as the mixing angle θ_{13} is small. Looking at the current best estimates for these parameters as given in Table 1.5, one find that this is indeed realized in nature, and thus also justifies the simplification of Equation 1.31 a posteriori. For measuring neutrino oscillations in experiments, the effective two flavor mixing can be described with the parameters δm^2_{small}, δm^2_{large} and two mixing angles. Dependent on the hierarchy detectors with a fixed L/E might be sensitive to only δm^2_{small} or δm^2_{large}. Which hierarchy - *normal* or *inverted* - is realized in nature is still an open question.

	normal hierarchy	inverted hierarchy
$\sin^2(2\theta_{12})$	0.846 ± 0.021	-
δm^2_{12}	$(7.53 \pm 0.18) \times 10^{-5}\text{eV}^2$	-
$\sin^2(2\theta_{23})$	$0.999^{+0.001}_{-0.018}$	$1.000^{+0.000}_{-0.017}$
δm^2_{23}	$(2.44 \pm 0.06) \times 10^{-3}\text{eV}^2$	$(2.52 \pm 0.07) \cdot 10^{-3}\text{eV}^2$
$\sin^2(2\theta_{13})$	$(9.3 \pm 0.08) \times 10^{-2}$	-

Table 1.5 – Numerical values for neutrino oscillation parameters, taken from [43].

1.2.4 The cosmic ray neutrino connection

Neutrinos are produced when cosmic rays interact with the ambient medium around their sources. The main production channel is the emission of π mesons by proton interactions, yielding neutrinos in the decay chain of secondaries from the π decay. In the most general picture, the protons at the astrophysical source are accelerated by shock acceleration (see subsection 1.1.2). The acceleration takes place in a denser region, which also acts as the interaction region for the accelerated protons.
In general the interaction region might either be a sort of material cloud, a photon field or a composition of both. Accelerated protons then might either scatter off nuclei, mostly protons, or interact with the ambient photon field. In general this leads to pion production as described in Equation 1.34.

$$p + X \rightarrow \begin{cases} p + \pi^0 + Y \;\; (I) \\ n + \pi^+ + Y \;\; (II) \end{cases} \tag{1.34}$$

Besides neutrinos, high energetic γ from the decay of π^0 in (I) are produced as well. The created neutron in (II) will be able to leave the source and regenerate a high energetic proton by its decay: $n \rightarrow p + e^- + \bar{\nu}_e$. Only about 1/100 of the fraction of the parent energy is transferred to the neutrino in this case, and thus the fluxes of detectable neutrinos for current neutrino telescopes are very low.
If X from Equation 1.34 represents a photon field, then the dominant reaction chain is typically started by the creation of the Δ^+ resonance, hence this channel becomes effective at the energy required to produce Δ^+. It might be noted, that in the case of dominant photohadronic production of neutrinos, mostly

neutrinos are produced while the production of anti-neutrinos is suppressed. However the neutrino anti-neutrino ratio depends on the specific source characteristics. In the case of IceCube, an observation of a Glashow resonance (see subsection 2.1.2) event would be a clear signal for an anti-neutrino, and thus observations or non-observations of Glashow resonance events can be linked to the production scenario, however the expectation of such a signal is about 1 event per year[63]. As no further interactions of the secondaries are assumed, the energy spectrum of the created neutrino beam would follow the spectrum of primary protons in the pp case, however for $p\gamma$ it depends on the γ spectrum as well. The flavor ratio of produced neutrinos at source in these scenario is fixed to 1:2:0 as π decay is assumed, with a negligible contribution of ν_τ. This ratio can be changed by assuming muon cooling, where the muons radiate most of their energy before they decay or an incident pure neutron beam instead of protons. The measurement of the flavor ratio might be able to distinguish between the different scenarios[80]. The individual flavor fluxes at Earth however are altered due to neutrino oscillation. The individual flavor fluxes F_{ν_α} can be calculated via:

$$F_{\nu_\alpha}(L, E) = \sum_\beta P_{\alpha,\beta}(L, E) F^0_{\nu_\beta} \tag{1.35}$$

With the numerical values from Table 1.5, a close to equal flavor ratio at Earth of the order of 1:1:1 can be calculated for a 1:2:0 ratio at the production site: For a 10 TeV neutrino, it follows that after a distance which is comparable to or larger than the extension of the solar system, the 1:1:1 flavor ratio at Earth is realized[81]. Such extended sources are indeed realized, e.g. in the case of AGN.

Diffuse neutrinos

When cosmic rays are produced in hadronic accelerators, this yields a guaranteed neutrino flux through the decay of charged pions, as described in subsection 1.2.4. A theoretical upper bound based on the observed cosmic-ray density for the intensity of this flux has been calculated[82] and served before the discovery of that flux[23] as benchmark scenario for diffuse neutrino searches, the work presented here included. Assumptions made in this calculation include a photo nuclear production mechanism of neutrinos by cosmic rays of the high-

est energy in jets of *active galactic nuclei* (AGN). The photo nuclear mechanism is preferred over the pp case, as it is thought that the cosmic rays are able to interact only once, as the created neutrons are highly boosted and live long enough to escape the source. The calculation has also been performed assuming a production of neutrinos in *gamma ray bursts* (GRB). However the limit derived from AGN production was found to be less stringent. From measurements of charged cosmic ray intensity as e.g. done here[83], a cosmic ray production rate $\dot{\epsilon}_{CR} \sim 4 \cdot 10^{44}\text{ergMpc}^{-3}\text{yr}^{-1}$ for the energy region of $10^{19} - 10^{21}$ eV is inferred. Assuming the generation spectrum to be E^{-2} following the prediction of the Fermi acceleration mechanism described in subsection 1.1.2, an energy dependent cosmic ray production rate can be formulated:

$$E_{CR}^2 \frac{d\dot{N}}{dE_{CR}} = \frac{\dot{\epsilon}_{CR}}{\ln(10^{21}\text{eV})/\ln(10^{19}\text{eV})} \approx 10^{44}\text{ergMpc}^{-3}\text{yr}^{-1} \tag{1.36}$$

The production rate of neutrinos in this energy interval can be estimated by multiplying the value from Equation 1.36 by a factor $\varepsilon < 1$ which is the fraction of "beam" energy which is transferred to secondaries in $p\gamma$ interactions. An additional factor of $1/2$ is introduced as charged and neutral pions are produced about equally in $p\gamma$ interactions, and an additional factor of $1/2$ accounts for the fact that about half the energy of a decaying pion is transferred to the neutrino. To calculate the neutrino flux from the production rate one multiplies the rate with the Hubble time t_H. Since this assumes a constant production of cosmic rays per comoving unit volume of the universe it needs to be taken into account, that the production of charged cosmic rays in this energy range evolves with the density and luminosity of their sources and that they interact with the CMB photons. This is taken into account by a correction factor ξ_Z, which also includes the luminosity evolution with time of the AGN in question.
Altogether, this gives a flux of (anti) ν_μ from pion decay of:

$$E^2\Phi_\nu = \frac{c}{4\pi}\frac{1}{4}t_H\xi_Z\epsilon E_{CR}^2\frac{d\dot{N}}{dE_{CR}} \tag{1.37}$$

Assuming that the luminosity evolution of AGN follows the star formation rate[84] leads to a value of $\xi_Z \approx 3$. Together with the most conservative value

$\epsilon = 1$ an upper bound for $\nu_\mu + \bar{\nu_\mu}$ from AGN can be calculated:

$$E_\nu^2 \Phi_{\nu_\mu} \approx 2.25 \cdot 10^{-8} \mathrm{GeV} \cdot \mathrm{m}^{-2} \mathrm{s}^{-1} \mathrm{sr}^{-1} \tag{1.38}$$

Updated cosmic ray measurements which reduced the flux quoted in Equation 1.36 led to a reduction of the lower bound[85]. The current value, multiplied by 3 to obtain a value for an all-flavor upper bound is then finally found to be:

$$E_\nu^2 \Phi_\nu \approx 3 \cdot 10^{-8} \mathrm{GeV} \cdot \mathrm{m}^{-2} \mathrm{s}^{-1} \mathrm{sr}^{-1} \tag{1.39}$$

2

Measurement of neutrino interactions in ice

2.1 Neutrino interactions

2.1.1 Deep inelastic neutrino nucleon scattering

Neutrinos are uncharged, weakly interacting particles as described in subsection 1.2.2. The interaction mediators are the three bosons of weak interaction $W^{\pm}$ and Z^0. Interactions via the charged bosons are denoted as charged current (CC) interactions whereas Z^0 interactions are denoted as neutral current (NC) interactions. In the case of neutrino nucleon interaction, depending on its energy the neutrino interacts with one of the sea or valence quarks inside the nucleons, transferring energy and momentum, which leads to a fragmentation of the nucleon and subsequent hadronization of the fragments. The process is denoted as deep inelastic neutrino nucleon scattering (DIS):

$$\nu_\ell + n \rightarrow \nu_\ell + hadrons \quad (NC) \tag{2.1}$$

$$\nu_\ell + n \rightarrow \ell + hadrons \quad (CC) \tag{2.2}$$

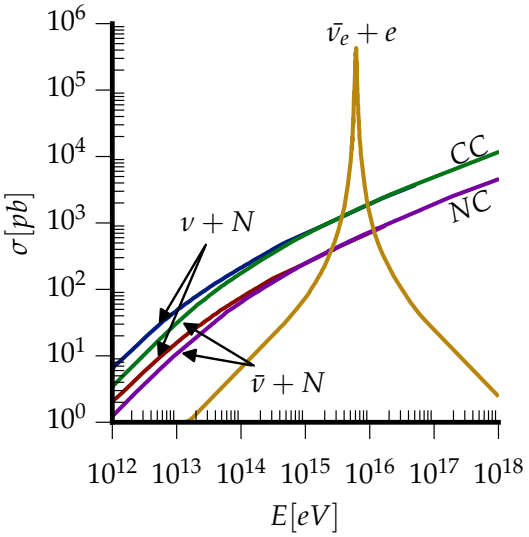

Figure 2.1 – DIS neutrino nucleon cross sections. The cross section for the resonant antineutrino electron scattering (Glashow resonance) is plotted as well. Figure adapted from [86].

where ν_ℓ is the incoming neutrino of flavor ℓ, n is an isoscalar nucleon and ℓ denotes the corresponding partner lepton.
As the lepton in the final state determines the topology of the observed hit pattern in IceCube, its further propagation and interaction with the target material is discussed in section 2.5.
In terms of the Bjorken variables x and y the DIS cross section is expressed by[87]:

$$\frac{d^2\sigma}{dxdy} = \frac{G_F^2 M E_\nu}{\pi} \begin{cases} 2\left(\frac{M_W^2}{Q^2+M_W^2}\right)^2 \left[xq(x,Q^2) + x\bar{q}(x,Q^2)(1-y)^2\right] & (CC) \\ \frac{1}{2}\left(\frac{M_Z^2}{Q^2+M_Z^2}\right)^2 \left[xq^0(x,Q^2) + x\overline{q^0}(x,Q^2)(1-y)^2\right] & (NC) \end{cases} \tag{2.3}$$

where G_F is the Fermi constant, M the mass of the target nucleon, E_ν the incoming neutrino energy, M_Z and M_W are the masses of the $W^\pm$ and Z^0 Bosons. The invariant momentum transfer is given by Q^2 and the Bjorken variables $x = Q^2/(2M(E_\nu - E_{\nu',l}))$ and $y = 1 - E_{\nu',\ell}/E_\nu$ describe the fraction x of the nucleon momentum carried by the interacting parton and the fraction y of the neutrino energy transferred to this parton. ν', ℓ indicate the neutrino or lepton respectively in the final state. The functions $q, \bar{q}, q^0, \overline{q^0}$ are the parton distribution functions, which are derived from experimental observations of DIS processes. The cross section in the energy range interesting for IceCube can not be measured directly, and is thus extrapolated from lower energies[88].

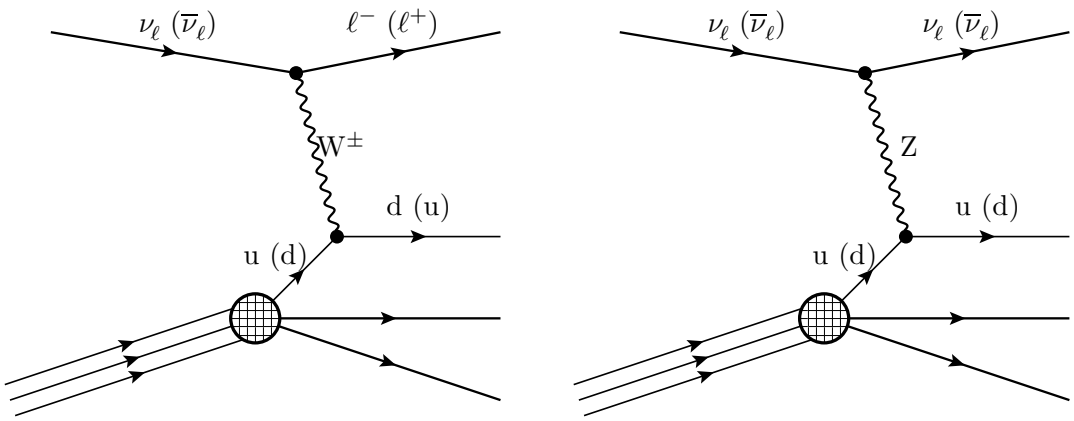

Figure 2.2 – Feynman diagrams for DIS scattering. Time dimension on the horizontal axis increasing to the right.

For low neutrino energies the momentum transfer Q^2 is much smaller than the mass of the exchanged boson, and the cross section scales linearly with the neutrino energy. At an energy of about $E_\nu \approx 10^4$ GeV, the term $[M^2_{W,Z}/(Q^2 + M^2_{W,Z})]^2$ suppresses the cross section, and it rises more slowly in the order of $\sigma \propto E_\nu^{0.4}$. At low energies where the valence quarks dominate the parton density distribution function, the cross section for antineutrino nucleon scattering is lower than for neutrino nucleon interactions, but with increasing energy, the contribution of sea quarks gets larger and the cross sections for both processes converge.

2.1.2 Neutrino electron scattering

The cross section for neutrino electron scattering is lower compared to the neutrino nucleon cross section by 4 orders of magnitude[58]. However, the situation is different in the case of anti-electron neutrino electron scattering. The $\bar{\nu_e} e^-$ cross section reveals a strong peak at an energy of about $E_{\bar{\nu_e}} \approx M^2_W/2M_e \approx$ 6.3PeV[89], as can be seen in Figure 2.1. At this resonance the energy of the $\bar{\nu_e}$ is sufficient to produce a W^- boson in the electron scattering process, as illustrated in Figure 2.3. The W^- then decays via the following channels:

$$W^- \rightarrow hadrons \;\; (67.6\%)$$
$$W^- \rightarrow \ell^- + \nu_\ell \;\; (10.8\% \;\; \text{for each} \;\; \ell = e, \mu, \tau)$$

At the peak energy, the cross section for the resonance is about 300 times higher than the cross section for neutrino nucleon scattering[58]. As the resonance

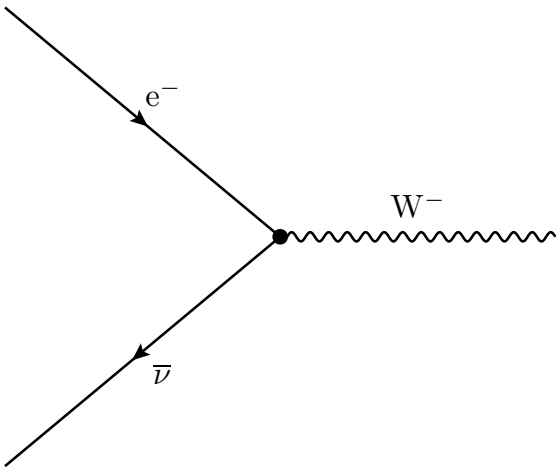

Figure 2.3 – Feynman graph of resonant W^- production for an incoming antineutrino with 6.3 PeV. Time dimension on the horizontal axis increasing to the right.

can only be observed for anti-neutrinos, it is possible to constrain production mechanisms at the neutrino source, assuming no transition probability for $\bar{\nu} \rightarrow \nu$. In the case that proton-photon collisions are the dominant process at the source, the π^- production is suppressed, hence the anti electron neutrino yield is suppressed as well.

2.2 Interactions of secondaries

The energy loss processes of charged particles produced in DIS processes at energies relevant for this work are listed in the following. Besides ionization processes as described in subsection 2.2.1, which lead to a smooth energy loss profile, particles will lose energy via radiative processes as discussed in subsection 2.2.2. These processes are of special interest in this work are as these produce the shower type signatures the event selection of this analysis is designed for. Although the energy loss via Cherenkov radiation is negligible, as it is the key process for particle detection in IceCube, it will be discussed in subsection 2.2.3.

2.2.1 Ionization

Charged particles with masses $m \gg m_e$ and medium energies entering a target material will scatter inelastically with the bound electrons of the target. In most of the individual scattering processes only small amounts of energy are

transferred - less than 100 eV in about 90% of the processes[43]. However these processes are frequent. The differential cross section of the process was calculated by applying corrections to the Rutherford differential cross sections for a free electron gas[90]. The stopping power of the target material is described by the average negative energy loss per unit length $dx = \rho ds$ with the density ρ of the target material and path infinitesimal ds[43]:

$$-\left\langle \frac{dE}{dx} \right\rangle = Kz^2 \left(\frac{Z}{A}\right) \frac{1}{\beta^2} \left[\frac{1}{2} \ln \left(\frac{2m_e c^2 \beta^2 \gamma^2 T_{max}}{I^2} \right) - \beta^2 - \frac{\delta(\beta\gamma)}{2} \right] \tag{2.4}$$

The constant K in units of $\mathrm{MeVg^{-1}cm^{-2}}$ depends on the target material, z is the charge of the incident particle, β its relativistic speed, m_e the electron mass, c the speed of light, the Lorentz-factor $\gamma = (1 - 1/\beta)^{-1}$, T_{max} describes the maximum amount of energy transferred in an individual collision and the number I gives the mean excitation energy for the target material.
The correction β^2 describes the contribution of the spin to the cross section, the term $\delta(\beta\gamma)$ is associated with the density effect[91]. The density effect describes a reduction of the energy loss for particles with relativistic velocities, as these might undergo collisions with a large value of the maximum impact parameter b_{max}. High density materials, where the average distances between the atoms are small compared to b_{max}, will then be effectively polarized, due to the overlap of the atomic electromagnetic fields, which reduces the amount of energy transferred in these collisions.
It has to be noted that for cases where the kinetic energy of the knocked on electron is larger than its ionization energy I the electron is emitted as δ-ray, however this is a rare process.

2.2.2 Radiative energy loss processes

Bremsstrahlung

For particles with high energies or low masses, bremsstrahlung is the dominant energy loss mechanism. Interacting with the Coulomb field of an nucleus of the ambient material, the particle is deflected and thus emits radiation.
However, it has to be noted that the electric field of the atomic nucleus is screened by its electron cloud, which alters the nucleus' field, especially in larger distances where the actual interaction is happening. The cross section

of the emitted radiation in terms of the energy k of the radiated photon for this "complete screening case" is given by[43]:

$$\frac{d\sigma}{dk} = \frac{A}{X_0 N_A k}\left(\frac{4}{3} - \frac{4}{3}y + y^2\right) \tag{2.5}$$

Where A is the atomic number of the ambient matter, and N_A is Avogadro's number. The quantity $y = k/E$ is the fraction of the incoming particle energy transferred to the photon. The constant X_0 is called radiation length and is material dependent. The equation is valid for the "infrared limit" for small y and accurate to 1.7 - 2.5% dependent on the Z of the target material[43]. Integrating over all possible energy losses k of a particle weighted by the cross section for each unit length $\delta s = 1/\rho dx$ yields the differential energy loss in the limit for $\delta s \to 0$:

$$\delta E = -\delta s \int_0^E k \frac{d\sigma}{dk} dk \tag{2.6}$$

The integration is elementary and yields:

$$\frac{dE}{dx} = -\frac{A}{X_0 N_A} E \rightarrow \quad E(x) = E_0 \exp(-x/X_0) \tag{2.7}$$

The energy loss by bremsstrahlung rises linear with the incident particle energy. The definition of X_0 as the radiation length is justified in this relation as X_0 describes the length after which the particle has lost all but $1/e$ of its energy.

Pair production

Closely related to bremsstrahlung, as indicated by the similar Feynman diagrams shown in Figure 2.4, a high-energy photon may convert to an electron positron pair in the Coulomb field of the nucleus, which is able to absorb momentum. The cross section in the "complete screening case" is given in units per $x = E/k$, the fractional energy transfer to the electron:

$$\frac{d\sigma}{dx} = \frac{A}{X_0 N_A}\left[1 - \frac{4}{3}x(1-x)\right] \tag{2.8}$$

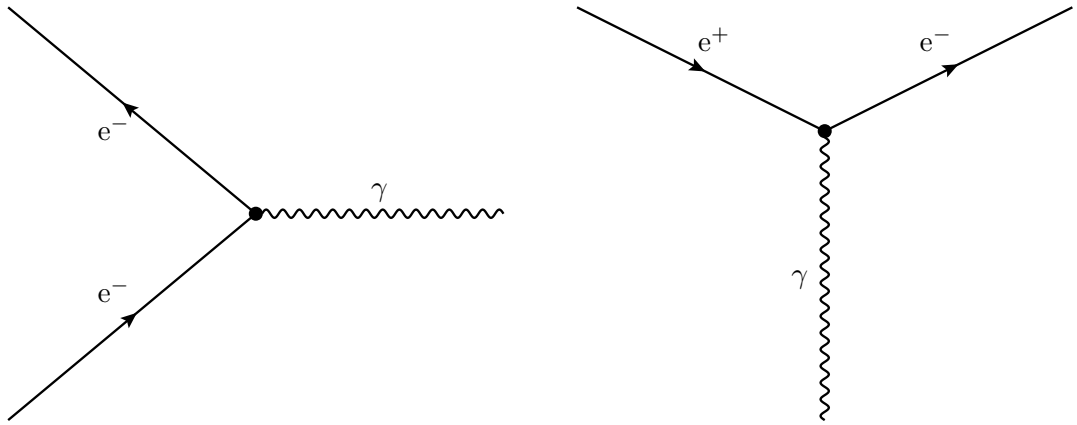

Figure 2.4 – Truncated graphs of bremsstrahlung (left) and pair production (right) processes. Time dimension on the horizontal axis, increasing to the right.

which can be easily integrated over all fractional energy transfers $x \in [0,1]$ to find the total cross section:

$$\sigma = \frac{7}{9}(A/X_0 N_A) \tag{2.9}$$

which is valid in the high energy limit down to a few GeV.

2.2.3 Cherenkov light

The polarization of the ambient medium due to a relativistic particle does not only lead to a reduction of the energy loss of the incident particle as it is described by the density effect (see subsection 2.2.1), but also to a contribution of the electric field in distances far away from the incident collision with the electron, as can be seen when solving the field equations for the density effect in the limit of large distances[92].
This radiation was first observed by P.A. Cherenkov while studying the luminescence of different solvents under the influence of gamma radiation, which he performed together with S. Vavilow[93].
The angle θ_C under which the Cherenkov radiation is emitted can be calculated by:

$$\cos(\theta_C) = \frac{1}{n\beta} = \frac{c'}{v} \leqslant 1 \tag{2.10}$$

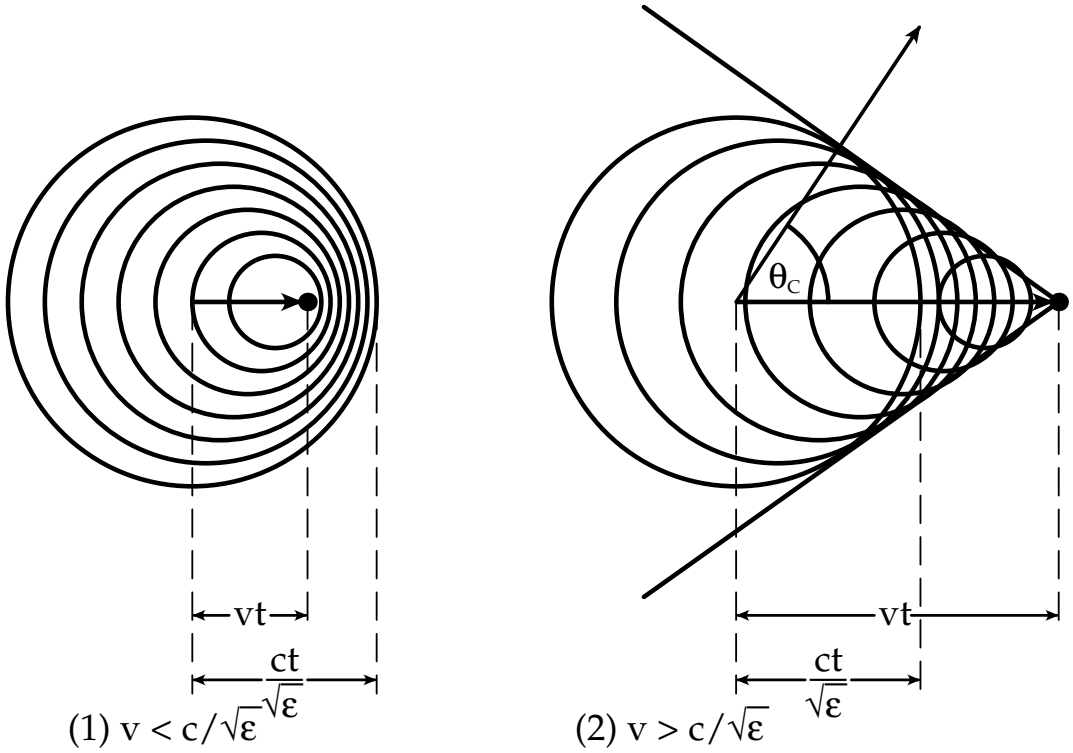

Figure 2.5 – A charged particle moving through a medium with a velocity smaller than local phase speed of light (1) and a velocity larger than the phase speed of light (2). Shown is the Huygens constructions of wavefronts for each emitting electron cloud, which interfere constructively in the case for a particle moving faster than the local speed of light. Figure adapted from [92].

with the relativistic velocity of the particle β, the refractive index of the material n and the phase speed of light c' in the medium. For a given medium with refractive index n the angle θ_C is only dependent on β, which can be assumed to be close to unity. For highly relativistic particles ($\beta \approx 1$), the detection of Cherenkov light allows a precise reconstruction of the direction of the particle track. Although Cherenkov radiation is a negligible mechanism of particle energy loss, the number of emitted Cherenkov photons scales linearly with the particle track length and thus provide a measure for it. The particle track length can then be used to derive proxies for the energy. The number of photons N created per unit length dx and energy dE is given by[43]:

$$\frac{d^2N}{dEdx} = \frac{\alpha z^2}{\hbar c}\sin^2(\theta_C) = \frac{\alpha^2 z^2}{r_e m_e c^2}\left(1 - \frac{1}{\beta^2 n^2(E)}\right) \tag{2.11}$$

with the fine-structure constant α, Dirac's constant $\hbar$, the classical electron radius $r_e = e^2/4\pi\epsilon_0 m_e c^2$ and the electron mass m_e. To obtain the number of emitted photons in a detector sensitive for a wavelength interval $[\lambda_1, \lambda_2]$, the substitution $E \rightarrow \frac{c\hbar}{\lambda}; dE \rightarrow \frac{d\lambda}{\lambda^2}$ is used to integrate Equation 2.11 over the sensitive wavelength interval of an IceCube optical module $\lambda \approx [350nm, 600nm]$ including the absorption of the glass housing in the near UV. With $\theta_C \approx 41^\circ$ for ice, this yields

$$\frac{dN_\gamma}{dx} \approx 260\text{cm}^{-1} \tag{2.12}$$

2.2.4 Electromagnetic cascades

Electromagnetic cascades, particle showers consisting only of $e^\pm$ and photons, are created by electrons at even moderate energies, due to their high cross section for bremsstrahlung. If the emitted bremsstrahlung photon has an energy above two times the electron mass, an electron-positron pair can be created, which itself can emit further bremsstrahlung photons.
The physics of electromagnetic cascades is described by the interplay between bremsstrahlung and pair production, two scaling variables are of further use to describe the characteristics of such a cascade:

$$t = x/X_0 \quad y = E/E_c \tag{2.13}$$

Material	$X_0[g \cdot cm^{-2}]$	E_{crit} for e^- [MeV]	E_{crit} for μ [GeV]
Air (dry, 1 atm)	36.62	87.92	1115
Water (ice)	36.08	78.99	1035
Water (liquid)	36.08	78.33	1029
Fe	13.84	21.68	347
Pb	6.37	7.43	141

Table 2.1 – Radiation lengths and critical energies of different target materials of interest. Numbers taken from [43].

with t being a measure of the longitudinal distance x in terms of the radiation length X_0 and y being a measure of the cascade energy in fractions of the critical energy E_c. The radiation length X_0 is an important quantity for the development of cascades, as it describes the mean distance an electron travels in matter and having lost all but $1/e$ of its energy by bremsstrahlung as well as X_0 is $7/9$ of the mean free path of a photon undergoing pair-production.
The radiation length is material dependent, tables are available (e.g. [94]). Numerical values for relevant materials are listed in Table 2.1 The critical energy E_{crit} is defined as the energy where the ionization loss of the electron per radiation length equals the electron energy[95]. Approximating $\left|\frac{dE}{dx}\right|_{rad} \approx E/X_0$ the critical energy can also be expressed as the turnover point from the radiation dominated to the ionization dominated energy loss regime:

$$\left(\frac{dE}{dx}(E_{crit})\right)_{ion} = \left(\frac{dE}{dx}(E_{crit})\right)_{rad} \tag{2.14}$$

As well as the radiation length, the critical energy depends on the target material, and can be expressed in a simple approximation as dependent on only the atomic number of the target material[96]:

$$E_{crit}/MeV = \frac{610}{Z+1.24}(\text{solids and liquids})$$
$$E_{crit}/MeV = \frac{710}{Z+0.92}(\text{gases})$$

The critical energy is different for solids, liquids and gases due to the density effect described in subsection 2.2.1.

The energy deposition of the shower in direction of t, which describes a longitudinal profile is approximately described by a gamma distribution[97]:

$$\frac{dE}{dt} = E_0 b \frac{(bt)^{a-1} e^{-bt}}{\Gamma(a)} \tag{2.15}$$

with the initial energy E_0 and material dependent parameters a and b. The maximum energy deposition is given at the maximum of the gamma function, which can be written as the following:

$$t_{max} = (a-1)/b = 1.0 \times (\ln y + C_{e,\gamma}) \ , C_e = 0.5, \ \ C_\gamma = -0.5 \tag{2.16}$$

with $C_{e,\gamma}$ taken for electron or photon induced cascades respectively. The parameters $a = 2.03 + 0.604 \ln(E_0/GeV)$ and $b = 0.6333$ were found for simulations of cascades in water[98]. It has to be noted, that the parametrization Equation 2.15 is not accurate at the onset of the cascade within the first two radiation lengths, as the gamma function rises more slowly than the actual cascade develops.
The transverse development of the shower is described by the Molière radius R_M:

$$R_M = X_0 E_s / E_C \tag{2.17}$$

with the scale energy $E_s = \sqrt{4\pi/\alpha m_e c^2} \approx 21.2 MeV$ defined by the fine structure constant α electron mass m_e, the speed of light in vacuum c and the material dependent critical energy E_c. The Molière radius depends only on the material, a typical value for e.m. cascades in ice is about 0.24 meters. In a cylinder with a radius of R_M centered around the longitudinal cascade axis, about 90% of the energy is deposited, increasing the cylinder to a radius of 3.5 R_M leads to a deposited energy of 99%. In conclusion, the electromagnetic cascade appears as an almost point-like energy deposition.

2.2.5 LPM effect

For very high energetic electrons and photons, the cross sections of bremsstrahlung and pair production will decrease[99]. This is also known as the LPM (*Landau-Pomeranchuk-Migdal*) effect. It can be described by a simple phenomenological model[100]: As in individual interaction processes the transfered lon-

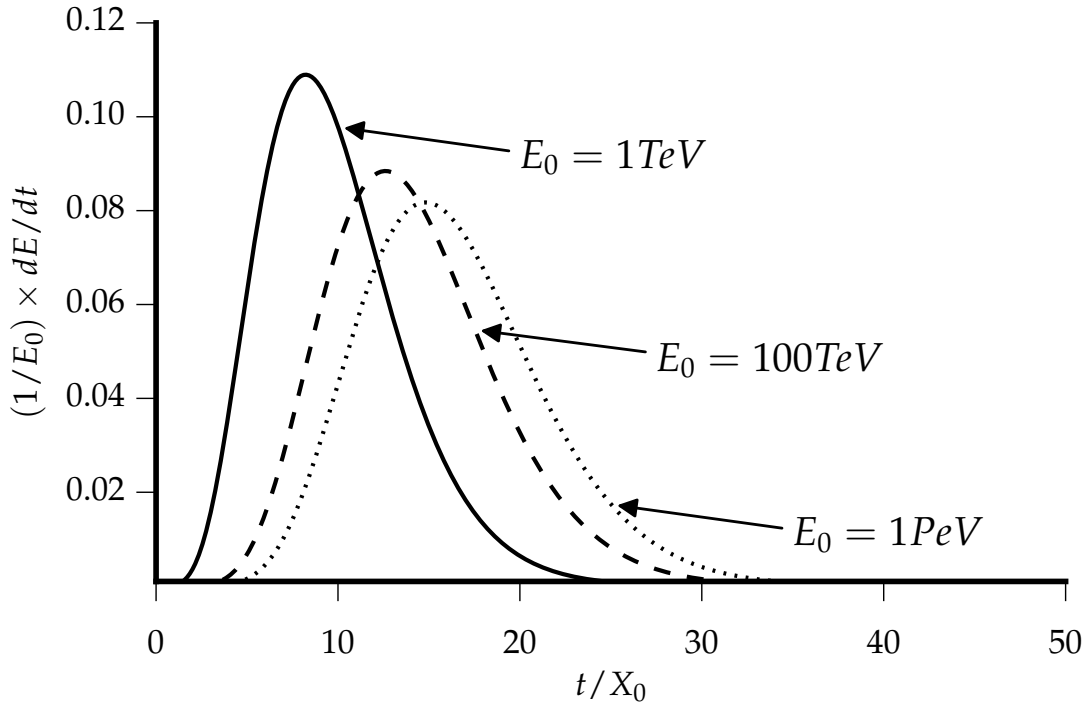

Figure 2.6 – Longitudinal energy loss profile of three electromagnetic cascade with energies of 1 TeV, 100 TeV and 1 PeV in water, following Equation 2.15, with the values for a and b taken from [98]. Using the value from Table 2.1 for ice, a 100 TeV cascade has its maximum energy loss at about 4.5 meters in longitudinal direction.

gitudinal momentum to a nucleus is small, the interaction is spread over a wide longitudinal distance, the formation length, due to the uncertainty principle. If the formation length gets larger than the inter atomic spacing of the target material, the cross-section is reduced by destructive interference of the amplitudes. The LPM effect is material dependent, and a characteristic energy E_{LPM} can be given:

$$E_{LPM} = \frac{m_e^2 c^3 X_0 \alpha}{4\pi\hbar} = 7.7 \frac{TeV}{cm} \cdot X_0 \tag{2.18}$$

with the electron mass m_e, the vacuum speed of light c, the fine structure constant α, the radiation length X_0, and Dirac's constant $\hbar$. For ice, E_{LPM} evaluates to a value of 303 TeV. The LPM effect becomes significant if the energies of the individually radiated bremsstrahlung photons $k = yE$ fulfill:

$$k < \frac{E^2}{(E + E_{LPM})} \tag{2.19}$$

The suppression is stronger for electrons than for photons, for electrons dE/dx is decreased by 50% for $E = E_{LPM}$ but the energy integrated photon cross section is decreased by 50% only for $E \approx 70 \cdot E_{LPM}$[100].
The suppression is also stronger for the lower energetic bremsstrahlung.
For ice, the elongation of e.m. particle showers due to the LPM effect becomes noticeable at initial energies of about 10 PeV.

2.2.6 Hadronic cascades

Hadronic particle showers are more complex than their purely electromagnetic counterparts, as more processes are involved during the development of the cascades. For DIS scattering, such cascades are created during the process, where besides the electromagnetic component, these cascades have a hadronic component consisting of fragments of the target nucleon as well. For the point of view of IceCube, it is important to note, that the observable - or *visual* energy of a hadronic cascade will always be lower than for an electromagnetic cascade of equivalent energy, but will approach it asymptotically. The visual energy is defined as the energy which can be reconstructed by observing the Cherenkov light of particles.
As a hadronic cascade will contain also neutral particles, or particles which are too heavy and thus fail the condition given in Equation 2.10, the amount

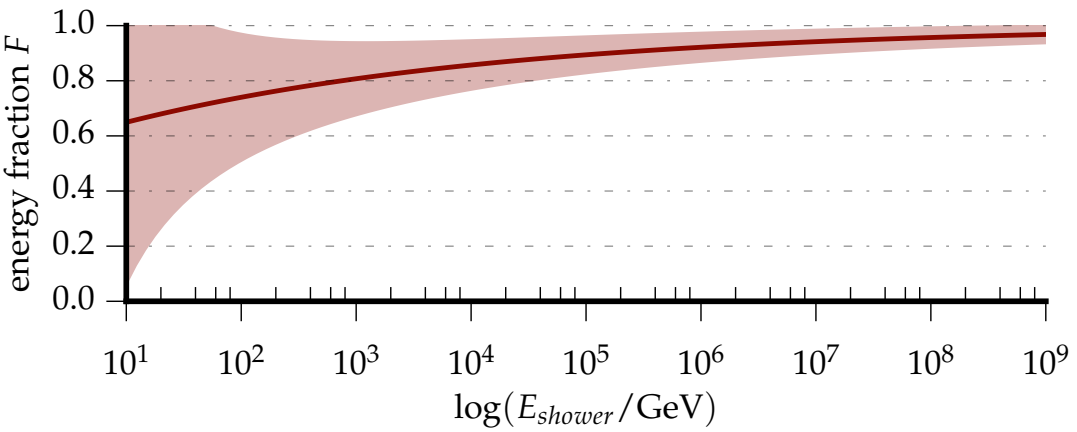

Figure 2.7 – Energy scaling factor F, the ratio of the visual energy of a hadronic cascade over the visual energy of a purely electromagnetic cascade with the same equivalent shower energy. Values taken from [101]

of Cherenkov light produced is reduced compared to a purely electromagnetic cascade. Also energy might be absorbed internally in hadronic bound states. For increasing initial energy of a shower, the amount of neutral pions in the shower increases, and the shower becomes more like an electromagnetic shower. The ratio of visible energy of a hadronic and a purely electromagnetic cascade is expressed by the scaling factor F[101]:

$$F = \frac{E_{vis}^{hadr}}{E_{vis}^{e.m.}} \tag{2.20}$$

$$= F_{e.m.} + (1 - F_{e.m.}) \cdot f_0 \tag{2.21}$$

which can also be written by the electromagnetic fraction $F_{e.m.} = 1 - (E/E_0)^{-m}$ of the cascade, with the parameters E_0 and m as well as f_0. The latter represents the Cherenkov activity of the purely hadronic part of the cascade. The parameters have been estimated by simulations[101] Especially for low energies, F might fluctuate widely for individual events. However, for the energies relevant for this work the spread is small and F reaches about 0.8 at a TeV, as can be seen in Figure 2.7.

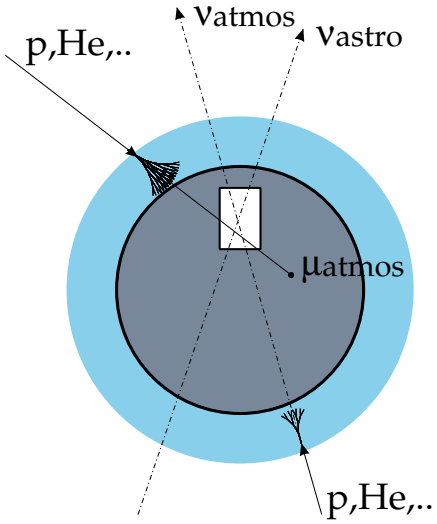

Figure 2.8 – Reducing the background for ν_μ searches by using the Earth as shield against atmospheric μ is possible by selecting only up-going track events. Figure adapted from [102].

2.3 The concept and prospects of neutrino observatories

Using the detection of up-going muons created by interactions of ν_μ as a clear neutrino signal in an Cherenkov counter deployed in a deep underground facility to shield it against atmospheric muons was first proposed in the 1960's [103]. The concept is illustrated in Figure 2.8.
The principle of measurement is quite simple and effective: Relativistic, charged particles will emit Cherenkov light if they travel faster than the speed of light in the ambient medium. As discussed in subsection 2.2.3, this light is emitted under a fixed angle dependent on the refractive index of the medium and thus allows a precise angular reconstruction, if the arrival time of this light is measured by a grid of sensors, as illustrated in Figure 2.9. The design of the first underwater neutrino detector was then inspired by these ideas. Expected ν fluxes from SNR shells, neutron star binaries or other high energy γ ray sources[1] were discussed to be measurable with a gigaton detector. A first

[1] Though none were yet detected at the time DUMAND was proposed

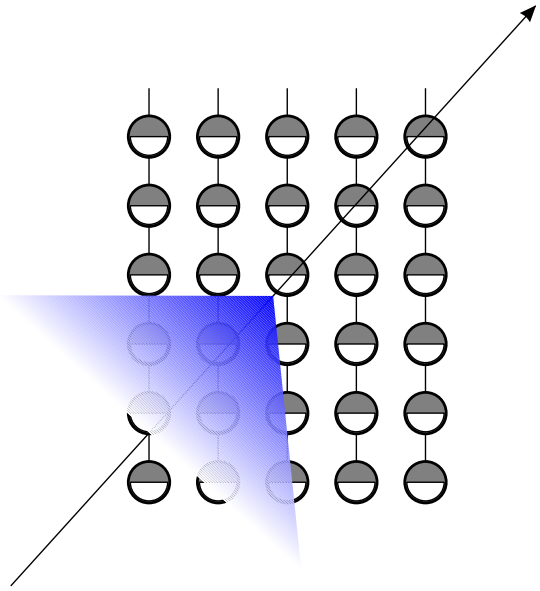

Figure 2.9 – A charged, relativistic secondary will emit Cherenkov light along its trajectory, which can be detected by a grid of sensors. Figure adapted from [102].

proposed cubic kilometer array, the DUMAND project managed to develop the technological concepts for such a detector. After facing technical difficulties, finally a single test string equipped with PMTs was deployed, which allowed to prove the detection concepts for the first time by measuring the atmospheric muon flux with an underwater Cherenkov detector[104]. It was also possible for the DUMAND collaboration to set upper limits on the extraterrestrial ν flux from AGN. The idea of large detector arrays underwater or in ice was carried on by the Baikal, Antares, Nestor and AMANDA neutrino observatories and a 1 km^3 detector is now realized with IceCube and operational. For further reading on the history of the development of large scale neutrino telescopes, the reading of [102] is recommended.

The angular resolution for signatures induced by muons achieved in latest generation neutrino telescopes is typically of the order of $0.1^\circ - 1^\circ$, allowing to separate effectively down-going trajectories from atmospheric muons and up-going trajectories from muons created in charged current interactions of ν_μ with nuclei in the vicinity of the detector, as described in subsection 2.1.1. As the muons can not penetrate the Earth, up-going tracks are a clear ν_μ signal, which are produced either in the atmosphere on the other side of the Earth or in outer space. The angular resolution allows searches for ν point sources and transients. Studies using the ν_μ channel were e.g. capable of setting the cur-

rently strongest constraints on ν_μ production in GRBs[105]. Reconstruction of the energy of tracks comes with a large error, in particular if the starting and end-point of the track is not known, however also searches for a diffuse ν_μ extraterrestrial neutrino flux have been conducted[106, 107] and the high energy tail of the atmospheric ν_μ and $\bar{\nu_\mu}$ spectrum was measured[61].
Including neutral current interactions of all ν flavors and charged current ν_e, ν_τ interactions, allowed to measure the atmospheric ν_e spectrum between 80 GeV and 6 TeV for the first time[67] and enabled the discovery of the extraterrestrial ν flux[23]. However, ν_ℓ NC and ν_e, ν_τ CC interactions will not leave a measurable track, but only a particle shower in the vicinity of the detector. As directional reconstruction of such events, is less precise, veto techniques are applied to suppress the atmospheric μ background. Introducing a fiducial volume and using parts of the instrumentation to veto incoming events, this reduces the effective volume usable for such a search in comparison to the volume which can be used for a ν_μ search only. In contrast to IceCube, for water Cherenkov neutrino observatories, such as ANTARES or KM3Net, the directionality of shower-type events can be resolved more precisely, and it has been recently shown that no veto regions are necessary[108]. The study presented in this work demonstrates the ability of IceCube to separate signal and background in the former veto-regions for shower-type events for an all-sky, all-flavor diffuse ν flux measurement, gaining sensitivity especially for high energetic events.

2.4 IceCube

2.4.1 Detector design

The design of IceCube is optimized for one of its primary goals: The discovery of an extraterrestrial neutrino flux.
As this flux is supposed to be small, and due to the small interaction probability of the neutrinos, the detector needs to be large to be capable of observing the target flux with high significance during its operation time. It has been already considered prior to the construction of the first underwater Cherenkov detector, that the target volume should be at least in the order of 1 km^3, as discussed in section 2.3. Such large detectors can only be implemented as ice or water

IC1	IC9	IC22	IC40	IC59	IC79	IC86-1
2005	2005/06	2006/07	2007/08	2008/09	2009/10	2010/11

Table 2.2 – Naming convention for IceCube operation seasons during construction.

Cherenkov detectors, with a relatively sparse instrumentation. Studies with the predecessor AMANDA showed that the ice in the depth of the glacier at the South Pole has the necessary transparency to achieve the desired sensitivity for the planned IceCube detector, however the optical scattering length is much shorter than in water[109].
For IceCube, a sensor array of digital optical modules, (DOMs)[110] was deployed in a hexagonal grid with 5160 modules on 86 strings. The strings support the structure and supply the modules with high voltage and provide the data connection to the surface. The individual strings have lengths of about 3500 meters, the instrumented part is deployed in depths of approximately 1450 - 2450 meters, where the hydrostatic pressure leads to a suppression of gas bubbles in the ice. The strings were deployed in the austral summers of the years 2005-2010. The DOMs deployed in each season were tested and calibrated after deployment and started physics data taking in May after the austral summer ended. The instrument thus provided data while under construction. The data from the construction seasons is identified by the number of strings in operation, plus an "IC" prefix. An overview over the seasons can be found in Table 2.2. The distances between the IceCube DOMs are approximately 125 meters in the direction parallel to the surface of the ice and 17 meters in normal direction.
For measurements at lower energies, the central part of IceCube has a denser instrumentation enhancing its sensitivity to energies of about 10 GeV at lowest. The IceCube detector is accompanied by a surface detector, IceTop which is designed to measure the cosmic ray spectrum especially in the not well understood region of the knee. A schematic of the IceCube neutrino observatory with the detectors IceTop and DeepCore is shown in Figure 2.10. Coincident measurements of the two detectors are possible, and allow the use of the IceTop array as a veto for in-ice muons which are created during cosmic ray air showers.

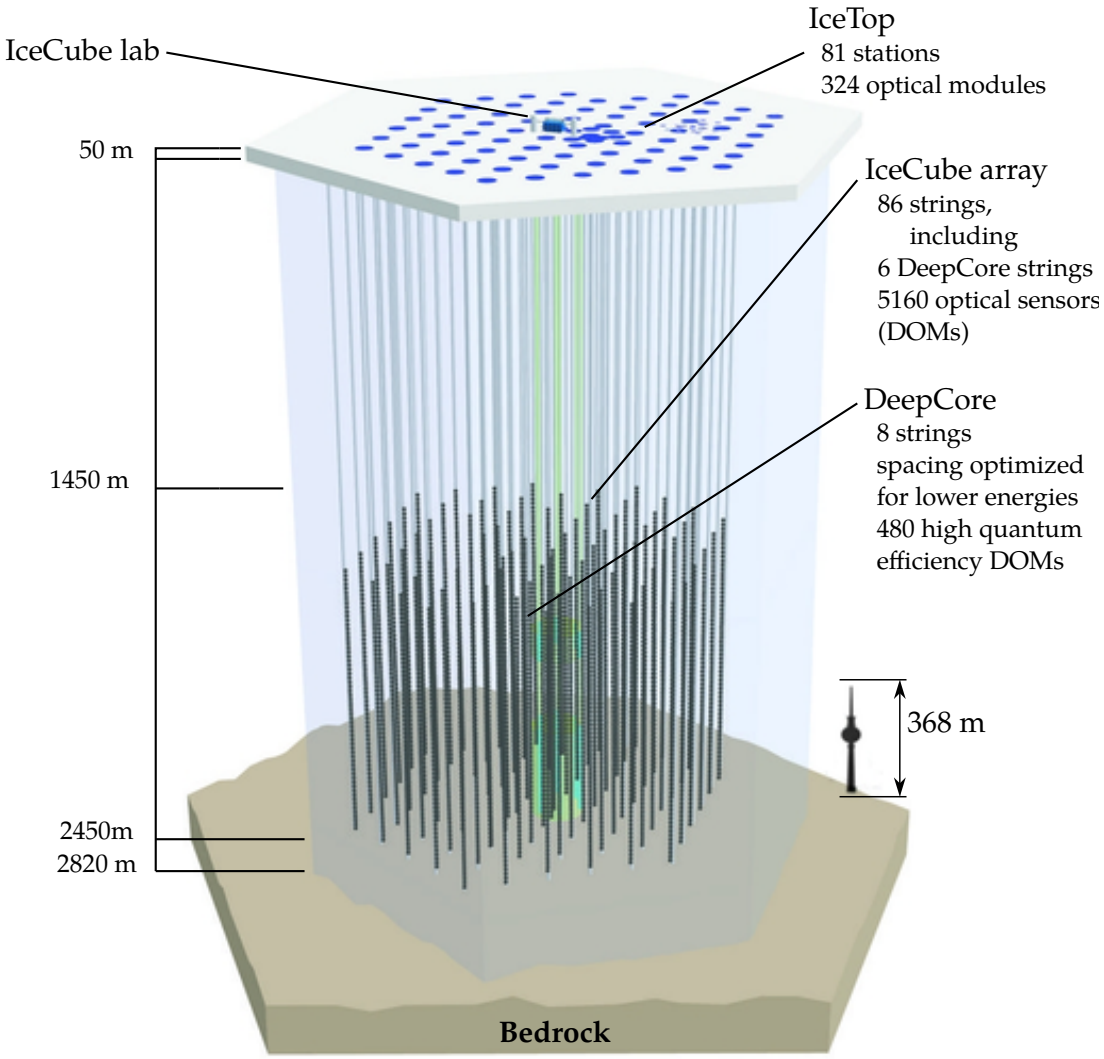

Figure 2.10 – Schematic of the IceCube neutrino observatory. Figure taken and adapted from [111, 112].

2.4.2 DOM - the basic detection unit

IceCube uses 10 inch photomultipliers (PMTs) fabricated by Hamamatsu[113] to measure the Cherenkov light emitted by neutrino interactions. The PMTs are enclosed in a spherical glass housing, to shield them against the pressure of the Antarctic ice. The housing also hosts the digitizing electronics as well as a calibration LED board. The housing is filled with nitrogen at a pressure of 0.5 atmospheres. The PMT is optically connected to the housing by a transparent gel. It is also enclosed in a μ-metal grid, which shields the PMT against the Earth's magnetic field. This basic detection unit is called *digital optical module* DOM, as it encloses optical signal detection, digitization and rudimentary data processing, a schematic is shown in Figure 2.11.
The PMT is connected by three lines to the digitization electronics. The first line connects the PMT via a discriminator to a FPGA, which hosts the trigger logic. If the measured PMT voltage exceeds 0.25 times the average single photo electron signal, the discriminator threshold is exceeded and the FPGA logic reads out the signal via the second line, which is implemented as a delay line of 75 nanoseconds, to provide the discriminator electronics and FPGA logic with enough time to form its decision. The second line is split into three different independent channels with different gains, $\times 16$,$\times 2$, and $\times 0.25$. This allows to switch to the next lower gain channel if a channel gets saturated and improves the dynamic range substantially. Each channel is connected to a custom designed ATWD, which is short for Analog Transient Waveform Digitizer[114]. The signal in each channel is fed to a bank of 128 capacitors, each sampling about $\approx$ 3.3 ns of the PMT signal. The capacitors are read out by 128 10 bit ramping Analog-to-Digital Converters (ADC). Thus about 422 ns of the PMT signal are covered by the ATWD. As the ATWD needs about 29μs for the digitization, a second ATWD is available to reduce the dead time introduced by the readout.
The ATWD is also equipped with a fourth channel, which allows to monitor the current which runs through the calibration LED system.
The third line connects the PMT to a Flash-ADC with 256 channels, which samples the full waveform continuously, however with a much coarser binning of 25 ns. This allows the waveform to be sampled up to 6.4 μs. The digitized PMT signal is transferred together with a time-stamp to a DOM hub on the ice sur-

face and further sent to the IceCube DAQ system, which provides the trigger logic for the whole detector array.
The dark noise of the individual PMTs varies, and is at the order of about 300-700 Hz. To reduce the noise rate, a coincidence criterion is implemented in the DOM: If a DOM exceeds its discriminator threshold, the criterion requires at least one of the two neighboring DOMs to exceed the discriminator threshold within 1 μs as well, to form a *hard local coincidence* (HLC) pair. If global trigger decisions are based on such HLC pairs, the rate of triggered events due to dark noise is reduced massively. Also the amount of transmitted data can be reduced by sending the full waveform information to the IceCube DAQ system only for HLC pairs and reducing the sent information for non-HLC pairs to a charge-stamp. The charge stamp consists of only the highest of the 256 FADC bins and its two second neighbors.

LED calibration system - flashers

Six pairs of LEDs are available for calibration tasks, geometrical measurements, ice measurements and several other purposes. One of the LED of the pair is mounted on the upper side and the other one on the lower side of a second electronics board above the DOM mainboard.
The pairs are mounted with a 60° angle between them, each upper LED tilted at about 50° to the DOM's vertical axes and the lower one facing out slightly downward. The LEDs have their emission peak at 405 nm, which is close to the peak of the Cherenkov emission.

2.5 Detector response

Dependent on neutrino flavor and interaction type, the final state of a neutrino interaction leads to different imprints on the detector. The spatial distribution of the triggered individual sensors in time weighted with the recorded light the individual DOMs have seen is called hit-pattern. It features two main topologies: Elongated patterns, which seem to move through the detector, called "track-like", as displayed in Figure 2.12 and "shower-like" patterns which are more stationary and expose a more spherical symmetry as shown in Figure 2.13. Events originating from $\overset{(-)}{\nu}_\mu$ charged current and $\approx$ 17% of $\overset{(-)}{\nu}_\tau$ charged current in-

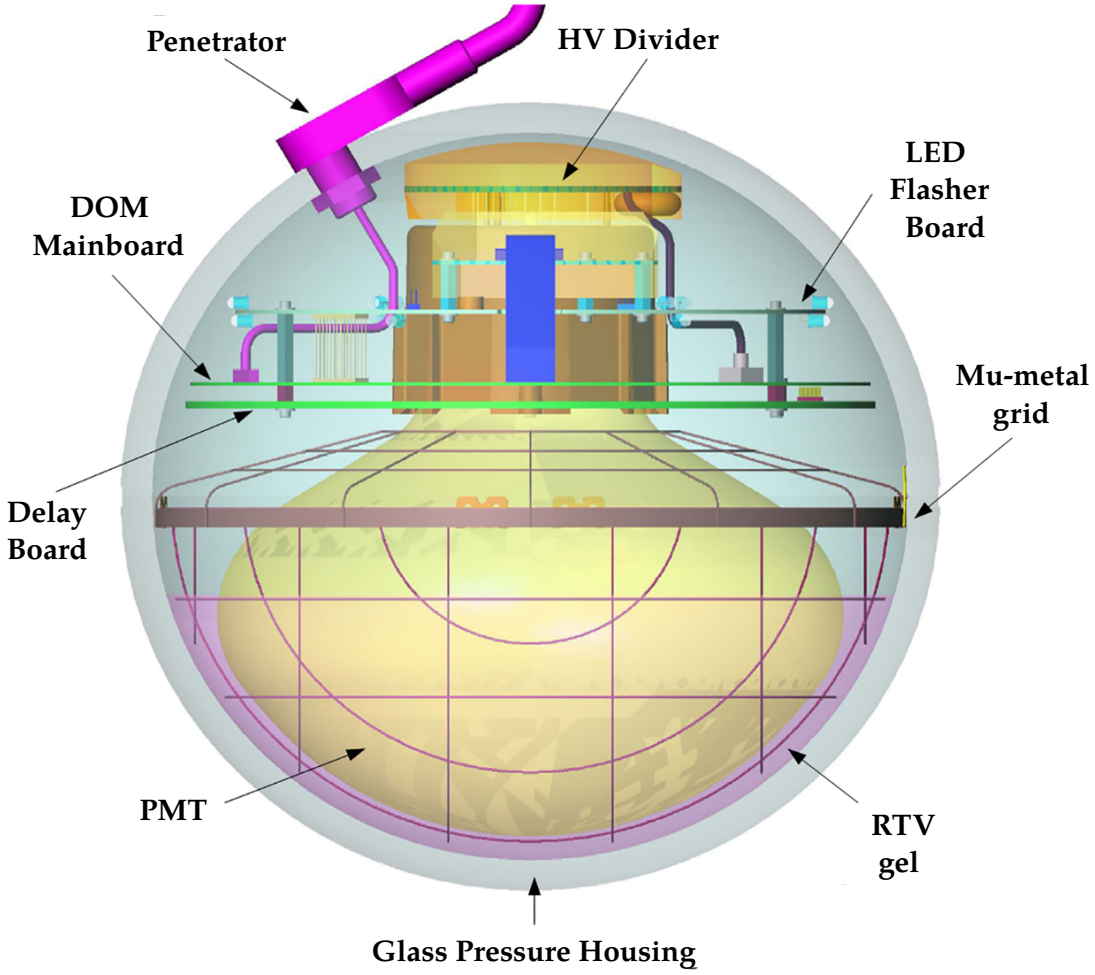

Figure 2.11 – Schematic of a DOM, the basic IceCube detection unit. Figure adapted from [111].

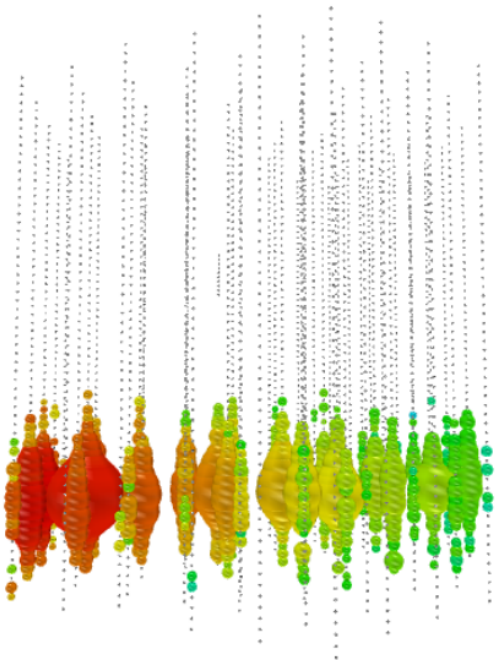

Figure 2.12 – A high energy muon track, found in IC59, entering the detector horizontally. The hit pattern is elongated, the different colors indicate the time development of the pattern, where red hits indicate the earliest times. Figure taken from [106].

teractions have a high energetic muon in their final state, which is capable of traveling long distances through the instrumented volume losing energy via ionization and radiation processes as described in subsection 2.2.1 and subsection 2.2.2. These muons leave an elongated signature in the detector. The other final states feature hadronic particle showers, and in the case of charged current ν_e and ≈ 17 % of ν_τ an electromagnetic shower as well. For energies below several PeV, the hadronic and electromagnetic shower dimensions are small compared to distances between the individual sensors for an IceCube like array, and thus look like almost point-like light sources from a detector point of view. For such events, the hit pattern has an almost spherical geometry.
For higher energies above several PeV, the LPM effect becomes notable and the geometry of the shower gets elongated, A special case are charged current ν_τ interactions above several PeV: At these energies the τ is able to travel significant distances, and the second shower gets spatially separated from the first, leading to a so called "double bang" event. In IceCube, this event type has not been observed yet.

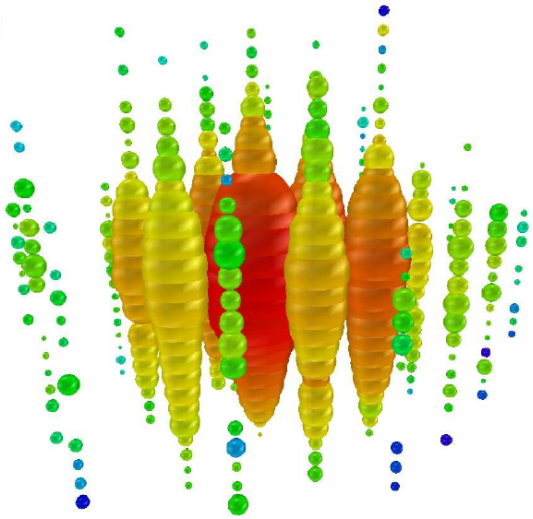

Figure 2.13 – The point-like light emission of a high energy cascade event found in a high energy event search for the season IC86. Reddish colors indicate early hit times in the event. The hit pattern has a spherical geometry. Figure taken from [24].

2.5.1 Modeling the glacial ice

If triggered, each IceCube DOM provides a digitized PMT signal curve. From this, two quantities can be derived: The observed number of photoelectrons Q, and the arrival time distribution of these photoelectrons. These quantities can be calculated by measuring the PMT voltage drop over time. This voltage cure is called the waveform.
As the photon paths in the ice are distorted compared to those in vacuum due to scattering, both values are sensitive to the optical properties of the glacial ice which the photons have to travel from their source before being measured. The two quantities can be modeled with two values which are expected at a DOM for a given source hypothesis $\underline{C}$:

1. $\mu^{\infty}(d, \underline{C})$, the expected charge in photoelectrons in a distance d from a source. The expected charge depends on the source characteristics like the emission profile.

2. The arrival time distribution can be modeled by $dP(t_d, d, \underline{C})/dt$ which is called the *delay-time* distribution. It depends on the distance d and source characteristics.

For a receiver at position $\vec{x}_{rec}$ measuring a hit at the time t_{hit}, the delay time t_d is given by the time a traveling photon, emitted at a source $\underline{C}$ at position $\vec{x}_{ref}$, is

"delayed" compared to a photon traveling a non-distorted path.

$$t_d = t_{hit} - \frac{|\vec{x}_{ref} - \vec{x}_{rec}|}{c_{ice}} \tag{2.22}$$
$$t_d = t_{hit} - t_{geo}$$

The flight time required for a non distorted path is commonly referred to as "geometric" time t_{geo}. The shape of the t_d distribution then allows to infer the probability of a hit being measured at the time t_{hit}. Together with the value of the total expected charge $\mu^{\infty}(d, \underline{C})$, the DOM waveform can be predicted for a given source hypothesis $\underline{C}$.

Bulk ice

The simplest model of the ice assumes a homogeneous medium with isotropic scattering and absorption. However simplistic, this model allows analytical calculation of light propagation and thus can be evaluated fast. It is thus used in cases where speed is more important than accuracy. A parametrization for the measured arrival time distributions was found and formulated as a delay-time p.d.f. $dP(t_d, d)/dt$[115], since named *Pandel* function. The p.d.f. has the shape of a Γ function and has three free parameters, a scattering parameter ℓ_s, an absorption parameter ℓ_a and a scattering time τ_s. A representation of this Pandel function is given by:

$$\frac{dP}{dt}(t_d, d) = \frac{a(at_d)^{(b-1)} \exp(-at_d)}{\Gamma(b)} \tag{2.23}$$

$$a = \frac{1}{\tau_s} + \frac{c_{ice}}{\ell_a}; \quad b = d/\ell_s$$

The numerical values of the three parameters were determined for ice in[101]:

$$\ell_s = 47\,\text{m}\ \ell_a = 450\,\text{m}\ \tau_s = 98\,\text{ns} \tag{2.24}$$

To account for PMT jitter, the Pandel function is convoluted with a Gaussian, which also allows negative values of t_d. These can occur due to the limited resolution of the reconstruction algorithms, where slightly misplaced vertices lead to negative timings. The Pandel function is plotted for three distances in Figure 2.14.

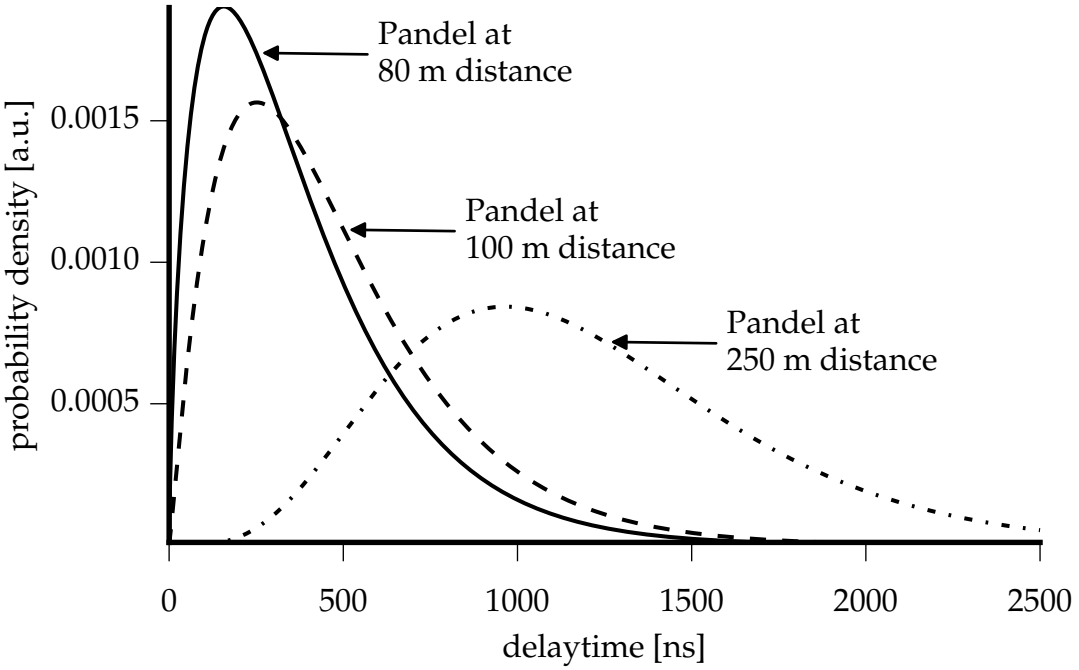

Figure 2.14 – Three representations of the Pandel function for different distances. The Pandel function is an analytical approximation of the delay time p.d.f.. $dP(t_d, d)/dt$ of the incident photons measured by one of the DOMs.

The total predicted charge μ^{∞} has been parametrized as well[101]:

$$\mu^{\infty}(E, d) = \frac{I_0}{d} \exp(-\frac{d}{\lambda_{attn}}) \cdot E \tag{2.25}$$

The parametrization is valid for distances d larger than the effective scattering length λ_c. Here, λ_{attn} describes an effective attenuation length, which has been found to be $\approx$ 29 meters[101]. The parametrization is directly dependent on the deposited energy in the detector, as the number of emitted photons scales linearly with energy. The normalization constant I_0 depends on the efficiency of the IceCube DOMs and is found to be close to 3.3 $\mathrm{GeV}^{-1}\mathrm{m}$.

Binned ice models

Studies of the antarctic glacier as well as the study of the light propagation from artificial light sources in AMANDA led to a more detailed description of the deep ice[109]. It was revealed, that the ice has a depth-dependent layered structure, with the scattering and absorption parameters varying from layer to

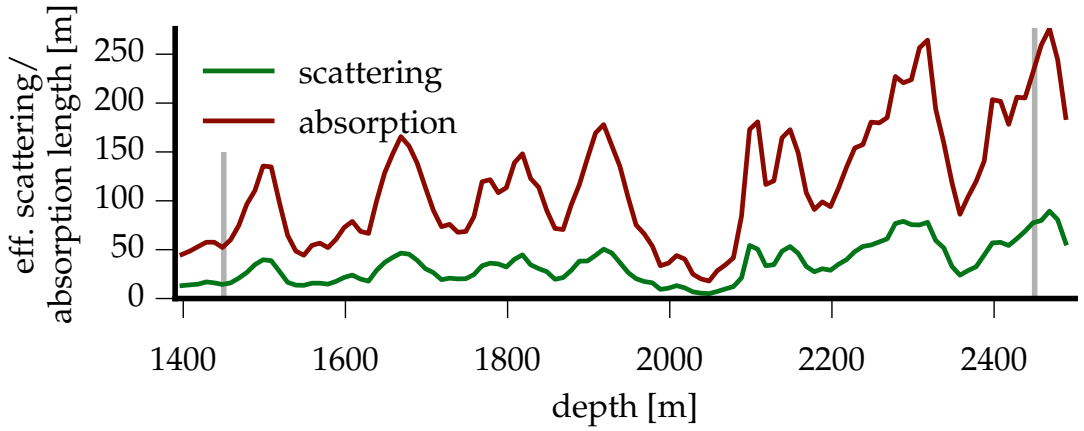

Figure 2.15 – Scattering and absorption lengths in the ice as used for the analysis. The instrumented volume of IceCube is indicated by the gray lines. Data taken from [116].

layer, dependent on the environmental conditions at the time the glacier was formed. The variations of the optical parameters for the individual layers were found to be large, layers with high concentrations of dust suppressing most of the photon propagation were identified, the extremest of these layers was in the context of IceCube dubbed “dust layer”, as the event rate in this region is notifiable lower.

The model of the glacial ice[116] provides absorption and scattering parameters for horizontal layers of 10 meters thickness, extending the range to regions underneath and above the detector as well. The model parameters were obtained by fits to data derived by flashing LEDs implemented in the DOMs. These so called “flashers” are further described in subsection 2.4.2. Later refinements of this model introduced a different scattering function, a global tilt of the ice layers and non-isotropic scattering[117]. For the here presented analysis a refinement of [116] was used, which incorporates Mie scattering.

3

Event simulation and reconstruction

3.1 Simulation

Simulation of atmospheric muons and neutrino simulation provides the possibility to develop and optimize an event selection for different signal hypothesis, without being biased by the need to interpret the data. For a diffuse search, background simulation provides the means to calculate a background estimate for the measured events.
The IceCube simulation chain is complex and comprises the simulation of the interaction of primary particles in the upper atmosphere as well as the propagation of the individual particles and the interaction and light propagation in the detector, and finally the simulation of the electronic components of IceCube. An overview of the simulation in IceCube can also be found in [118].

3.1.1 Simulation of atmospheric muons

For the simulation of atmospheric muons, first the atmospheric shower induced by the incident cosmic ray primary is simulated using a modified version of the software package CORSIKA[119]. In the ice, random catastrophic bremsstrahlung losses are simulated along the muon trajectory as well as the smooth

Cherenkov light. Due to the high suppression factor of atmospheric muons of the analysis, a large amount of atmospheric muons need to be simulated in order to have a background estimate for the final sample. The simulation has thus been optimized for the needs of this and similar analysis. Simulated are five components of the cosmic ray model, H, He, N, Al, Fe which are most abundant in the universe and also each representing a group of elements. This allows to individually scale the normalization of each production p.d.f., which is important as for searches for shower-type events the different elements contribute differently to the estimated background. The reason is that for heavy elements, mostly muon bundles with high multiplicity are generated, where the energy of the primary is distributed smoothly among the individual muons. Bundles where single muons carry most of the energy and thus undergo large catastrophic losses which lead to high energetic, cascade like events in the detector are more likely to be produced by light elements. The generation spectrum is then re-weighted to match the H3a prediction. All datasets are combined to form a joint generation p.d.f. which is then weighted according to the H3a model, as described in subsection 1.1.1. The comparison of the muon flux predicted by H3a and the generated p.d.f. is shown in Figure 3.1, where the number of expected events per year is compared to those simulated. This allows to identify regions in the generation spectrum where much less events are generated than there exist in nature. It can be seen that for IC86 the produced background statistics is much lower than for IC79, however still the produced p spectrum matches the H3a spectrum at about 170 TeV. Considering that the visual energy of a catastrophic energy loss of a muon is scaled down by some factor and the energy threshold of this analysis is at 34 TeV, this still seems to be a reasonable amount to estimate the background of the final sample.
As the IceCube trigger window with at least 10 μs is rather long compared to the rate of about 2000 - 3000 events per second of atmospheric muons, simultaneous or subsequent registered muons might end at up in the same event - where event is defined by the time duration of a trigger window. The probability to observe an event of multiplicity n of with an individual event rate r during a time window Δt is given by:

$$P(n|r\Delta t) = \frac{(r\Delta t)^n e^{-r\Delta t}}{n!} \tag{3.1}$$

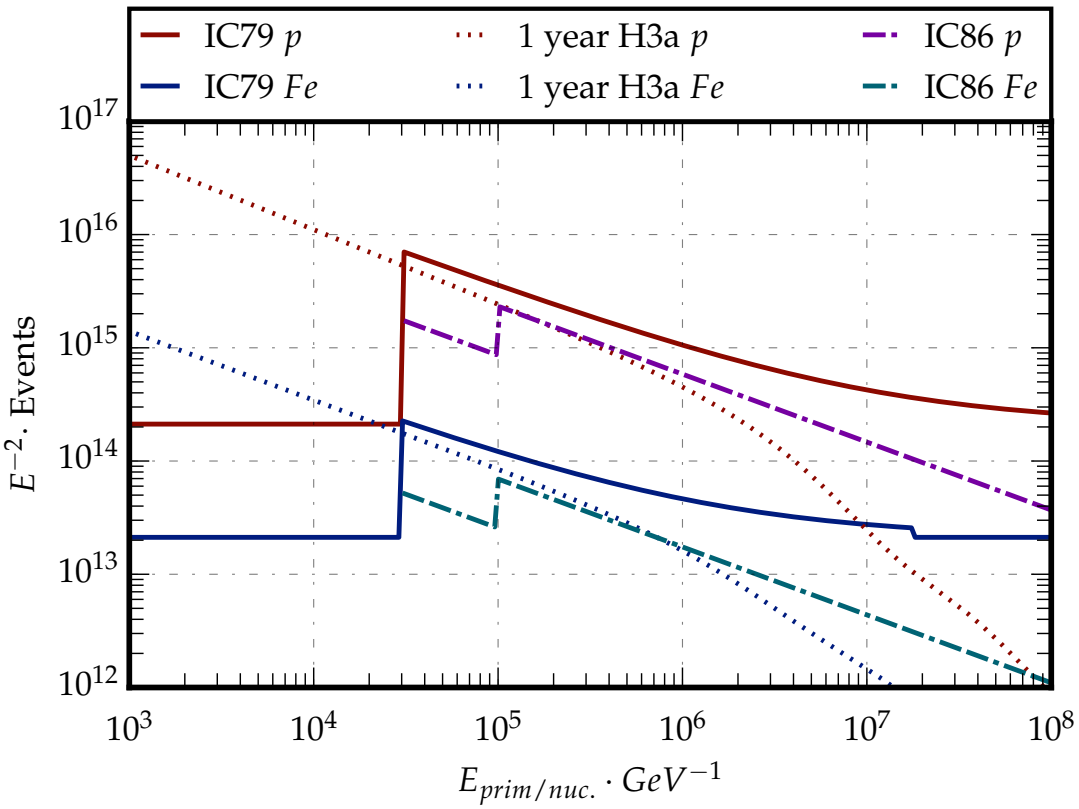

Figure 3.1 – Generated atmospheric muon background. The combined generation p.d.f.s for IC79 and IC86 are plotted for proton and iron primaries. For comparison the expected number of events from a H3a flux are shown as well.

In simulation, coincident events are mixed into the normal production. The event weight is then extended by Equation 3.1. For IC79, a dedicated production of coincident events was performed, and the influence of coincident events on this analysis was studied. However, the statistics of this dedicated coincident simulation is low. Only about 1 month of effective livetime of dedicated coincident simulation was available, yet it was found that coincident events are very unlikely to be present in the final sample, as they are strongly suppressed by the used causality and timing criteria even in early stages of the event selection.

3.1.2 Simulation of neutrinos

Interactions of all neutrino flavors have been simulated for this work. Simulated was an isotropic flux of neutrinos with an 1:1:1 flavor ratio and an equal

amount of neutrino and anti neutrinos. The neutrinos are produced above the surface of the Earth and propagated through the Earth until they reach the detector, where an interaction is enforced. The Earth is modeled with the *Preliminary Reference Earth Model*[120] and neutrino attenuation as well as ν_τ regeneration[1] is simulated. The DIS is simulated with CTEQ5 structure functions. The simulation is done with either an E^{-2} or E^{-1} generation spectrum. In this work both generation spectra are combined to a single generation p.d.f. and weighted to an E^{-2} isotropic astrophysical benchmark model with a flux normalization of 3×10^{-8} GeVcm^{-2}s^{-1}sr^{-1}and to two atmospheric neutrino components: The conventional, where the HKKMS07 model is used and the prompt component emerging from instantly decaying mesons with a charm contribution described by the BERSS model. As the original HKKMS07 model is calculated for an unbroken power law, it has been re-weighted to take a cosmic ray spectrum with a broken power law into account. The simulation is done by the software package NUGEN, which is based on the ANIS neutrino generator[86]. After neutrino interaction, the secondary muons or taus are propagated. Cascades are simulated as purely electromagnetic, and in the case of a hadronic cascade, the light output is scaled down as described by Equation 2.21 with a corresponding smear accounting for the width of the distribution. If the energy of a cascade is smaller than 1 TeV, it is simulated as point-like with a Cherenkov emission profile, higher energetic cascades are split up in subsequent 1 TeV cascades along a track segment. This allows also to take the LPM effect into account, as it is described in subsection 2.2.5. The simulation allows to estimate the number of photons emitted by the event, which are then propagated through the ice. For this work, although direct propagation of photons was already possible, due to computing constraints the p.d.f.s for the photon field were generated beforehand and then used in the form of look-up tables, as described in subsection 3.1.3. In a final step, the entire DOM is simulated, including the electronic components. In this last step, also simulated electronic noise is added.

[1] The term regeneration refers to the production of a secondary ν_τ from the decay products of the τ created in the primary CC interaction of the incoming ν_τ

3.1.3 Simulation of photon propagation in ice

The goal of the photon propagation step is to predict the two quantities total expected charge μ^{∞} as well as the delay time distribution $dP(t)/dt$ for each receiver position for a given source position, direction and type of the emitter.
The Photonics code provides tables with distributions of μ^{∞} and $dP(t)/dt$. The ice is assumed to be homogeneous in horizontal direction for each equi-distant slice in vertical direction. Scattering and absorption in each layer is assumed to be isotropic. The emission profile of the source is assumed to be azimuthally symmetric. These simplifications reduce the amount of tables to be produced as they only have to be generated for each bin of the zenith angles of the source orientation per each vertical slice.
For a 30° zenith binning a slicing of 10 m in the vertical direction, e.g. 600 individual tables have to be simulated, which requires cluster-sized computational resources. These tables are created once and can then be used for look-up by the individual reconstruction and simulation codes.
For each table the emission axis is fixed and defines the coordinate system of the source, which can be chosen accordingly to the source geometry to be either cylindrical for a track-like light emitter or to be spherical for a point-like light emitter, that a cascade is expected to be. The performed simulation is straightforward: A table of scattering and absorption coefficients for each depth as well as an emission profile has to be provided. The software injects photons in the simulation volume, with directions drawn from the emission profile. Each injected photon is propagated to the next scattering vertex that is chosen based on the scattering length. After each scattering length, the angle of the photon travel path is altered based on the expected distribution of scattering angles. After each traveled absorption length, the survival probability of the photon is calculated based on the absorption length and added to the photon weight. Every time a photon enters a cell border of the tabulated volume its weight is added to the $dP(t)/dt$ histogram in the according timing bin. The ice parameters necessary to calculate these quantities are taken from ice model tables, see subsection 2.5.1.
The values of the total expected amplitude in each bin and the p.d.f.s are then stored in a set of tables. A part of such a set of tables is visualized in Figure 3.2. Taken from the set of tables produced for a cascade emission profile, the total

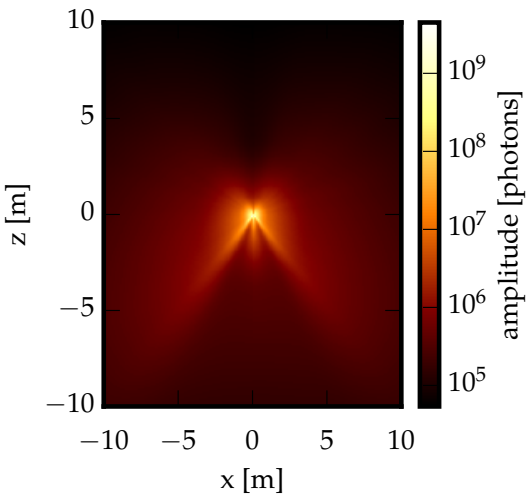

Figure 3.2 – A visualization of the expected amplitudes taken from tables produced by the photon propagation simulation. Shown is the expected amplitude in the plane of an up-going particle shower. The Cherenkov cone is clearly visible.

expected amplitude is plotted for a directly up-going cascade.

The discreteness of the binning in each individual table, as it is provided by the software is problematic for commonly used minimization algorithms. As the values of $dP(t,r)/dt$ enters the calculation of likelihoods used for event reconstruction as described in subsection 3.4.6, it must be a smooth and differentiable function of t and r in all points to allow for a proper minimization.

A method to ensure the desired smoothness is the interpolation with splines: Each histogram in each volume bin is approximated by a spline-fit, eliminating statistical fluctuations. The coefficients of the b-splines are members of a smooth function of the base vectors in the source coordinate system. This function itself can be constructed by a set of b-splines. In this interpolation scheme there is no difference between intra- and inter-table binning interpolation, as for a large enough coefficient matrix, the scheme can be extended over the whole table set. The method is further described in [121]. A simple example of the interpolation by b-splines is illustrated in Figure 3.3. Interpolated tables generated by Photonics are used despite their known limitations as look-up tables for the atmospheric muon background simulation. Due to the needed statistics, the computationally least expensive method needed to be chosen. All reconstructions which include a more detailed description of the ice than the bulk ice model rely on such tables as well. Recent work is done to overcome some of the limitations and to include a non-isotropic model of light scattering in the tables[122], however it was not yet available for this work.

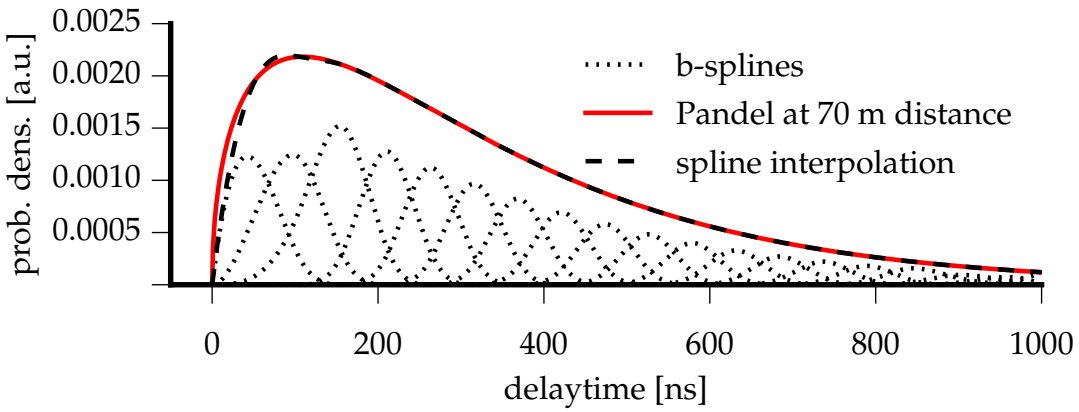

Figure 3.3 – A very simple example to illustrate the method of fitting with a set of b-splines. In this example, the b-splines are of order 3, and thus have 3 internal knots, which are points on the spline. Each b-spline is entirely parametrized by a single coefficient, if the interval for its existence is fixed. The spline fit (dashed curve), which approximates the Pandel function (red solid curve) is expressed by the addition of all 20 b-splines (dotted curves). Accuracy can be increased by adding more b-splines. The Pandel function itself is an analytical representation of the delay-time p.d.f and thus not needed to be approximated, which is solely done to illustrate the general concept.

3.1.4 Weighted simulation

To be able to describe multiple models with a single simulation set of cosmic ray background or neutrinos, a generic spectrum Φ_{gen} in a chosen energy range E_1, E_2 is simulated. The simulated flux can then be re-weighted to any desired target flux Φ_{target}. In the case of cosmic ray background simulation, the dependency on a certain model concerning the elemental composition is avoided by simulating the individual primary components of the cosmic-ray flux separately.

Another advantage of this approach is the better management of computing resources. As the computing time per event increases with energy, one is able to chose the generation spectrum in such a way that statistics is maximal to the analysis.

To compensate for the difference in generation and target spectra compared to a certain target flux Φ_{target} weights w_i^{flux} have to be applied to each simulated event i:

$$w_i^{flux}(E) = \frac{\Phi_{target}(E)}{\Phi_{gen}(E)} \tag{3.2}$$

In the case of cosmic ray background simulation the weight is also dependent on the atomic number Z of the simulated primary.
The generated flux Φ_{gen} can be expressed in terms of number or generated events N_{gen} times the probability density function $p_{gen}(E)$ per generation area A_{sum} and observation time T. Substituting this in Equation 3.2 results in:

$$w_i^{flux}(E) = \frac{A_{sum} T \cdot \Phi_{target}(E)}{N_{gen} \cdot p_{gen}} \tag{3.3}$$

Dividing by T, this yields an effective event weight w_i which when applied to a simulated events gives the rate of its occurrence for the target flux Φ_{target}.

$$f_i(E) = \frac{w_i^{flux}(E)}{T} = \frac{A_{sum}}{N_{gen} p_{gen}(E)} \Phi_{target}(E) \tag{3.4}$$

Summing over all the individual event rates the total rate f_{sim} over all energies observed for this target flux can be calculated:

$$\sum_{i=0}^{N} f_i = f_{sim} \tag{3.5}$$

Using the relation Equation 3.5 and the Poisson error of $\sqrt{N}$ it is possible to calculate the error of the simulated rate Δf_{sim} by propagating the errors which yields[123]:

$$\Delta f = \sqrt{\sum_{i=0}^{N}} \tag{3.6}$$

An often quoted number is the *effective livetime* T_{eff}, which is defined as the time for which the relative error $\frac{\Delta f}{f}$ on the total simulated rate Δf is the same as the relative uncertainty in a real experiment[124]. To obtain the effective livetime, we set these two relative uncertainties equal:

$$\frac{\Delta f}{f} = \frac{\Delta f_{exp}}{f_{exp}} = \frac{T \sqrt{\sum_{i=0}^{N} w_i^2}}{\sum_{i=0}^{N} w_i} = \frac{1}{\sqrt{N_{exp}}} \tag{3.7}$$

With the requirement of $N_{exp} = \sum_i^N w_i$ it is possible to write:

$$T = \frac{\sum_i^N w_i}{\sum_i^N w_i^2} \tag{3.8}$$

where T is identified with the effective livetime T_{eff}. However a useful quantity, it has to be mentioned that the so obtained value can be misleading if used on a filtered set of events. Due to this reason, in this analysis the estimation of the statistical power of the background simulation is performed by comparing the production spectrum to the expected flux in nature as described in subsection 3.1.1.

3.2 General notes on event reconstruction

3.2.1 IceCube coordinate system

Convention places the origin of the right-handed, Cartesian IceCube coordinate system close to the center of the instrumented volume of the final configuration of the detector. The z axis is pointing away from the center of the Earth and is thus normal to its surface. The z position of the ice surface is then defined at a z position of 1948.07 meters. The x axis is aligned with the zero meridian and points directly to Greenwich. Directions in this coordinate space are defined by the two angles Θ, Φ of a corresponding spherical coordinate system. By convention, the coordinate vector is pointing in the direction of an incoming particle. The zenith angle in the IceCube coordinate system is related to the zenith angle in any standard spherical coordinate system by the relation:

$$\Theta_{IceCube} = \pi - \Theta_{std.sph.} \tag{3.9}$$

I.e. a particle entering the detector directly from above has a zenith coordinate of 0°.

3.2.2 Charge reconstruction

To extract the PMT response and finally the charge from the digitized PMT signal, the channel counts need to be converted to Volts, and eventually the

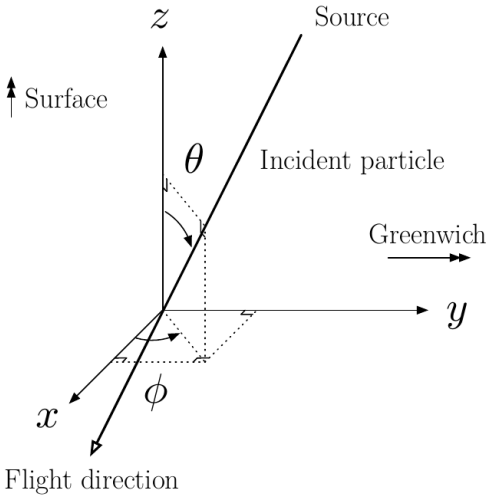

Figure 3.4 – The IceCube coordinate system, figure taken from [125]

raw waveform has to be calibrated. One of the most important calibration features is the correction of droop, which is a non-constant PMT signal baseline voltage. After these corrections, the digitized PMT signal is unfolded with a pulse template, and each of the unfolded pulses is assigned a starting time, charge and width. For this task, several algorithms are available to the IceCube collaboration. For the data used in this work, the Lawson-Hanson non-negative linear solving algorithm was applied[126].

3.2.3 Cascade energy measurement

A particle of initial energy E_{in} interacting in or close to IceCube will lose a fraction of its energy in the detector, the so called deposited energy E_{dep}. Of the deposited energy, again only a fraction can be directly measured by IceCube, as the detector is only sensitive to optical light in a certain range of wavelengths. Performing an energy measurement thus needs the definition of a figure of merit, which allows to infer the initial energy.
In the case of an interacting neutrino of energy E_{in} a cascade might emerge close or inside the instrumented volume. As discussed in subsection 2.1.1, the process which creates such a cascade is typically *deep inelastic neutrino nucleon scattering* (DIS). Two scenarios exist, neutral current and charged current interactions. In neutral current interactions, the neutrino loses energy and continues traveling, leaving the detector. In the second scenario, the neutrino transforms to its correspondent charged partner lepton which then will create ei-

ther a secondary cascade or in the case if a muon is created, it can also leave the detector. Both cases are indistinguishable for the here presented analysis, however a lower sensitivity of the analysis to ν_μ charged current interactions is expected due to the fact that tracks are more likely to be rejected by the event selection as they have a high probability to be created by incident cosmic ray muons. As further discussed in subsection 2.2.6, the primary cascade induced by DIS, includes hadronic fragments, which might fail the requirement to produce Cherenkov light and are thus invisible to the instrument. To define the above requested figure of merit, the *visible* energy E_{vis} is introduced. It is the energy a single, purely electromagnetic cascade needs to have to produce the amount of measured Cherenkov light.
The visual energy is a lower limit for E_{in} and E_{dep}. To measure the visual energy, several energy proxies exist, such relevant to this analysis are described in section 3.4. To infer to the true energy, in principle an unfolding with the detector response has to be done, however as can be seen in Figure 3.5, the reconstructed energy - the measure for the visible energy - is in the case of cascades strongly correlated to the incoming particle energy. Hence the measured energies are all given in reconstructed energy.

3.3 Hit cleaning

A certain fraction of pulses in each event can be attributed to electronic noise of the individual optical modules. Especially so called timing variables exploit heavily the fact that the detector response to a particle interaction has certain but often only small features. These features might be superimposed by noise pulses, and such it is of great interest to remove these noise pulses from the series before applying such algorithms.

3.3.1 Time window cleaning

A simple, though effective way to perform a pulse cleaning is the application of a time window cleaning, where the time window is the approximate time needed by a muon to travel through the instrumented volume of IceCube. This is about 6 µs and can be understood as an upper limit on the average expected event duration time for the events of relevance to this analysis.

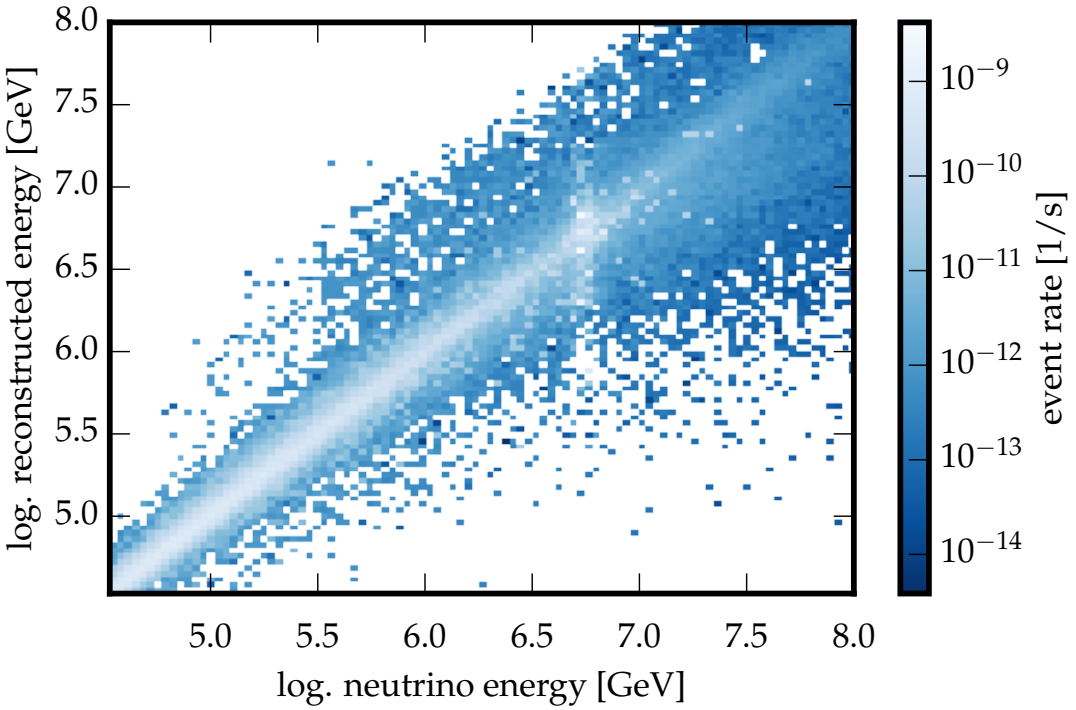

Figure 3.5 – The correlation between true neutrino energy and the reconstructed energy which is a measure for the visible energy is strong up to high energy. The Glashow resonance is visible at 6.3 PeV. The ν_e dataset is shown, which is weighted to an E^{-2} spectrum after the application of all filters. For a description of the filtering, see chapter 4.

The algorithm works in such a way, that a time window of pre-defined length is shifted over the pulse series until the pulse sequence with the highest charge in this time window is found. All pulses outside this time window are removed. While useful for algorithms which rely on the timing of certain features in the pulse series, such a clean pulse series can not be used for likelihood reconstructions which incorporate the noise contribution.

3.4 Reconstruction of event properties

In the following, the algorithms which calculate quantities which allow to infer the interaction parameters are briefly discussed. The reconstructed event properties like energy, direction or topology are useful for the separation of background and signal. The description is based on mainly on [118, 127].

3.4.1 Simple energy proxies & quality parameters

In cases where a fast calculation is more important than an accurate result, the energy of an event can be estimated by counting the number of DOMs which were triggered or summing up the total charge they have observed. However simplistic, using this values as energy proxies is justified due to the fact that the light yield of a cascade scales linearly with its energy. Although in the case of uncontained cascades, light will not be recorded due to the lack of instrumentation and thus the correlation of these variables and the energy of the cascade is much weaker. For this event class, these values will systematically underestimate the true energy. As they will underestimate the energy of signal and background events similarly, this is not a problem as long as these variables are only used for the purpose of background suppression, as they are in the analysis presented.

NChannel

The number of active channels or DOMs with observed pulses is a crude energy proxy as it varies largely with the position of the interaction vertex. The variable *NChannel* yields naturally small values for low energetic events, or for events which are outside the detector, or for muon tracks with only a few, dim

catastrophic energy losses. Besides rejecting low energy background events, *N-Channel* serves in the scope of this work as an estimate of event quality, as e.g. topology variables need a certain amount of active modules to be able to derive the spatial form of the event. This is especially important as for vertices at the edge of the instrumented volume, the hit pattern might look different than the patterns these algorithms were optimized for. For a series of events with an increasing number of active channels, however this differences are getting smaller, and thus requiring a minimum of active channels ensures that the calculation of such variables yields the expected result.

QTot

The total amount of collected charge of all active DOMs in an event serves as a crude energy proxy. It provides also a measure of cascade event quality for this analysis, which is complementary to *NChannel*: In events with many active DOMs, *NChannel* is large, but when only little light in the event is deposited, *QTot* yields a small number, even if *NChannel* is large. This might be e.g. the case for a dim muon track, which crosses the entire detector, leaving only a few hits in each optical module, or for a cascade far outside the instrumented volume where the registered light is scattered multiple times and thus many DOMs record only few photons.
Requiring thus a minimum amount of observed charge in combination with a minimum number of hit DOMs suppresses not only a large fraction of muon background, but also ensures a minimum event quality so that the calculation of sophisticated variables yields the expected result, as this variables rely on a meaningful hit pattern.

3.4.2 Topological event properties

The different hit pattern topology of shower-type and track-like events is exploited by a series of variables which use simple geometrical criteria to deduce the topology of an event.
These variables are designed to reject the large and mostly track-like atmospheric muon background. As the variable calculations can be done analytically by solving simple equations, the computing power needed to calculate these variables is low.

FILLRATIO

The algorithm which calculates the variable FILLRATIO deduces the sphericity of a measured hit pattern by calculating the ratio of hit DOMs over the number of all DOMs inside a chosen sphere. For a reasonable chosen radius, this number should be close to 1 in the case of a high sphericity, as it is expected for a shower-type event.
In contrast, for a track-like event, most chosen radii lead to spheres with a FILLRATIO much less than 1. However, the challenge is to find a suitable radius. Several options are provided by the algorithm, but using the RMS of the distance of all hit DOMs to a pre-defined vertex seems to be the most powerful choice and is used in this and other cascade analysis[118, 127].
This variable has also proven useful to reject coincident atmospheric muon events, that is events where two or more muons - or bundles - from different air showers are present within the time of a trigger window in the detector.

DIPOLEFIT

The dipole moment $\vec{M}$ of a hit pattern is calculated as the sum over all unit vectors which point from a hit DOM at position $\vec{r}_{i-1}$ to the DOM at position $\vec{r}_i$ which has observed the next hit closest in time[128].

$$\vec{M} \equiv \frac{1}{N_{ch}-1} \cdot \sum_{i=2}^{N_{ch}} \frac{\vec{r}_i - \vec{r}_{i-1}}{|\vec{r}_i - \vec{r}_{i-1}|} \tag{3.10}$$

The direction of $\vec{M}$ gives a very rough direction estimate. The value $|\vec{M}|$, is sensitive to the isotropy of the photon flux emitted by the source. As a cascade signature emerges from a close to isotropic light source in its center, small values are expected for that hypothesis, in contrast to the moving Cherenkov cone moving along the track of a muon.

CFIRST

CFIRST provides a vertex estimate by calculating the center of gravity (COG) $\vec{x}_{COG}$ of the observed hit pattern[101], which is the weighted mean of pulses

observed at DOM positions $\vec{x}_o$:

$$\vec{x}_{COG} = \frac{\sum_o w_o \vec{x}_o}{\sum_o w_o} \tag{3.11}$$

The weights can be chosen in such a way that either only the first pulse is weighted with the total charge observed by the DOM or all pulses are weighted with their observed charge respectively. The weighting can also be disabled by setting each $w_o = 1$.
As the COG does not include timing information, the vertex time is calculated with a sphere around the center of gravity. The radius of the sphere, which can be also expressed as a flight time of photons, is then optimized so that a given threshold number of observed hits can be causally connected to the found center of gravity. The performance of CFirst is limited in case of uncontained events, as per construction the COG can only be inside the instrumented volume. However, for the analysis presented, the calculated vertices by CFirst are only used to seed more elaborate reconstructions and thus only serve as a rough estimate for the vertex position.

TensorOfInertia

In analogy to the construction of a tensor of inertia in classical mechanics for an ensemble of mass points, a similar quantity $I^{k,l}$ can be constructed for an ensemble of hit DOMs $o^{k,l}$ at position $\vec{x}_o$, if they are weighted by their observed charge n_o instead.

$$I^{k,l} = \sum_o n_o^\alpha \left(\delta^{kl} \, \vec{x}_o^2 - x_o^k \, x_o^l \right) \tag{3.12}$$

The index α is used to adjust the weighting of the individual DOMs. In the simplest case, if $\alpha = 0$ all DOMs are treated equally independent of their observed charge. Knowing the quantity $I^{k,l}$ for a given hit pattern and α allows to derive the eigenvalues of this tensor. The eigenvalues $J_{1,2,3}$ can be used to deduce the sphericity of the hit pattern, by calculating:

$$J_R = \frac{J_3}{J_1 + J_2 + J_3} \tag{3.13}$$

which is the eigenvalue ratio J_R, and J_3 is the smallest of the eigenvalues. For a perfectly spherical hit pattern, three equal eigenvalues are expected, and thus

$J_R = 1/3$. In contrast the elongated hit pattern of a muon track will yield smaller values.

LINEFIT

This fast first guess reconstruction is designed to calculate a first estimate of the incoming particle direction[129]. This is achieved by minimizing the distance between the recorded hits. Therefore the following defined quantity χ^2 is minimized [128]:

$$\chi^2 \equiv \sum_{i=1}^{N} (\vec{r_i} - \vec{r} - \vec{v} \cdot t_i)^2 \tag{3.14}$$

In this equation N denotes the number of hits, $\vec{v}$ is the velocity of a track connecting the hit DOMs at position $\vec{r_i} \approx \vec{r} + \vec{v_{LF}} \cdot t_i$. The minimization is done with respect to the fit parameters $\vec{r}$ and $\vec{v}$, which define the fitted track. The differentiation can be done analytically and yields for the two parameters:

$$\vec{r} = \langle \vec{r_i} \rangle - \vec{v_{LF}} \langle t_i \rangle, \quad \vec{v_{LF}} = \frac{\langle \vec{r_i} \cdot t_i \rangle - \langle \vec{r_i} \rangle \cdot \langle t_i \rangle}{\langle t_i^2 \rangle - \langle t_i \rangle^2} \tag{3.15}$$

where the mean of a parameter $\langle x \rangle = \frac{1}{N} x_i$ is defined as the mean with respect to all hits N. With these resulting vertex point and velocity vector a direction can be calculated. The value of $|\vec{v_{LF}}|$ is interesting by itself, as it is an approximation of the speed by which light propagates through the detector along the calculated track. This quantity will be close to the velocity of light for an accurate enough reconstructed track and an incoming muon. In contrast, for a particle shower emerging from the interaction vertex, this quantity will be close to zero. Exploiting this fact, the variable $|\vec{v_{LF}}|$ can be used to reject track-like background. Meanwhile, a refined version of this algorithm is available[130], which performance has been improved especially for coincident events, and the emission profile of Cherenkov light has been added.

QMax/QTOT

Tracks of atmospheric muons which pass very close or even through a single DOM might deposit a large amount of charge in that single DOM - especially if the incident muon has a catastrophic energy loss at that position. Such events are thus often called “balloon events”. If the rest of the track is dim, events

might falsely be classified as a high quality cascade like event by many of the variables described above. Oftentimes, sophisticated reconstructions as described in subsection 3.4.6 falsely attribute high reconstructed energies to such events.
A variable, which is sensitive to such events is the ratio *QMax / QTot* of the maximum of the observed charges by all active DOMs and the sum of all observed charges.

3.4.3 Geometry & Containment

The event rate is not uniform over the instrumented volume of IceCube. In the upper part, atmospheric muons are more present than in the lower part, and there are regions where the transparency of the glacial ice is reduced.
Variables like the topology variables described in subsection 3.4.2 perform slightly different at different positions in the detector, due to different transparency of the ice or due to the fact that only parts of the hit patterns are present as it happens at the sides or the corners of the detector. To avoid large spreads in the values which are qualifying a high quality event, it might be desirable to exclude certain regions of the detector from an event selection.
Containment variables provide veto criteria, to shield a fiducial volume again incoming atmospheric muons as e.g. used in [127, 131]. As the here discussed analysis searches explicitly for events with vertices in such veto regions containment variables are used to identify these regions.

XYSCALE

The parameter XYSCALE provides a quantity which allows to distinguish if the x and y coordinates of an event vertex are contained within the polygon which traces the detector boundaries in these dimensions. Its implementation follows the idea to scale the polygon in such a way, that the point with the reconstructed vertex coordinates x and y is an element of the scaled polygon. XYSCALE is then the fraction of the areas of the scaled polygon and the polygon tracing the detector boundaries. This yields:

$$\text{XYSCALE} \begin{cases} < 1 \text{ for vertices inside the detetector boundary polygon in x and y} \\ > 1 \text{ all other vertices} \end{cases}$$

z-position of the vertex

To complement the information given by XYSCALE in the x and y plane, the reconstructed vertex z-position is used. Both variables together allow to identify if the vertex is in the region of interest to the analysis.

Distance from bottom edges

The distance of the reconstructed vertex from the most bottom DOM on each of the strings which mark the edges is a helpful criterion to identify the bottom corners of the detector.
Due to the exposed position of the DOMs in this corners, events with vertices close the bottom DOM on these strings are often classified as high quality cascade events, because oftentimes any hints of a track can not be seen by the instrument due to the lack of instrumentation. Also the phase space which muon tracks can occupy without leaving light in the detector is largest in this region, thus background rejection techniques may fail fairly often in this region. The distance from the bottom edges provides the possibility to exclude this worrisome region from the analysis.

3.4.4 Split reconstructions

Testing the stability of the fitted parameters of a shower under the removal of pulses from the event, yields a hint if the assumption of a shower-type event is reasonable.
Two ways of splitting the hit pattern are possible: Splitting in time or in space. After splitting, each sub pattern is reconstructed individually with a cascade hypothesis. For this purpose, the algorithm CASCADELLH (see subsection 3.4.6) is used to provide vertices for both sub-patterns. Variables which are then calculated are the spatial and temporal displacement of the vertices.

CORECORONASPLIT

If the algorithm is given a pre-calculated vertex, an energy dependent radius is calculated. The calculation follows a parametrization, which is based on an estimate how far the emitted light from the vertex can travel without being scattered.

Within this so-defined sphere all pulses are attributed to be “sphere-type” pulses, the pulses outside are attributed to be “shell-type” pulses.
Applying a cascade reconstruction algorithm on both split pulse series allows to calculate vertex displacement. As for the point like, isotropic light emission profile of a cascade hypothesis, the vertex is expected to be invariant switching between both pulse series, the spatial displacement and time difference provide criteria to reject track like background.

TimeSplit

The pulse series is sorted in time and split in two halves, yielding two disjoint pulse series. For both pulse series, reconstructions are performed individually and the differences between the two sets of individual reconstruction results are calculated. As for CorecoronaSplit, a cascade like event is expected to be reconstructed the same when exchanging the two pulse series in the reconstruction.

3.4.5 Causality criteria

TOPOSPLITTER

The IceCube trigger logic in its implementation at the time of this work is not able to trigger on individual *physics* events, e.g. a muon entering the detector. Instead it does trigger on on a certain number of DOMs observing pulses in a certain time window. If ongoing activity in the detector is registered, the trigger window is elongated to account for that. Coincident, but causally unconnected events, e.g. an incident atmospheric muon followed by a later cascade induced by an atmospheric neutrino might end up in the same triggered event.
To separate these coincident events, the algorithm TOPOSPLITTER was introduced. It searches for causally connected sub-patterns in an event and splits the event accordingly, storing the number of splits of the event as well. Two pulses are seen as causally connected, if their distance in time and space is compatible with a hypothetical particle moving with the speed of light could cause these pulses. An additional error margin can be configured for the algorithm, which was set to a microsecond for this work. Also requirements on the hit-cluster size can be set, which were fixed to 4 microseconds in time and 400 meters in horizontal as well as 30 meters in vertical directions.
In this work, TOPOSPLITTER was used to tag and remove coincident events which have a split count larger than 1.

DTNEARLY

Assuming a simple point-like light emitter hypothesis at a given vertex $\vec{x}$ and no scattering, light will travel isotropically with the local speed of light in the ice from this point to the individual sensors o_i and be recorded.
If the vertex assumption is correct, no sensor o_i will register hits at times earlier than the direct travel time added to the vertex interaction time. The direct travel time is given by $t_{geo} = d/c_{ice}$ with the distance d between sensor and vertex and the speed of light in ice c_{ice}. Calculating the time difference $dt_{first\ hit}$ between the first recorded hit $\min(t^{hit}_{o_i})$ and t_{geo} allows to identify deviations in the hit pattern from the hypothesis:

$$dt_{first\ hit} = \min_{all\ o_i} \left(t^{hit}_{o_i} - t_{geo} \right) \tag{3.16}$$

If $dt_{first\ hit}$ is found to be negative, this indicates that either the given vertex position or the event hypothesis of a shower type event is not accurate. However, to account for the uncertainty in a vertex reconstruction even for high quality cascades one needs to allow slightly negative values. Due to its sensitivity to individual hits - a muon track only needs to leave a single pulse which does not match the cascade hypothesis in the detector - the background rejection power of DTNEARLY is the largest among the variables used to suppress background for this work. It is especially useful when large parts of the track remain undetected, e.g. when a muon flies by the instrumented volume, leaving only very few hits of the track in the detector, but a large catastrophic energy loss. In these cases, oftentimes DTNEARLY is the only variable classifying these events correctly. The variable profits massively from a very accurate vertex reconstruction and a cleaning of the pulses series which is provided to DTNEARLY, because uncorrelated noise hits remnant in the pulse series will lead to a false classification of the event if being "too early".

Reconstruction quality Q_{exp}/Q_{obs}

One specific class of background events which are rare, but able to pass the track-rejecting criteria are especially critical for a diffuse analysis as described in this work: Low or medium energetic events which are reconstructed to very high energies by the sophisticated energy estimators as described in subsection 3.4.6. Such misclassification is rather rare, however even a single of these events will distort the measured spectrum if found in the final sample.
The reason for misclassification is in most cases caused be a wrong event hypothesis: Muon bundles which strife the detector close to the edges or the large dust layer might deposit light which triggers a hit pattern which obeys all imposed shape and timing criteria conditions, but its nature is a smother light deposition in time than the point-like emission of a catastrophic loss.
Sophisticated energy estimators incorporating likelihood methods then tend to reconstruct such events as far outside the detector, however with a large reconstructed energy, based on the wrong vertex. The value of the likelihood provides a handle on the accuracy of the used event hypothesis, however at the time of this work the value of the likelihood had a poor agreement between data and simulation. A more robust criterion to identify the accuracy of the event hypothesis with a better agreement of data and simulation is provided

by the ratio of the measured charge Q_{obs} and the expected charge Q_{exp} for the given event hypothesis. If this values deviates from unity, this can indicate that the reconstructed energy is not accurate.

3.4.6 Likelihood reconstructions

The probability $P(\underline{R}|\underline{C})$ to observe a given detector response $\underline{R}$ can be reinterpreted as the *likelihood* $\mathfrak{L}(\underline{C}|\underline{R})$ for the hypothesis $\underline{C}$ being true given the detector response $\underline{R}$. Then $\mathfrak{L}$ differs only by a constant factor from P. Maximizing the likelihood with respect to the hypothesis will return the best possible hypothesis if the likelihood models the detector response perfectly.
The detector response can e.g. be expressed by the times t_i^{hit} of recorded charge in a time bin i and the charges n_i^{hit} per bin, or in simpler cases only by observed charge per DOM. For shower-type and track-like events, an event hypothesis with 7 parameters can be formulated, which yields an accurate description of the observed event for most cases: Interaction vertex (x,y,z,t), direction (Θ,Φ) and a the visible energy E_{vis}. The latter is further described in subsection 3.2.3.
The probability that a given DOM o records some charge in a time bin i corresponding to a number of photo electrons n_{oi} is given by the Poisson probability for the expected number of photo electrons μ_{oi} assuming a certain event hypothesis. This leads to the following expression for the likelihood:

$$\mathfrak{L} = \underbrace{\prod_{\substack{\text{DOMs}\\ o}} \prod_{\substack{\text{bin}\\ i}} \frac{\mu_{oi}^{n_{oi}}}{n_{oi}!} \exp\left(-\mu_{oi}\right)}_{\text{(I)}} \underbrace{\prod_{\substack{o\\ \text{nohit}}} \exp(-\mu_o)}_{\text{(II)}} \tag{3.17}$$

This likelihood includes a term (I) for each hit optical module, which can itself be written as a product of individual terms per each time bin i. The term (II) in the likelihood accounts for the probability that an optical module does not record any hits. The most likely event hypothesis $\underline{C}$ to cause the observed response $\underline{R}$ is then found by maximizing L with respect to the hypothesis. To avoid numerical instabilities, this is typically done by minimizing $L = -\ln \mathfrak{L}$. This is justified, as the likelihood is not normalized and thus its absolute value is of no relevance for a probabilistic statement. The likelihood in Equation 3.17 is implemented by different algorithms used throughout this work. Dependent on the use case for such an algorithm, the number of bins, the noise model used

to calculate n_{oi}, the calculation to obtain $\mu_{oi}(\underline{C})$ or the number of parameters in the event hypothesis $\underline{C}$ differ.

AtmosphericCascadeEnergyReco

Implementing a per-DOM likelihood following Equation 3.17 by setting one time bin per DOM o, the reconstruction algorithm AtmosphericCascadeEnergyReco - or short ACER - allows the fast energy reconstruction for shower-type events[132].
Using only one time bin per DOM and taking the negative logarithm of Equation 3.17 yields.

$$L_o = \sum_{o_{hit,nohit}} (\mu_o - n_o \log(\mu_o) + \log(n_o!)) \tag{3.18}$$

The energy is reconstructed by assuming that the observed charge μ_o per DOM scales linearly with the energy, which is justified as described in subsection 2.2.4.

$$\mu_o = \Lambda_o \cdot E \tag{3.19}$$

Where Λ_o is the scaling factor. The linear assumption is justified, except in the very high energy regime where DOMs get saturated.
Using Equation 3.19 with Equation 3.18 and solving $dL/dE = 0$ allows to find the minimum value of the likelihood with respect to the energy. For the case of no noise contribution by the individual DOMs this is trivial:

$$\frac{dL}{dE} = \frac{dL}{d\mu_o}\frac{d\mu_o}{dE} \stackrel{!}{=} 0 \rightarrow E[GeV] = \frac{\sum n_o}{\sum \Lambda_o} \tag{3.20}$$

The value of Λ_o for an energy of 1 GeV is stored in lookup-tables, which incorporate the optical properties of the ice. These tables are further described in subsection 3.1.3.
In the case of noise, μ has to be substituted with $\mu_0 + rT$ where r is the noise rate and T the event duration. After substitution, the derivative of Equation 3.18 reads:

$$-\sum_o \frac{n_o}{E + \frac{rT}{\Lambda_o}} + \sum_o A_o = 0 \tag{3.21}$$

which can not be solved analytically, so AtmosphericCascadeEnergyReco utilizes a simple root finding algorithm for that purpose.

SPEFit

In a simple model, assuming only Cherenkov light emitted by a muon track and no scattering, the DOMs will measure the pulses at relative hit times $t_{hit} = t_{geo}$, where the geometrical time t_{geo} is given by the flight time of light on the shortest possible path. For scattered light, the actual travel path might be longer and a relative residual time $t_{res} = t_{hit} - t_{geo}$ can be defined. The first recorded pulses in each DOM are those for which scattering had the least impact.
For SPEFit, short for *single photo electron fit*, only the very first pulse of each DOM is considered[1]. The algorithm is implemented as a direction reconstruction for muon tracks and thus does not fit for the energy. The likelihood is minimized by numerical methods. As most muon tracks traverse large parts of the detector the reconstructed angle depends in this cases only mildly on the local ice parameters and a bulk ice model can be chosen to calculate the value of the p.d.f. to measure a pulse at the time t_{hit}, as further discussed in subsection 2.5.1.
The algorithm SPEFit provides a robust and accurate track, however for high energetic muons above about 1 TeV stochastic losses will occur frequently and the first hit observed by the individual DOM might actually be induced by a catastrophic energy loss which distorts the likelihood. For a more elaborate discussion of SPEFit, the reading of [133] is recommended.

CascadeLLH

Similar to SPEFit described above, the algorithm CascadeLLH[134] is designed as a fast particle shower reconstruction. The implementation follows a modular way: Analyzers can select the most suitable for their needs among different likelihoods and minimizers.
In the context of this work, CascadeLLH is configured to use a likelihood similar to SPEFit implementing a Pandel p.d.f., which is then minimized using a Powell algorithm[135]. Only the leading edge times of the first measured pulses and the total charge of the DOMs are considered. The algorithm is not able to take DOM saturation into account and does not account for the layered structure of the ice. Besides the vertex, the algorithm provides also the absolute value of the calculated log-likelihood, normalized to the number of pulses

[1] It has to be noted that this pulse might have a charge other than 1 PE, despite the name of SPEFit

used in the calculation. This variable is denoted as "reduced log-likelihood" and used in the context of this analysis to provide a vertex reconstruction on lower cut levels. CascadeLLH does not provide an estimate for the energy.

CREDO

Implementing the full log-likelihood following Equation 3.17, the algorithm referred to as CREDO [136] provides estimates for all 7 parameters of the event hypothesis $\underline{C}(x, y, z, t, \Theta, \Phi, E_{vis})$.
The time binning used for this algorithm is given by the individual extracted pulses, each pulse considered as its own bin. The expected charge μ_{oi} in each bin i is given by the tabulated delay-time p.d.f. $\frac{dP}{dt}\left(\vec{x}_o, t_{oi} - t_{geo} - t_{cscd}\right)$ with the direct travel time of photons t_{geo} and the interaction time t_{cscd}, scaled by the average expected charge for this DOM $\langle \mu_o^\infty \rangle$ times the read out time Δt_{oi} per DOM o_i:

$$\mu_{oi}(\vec{x_o}, t_{oi}, \underline{C}) = \left(\langle \mu_o^\infty \rangle \frac{dP}{dt}\left(\vec{x}_o, t_{oi} - t_{geo} - t_{cscd}\right) + \nu_{\text{noise}} \right) \cdot \Delta t_{oi} \tag{3.22}$$

The tabulated delay-time p.d.f.s are further discussed in subsection 3.1.3. The dark noise ν_{noise} is assumed to be the same for all DOMs.
The minimization of the 7 parameter log-likelihood is performed by the MIGRAD minimizer.
The algorithm provides a large variety of parameters and correction functions for high energetic events to avoid problems for the breaking linearity between observed charge and energy due to saturation of DOMs. CREDO is an accurate reconstruction algorithm with resolutions for the reconstructed vertices in the order of several meters and the reconstructed energies in the order of about 20%.

Monopod

Basically a refinement of CREDO, the algorithm Monopod [137] exploits the fact that the energy can be calculated from the likelihood analytically or by root solving, as it is implemented in the reconstruction algorithm AtmosphericCascadeEnergyReco, described in Equation 3.4.6. To do so, the likelihood

is first minimized in 6 dimensions and then the corresponding energy is calculated. The need to minimize only a 6 dimensional likelihood instead of a function in 7 dimensions reduces the execution time massively[138]. The algorithm MONOPOD allows a few improvements over CREDO. Among these, it features individual dark noise rates per DOM and a more sophisticated handling of saturated DOMs, which includes a more elaborate criterion to identify these.

4

Event selection

The main goal of the presented analysis was to develop and establish an event selection for shower-type events which have their reconstructed vertices outside or at the edge of the instrumented volume of the IceCube detector. Since IC40[118], events which fall in this category have been removed from analysis which focus on shower-type events[127, 139].
In this chapter, an event selection is described which is capable of selecting shower type neutrino candidate events at the edge of IceCube with reconstructed energies larger than 34 TeV. Individual filter steps of the event selection are discussed in detail and the obtained sample is presented.

4.1 Overview

The event selection presented here targets events above an energy threshold of 34 TeV. It has an effective area exceeding the effective area of a typical contained analysis at 100 TeV[63]. The selection has a lower neutrino purity ($\approx$70 %) when comparing with searches for well contained particle showers (purity $\approx$ 95%[63]). However it has to be taken into account, that this selection is not tailored towards a discovery of an astrophysical neutrino signal, as previous searches were, as IceCube already claims discovery of such a signal[23]. Follow

up analysis of the discovery try to measure the spectrum more precisely and address questions about flavor ratio and a preference of a cut off. The results on the measurements of these properties are suffering from a large statistical error. An approach to face the large statistical error is the combined fit of multiple event samples simultaneously[59]. The combination with other event samples then increases the statistical power to search for features in the energy spectrum. The here presented event selection is tailored to be combined with other samples, therefor the overlap with other sample was kept as low as possible. The here presented sample was developed under these considerations:

1. It was especially designed to be independent to a recent IceCube contained particle shower search, thus ensuring a minimal overlap to similar searches.

2. Being the first of its kind, it needs to be shown that a good signal-to-noise ratio and a reasonable selection efficiency can be achieved for this sample. Only then it can contribute valuable information in IceCube's task to reveal the nature of the sources of cosmic rays.

3. Relying on a background estimate derived entirely from Monte Carlo simulation, the sample has to be consistent with the prediction. A clear focus on agreement between data and Monte Carlo was set during the development of the sample. Following a simple straight cut approach instead of using machine learning techniques helped the understanding of differences between data and the Monte Carlo simulation.

4.2 Dataset

The here discussed event selection was developed based on simulation for signal and background as well as a subset of the experimental data. For the development, signal and background simulated specifically for the IC79 season was used, together with 10% of the experimental data of this season. This so called blind approach is a common technique when the specific properties of a signal are unknown. After an collaboration review process, the developed filter criteria were applied to the 90% of the experimental data. Being confident of the results, the selection was then applied to the following year of experimental

data as well, following the same procedure. In the final fit, also the 10% data used for the development of the analysis were included.
Within the first of these two seasons, IceCube was still under construction and the last 7 strings were deployed to complete the array. The detector configurations with 79 and 86 strings are not very different in terms of physics capabilities. The geometry was only slightly changed as illustrated in Figure 4.1. The larger footprint of the detector at the surface resulted also in an increase of the fiducial volume for the selection, which can be seen in Figure 4.1 as well. Trigger rates increased due to the additional instrumentation as can be seen in Figure 4.2. The criteria for the filtering which is performed directly at the Pole as (described in subsection 4.4.2) and L3 filtering to select shower-like events (see subsection 4.4.3) changed as well. Despite these changes, it was found that the selection needed only a minimal adaption when applied to IC86 data.

4.3 The sister analysis - contained cascade search

As this event selection was designed to be statistically independent from a specific other IceCube analysis[63], the analysis in question is briefly discussed here.
Having two separate samples allows to optimize separately for contained and uncontained events, which is also quite naturally a split of a low-and-high energy sample and a high-energy sample only. This also allows for consistency checks between the two samples.
The sister analysis is optimized for well contained particle showers starting at reconstructed energies of 10 TeV. It features a straight cut event selection with a Monte Carlo background estimate. The same Monte Carlo was used for both analysis, with the exception of low energy background simulation, where low energy means energies of the primaries per each nucleon smaller than 30 TeV. This low energy simulation was not used by the uncontained event selection, due to the final energy cut of 34 TeV. The sister analysis utilizes variables described in chapter 3. One of its strongest background suppressive variables is the reduced log likelihood of CASCADELLH, which was not used for the uncontained search. The reason for this was that the quality of the description of the variable by the background Monte Carlo simulation decreases with increasing distance of the vertices from the instrumented volume of IceCube. However in

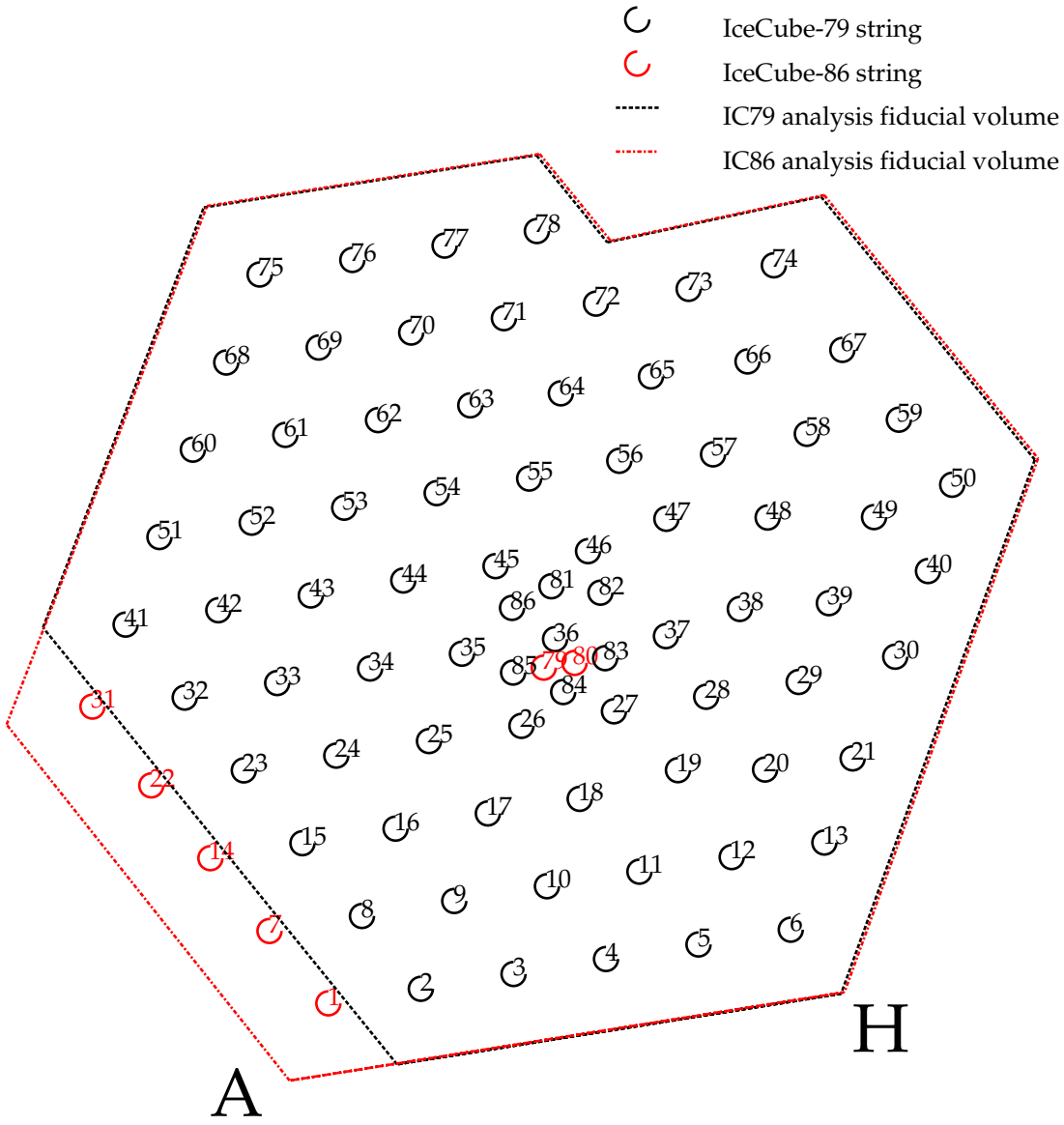

Figure 4.1 – A view on IceCube from above, string numbers indicated. The scale is about 1:11759. The corners of the array are labeled with capital letters, starting from "A" in the lower left corner in the figure at string number 1 (or 2 in the case of IC79), going clockwise to the lower left corner.

the inner part it shows a decent agreement. The effective area of this analysis is displayed in Figure 4.17. The contained analysis observes 152 events, from which about 60% have not been reported previously. Fitted to Monte Carlo templates of atmospheric muons, neutrinos and a astrophysical benchmark signal, the data prefers an astrophysical flux with a soft index of about 2.7. No indication for features in the power law have been observed and the data is consistent with itself if split in Northern and Southern hemisphere.

4.4 Filtering

As can be seen in Figure 4.2, IceCube records each second about 2000 - 3000 events, the exact number dependent on seasonal variations. The overwhelming part of these events are atmospheric muons. The number of expected signal events, which can be roughly estimated by taking an astrophysical flux with the approximate intensity in the order of the Waxman-Bahcall limit (see Equation 1.2.4) and the effective area of IceCube results in several observed events per year in the energy region of interest.
The reduction of the background is done by the use of the variables presented in section 3.4. The filtering reduces the massive amount of data to manageable levels, which is about in the order of 100 - 200 TB per season. It is organized in different filter levels, each dedicated to remove a certain class of background. The division of the filtering in different levels has also another purpose: Many algorithms need intensive computing resources and can not be applied to all triggered events. On a filter level higher in the filtering chain, this is however possible.

4.4.1 Trigger

The basic trigger condition requires 8 individual optical modules to register a photon. To trigger it is also required that these 8 individual modules fulfill a local coincidence criterion which is satisfied when neighboring DOMs are triggered (see HLC as discussed in subsection 2.4.2). The full detector is then read out within a time window of 4 microseconds before the trigger and 6 microseconds after the trigger. The trigger rate as shown in Figure 4.2 varies by about 10% due to seasonal variations. Seasonal variations occur due to changes of

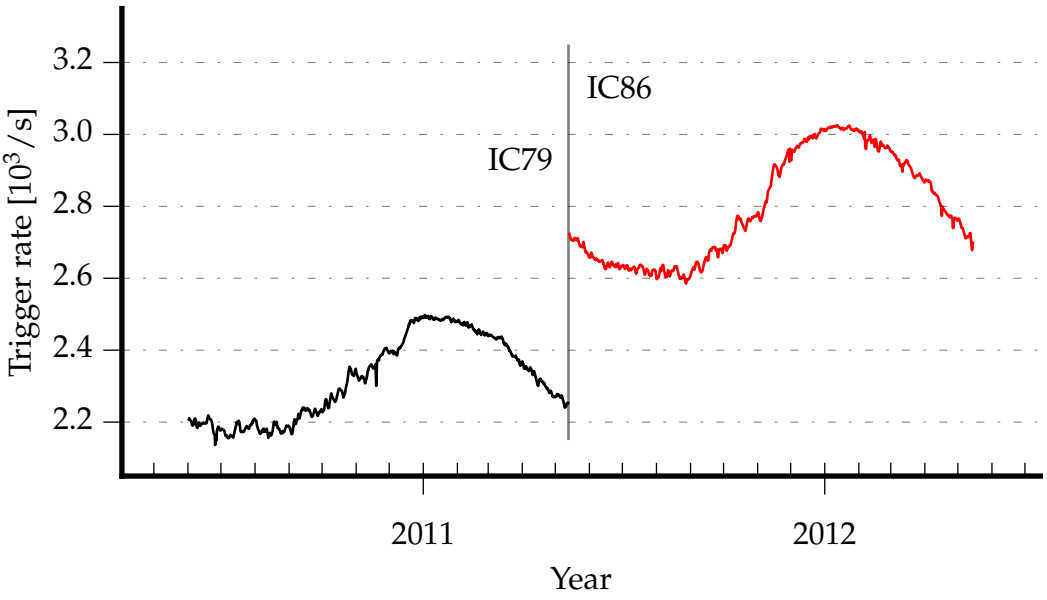

Figure 4.2 – IceCube trigger rates for the 2011/2012 datasets used in the analysis.

atmospheric conditions. The atmospheric overburden at the South Pole varies, and these density changes alter shower topology and the interaction probability of muons with the atmosphere and thus the rate of muons registered at Earth's surface varies.
The information of all triggered events is stored on disk or tape at South Pole. Due to the limited bandwidth of the satellite connection of about 100 GB/day to the South Pole only a subset of the triggered events is transfered to the North, which is the starting point for any further filtering and processing.

4.4.2 Level 1 filtering

A full-grown data center at South Pole provides the capability to filter the triggered data according to the requirements of the different physics working groups in the collaboration. The primary need for the filtering at South Pole is given by the limited bandwidth of the satellite connection, hence a reduction of the data rate is required. For this analysis, only events which were tagged as shower-type at the Pole were used. As the computing power at South Pole is limited, it is required to use filter criteria which use as less resources as possible.

ToI	LfV	background suppression	$E^{-2}\nu_e$ efficiency	bandwidth GB/day	data rate (1/s)
> 0.06	< 0.09	98%	74.28	5.98	21

Table 4.1 – IC79 cascade filter run at Pole. Two criteria are invoked: Eigenvalue ratio calculated by TENSOROFINERTIA (ToI) and the calculated velocity by LINEFIT (LfV). The efficiency for a simulated astrophysical cascade signal with the benchmark E^{-2} spectrum the filter was optimized as well as the used satellite bandwidth for the satellite transfer and data rates are given. Values taken from [140].

	"up-going"	"down-going"
zenith	$> 56.03^\circ$	$< 56.03^\circ$
rlogl	$\leqslant 10.5$	$\leqslant 10.7$
Lfv	$\leqslant 0.12$	-
ToI	$\geqslant 0.05$	-

Table 4.2 – The selection criteria for the cascade Filter for the IC86 season, taken from [141]. The sample is split in two regions defined by the zenith angle of a track likelihood algorithm. Further applied are filter criteria based on a likelihood calculated by CASCADELLH (rlogl) and the same first guess algorithms as in the IC79 season, the eigenvalue ratio of TENSOROFINERTIA (ToI) and the LINEFIT velocity (Lfv).

IC79

For the needs of the cascade filter, the eigenvalue ratio of TENSOROFINERTIA described in Equation 3.4.2 as well as the absolute velocity $|\vec{v}_{LF}|$ calculated by LINEFIT as defined in Equation 3.4.2 provide such criteria. The rate of events tagged by the cascade filter is about 30 events per second, which is a reduction by about 2 orders of magnitude compared to the trigger rate. The settings of the filter for the IC79 season can be found in Table 4.1.

IC86

For the dataset of the IC86 season, a slightly different approach was chosen for the cascade filter. The reason was a higher desired efficiency for low energetic events. The eigenvalue ratio J_R of TENSOROFINERTIA as described in subsection 3.4.2 will result in a value of 0 for single and two string events where the value for the smallest eigenvalue is always 0. Therefore the sample is divided

in two filter regions, the split is defined by the calculated zenith angle of a track likelihood reconstruction. Naturally, the up-going region is less background dominated, and so no further requirements on values calculated by TensorOfInertia or LineFit were necessary. For the down-going sample however, the values from the IC79 season were re-optimized and altered accordingly. As from this season on also CascadeLLH (see Equation 3.4.6) is run at Pole, the calculated likelihood by this algorithm is exploited as filter criterion. The settings for the two branches of the IC86 cascade filter are listed in Table 4.2.

4.4.3 Level 2 processing & level 3 filtering

The next filtering steps on the data stream are performed on the transferred data in the Northern hemisphere. This allows for more CPU intensive algorithms, e.g. for reconstruction and hit cleaning to be run on the data stream. Before the filtering happens, a joint processing level, denoted as level 2 processing is performed. The level 2 processing is run on all events which are transmitted to the North, afterwards the individual level 3 filters split the data stream in physics related sub-streams, where events which do not fulfill the respective quality criteria are discarded from the stream.
The reconstructions which are needed for the filter decision are calculated mostly at the level 2 step, these are e.g. SPEFit and CascadeLLH. More cascade specific reconstruction algorithms like AtmosphericCascadeEnergyReco or CREDO are part of the level 3 processing (for a description of reconstruction variables see section 3.4). Between the two seasons of data used in this analysis, the filter were changed: The level 2 filtering was changed only slightly, one of the changes of relevance in the context of this analysis was the reduction from 4 to 2 iterations of the SPEFit track reconstruction, which provides the zenith angle which is used as filter criterion in this event selection. The level 3 processing however was changed more dramatically, which results in an overall drop of rate for the IC86 season when compared with the IC79 season. The requested baseline for the level 3 processing is a reduction of about 2 orders of magnitude compared to the level 2 data stream.

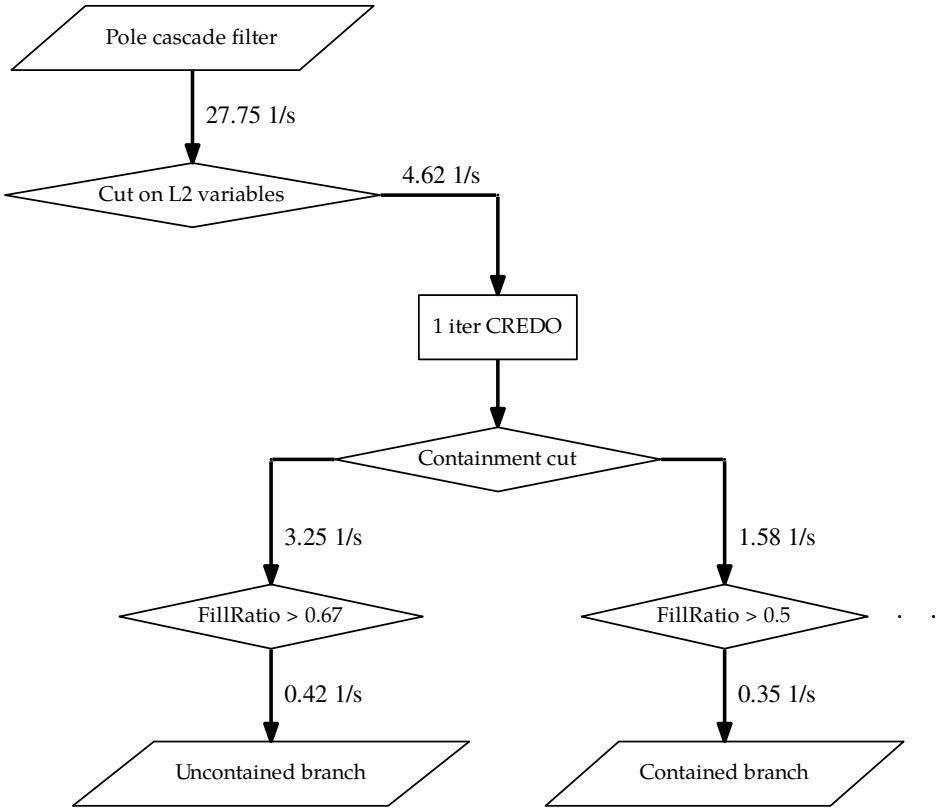

Figure 4.3 – Schematic of the IC79 Level 3 cascade filter, passing rates indicated. First a nested cut on the quality parameter *LLHRatio* and the zenith angle of the muon track reconstruction SPEFIT, dependent on the energy is performed. The CREDO reconstruction is applied afterwards. With the vertex of this reconstruction, a simple containment criterion "L3 Containment" is defined. After this, the stream splits in “uncontained” and “contained”, depending on the calculated vertex position. Different cuts on the topology variable FILLRATIO are performed for each of the sub-streams.

IC79 level 3 cascade filter

Designed to retain a high signal efficiency for a wide range of analysis searching for a cascade-like neutrino signal of atmospheric or astrophysical origin, the level 3 filter provides a high signal efficiency over a wide energy range from the 1 TeV up to the PeV regime for an atmospheric neutrino spectrum. The signal efficiency for an astrophysical neutrino spectrum which is expected to be harder than the atmospheric neutrino spectrum is the same or larger as the efficiency of the selection increases with energy. To achieve this goal the filter defines two regions, dependent on the reconstructed energy by AtmosphericCascadeEnergyReco. Events with reconstructed energies larger than 10 TeV pass this first filter step, where events with a lower reconstructed energy have to fulfill the following two conditions:

1. an energy dependent zenith angle cut based on the SPEFit reconstruction to reject downgoing low energetic muon tracks:

$$\cos\theta_{\text{track}} < \cos\theta_{\text{crit}} \equiv 0.36 + 0.16 \times \log_{10}(E_{\text{ACER}}/\text{GeV}) \tag{4.1}$$

2. the likelihood ratio between a cascade and track hypothesis, where the calculated likelihoods of CascadeLLH and SPEFit are used:

$$\ln L_{\text{track}}/L_{\text{cascade}} < 5 \tag{4.2}$$

After the first filter step, CREDO (see subsection 3.4.6), an elaborate likelihood reconstruction is run on the sample. With the help of its reconstructed vertex, a simple containment criterion is defined. To fulfill this criterion, noted further as “L3 Containment”, the following two conditions must hold.

1. The DOM which observes the largest charge must not be part of the outer layer of the detector.
2. The reconstructed CREDO vertex must be inside a polygon which is defined by the strings of the outer layer of the detector.

No requirement on the z-position is needed to fulfill the “L3 Containment” criterion.

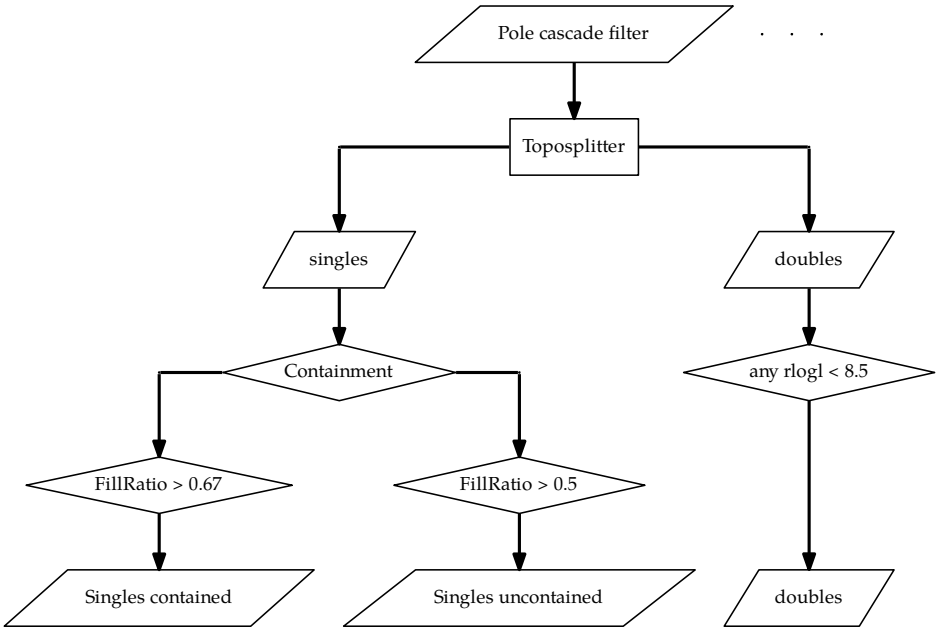

Figure 4.4 – IC86 level 3 filtering, schematic

Based on this containment criterion, the Cascade level 3 splits into an "contained" and "uncontained" stream. For both streams, the background is reduced further with the help of FILLRATIO, although with different cut values. The FILLRATIO cut for the "uncontained" stream has especially been optimized for an E^{-2} neutrino spectrum. The structure of the IC79 level 3 filter is sketched in Figure 4.3.

IC86 level 3 cascade filter

With the introduction of the event splitting algorithm TOPOSPLITTER, described in subsection 3.4.5, the level 3 cascade filter was altered after the IC79 season. In contrast to IC79 there is no different treatment of high and low energetic events, instead a different split scheme was chosen. In a first step, a multiplicity of the event is calculated using TOPOSPLITTER. The multiplicity indicates if during the trigger window another particle interaction that happened independently from the triggering interaction was registered by the detector. The IC86 level 3 stream is split by multiplicity in two streams, single events and double coin-

cident events. Events which yield a higher multiplicity were removed. On the two streams, different filter criteria were applied:

Double coincident stream: Events are only kept if one of the two sub-events yields a value of reduced log-likelihood calculated by CascadeLLH < 8.5

Single coincident stream: For this stream a containment criterion similar to the IC79 level 3 processing is applied. This further on splits the stream in two more sub-streams. Both of them are required to score high when the algorithm FillRatio is applied. Besides that additional requirement on the two streams are:

Contained: Number of strings with active DOMs > 3 and reduced log likelihood calculated by CascadeLLH < 9

Uncontained: The number of active DOMs in the event, *NChannel* > 120

As the requirements on the data stream are stricter than for IC79, the experimental data is reduced to a rate of 0.30 events per second, compared to 0.77 events per second for IC79.

4.5 Analysis specific filtering steps

The filter levels especially designed for this analysis fulfill various purposes. First the data rate needs to be reduced, so that computing intensive variables can be calculated on the reduced dataset. The reduction is done by the level 3a filter, which reduces the data rate by roughly one order of magnitude compared to level 3. The computing intensive variables are needed, as the special topology of the events which are searched for requires a careful treatment, which e.g. includes running minimizations with a large number of iterations and selecting the best result. Third, a fiducial volume is defined and events which were

found to be too difficult to reconstruct are removed. Also, it is ensured that the overlap of this and other samples is small by removing contained events. After this, the large fraction of track-like background is reduced in the filter level 5, the next filter level reduces then the remaining cascade like background. The final step exploits the fact that the astrophysical neutrino spectrum is less steep than the atmospheric spectrum and sets a lower energy threshold for the analysis.

4.5.1 Level 3a analysis filter

The first filter level introduced by the analysis requires two conditions for the data to pass:

1. As the background prediction relies on Monte Carlo simulation which has a large drop in statistics for cosmic ray primaries with energies smaller than 30 TeV per nucleon, the background modeling is inaccurate for low energetic events. Therefore it is required that the reconstructed energy by AtmosphericCascadeEnergyReco is larger than 10 TeV. This is sufficient, since it is very unlikely for a 30 TeV primary cosmic ray nucleon to yield a muon which deposits a 10 TeV cascade in the ice. Side-effect of this condition is a large suppression of background muons due to the steeply falling atmospheric muon spectrum.

2. Due to the reduced ice overburden at the top of the instrumented volume compared to the bottom, the exposure of the region above the detector to atmospheric muons is higher than at the bottom region. Also the ice is less clear and thus reconstructions performance is relatively poor. In consequence, the region above the instrumented volume of IceCube is removed with the help of the reconstructed z-position of the vertex calculated by the single iterative CREDO fit performed at level 3.

After the removal of these events, the remaining ones are reconstructed with 2 different implementations of a 4-fold iterative likelihood reconstructions, CREDO and Monopod, where the first serves as seed for the latter. The Monopod vertex serves as input for the calculation of the variables DTNearly and FillRatio. Toposplitter was calculated at level 3 for the IC86 dataset, is run

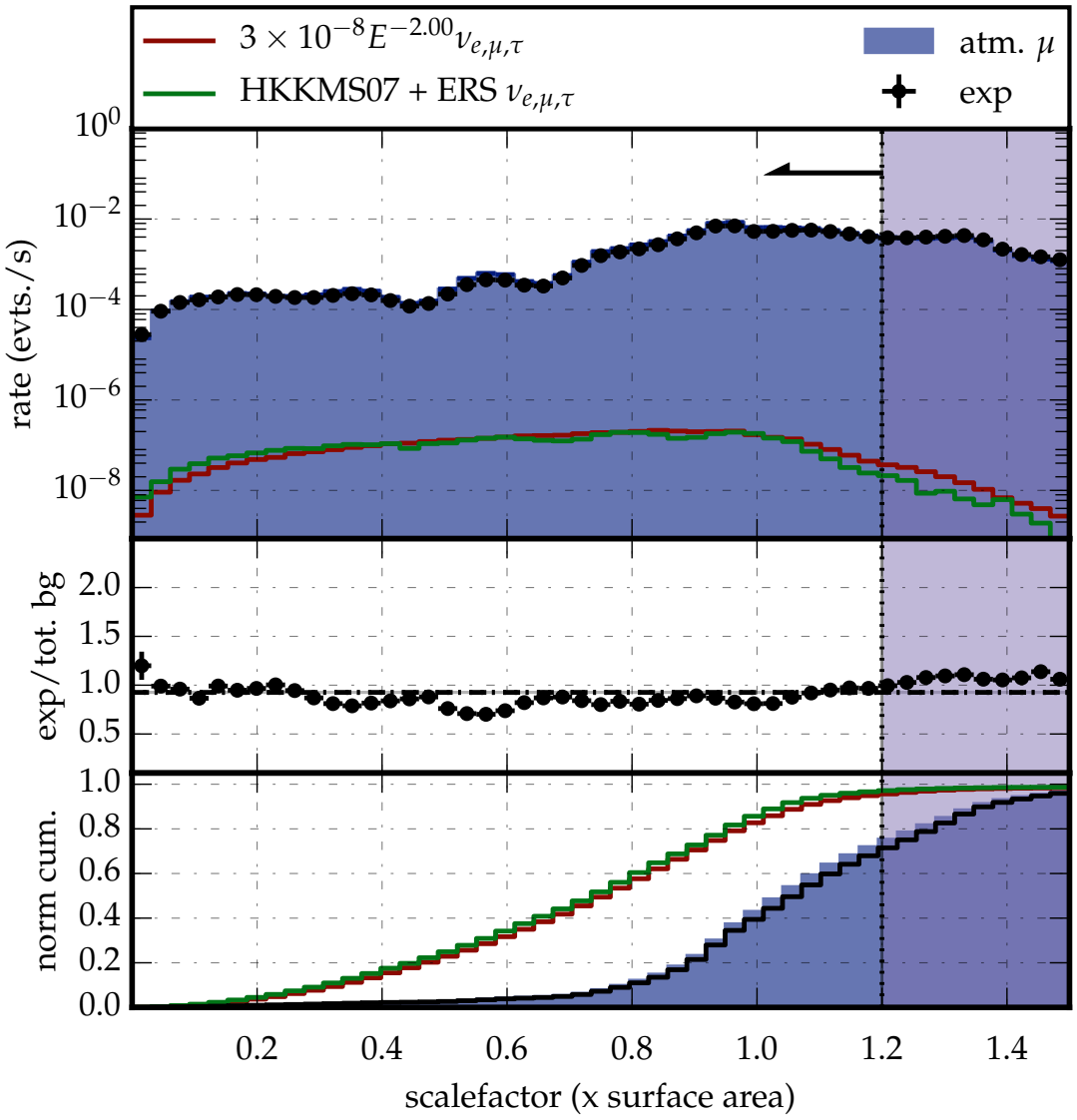

Figure 4.5 – The distribution of the polygon scaling variable XYScale, level 3a cuts applied, is shown in the upper panel. The middle panel shows the ratio of data and all background simulation, the weighted mean value of all bins is indicated with the horizontal line. The lower panel shows the distribution as in the upper panel, however cumulative. Besides the experimental data, an astrophysical E^{-2} flux and the background components of atmospheric neutrinos predicted by the HKKMS07 and ERS models, as well as atmospheric muons are shown. The arrow indicates the chosen value for the fiducial volume of 1.2 in XYScale. The wiggles in the distribution occur where the scaled polygon matches a layer of strings.

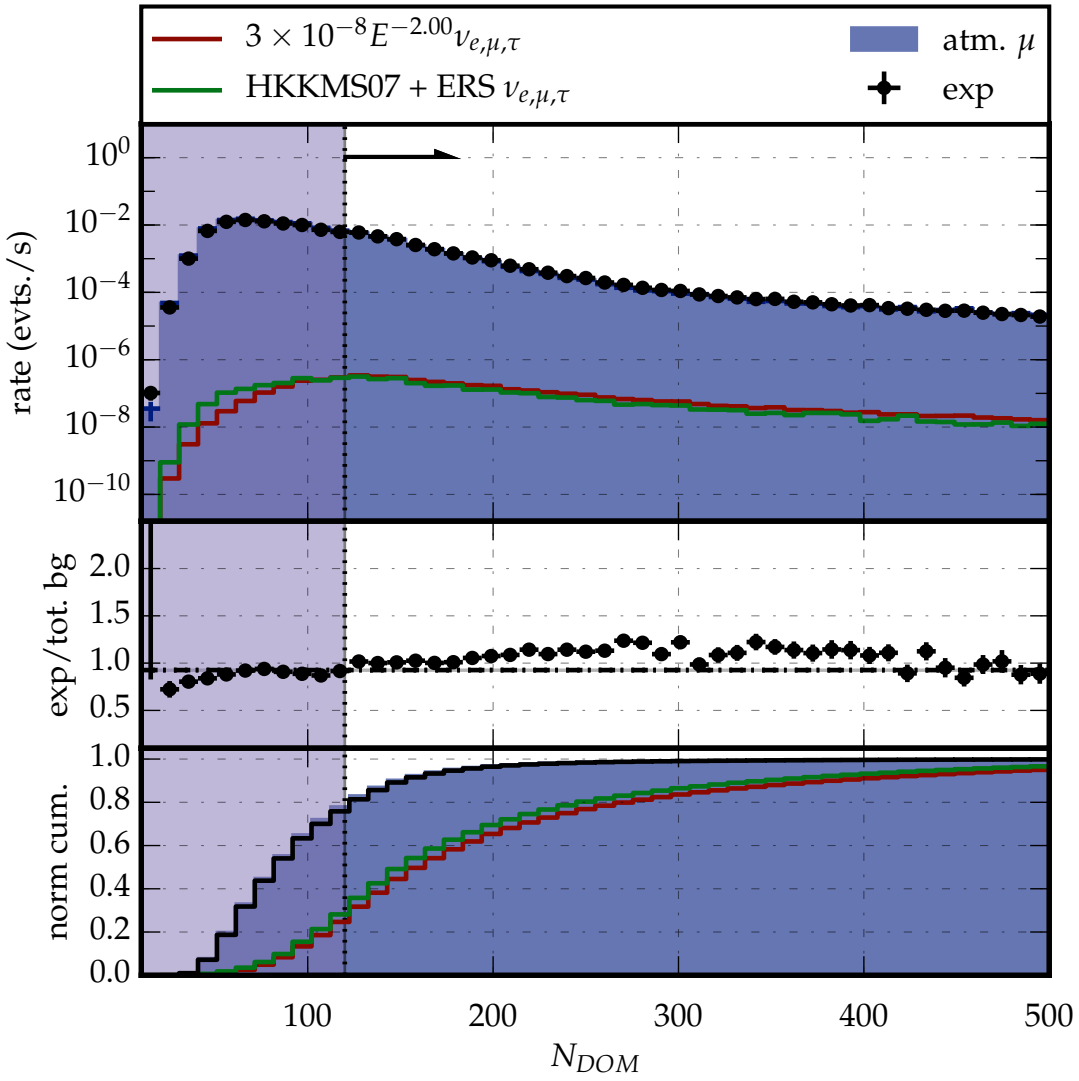

Figure 4.6 – The distribution of number of modules that recorded photoelectrons, level 3a filter criteria applied. The arrow indicates the requirement of 120 modules, which is set at level 4. The small kink in the distribution at exactly this value is caused by the removal of a fraction of these events at IC86 level 3, where the same cut is applied to the there defined sub-stream of uncontained singles. See Figure 4.5 for a description of the individual panels of the plot and the individual distributions.

for the IC79 season at this level.
The reason why contained events are kept on this filter level is that they can be used for systematic studies later on. All sub-streams of the IC79 and IC86 level 3 filtering enter the level 3a filtering. The data stream is reduced by the level 3a filter to 0.19 events per second for IC79 and 0.01 events per second for IC86.

4.5.2 Level 4 analysis filter

The L4 analysis filter serves as a first step to ensure event quality, by defining a fiducial volume and a very simple quality criterion for the data sample. Cascades which have their vertices outside the instrumented volume of IceCube can only be detected up to a physical limit: The individual DOMs need to register a certain amount of photoelectrons above their noise rate in order for reconstructions algorithms to effectively reconstruct the event. As the light intensity decreases with the distance squared from the event vertex for cascades, not taking into account scattering and absorption in the ice this limit prohibits to go further out than about 500 - 800 meters. However, as the phase space for mis-identified muon tracks increases rapidly when going outside the instrumented volume, one finds that even before this limit the signal is buried underneath non-rejectable background. Studies on the level 3a sample revealed that the distance from the detector of about one string spacing (125 m) outside of the instrumented volume independent from the energy of the event is a good compromise between the desire of the largest volume possible and confidence in the selected events. Level 4 filtering takes account for this by removing events which are further outside. The exact calculation invokes the scaling of the footprint of the detector at the surface, as described in subsection 3.4.3. The distribution of this variable is shown in Figure 4.5. It shows a good agreement between data and simulation.
The fiducial volume of the analysis extends also below the detector, the events must have a reconstructed vertex z-position of not lower than 100 meters underneath the instrumented volume.
At this filter step, also the events inside the instrumented volume are removed, as the goal of this analysis is to explicitly find events which have not been observed yet. This is done as statistical independence is required when combining this sample with other samples. The removal of the contained events is done

by inverting containment cuts of a specific other IceCube analysis[63]. On this filter level, two further event classes were removed, that were not useful for the final analysis:

coincident events: Only events were kept where the multiplicity calculated by TOPOSPLITTER is 1.

dim events: In this case "dim" refers to "not triggering a large amount of optical modules". If only a low amount of optical modules has been triggered by the event, some of the chosen selection criteria fluctuate wildly and the distinction between signal and background region is difficult. For this reason, events which have triggered less than 120 optical modules are removed from the data stream. The distribution for this value is shown in Figure 4.6.

4.5.3 Level 5 analysis filter

This filter step has a single purpose: The massive suppression of track-like background. As previous filter levels ensured that the events have a decent quality for the reconstruction of hit-pattern characteristics to work properly, even in the case of events with their vertex outside the detector, the resulting reconstruction results can now be exploited to separate shower events from mis-reconstructed tracks. A description of the variables used at this level can be found in section 3.4. The used criteria divide in three classes:

shape & geometry: The spherical geometry of cascade-like events contrasts the elongated shapes of tracks. Variables which exploit this are .e.g. FILLRATIO, TENSOROFINERTIA and DIPOLEFIT. The distribution of FILLRATIO is shown in Figure 4.7, it is especially powerful in removing remaining coincident events in the sample.
Also the fact the atmospheric muons enter the detector from the Southern hemisphere is exploited by requiring a minimum zenith angle derived by the track reconstruction SPEFIT. The corresponding distribution is shown in Figure 4.8.

timing & causality: A cascade-like event appears to be "stationary" in the detector as the light emission profile is isotropic after several scattering lengths. In contrast to that, a muon moving through the detector exhibits an event pattern which has a certain direction and velocity. This fact is exploited by split variables, as described in subsection 3.4.4. The distributions for the TimeSplit spatial vertex displacement and the time displacement calculated by CoreCoronaSplit are shown in Figure 4.11 and Figure 4.10 respectively. Due to this nature of the observed signal, also causality criteria can be applied, exploiting the fact that muons are traveling faster than the local speed of light in ice. DTNearly, as described in subsection 3.4.5 provides such a criterion, its distribution shown in Figure 4.9. The here mentioned criteria are very powerful for the suppression of track-like background and show a very good agreement of data and simulation.

quality: If muons have a catastrophic energy loss very close to a DOM or even hit the DOM, the single DOM in question might record a high charge. Events of that class are often dubbed "balloon-type" events for this reason. Despite the rest of the charge is distributed smoothly over the muon track, the point like accumulation of charge in a single DOM likely causes the event to score high in the above two mentioned classes of track suppression criteria. Such events can be removed by requiring that the most of the charge is not deposited in a single DOM. This can be identified by the variable $QMax$ /QTOT. Removing these types of events is common among most recent cascade analysis[63, 127].

Selecting filter criteria was done under the prerequisite of best possible agreement of experimental data and simulation. The values were optimized by maximizing a simple signal-to-noise criterion of $N_{sig}/\sqrt{N_{bg}}$ which assumes that both expected number of signal and expected number of background events are Poisson distributed.

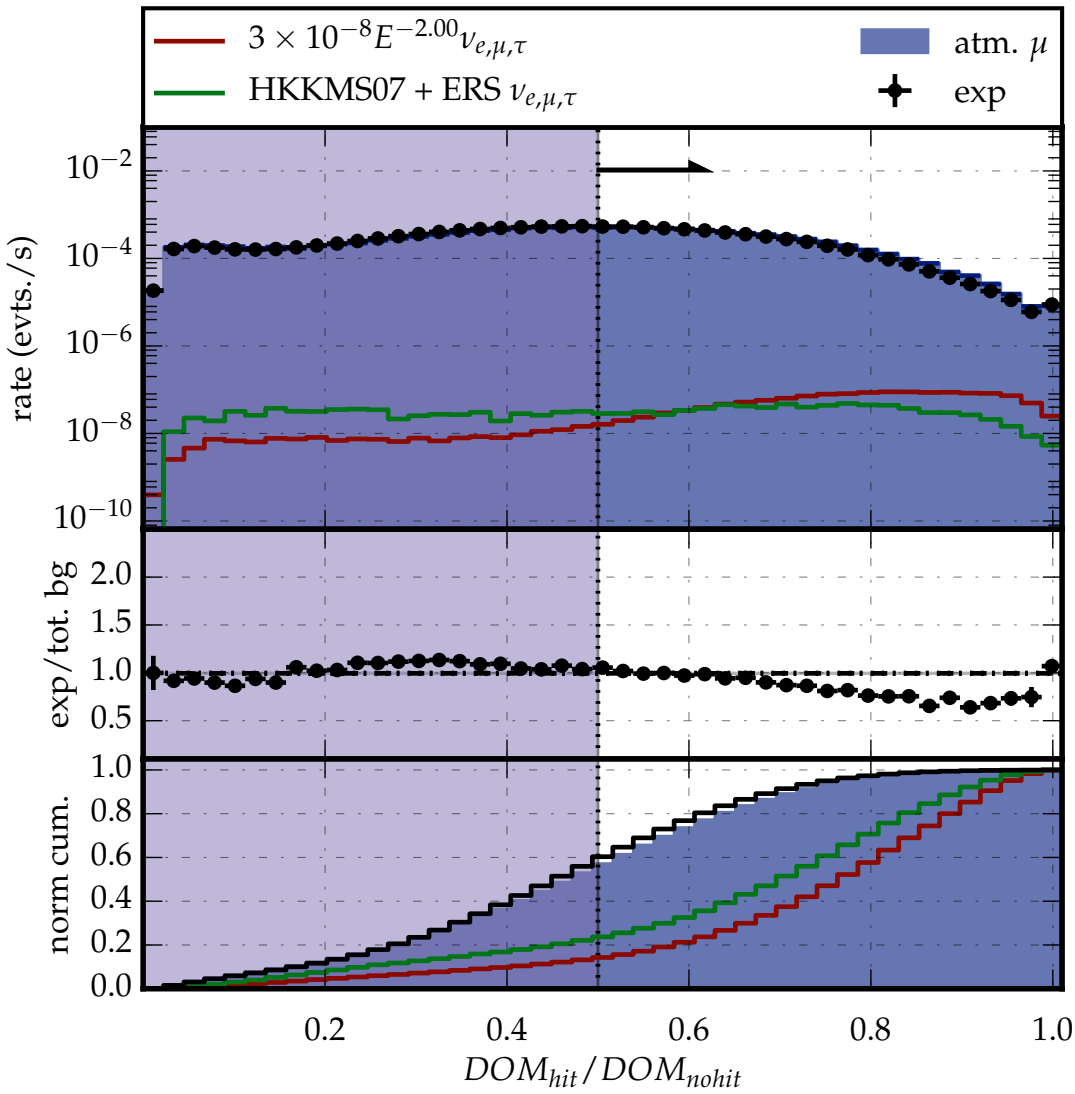

Figure 4.7 – The distribution of the calculated values for FillRatio after the level 4 cuts. The slope of the ratio plot of data and simulation in the middle panel left to the line indicating the cut can be explained by the lack of coincident simulation compared to data on this level. The arrow indicates the chosen value for the L5 filter. See Figure 4.5 for a description of the individual panels of the plot and the individual distributions.

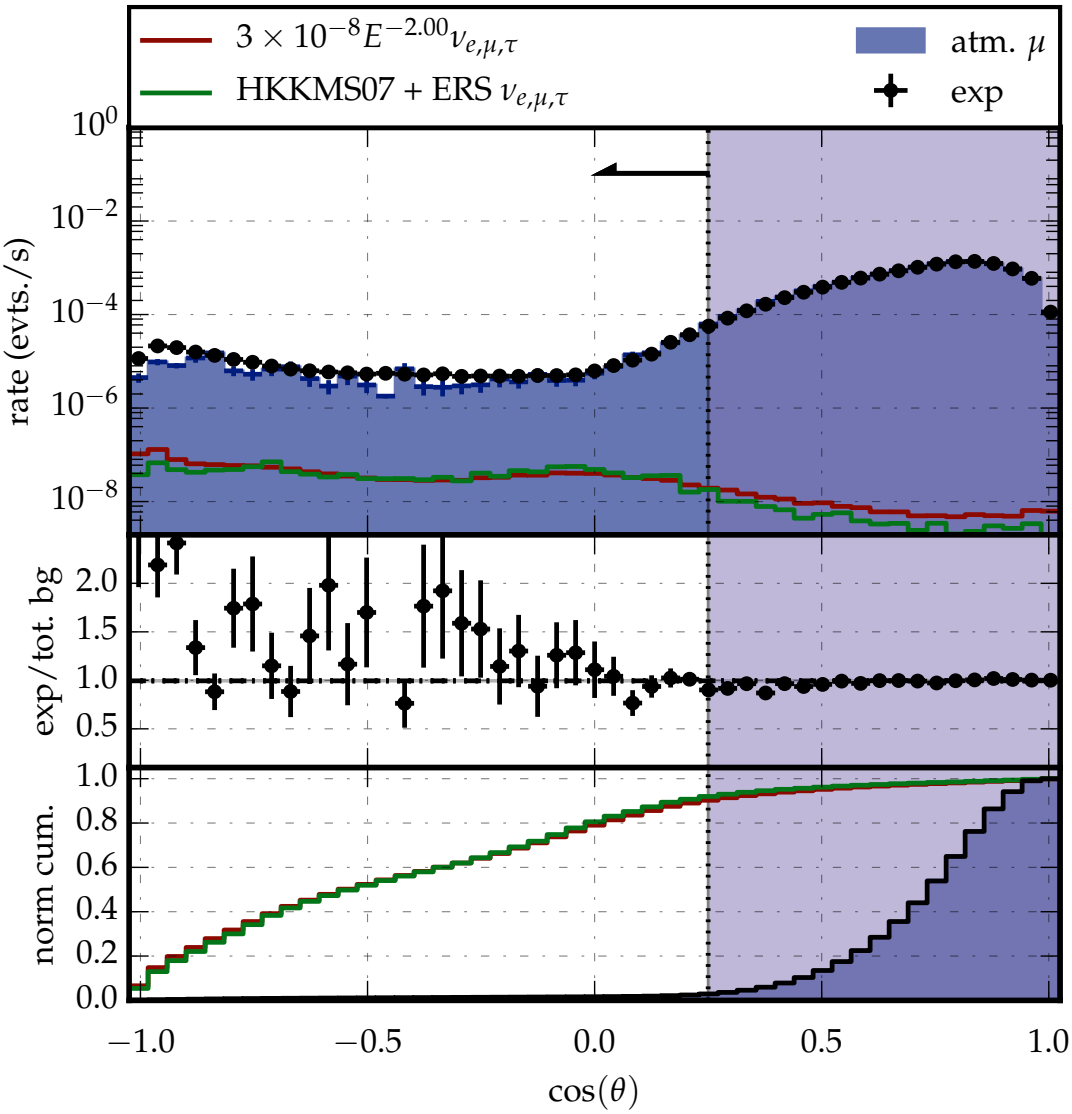

Figure 4.8 – The cosine of the zenith angle of the track reconstruction SPEFit ÷. The value "1" indicates "down-going" events coming from the sky above the surface on top of IceCube, whereas "-1" indicates "upward-going" in the detector. The distribution is shown after the application of the level 4 filter criteria. The arrow indicates the value chosen for the level 5 filter. The mismatch of data and simulation in the up-going part can be explained by a lack of coincident events in the simulation at that level. As the algorithm does not penalize hits which are not causally connected, but is sensitive to the ordering of hits in time, two tracks coming from above can be identified as a single, up-going track. See Figure 4.5 for a description of the individual panels of the plot and the individual distributions.

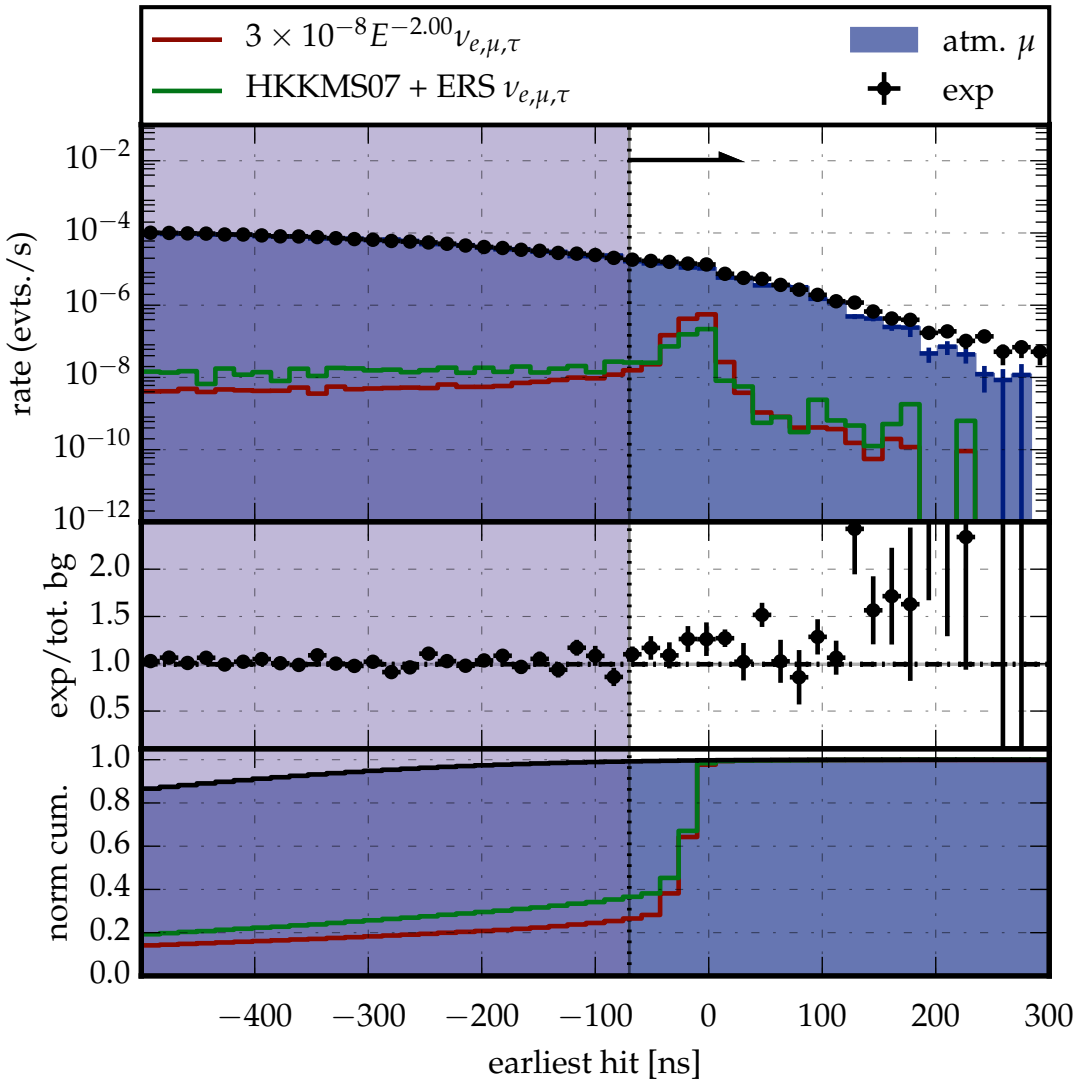

Figure 4.9 – DTNearly is the most powerful variable to suppress atmospheric muon background, its distribution show here after the application of the level 4 filter. The signal peak at zero is spread out due to the limited vertex resolution. The variable shows a good agreement between data and simulation, as can be seen in the ratio plot in the middle panel. The mismatch in the signal region at large, positive values of DTNearly especially > 200 ns can be attributed to statistical fluctuations, as the individual event count in the bins at this part of the distribution is only a few events. Also coincident events contribute to the mismatch, as only few coincident events were simulated. For coincident events, the reconstructed vertex is not causally connected to the first hit in the event, thus high values of DTNearly can be obtained. See Figure 4.5 for a description of the individual panels of the plot and the individual distributions.

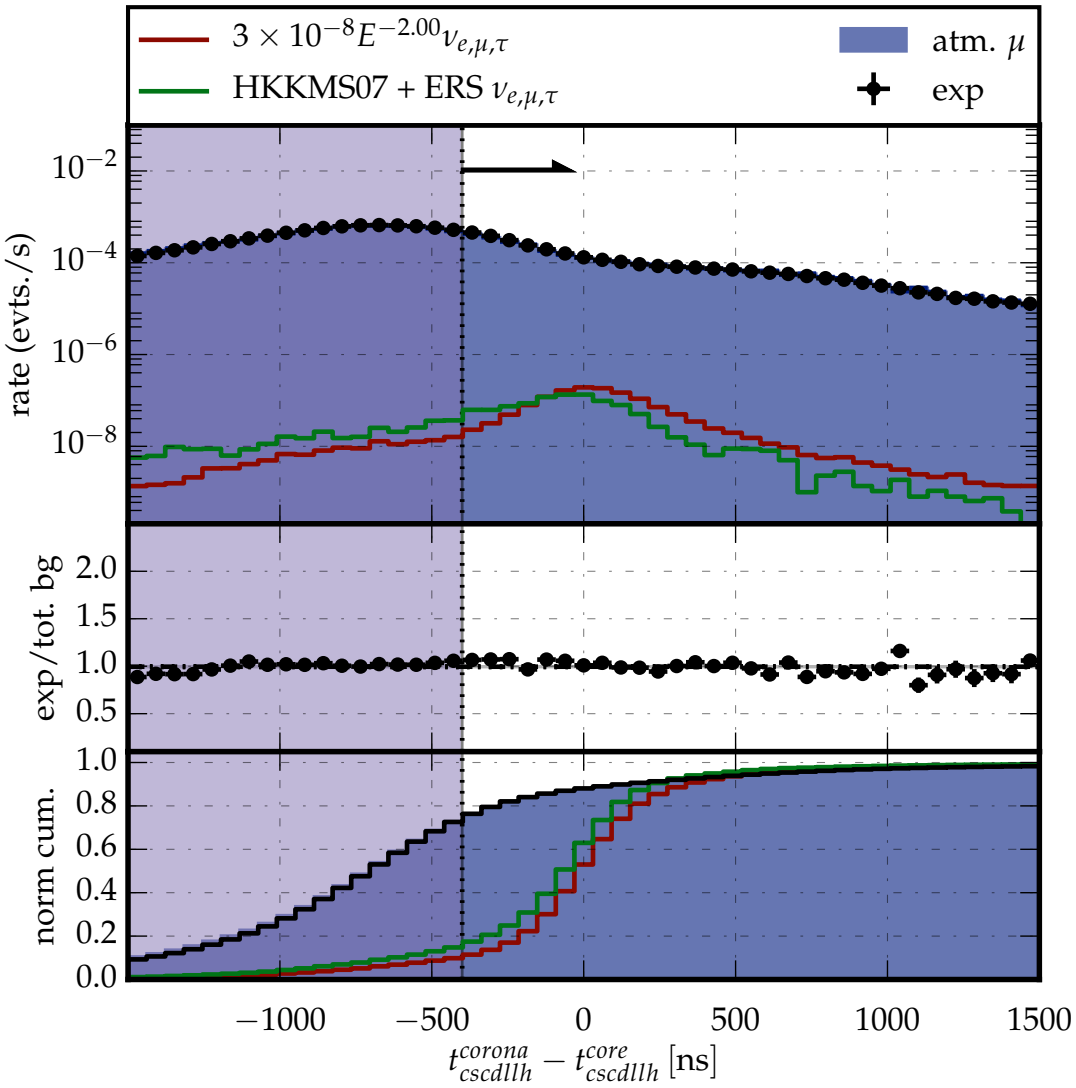

Figure 4.10 – Splitting the hit pattern in a "core" in close proximity to an initial vertex and a "corona" which is a spherical shell in some distance, and reconstructing both patterns individually yields the variable CoreCoronaSplit. The arrow indicates the chosen value for the level 5 filter. The distribution is shown for the time difference of the two reconstructed vertices. See Figure 4.5 for a description of the individual panels of the plot and the individual distributions.

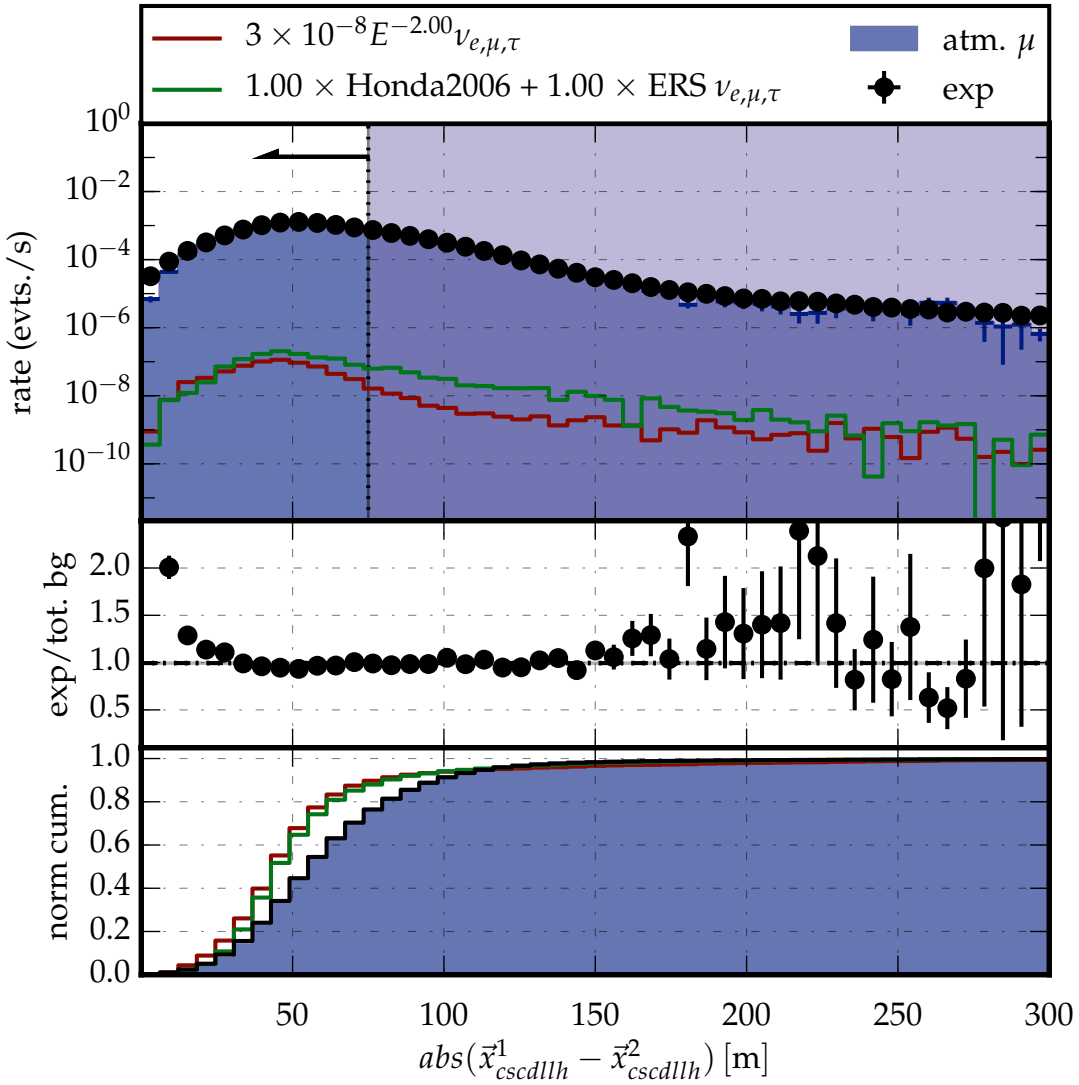

Figure 4.11 – Splitting the hit pattern in two equal halves in time and reconstructing both patterns individually yields the variable TimeSplit. The distribution is shown for the spatial difference of the two reconstructed vertices after the level 4 filter criteria had been applied. The arrow indicates the chosen value for the level 5 filter. See Figure 4.5 for a description of the individual panels of the plot and the individual distributions.

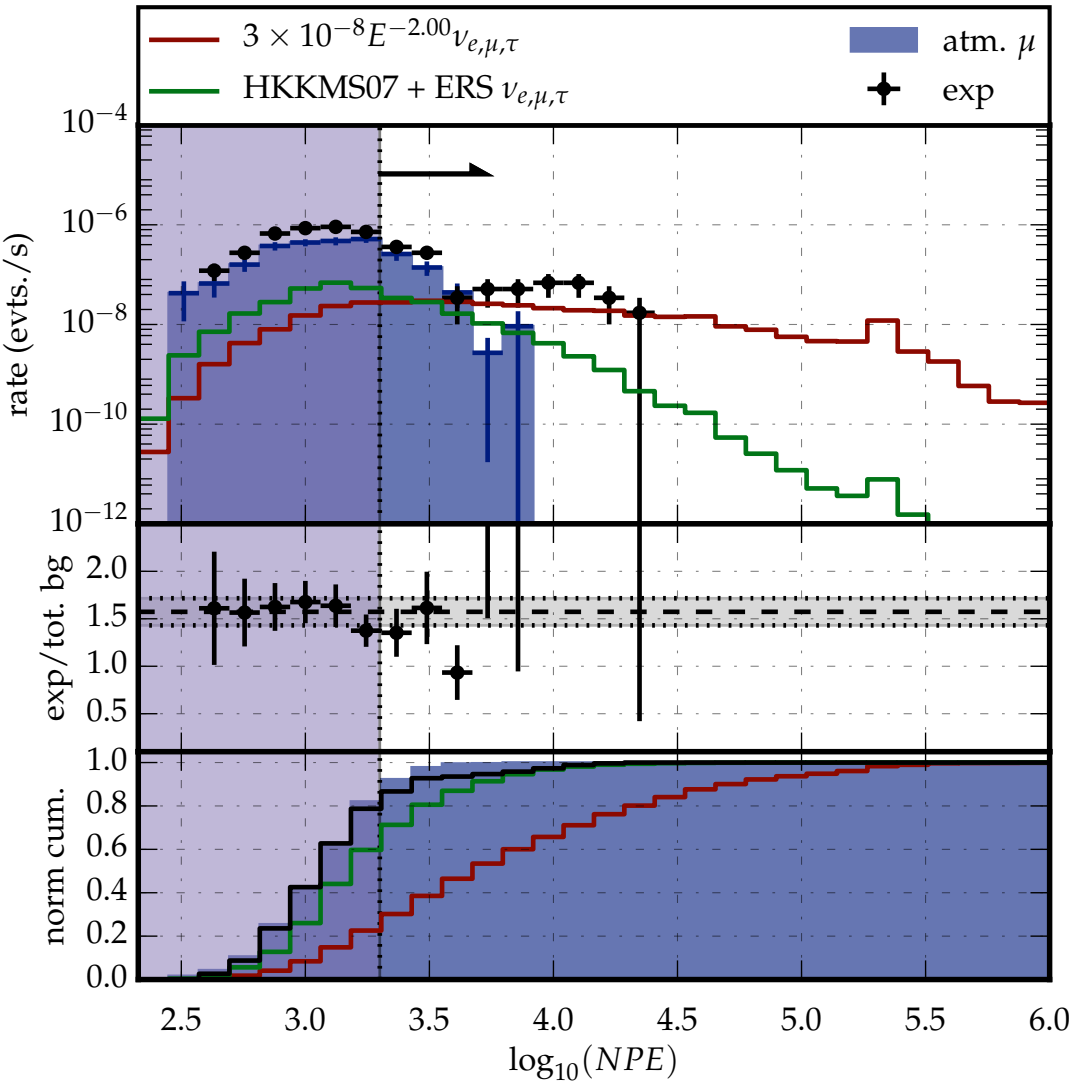

Figure 4.12 – The total charge per event, after the application of level 5 filter criteria. The arrow indicates the value of the cut at level 5. The distribution is plotted for 2 years, the shown data is the full 100% sample, to better visualize the agreement of data and Monte Carlo simulation. The mismatch between data and simulation in the signal region where no atmospheric muons are present is attributed to the fact that an E^{-2} spectrum for the astrophysical neutrinos is plotted, where the data prefers as softer spectrum[59]. See Figure 4.5 for a description of the individual panels of the plot and the individual distributions.

4.5.4 Level 6 analysis filter

After suppression of most of the track-like background, the sample was inspected carefully, and two classes of remaining shower-type-like background were identified:

"corner-clipper" events: Due to the detector topology, events which deposit most of their light at the corners of the detector polygon at the bottom or top of the detector have a spherical shape and are thus often classified as signal. For these events, it is most unlikely to measure light from a muon track which passes outside of the detector, and thus also timing variables classify these events often as signal events. To avoid these, events which have their vertex in the bottom corner regions of the detector or in the upper 50 meters of the detector are removed.

muon bundles at the edges: Muon bundle events with relatively low individual muon energy exhibit a rather uniform light emission along their track and do not look like showers. However, if a bundle only touches the edge, it might still look cascade-like, as large parts of the track can not be seen. After filter level 5 quite a fraction of such events are still present in the sample. This is problematic, because when such events are misclassified as signal, they are often reconstructed to high energies. To suppress these kind of muon bundles the reconstruction quality variable Q_{exp}/Q_{obs} is used. It is the ratio of observed and expected charge, derived by the final energy estimator. If the absolute of this ratio is larger than one by 20%, the events are removed from the sample.

Besides this two classes, also a remaining fraction of relatively dim events are present in the sample. These are removed by requiring the deposition of about $\approx$ 2000 photo electrons in the detector, the corresponding *QTot* distribution is shown in Figure 4.12.

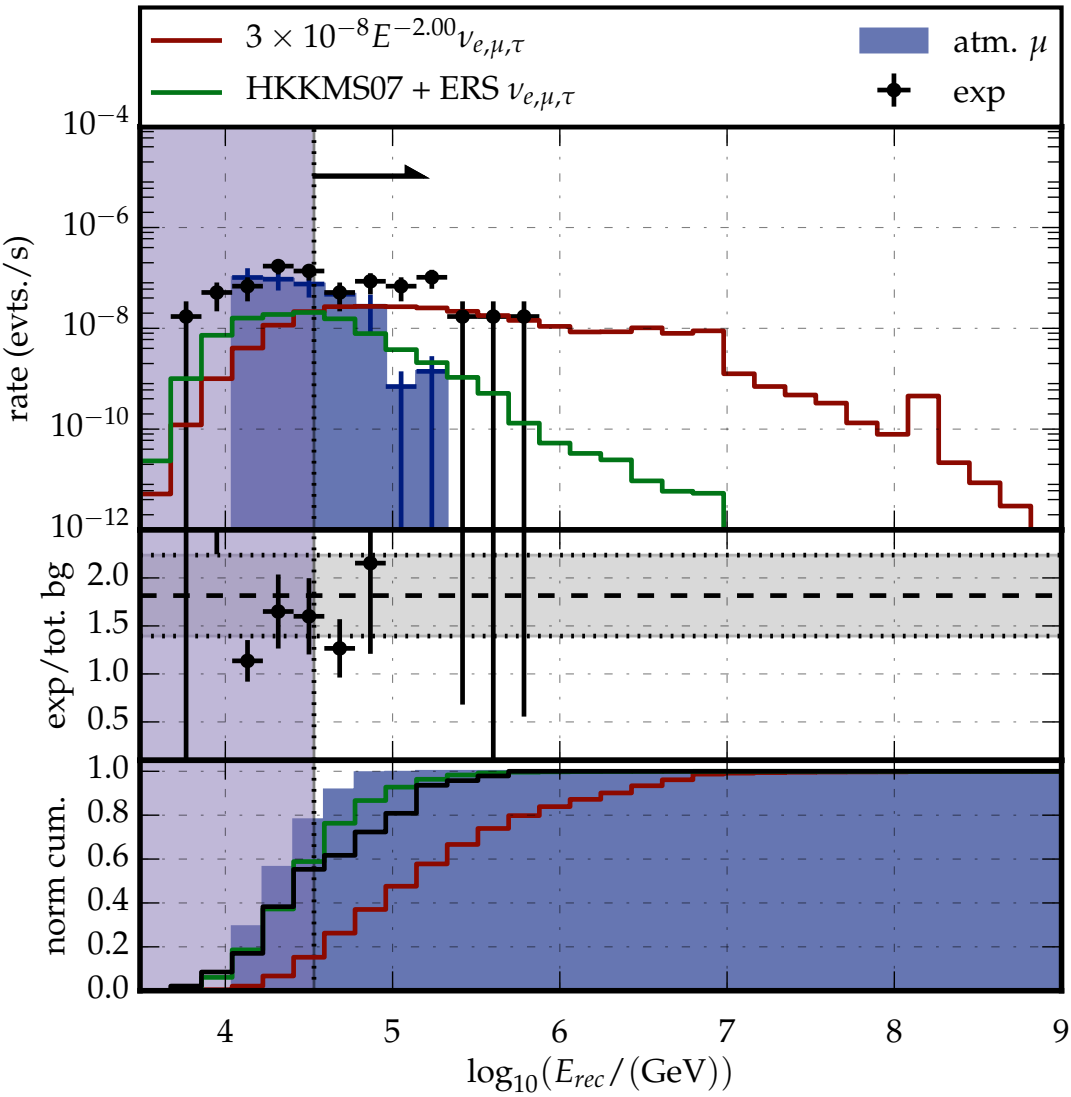

Figure 4.13 – After the application of the level 6 filter criteria, at level 7 a final energy cut at $\approx$ 34 TeV is applied, which is indicated by the arrow. See Figure 4.5 for a description of the individual panels of the plot and the individual distributions.

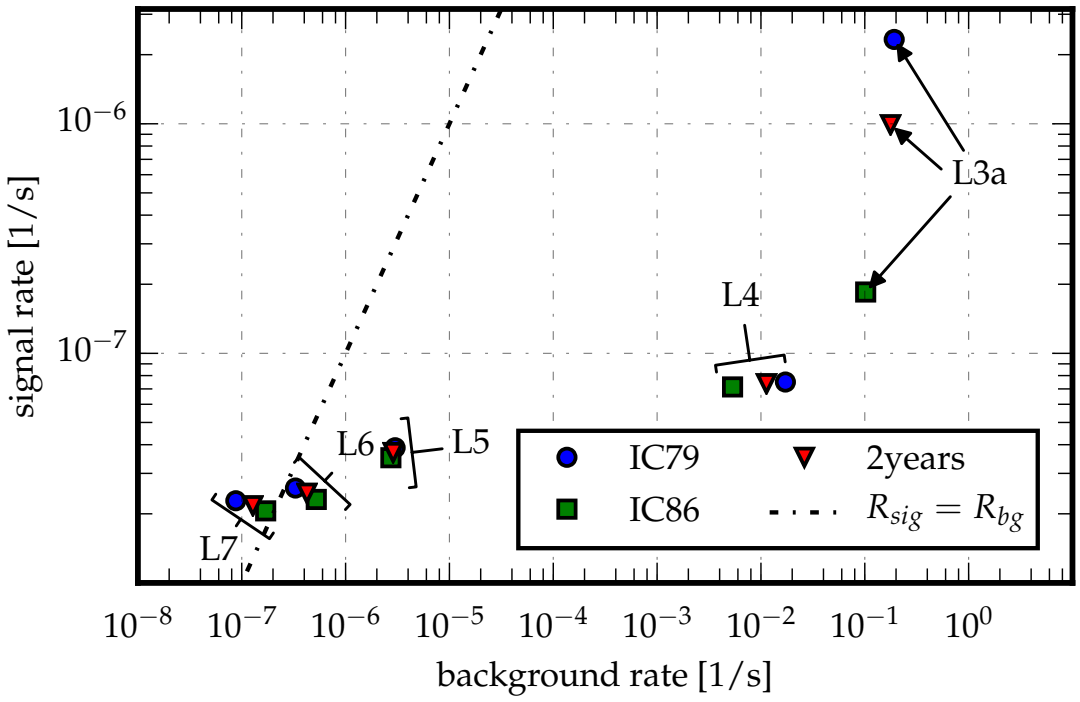

Figure 4.14 – The trajectory of the event selection through the parameter space spanned by the combined rate of all background components on the x-axis and the combined rate of the three flavors of an anticipated E^{-2} astrophysical neutrino signal. The line indicates where the signal and background rates are equal, the space left of it is the region where the signal-to-noise ratio is larger than unity. Different filter levels introduced by this analysis indicated for both individual years and the combination of the two.

4.5.5 Level 7 filter

Following the classical approach of diffuse searches for an astrophysical signal, the event selection is finalized by a single filter criterion: All events must have a visible energy larger than ≈ 34 TeV reconstructed by the final energy estimator, MONOPOD.

The distribution of the energy reconstructed by MONOPOD is shown in Figure 4.13. The value of 34 TeV is chosen because the atmospheric muon simulation is only available for primary energies per nucleon larger than 30 TeV. It is also slightly higher, as it was optimized for the best signal-to-noise ratio under the condition to be as close to 30 TeV as possible to yield maximum signal efficiency.

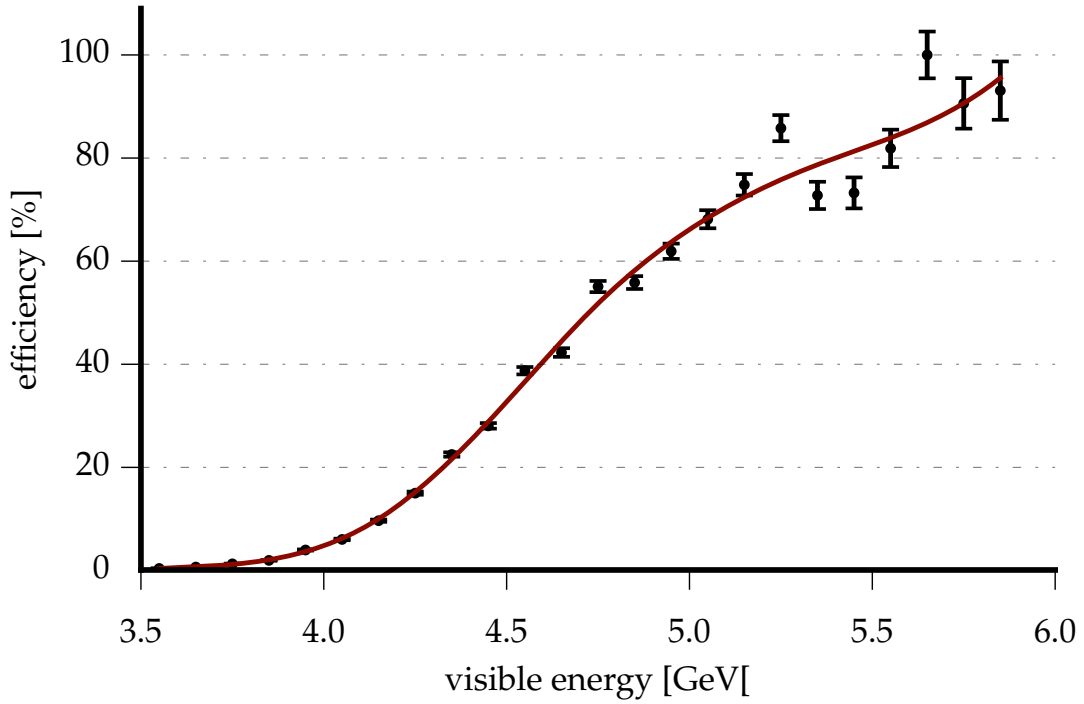

Figure 4.15 – Passing fraction of the analysis filter levels applied to a cascade signal of increasing true visual energy. The efficiency is defined with respect to the trigger level.

4.5.6 Summary of the analysis filters

The filter levels designed for this analysis - as they are described from subsection 4.5.1 to subsection 4.5.5 - include in total 36 different variables. A summary of these variables, together with the selected filter values is given in Table 4.3. Many of these variable do not have a strong background suppression power if applied individually, but most of them are only mildly correlated, so the combination of these yield the necessary background suppression power. As defined in the preamble to this chapter as figures of merit, the event selection fulfills three tasks:

1. It is designed to have a minimal overlap with searches for contained cascades.

2. If is able to achieve a signal to noise ratio > 1, with a reasonable signal efficiency. The signal-to-noise ratio of the filter levels is shown in Figure 4.14. In this figure, for each filter step the rate of remaining background and signal events defines a point in the plane, and two things can be noted:

a) The difference between the two years used in this analysis is large at the lowest filter level due to differences in the previous filter steps. However, it smooths out after the first filters are applied.

b) The last filter level reaches the region of signal-to-noise > 1.

Typically searches for contained cascades yield a total selection efficiency of several per cent, when the number of observed events is compared to the number of expected events at trigger level. The selection efficiency depends on the energy, and an increasing efficiency with energy is desired. The selection efficiency for this analysis is rising monotonically with the energy as expected, this is shown in Figure 4.15, where the fraction of cascades of a specific visual energy which were selected by the event selection is compared to the total number of cascades which triggered the detector is compared.

3. The agreement of data and simulation is good. This can be seen by looking at the distribution for the individual variables, e.g. Figure 4.10. A more general illustration is given in Figure 4.16. Here the absolute ratio of the number of observed events over the number of simulated events at each filter level is shown. It can be seen that it is uniform over a wide energy range. The slight excess after the application of the level 5 filter is corrected by the level 6 filter, which removes the problematic regions from the data sample.

4.5.7 Effective Areas

A figure of merit to compare different event selections even between different types of experiments is provided by the neutrino effective area A_{eff}. It answers the question, what area an ideal detector with a 100% detection and selection efficiency and the area A_{eff} would need to measure the same number N_ν of neutrino events over the solid angle Ω and energy spectrum E of during observation time t as the event selection:

$$N_\nu = \int_t dt \int_\Omega d\Omega \int_E dE \Phi_\nu(\Omega, E, t) A_{eff}(\Omega, E) \tag{4.3}$$

For this ideal detector and an isotropic flux, the measured number of events depend only on the geometrical detector area A_{eff}. Thus this number can be

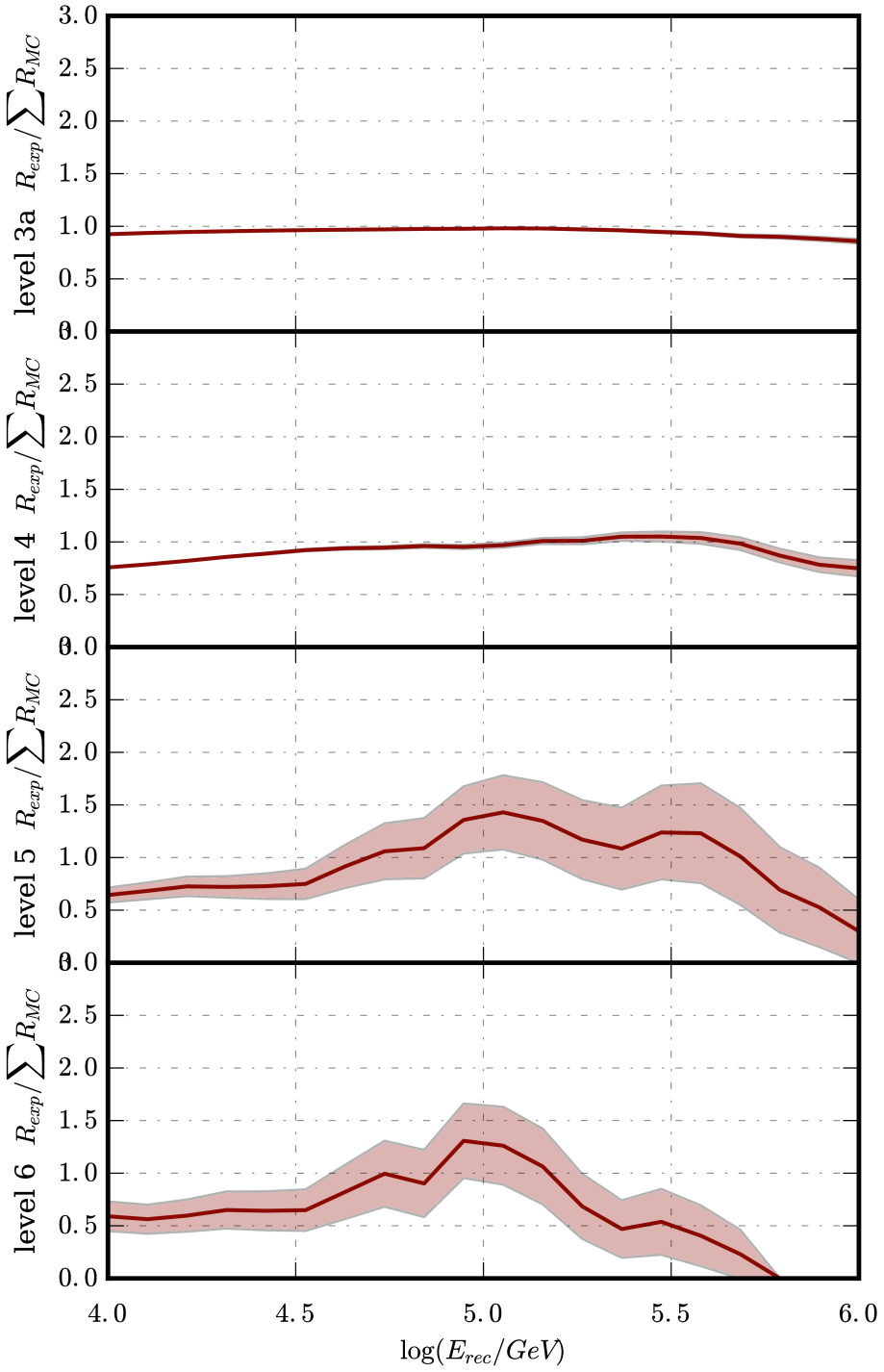

Figure 4.16 – The ratio of observed data events over the expected number of events from all Monte Carlo simulation. The ratio is shown above a reconstructed energy. The statistical error is indicated with the error band. The lack of data at high energies at high filter level can be attributed to statistical fluctuations, as only about 1 event is expected beyond 1 PeV.

L3a - "high energy"	
$E_{acer} > 10$ TeV	$z_{credo_{L3}} < 500$
L4 - "geometry"	
$N_{DOM} > 120$	$Multiplicty < 2$
$non-contained$	XYScale < 1.2
	$z_{credo_{L3}} > -600$
L5 - "anti track bg"	
$\cos(\Theta_{track}) < 0.25$	FillRatio $> .5$
$max(Q_o)/\sum Q_o < 0.3$	DTNearly $>$ -75 ns
$\lvert\vec{M}\rvert < 0.1$	TimeSplit $\Delta t < 550$ ns
TimeSplit $\Delta\vec{r} < 75$ m	Corecoronasplit $\Delta t >$ -400 ns
	ToI Evalratio $> .1$
L6 - "anti cascade bg"	
IC79	IC86
$dist(A) > 100$	$dist(A > 150$
$dist(B) > 100$	$dist(B) > 150$
$dist(C) > 100$	$dist(C) > 200$
$dist(D) > 100$	$dist(D) > 150$
$dist(F) > 180$	$dist(F) > 180$
$dist(G) > 100$	$dist(G) > 150$
$dist(H) > 200$	$dist(G) > 200$
	$z_{Monopod^{(4)}} < 450$ m
	$\log(\sum Q_o) > 3.3 \log(\text{PE})$
	$(\sum Q_o) / \left(\sum < \mu_{o_{Monopod^{(4)}}} >\right) > 0.8$
	$(\sum Q_o) / \left(\sum < \mu_{o_{Monopod^{(4)}}} >\right) < 1.2$
L7 - "final energy"	
$\log(E_{Monopod^{(4)}}) > 4.53 \log(\text{GeV})$	

Table 4.3 – Filter selection criteria, starting at L3a. The different variables are listed. The distance variables $dist(X)$ denote the distance of the vertex from the bottommost DOM on a string of a corner. For the naming of the corners, see Figure 4.1.

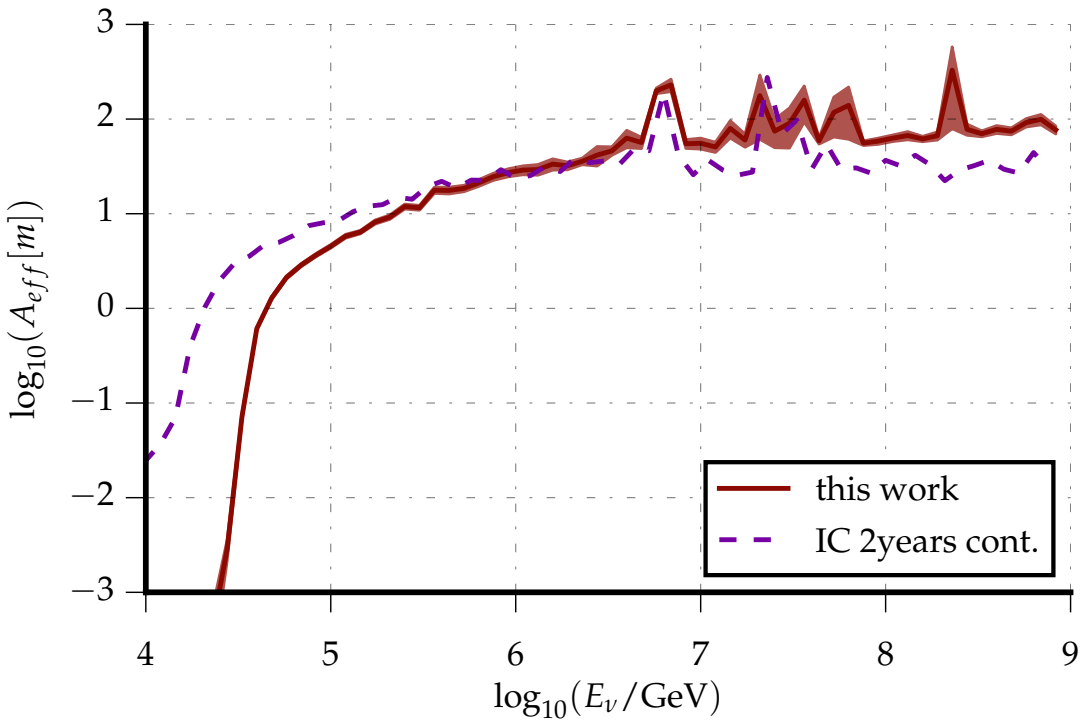

Figure 4.17 – Neutrino effective area for the final sample. Plotted are the values obtained by an $E^{-2}\nu_{e,\mu,\tau}$ signal. The Glashow resonance for $\bar{\nu}_e e^-$ scattering (see subsection 2.1.2) results in a peak at 6.3 PeV. Above this peak, the effective area fluctuates due to statistical limitations in the ν_μ and ν_τ simulations.

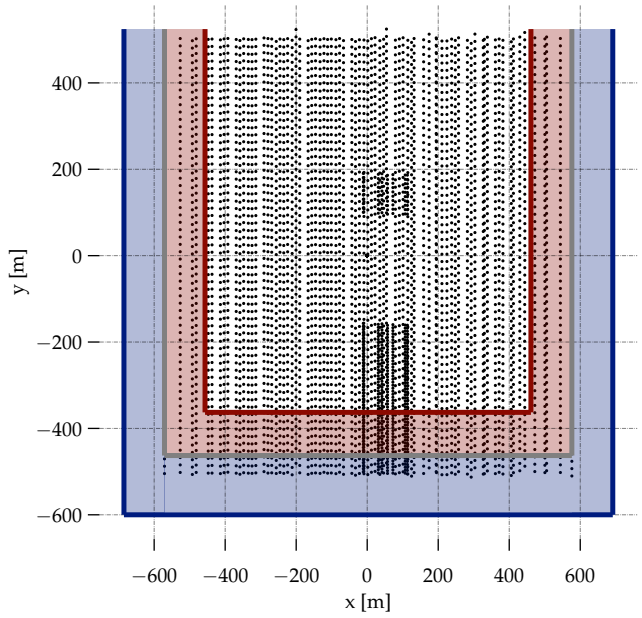

Figure 4.18 – The shape of the off-signal region. IceCube instrumentation is indicated. The region from the blue line to the gray line, shaded in blue is the region used for the final analysis. The off-signal region is defined between the gray and red line and shaded in red. All instrumentation in this region was masked and the event selection was reapplied. The actual off-signal region is smaller than this illustrational graphics indicates, since the scaling was done in two dimensions.

used to compare different types of analyses.
The effective area as a function of neutrino energy for an astrophysical E^{-2} neutrino flux of all flavors is shown in Figure 4.17 and compared to the effective area of the analysis searching for contained showers described in section 4.3. Although the partially contained event selection is less effective for lower energies due to tighter quality selections and the final energy cut of ≈ 34 TeV than the compared contained analysis, the analysis begins to surpass the efficiency at energies above several 100 TeV.

4.6 Systematic sample

The above described filtering methods rely heavily on variables which are designed to quantify cascade-like characteristics. Many of these variables were developed using samples of well contained, high quality events. However, in the here described analysis, the final sample obtained does not meet this requirements. Naturally, this raises the question if the used variables are indeed suitable for such a sample.
To study this, and to provide the ability to have a sample for a dry-run test prior to the unblinding of the final sample, an off-signal region has been defined. The anti-containment cuts of the analysis have been reversed, and the inner part of

the so obtained volume has been removed. The so-defined off-signal region is shown in Figure 4.18. The sample has been used to apply the developed filter criteria to one year of livetime of detector data, no events have been found over an expectation of ≈ 1 event. For each variable the ratio of the distributions of data and the sum of the expectations from MC have been inspected and no indications have been found that the used method is not capable of producing the desired results.

4.7 Performance of the event selection

4.7.1 Accuracy of the reconstructed cascade parameters

In order to estimate the accuracy of the reconstructed values for the cascade parameters, error distributions as shown in e.g. Figure 4.20 can be studied.
The error distributions are constructed for all simulated signal events which survive the filter conditions of the event selection. The true values from the simulation are used as reference. The visible energy (see subsection 3.2.3) is used to measure the performance of the energy reconstruction.
The error distributions are fit with a Gaussian, however due to the more elongated tails, also the 68th and 95th percentile of the distributions are indicated. It can be seen in Figure 4.20 that the so obtained resolutions are in the order of several meters for the vertex position. There is also no systematic shift in a certain direction. The reconstructed energy is also unbiased, as shown in Figure 4.21. From this distribution we estimate a value for the energy resolution of about 20%. As this sample consist of only uncontained showers, where the spread of reconstructed energy is comparatively large, the slightly worse resolution compared to [137] ($\approx 15\%$) is expected. The reconstructed angle is compared to the true neutrino direction in the lower panel of Figure 4.21. If the opening angle Ψ between the two vectors is small, than the reconstruction is accurate. Although the distribution has a prominent tail, most of the events are reconstructed with an error on the true direction smaller than 35°. The reconstructed direction is not used to derive a result in the analysis, however this number is surprisingly small, if one takes the topology of the events into account and indicates a good over-all reconstruction quality of the events.

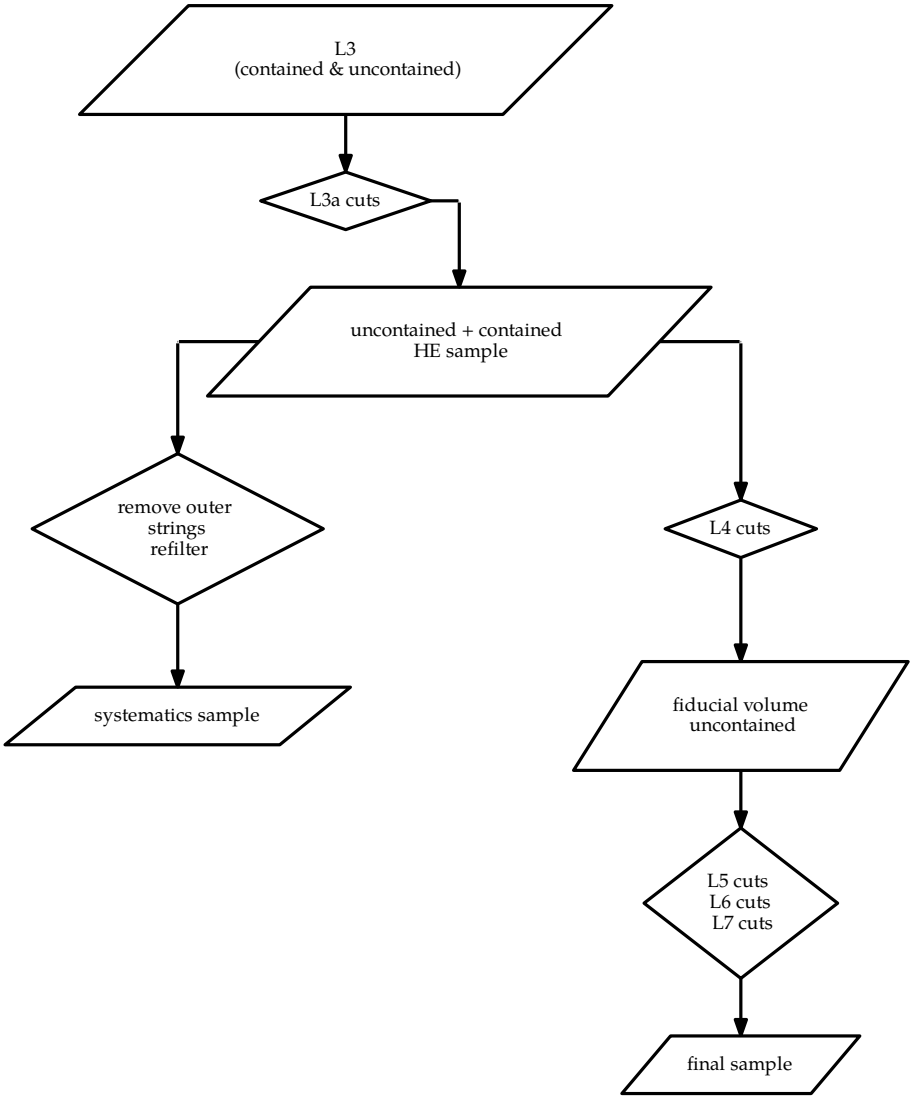

Figure 4.19 – Schematic view of the individual filter steps used for the isolation of the final sample. The systematics sample from the contained part of the sample after the level 3a cuts and thus statistically independent from the final sample.

As a further check, the likelihood of the final energy estimator, as described in subsection 3.4.6 which is function in 6 parameters has been investigated for the final data sample. Due to uncertainties in the likelihood description of the event, e.g. uncertainties of the scattering and absorption coefficients of the ice at the vicinity of the detector, the likelihood landscape might be distorted and commonly used minimization techniques, e.g. minimization by MIGRAD might not find the global minimum of the likelihood. To check for such numerical problems, the likelihood function was evaluated on a healpix grid with a value of the healpix parameter *nside* of 16, which corresponds to an angular resolution of about 3.7 degrees. For each pixel, the vertex was minimized and the respective energy was calculated. The question which can be answered by the method is if the energy reconstruction is influenced by the angular uncertainty. In general, it was found that the calculated energy by MONOPOD is accurate within the expected resolution, and the slight excess of events with horizontal directions was confirmed.
The test was performed a posteriori and served as a cross-check and thus the values for the energy obtained by this method were not used further in this analysis. However, the obtained spectrum by the altered likelihood minimization scheme has been investigated, and it was found that it is compatible with the presented spectrum within 1 sigma uncertainties. The scanned likelihood sky maps and the numerical values for the best found minimum by the scanning procedure can be found in chapter 6.

4.8 Final data sample

Investigating the 90% of the data that were kept "blind" during the event selection development, in total 18 additional events were found. These were 9 events for the IC79 season and 9 additional for the IC86 season, plus 2 in the 10% sample for IC86.
The reconstruction values of the observed events are listed in Table 4.5, an overview of the event rates of the final sample also for simulation can be found in Table 4.4. The vertex distribution of the events in the detector is compatible the expectation of a neutrino signal with a minor background contribution due to atmospheric muons. The distribution of the vertices of the observed data together with an astrophysical signal is shown for the three projections along

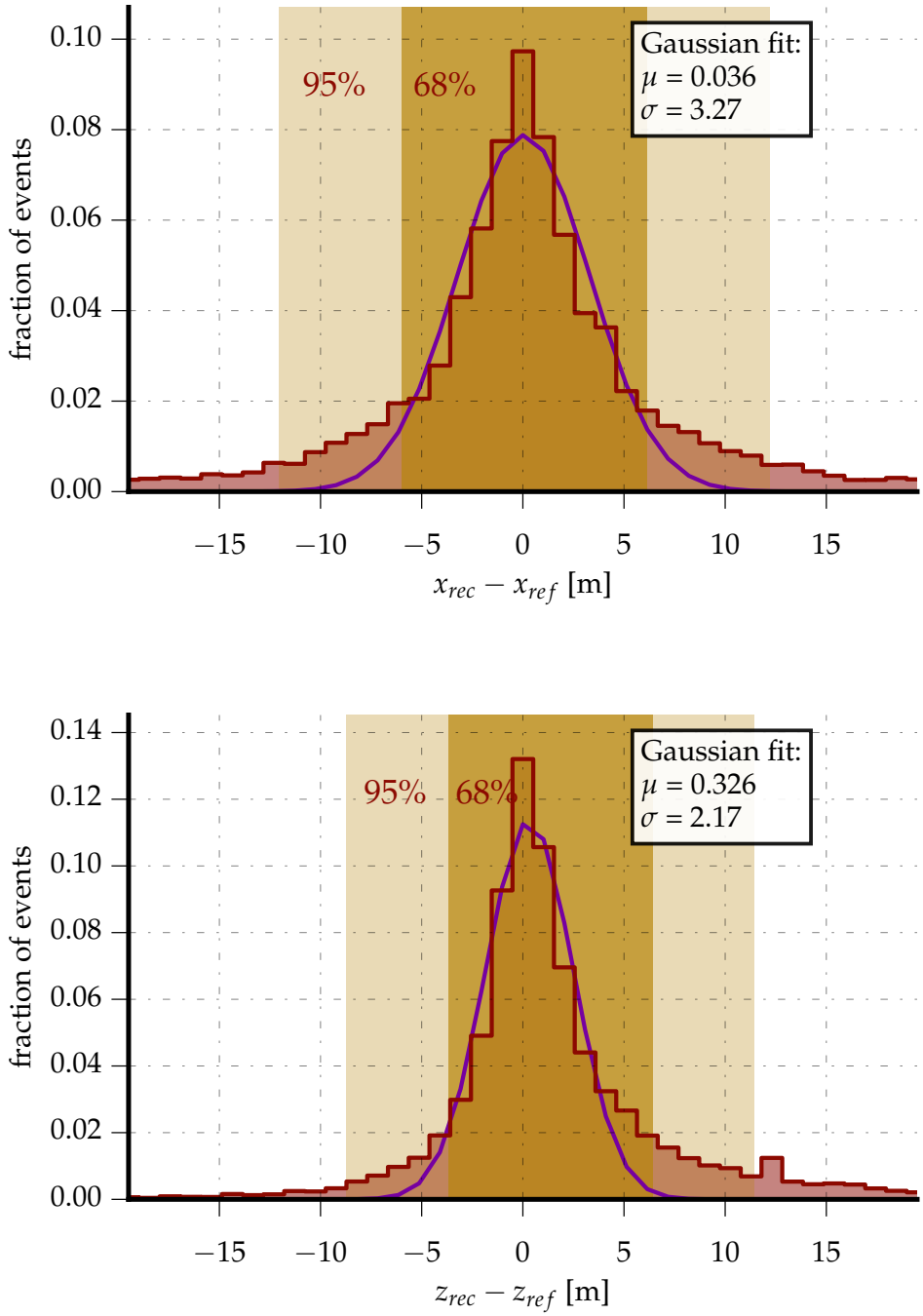

Figure 4.20 – Performance of the applied cascade reconstruction, a 4-iterative Monopod fit. Shown in the upper panel is the difference of reconstructed x position and the reference x position from simulation. The same is plotted in the lower panel for the z position. A Gaussian is fit, however as the tails are longer than for a Gaussian, the actual 68th and 95th percentiles of the distribution are indicated separately.

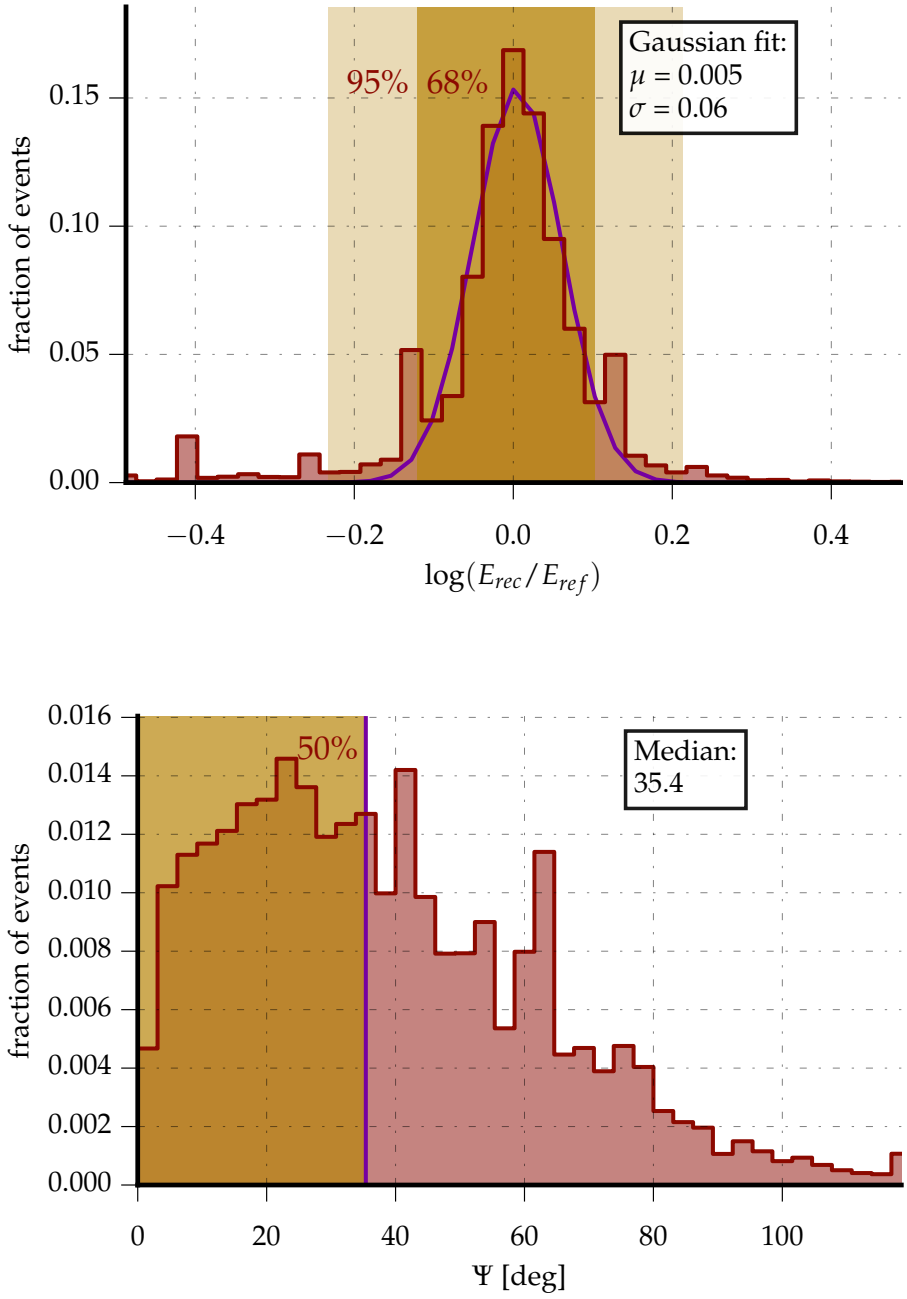

Figure 4.21 – Performance of the applied cascade reconstruction, a 4-iterative Monopod fit. In the upper panel the logarithmic ratio of the reconstructed energy and a reference energy E_{vis} is plotted. A Gaussian is fit, however as the tails are longer than for a Gaussian, the actual 68th and 95th percentiles of the distribution are indicated separately. The lower panel shows the opening angle between the reconstructed direction and the true direction of the incoming neutrino. The median of the distribution is indicated.

	surviving events in 675 d
$E^{-2}\nu_e$	6.74 ± 0.37
$E^{-2}\nu_\mu$	2.01 ± 0.11
$E^{-2}\nu_\tau$	3.91 ± 0.10
HKKMS07 ν_e	0.27 ± 0.00
HKKMS07 ν_μ	1.42 ± 0.13
ERS ν_e	0.32 ± 0.00
ERS ν_μ	0.05 ± 0.00
atmos μ	5.43 ± 1.95
data	20
Σbg	7.50 ± 1.95
Σsig	12.1 ± 0.40

Table 4.4 – Number of events in the final sample of 675 days obtained by simulation as well as data. The shown error is the statistical error only. The fluxes in the table are from top to bottom: a 1:1:1 isotropic flux for the astrophysical component which follows an E^{-2} energy spectrum, a conventional atmospheric neutrino flux[57], a prompt atmospheric component[68] as well as a prediction for the atmospheric muon flux from the model described in subsection 1.1.1.

the detector axes in Figure 4.22, Figure 4.23 and Figure 4.24. The highest energetic observed event was found with a reconstructed energy of 578 TeV. Two events which were observed in a previous analysis[23] are also present in the final sample. The veto region in the previous analysis[23] at the bottom of the detector is defined dependent on the position of the DOM which observes first light, while in the analysis described in this work the split line is defined at a reconstructed vertex z coordinate of -450 m. There is consequently some overlap region, because of the different bottom position of the individual strings, which is different by up to 20 meters.

season	sample	run	event	E_{rec}	Θ_{rec}	x_{rec}	y_{rec}	z_{rec}
IC79	90%	116351	5378257	54	111	2	-420	308
IC79	90%	116457	702481	174	83	497	187	-309
IC79	90%	116522	17216576	200	50	-340	85	-571
IC79	90%	116532	28124500	62	40	-617	1	-355
IC79*	90%	116698	10198436	53	247	303	-470	168
IC79	90%	116794	31146792	41	86	468	311	-460
IC79	90%	117273	15914878	93	26	227	-464	-354
IC79	90%	117721	55150085	146	87	471	-59	68
IC79	90%	117744	54888465	34	145	44	460	-306
IC86	90%	118178	6251579	38	61	-453	-364	-501
IC86*	90%	118178	66452255	89	73	-60	3	-500
IC86	10%	118420	72256529	127	59	-126	453	-145
IC86	10%	118670	58852406	300	0	638	254	-401
IC86	90%	118466	21256734	387	90	-202	-562	48
IC86	90%	118692	5825484	62	78	-424	-288	308
IC86	90%	119117	23529568	578	65	320	-482	207
IC86	90%	119507	35825553	130	78	-385	475	162
IC86	90%	119651	30979523	36	67	495	-217	-464
IC86	90%	119736	73354228	116	100	626	145	149
IC86	90%	119962	11948966	63	50	-466	89	-532

Table 4.5 – The final sample: 20 events survived all filter levels. Distributed over the years, this were 0 events in the IC79 development sample, 2 events in the IC86 development sample, 9 in the IC79 analysis sample and 9 in the IC86 analysis sample. Stated are the reconstructed energy and zenith angle from the final energy and vertex estimator, a 4-fold Monopod reconstruction. Two events, were also found in a previous analysis[23], these are labeled with a "*".

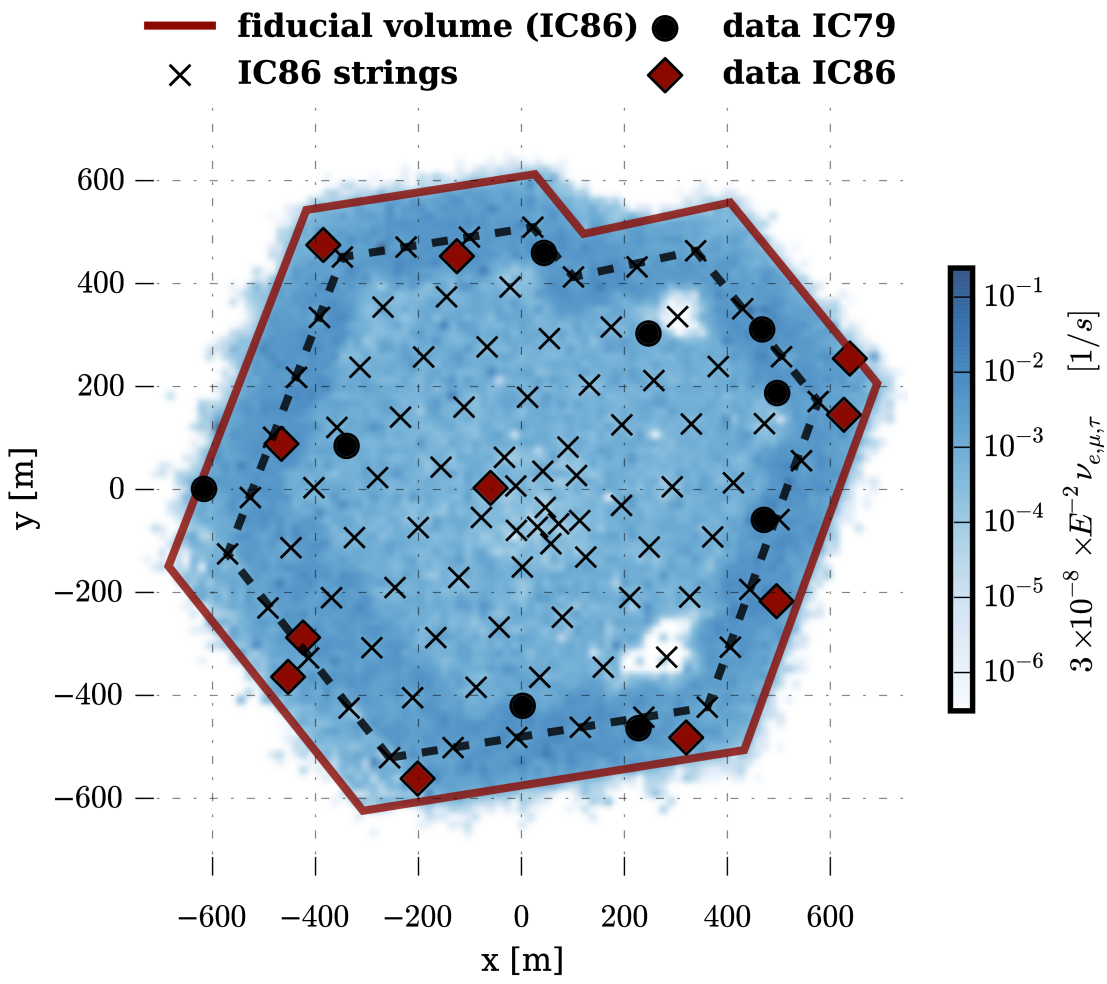

Figure 4.22 – Reconstructed vertices of the events in the final sample in *xy* projection. Events from the IC86 season are marked with a diamond-shaped marker. Strings of the final configuration indicated. Also the boundary of the fiducial volume is marked with a red line. The expected vertex distribution of an $E^{-2}\nu_{e,\mu,\tau}$ flux is overlaid with a blue color. The blue color outside of the red line results from the interpolation of the signal histogram.

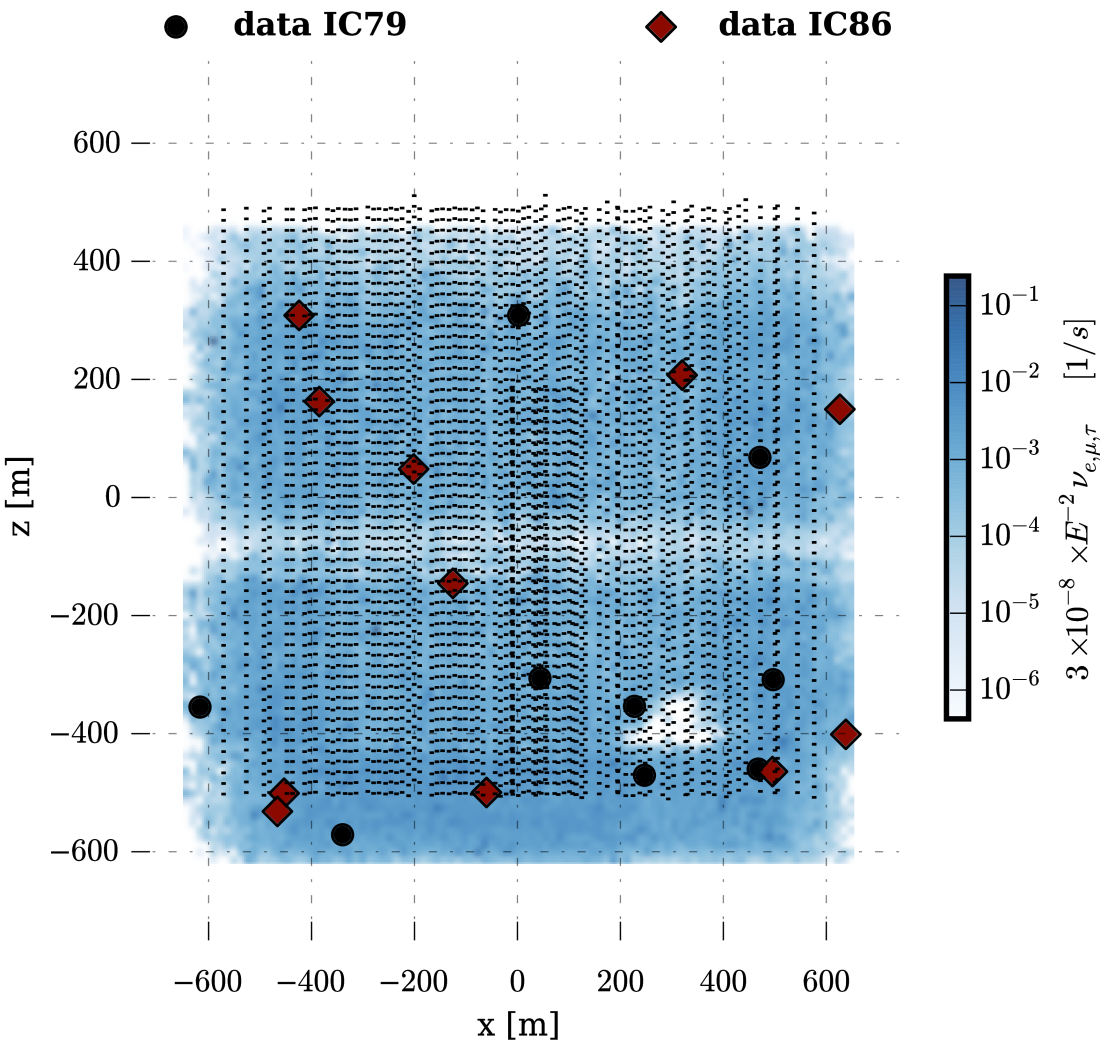

Figure 4.23 – Reconstructed vertices of the events in the final sample in xz projection. Events from the IC86 season are marked with a diamond-shaped marker. Strings of the final configuration indicated. The expected vertex distribution of an $E^{-2}\nu_{e,\mu,\tau}$ flux is overlaid with a blue color.

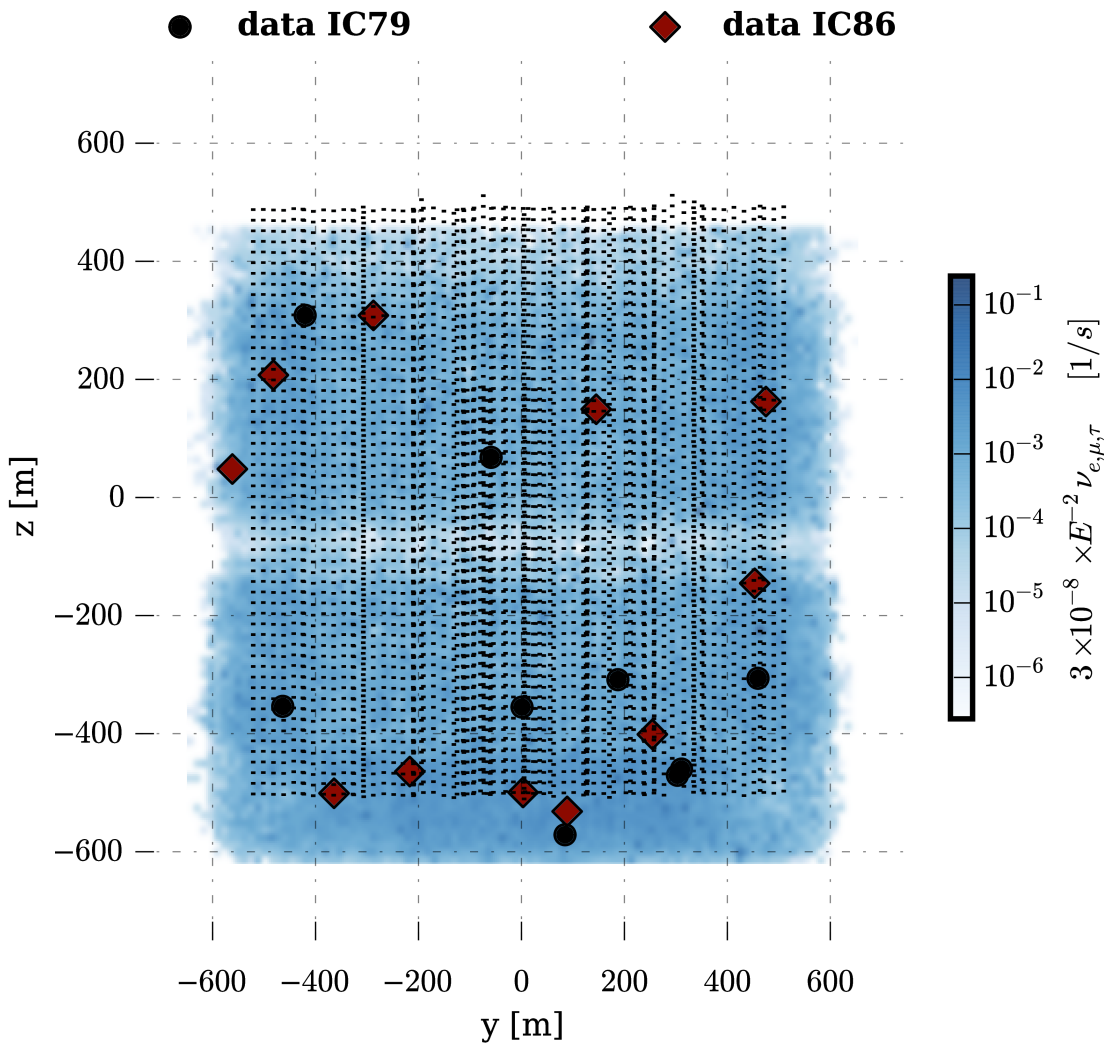

Figure 4.24 – Reconstructed vertices of the events in the final sample in yz projection. Events from the IC86 season are marked with a diamond-shaped marker. Strings of the final configuration indicated. The expected vertex distribution of an $E^{-2}\nu_{e,\mu,\tau}$ flux is overlaid with a blue color.

5

Analysis

To interpret the observed events, their energy spectrum is fitted with background and signal templates for different hypothesis in a likelihood fit. For this purpose, the methods from [59] were adapted for this work. The assumptions of atmospheric background only are tested, as well as an astrophysical component with a spectral index of -2, which is often used as a benchmark model. Finally a model with an astrophysical component with a power law spectrum and a free spectral index has been studied as well. In this chapter, the fit method and the fit parameters are briefly introduced. Possible systematic uncertainties are discussed and the results are presented. At the end of the chapter, the results are compared to other results recently obtained by IceCube.

5.1 Likelihood analysis of a binned energy spectrum

In counting experiments, the probability to observe n events over an expectation of μ events is described by Poisson statistics:

$$P(n|\mu) = \frac{\mu^n}{n!} \cdot \exp(-\mu) \tag{5.1}$$

After the experiment is performed, a fixed number n of events in a certain range of the parameter space is measured and the best value for μ needs to be esti-

mated for that value. The re-interpretation of the probability $P(n|\mu)$ leads to the formulation of the likelihood $\mathcal{L}$[142]:

$$\mathcal{L}(\mu|n) = a \cdot P(n|\mu) \tag{5.2}$$

where a is an arbitrary constant, so the likelihood is generally not normalized. If a set of parameters κ are measured that describe the events, as e.g. the energy E, it is possible to treat each range independently. One categorizes the measured events n in N intervals $j_{[\kappa_1,\kappa_2]}$ with unknown expected event mean μ_j, so that:

$$n = \sum_{j_{[\kappa_1,\kappa_2]}}^{N} n_j \tag{5.3}$$

The probability to observe n events, splits up in a product over each interval - or in the case of the analysis a bin of the energy spectrum $j_[E_1, E_2]$. Following Equation 5.2, this can be interpreted as a likelihood which is the product over all the contributions from the individual bins:

$$\mathcal{L}(\mu|n) = P(n|\mu_i) = \prod_{j_{[\kappa_1,\kappa_2]}} P(n_j|\mu_j) \tag{5.4}$$

where the unknown constant a has been neglected in the equation. The calculation for the Poisson case yields[43]:

$$-2\ln\mathcal{L} = 2\sum_{j_{[\kappa_1,\kappa_2]}}^{N}\left[\mu_j - n_j + n_j \ln\cdot\left(\frac{n_j}{\mu_j}\right)\right] \tag{5.5}$$

where $-2\ln\mathcal{L}$ has been calculated, as it is a more useful quantity as is illustrated in the next section.

5.1.1 Rating different models

To decide if a model is preferred over the null hypothesis, likelihood ratio tests are performed. The likelihood ratio $\mathcal{R}$ is given by the ratio of the likelihoods of the model to test M_T and the null hypothesis model M_0:

$$\mathcal{R} = -2\ln\left(\frac{\mathcal{L}_{M_T}}{\mathcal{L}_{M_0}}\right) \tag{5.6}$$

Strictly, the test requires "nested" models, which means that the parameter set of the test model M_T is a superset of the parameters of the reference model M_0. The factor 2 results in the choice of the definition of the likelihood in Equation 5.5. This allows to obtain the 1σ confidence interval for the best fit parameters by raising the value of $\mathcal{L}$ by $\Delta\mathcal{L} = 1$, similar to a χ^2 test, which is actually a likelihood test for Gaussian statistics.
The p-value describes the probability to obtain the same or a higher value of the likelihood ratio for the provided data if the test model M_T is true. It can be obtained from an ensemble of toy experiments where the likelihood ratio is calculated for different realizations of the null hypothesis.

5.1.2 Goodness of fit

To obtain a probability to obtain a set of best-fit parameters for a certain model, the method of likelihood ratio tests is also used. The goodness of fit test statistic is defined by likelihood ratio tests performed for different representations of the test hypothesis with a "saturated" model[143], which predicts the exact outcome of the measured data:

$$\mathcal{R} = \frac{\mathcal{L}(\mu|n)}{\mathcal{L}(n|n)} \tag{5.7}$$

The goodness of fit p-value can then be obtained from this distribution: It is the probability to observe a value the same or larger than that yielded by the experimental data.

5.1.3 Profile likelihood

The errors on the best fit values are obtained by profile likelihood scans which means that the likelihood ratio function is re-evaluated for fixed values of the scanned parameters with the other parameters refitted. The error is defined as a likelihood difference of $\Delta Llh = 1$ with respect to the minimum, which corresponds to 1σ error intervals assuming the shape of the likelihood ratio function can be approximated by a Gaussian.

5.1.4 Treatment of systematic uncertainties in the likelihood

If an uncertainty i can be parametrized by a continuous parameter θ_i, it is possible to include a nuisance parameter ζ_i in the Poisson likelihood, using the following expression:

$$\zeta_i = \frac{\theta_i - \theta_i^*}{\sigma[\theta_i]} \tag{5.8}$$

In the above equation θ_i^* and $\sigma[\theta]_i$ represent the best estimate for the parameter θ_i and its assumed uncertainties respectively. Implemented in this way, the nuisance parameter ζ_i is actually contributing with a Gaussian penalty term to the likelihood:

$$\exp(-\frac{1}{2}\zeta_i^2) \tag{5.9}$$

The width of this Gaussian is given by the uncertainty of the nuisance parameter. In the following section, the nuisance parameters in the fit are discussed, an overview together with the assumed uncertainty can be found in Table 5.1.

5.2 Models & Parameters

5.2.1 Models for the astrophysical neutrino signal

The **astrophysical benchmark model** which was used to develop the filter criteria predicts a flux of neutrinos of mainly extragalactic origin, accelerated during hadronic interaction processes at the sources. It is assumed that the neutrinos are created during pp interaction and thus created with a neutrino-antineutrino ratio of 1:1 and a flavor ratio of $\nu_e : \nu_\mu : \nu_\tau = 1 : 2 : 0$, which is altered due to oscillations to an approximately $1 : 1 : 1$ ratio at Earth. The ratio of $\nu : \bar{\nu}$ is $1 : 1$. The energy spectrum is predicted to be an unbroken, featureless power law with an index of E^{-2}. Being extragalactic, the flux is assumed to reach the Earth isotropically. The model has one free parameter, which is the total integrated flux over all energies, Φ_0. Although recent studies suggest that this model is disfavored in favor of more elaborate models[59], it is considered as a benchmark test.

An **astrophysical model with free spectral index** is the extension of the astrophysical benchmark model, all assumptions are kept, however the spectral index γ_{astro} is fitted as a free parameter to the data. Indications for a softer

spectrum than $\Phi \propto E^{-2}$ have been seen in several analysis, e.g. [59, 131, 139].

5.2.2 Background models

Conventional atmospheric neutrinos: The fraction of the atmospheric neutrino flux, which is mainly produced by the decay of pions and kaons is predicted by using the neutrino simulation events that pass the event selection criteria. They are weighted according to the HKKMS07 model, and re-weighted to take the knee of the cosmic ray spectrum into account. This distribution serves as template in the fit. The normalization of this model is included as a nuisance parameter $\zeta_{\Phi_{cv.\nu}}$ in the fit. Its uncertainty is estimated by the authors to be in the 10% regime, however growing with energy, the uncertainty is in the 30% regime for the energies relevant for this work[144].

Prompt atmospheric neutrinos: The prediction for the prompt atmospheric neutrino background is using the neutrino simulation events that pass the event selection criteria. They are weighted according to the ERS model, and re-weighted to take the knee of the cosmic ray spectrum into account. Experimentally, upper limits have been set on this model, so the normalization of the model is included in the fit as nuisance parameter $\zeta_{\Phi_{pr.\nu}}$, with an uncertainty reflecting the reported upper limit[106] at $\Phi_{pr.\nu} < 3.8 \times$ ERS at 90% confidence level.

Atmospheric muons: These are simulated with CORSIKA and weighted to the H3a cosmic-ray composition model as described in subsection 1.1.1. The atmospheric muon template is obtained from the energy distribution of the CORSIKA events present after all filter criteria are applied, which are 13 events in number. The total expectation from this 13 events is given in Table 4.4. As the prediction has a statistical uncertainty of 35%, and deviations of the number of predicted muons and the data on lower filter levels were seen up to about 50%, the normalization of the muon flux is included as a nuisance parameter ζ_{Φ_μ} with an uncertainty of 50% in the fit.

Systematic parameters

To account for systematic uncertainties in the fit, three additional nuisance parameters have been introduced:

Detector systematics: The precision of the energy measurement of an event is limited by the detector itself. Uncertainties in the optical properties of the ice and in the absolute DOM efficiency can lead to a systematic over or underestimation of the reconstructed energy.
The effect is accounted for in the fit by an energy shift parameter, ζ_{Φ_E}. The actual uncertainty of this parameters is set to 20%, following the considerations of energy reconstruction studies[137], plus an additional uncertainty attributing the fact that the spread in reconstructed energy is larger for uncontained then for contained shower-type events. The value of 20% also reflects more the energy resolution as shown in Figure 4.21. If the parameter is applied, events are shifted to neighboring energy bins. As this might lead to the effect that events fall below the final energy cut, the histograms which were provided to the fit do not include the energy cut, and thus also events with energy down to 10 TeV. However, the fit range is restricted to the actual energy cut of $\approx$ 34 TeV.

π/K **ratio:** The fluxes of atmospheric neutrinos are sensitive to the ratio of created π/K in the upper atmosphere during the interactions of cosmic ray primaries, as described in subsection 1.2.1. The value of this ratio is only known to a level of about 10%. This can be modeled with a nuisance parameter $\zeta_{K/\pi}$.

Cosmic ray index: The cosmic ray primary spectrum is an important input parameter for the predictions of atmospheric neutrinos. However, the steepness of the spectrum is only known with limited precision. To account for this, the parameter $\zeta_{\Delta\gamma_{cr}}$ is introduced. Positive values of this parameter indicate a steeper spectrum.

nuisance ζ	min(ζ)	max(ζ)	$\sigma(\theta)$	description
ζ_{Φ_E}	-75%	+75%	$\pm$ 20%	global energy shift for all distributions
ζ_{Φ_μ}	-100%	+100%	$\pm$ 50%	normalization of the muon background component
$\zeta_{\Phi_{pr.\nu}}$	-100%	+400%	$\pm$190%	normalization of the prompt atmospheric component
$\zeta_{\Phi_{cv.\nu}}$	-100%	+130%	30%	normalization of the conventional neutrino background component
				tested, but not used
$\zeta_{\Delta\gamma_{cr}}$	-100%	+100%	$\pm$ 5%	cosmic ray primary spectral index
$\zeta_{K/\pi}$	-50%	+50%	$\pm$ 10%	ratio of kaon/pion production in the upper atmosphere
$\zeta_{\Delta\gamma_\mu}$	-100%	+100%	$\pm$ 20%	muon spectral slope uncertainty

Table 5.1 – Allowed nuisance parameter variations relative to the best current estimate. The prior on the prompt component is chosen with an uncertainty of 190%, so that the 90th percentile of the corresponding Gaussian reflects the value of 3.8 $\times$ ERS which is the 90% upper limit taken from [106].

5.3 Results

The final sample derived by the applied event selection discussed in chapter 4, reduced 2 years of IceCube data to 20 data events. The background estimate for this sample is ≈ 8 events, thus resulting in a certain tension. In the following, this tension is quantified and interpreted with an astrophysical neutrino component present in the sample.
During the fitting procedure, it was found that the systematic parameters described in subsection 5.2.2, the π/K ration and the uncertainty on the index of the cosmic ray spectrum were never changed from its original values. It was then decided to remove these parameters from the presented fits, as it seems the present statistics in the dataset is too low for the fit to be sensitive to this effects.

5.3.1 Background only hypothesis

The question which is answered by this test is how likely the data can be explained by pure background. Although the extraterrestrial neutrino flux was already measured[131], and thus the rejection power of these hypothesis is not important from a discovery perspective, this test allows to infer if the measured data contributes significantly to the extraterrestrial neutrino signal.
The best fit distribution is shown in Figure 5.1, the corresponding parameter values are given in Table 5.2. As can be seen, the prompt atmospheric component is fitted at its maximum allowed value, exceeding its expected uncertainty. Also a general mismatch of the prediction and the data can be observed. The fitted nuisance parameter for the energy shift ζ_{Φ_E} is also fitted to a value larger then the assumed 20%, which indicates a bad agreement of data and the fitted templates. Not restraining the prompt atmospheric component at all and setting it as a free parameter in the fit leads to a value of about 13.4 times the nominal ERS model normalization. This is excluded by various limits on the prompt atmospheric flux[106, 139].
The goodness of fit p-value, calculated by a likelihood ratio test with a saturated model as described in subsection 5.1.2 evaluates to 0.1%, and thus reflects the impression that the fitted templates are not very well describing the data.

parameter	value	systematic pull
ζ_{Φ_E}	-	$+1.38^{+0.00}_{-0.45}$
$\zeta_{\Phi_{cv.\nu}}$	-	$+0.16^{+0.80}_{-0.93}$
$\zeta_{\Phi_{pr.\nu}}$	-	$+1.66^{+0.00}_{-0.27}$
ζ_{Φ_μ}	-	$-0.02^{+0.68}_{-0.68}$
$-2\,\ln\text{Llh} = 16.06$		

Table 5.2 – Fit results for a background only hypothesis

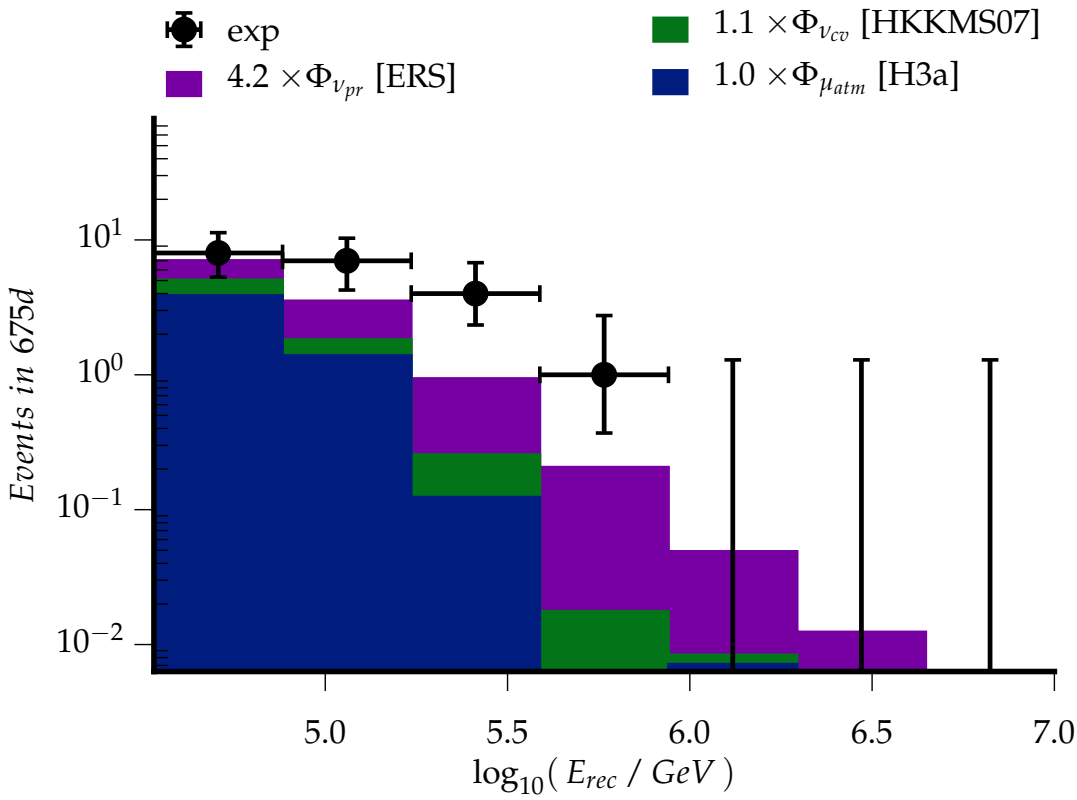

Figure 5.1 – Energy distribution of observed events compared to the best-fit background-only model. The cumulative contributions from atmospheric neutrinos (HKKMS07, ERS) are shown, as well as the distribution of atmospheric muons (H3a) predicted by CORSIKA.

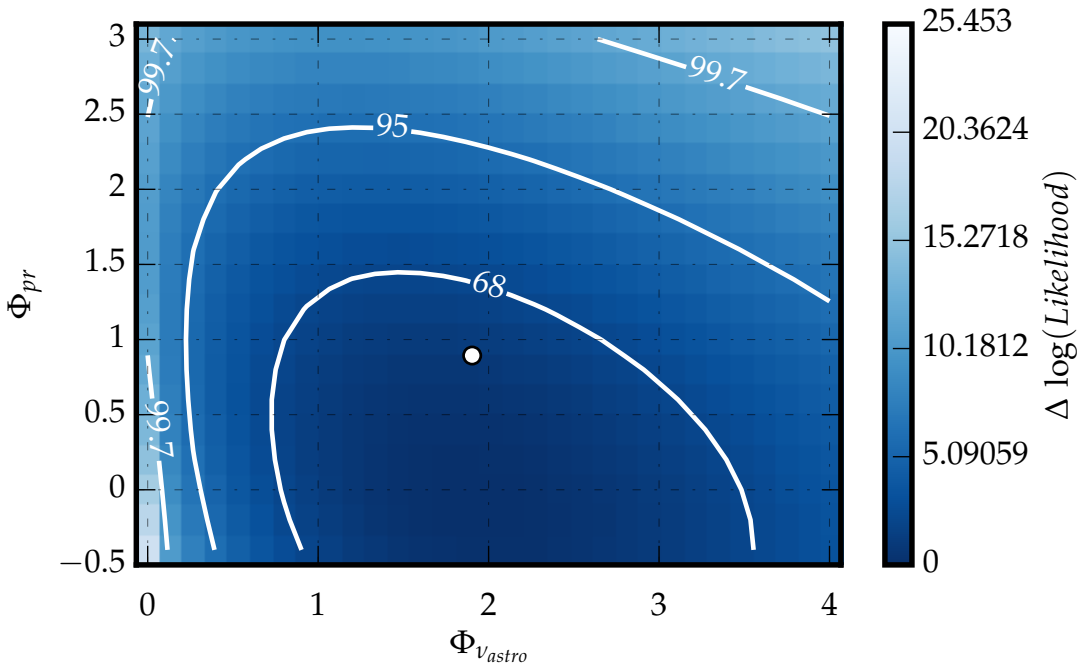

Figure 5.2 – The correlation of the prompt atmospheric and the astrophysical neutrino flux when a power law with a free index for the astrophysical component is fit.

5.3.2 Astrophysical models

The $\Phi_\nu \propto E^{-2}$ isotropic, 1:1:1 flavor ratio model serves as a benchmark model for many analysis searching for a diffuse, extraterrestrial flux of neutrinos. The only parameter of this model is the normalization of the astrophysical neutrino spectrum, Φ_ν, which is given in units of flux per neutrino flavor. As discussed in subsection 5.1.4, several other parameters describing the background templates and systematic effects are fitted as well and treated as nuisance parameters.

The best-fit parameters for this model can be found in Table 5.3, and the best-fit spectrum to that hypothesis is given in Figure 5.3. The tension between data and the fitted flux templates is smaller than for the background-only model. The model is mildly preferred over the background-only model by 1.8σ. The model yields a goodness of fit p-value derived by ensembles of toy data sets of 18.6%.

If the constrains on the prompt atmospheric component are removed and it is set to a free parameter in the fit, the observed data is explained by a prompt component which is about 9 $\times$ higher than the normalization predicted by the

ERS model. This is already excluded by various limits on the prompt atmospheric flux[106, 139] with high confidence.
For the astrophysical model of a neutrino spectrum with a spectral index that is a free parameter in the fit, the best-fit spectra are displayed in Figure 5.4. The data prefer a softer index of $\gamma_{astro} = 2.5^{+0.28}_{-0.24}$. The flux templates seem to fit well to the data, and all components are fitted close to their nominal values. In case of the nuisance parameters, the errors reflect the assumed uncertainties. This softer flux is not dependent on the assumptions made on the prompt atmospheric component and does not change significantly with respect to its error boundaries if the prompt normalization is not constrained in the fit. For that case, a vanishing prompt component is preferred, however with a huge error of $10 \times$ the normalization of the ERS model. The spectrum is then explained by a higher astrophysical component. This occurs due to the correlation of the two fluxes in the fit, especially if a softer index for the extraterrestrial component is fit. The separation power of the event sample to distinguish a prompt flux from an astrophysical is poor, due to the low statistics especially in the bins at the upper end of the energy spectrum. Also due to the indicated softer index of the astrophysical spectrum, both spectra feature a very similar slope if the large error on this measurement of the astrophysical flux is taken into account. The correlation is illustrated by a 2d profile likelihood scan, as shown in Figure 5.2. The goodness of fit for the hypothesis with a free spectral index is calculated with an ensemble test. It is 56.3% and thus indicates a reasonable good fit. The free-floating power law hypothesis is preferred by 1.6σ over the E^{-2} hypothesis and by 2.7σ over the background only hypothesis, numbers obtained from likelihood ratio ensemble tests.

Northern and Southern hemispheres

The sample can be split in a background dominated and a higher signal purity sample, if divided in Northern and Southern hemisphere by the reconstructed direction of the incoming neutrino. However this value suffers from a low precision, Figure 4.21 indicates that about 50% of all events have a deviation from the reconstructed to the true direction less than 35 degree, which is in principle sufficient. Unfortunately, the incoming direction of a large fraction of the events is reconstructed parallel to the horizon, so the distribution is dependent on the chosen value for the split. In Figure 5.5, a value of about 12 degree lower than

Table 5.3 – Fit results for the astrophysical E^{-2} benchmark scenario. The flux $\Phi_{astr.\nu}$ is given in GeVcm^{-2}s^{-1}sr^{-1}.

parameter	value	systematic pull
$\Phi_{astr.\nu}$	$0.80^{+0.41}_{-0.28}$	-
$\zeta_{\theta_{\Phi_E}}$	-	$+0.25^{+0.74}_{-0.95}$
$\zeta_{\theta_{\Phi_{cv.\nu}}}$	-	$+0.02^{+0.93}_{-0.93}$
$\zeta_{\theta_{\Phi_{pr.\nu}}}$	-	$+0.30^{+0.86}_{-1.08}$
$\zeta_{\theta_{\Phi_\mu}}$	-	$-0.03^{+0.86}_{-0.68}$
$-2\,\mathrm{lnLlh} = 8.28$		

Table 5.4 – The best-fit values for an astrophysical model with a free power-law index. The flux $\Phi_{astr.\nu}$ is given in GeVcm^{-2}s^{-1}sr^{-1}.

parameter	value	systematic pull
$\Phi_{astr.\nu}$	$1.90^{+0.97}_{-0.83}$	-
$\gamma_{astr.\nu}$	$2.50^{+0.28}_{-0.28}$	-
$\zeta_{\theta_{\Phi_E}}$	-	$0.02^{+0.97}_{-0.97}$
$\zeta_{\theta_{\Phi_{cv.\nu}}}$	-	$-0.05^{+0.97}_{-0.97}$
$\zeta_{\theta_{\Phi_{pr.\nu}}}$	-	$-0.05^{+0.97}_{-0.48}$
$\zeta_{\theta_{\Phi_\mu}}$	-	$-0.48^{+0.86}_{-0.86}$
$-2\,\mathrm{lnLlh} = 5.34$		

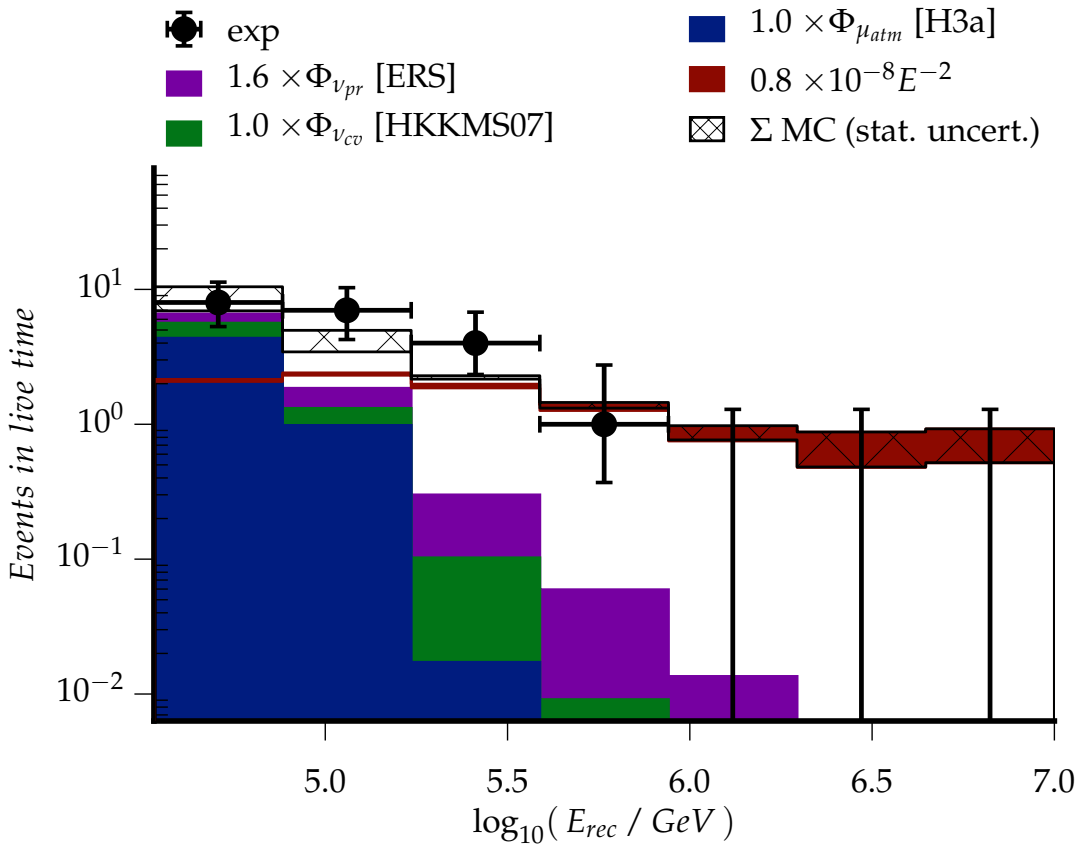

Figure 5.3 – Energy distribution of observed events compared to the best-fit astrophysical $\Phi_\nu \propto E^{-2}$ model. The cumulative contributions from atmospheric neutrinos (HKKMS07, ERS) and atmospheric muons (H3a) as predicted by CORSIKA are shown. On top of that, an astrophysical component with $\Phi_\nu \propto E^{-2}$ is overlaid. The sum of the stacked background contributions and the astrophysical model is indicated and labeled as "$\sum$ MC". The fluxes are given in GeVcm^{-2}s^{-1}sr^{-1}.

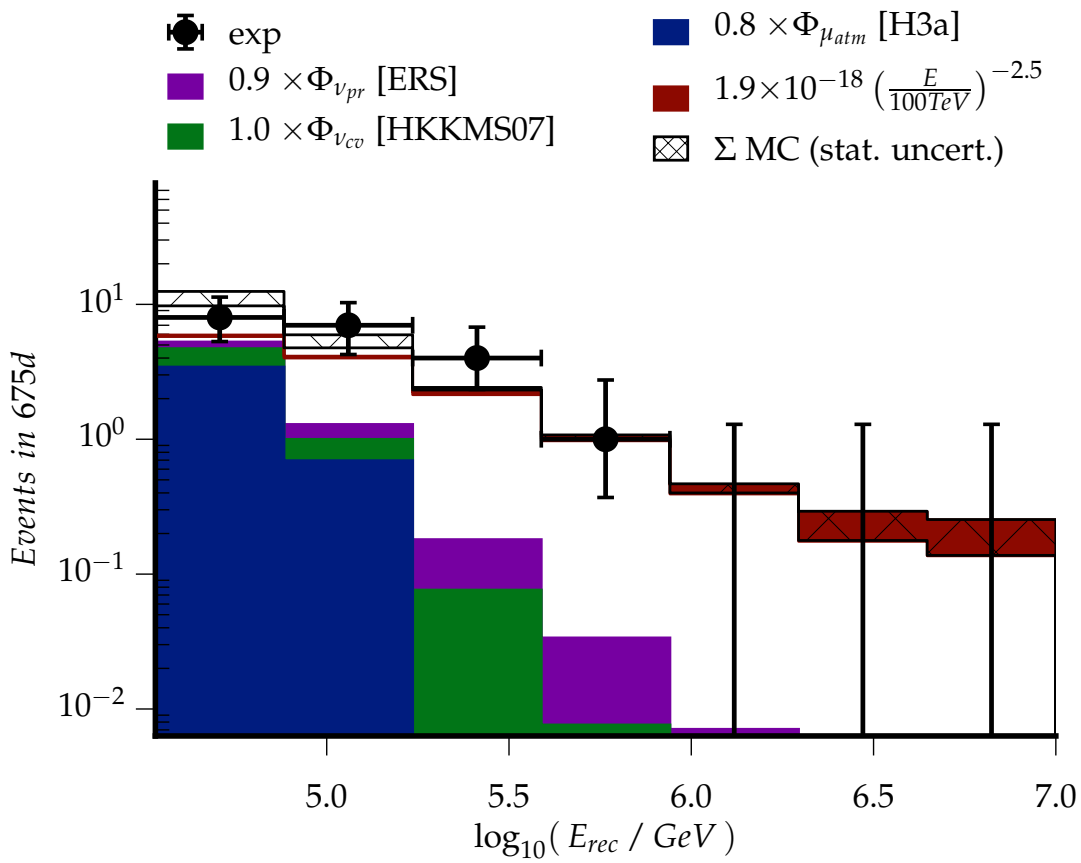

Figure 5.4 – Energy distribution of observed events compared to the best-fit astrophysical $\Phi_\nu \propto E^{-\gamma}$ model. The cumulative contributions from atmospheric neutrinos (HKKMS07, ERS) and atmospheric muons (H3a) as predicted by CORSIKA are shown. On top of that, an astrophysical component with $\Phi_\nu \propto E^{-2}$ is overlaid. The sum of the stacked background contributions and the astrophysical model is indicated and labeled as "$\sum$ MC". The fluxes are given in GeVcm^{-2}s^{-1}sr^{-1}.

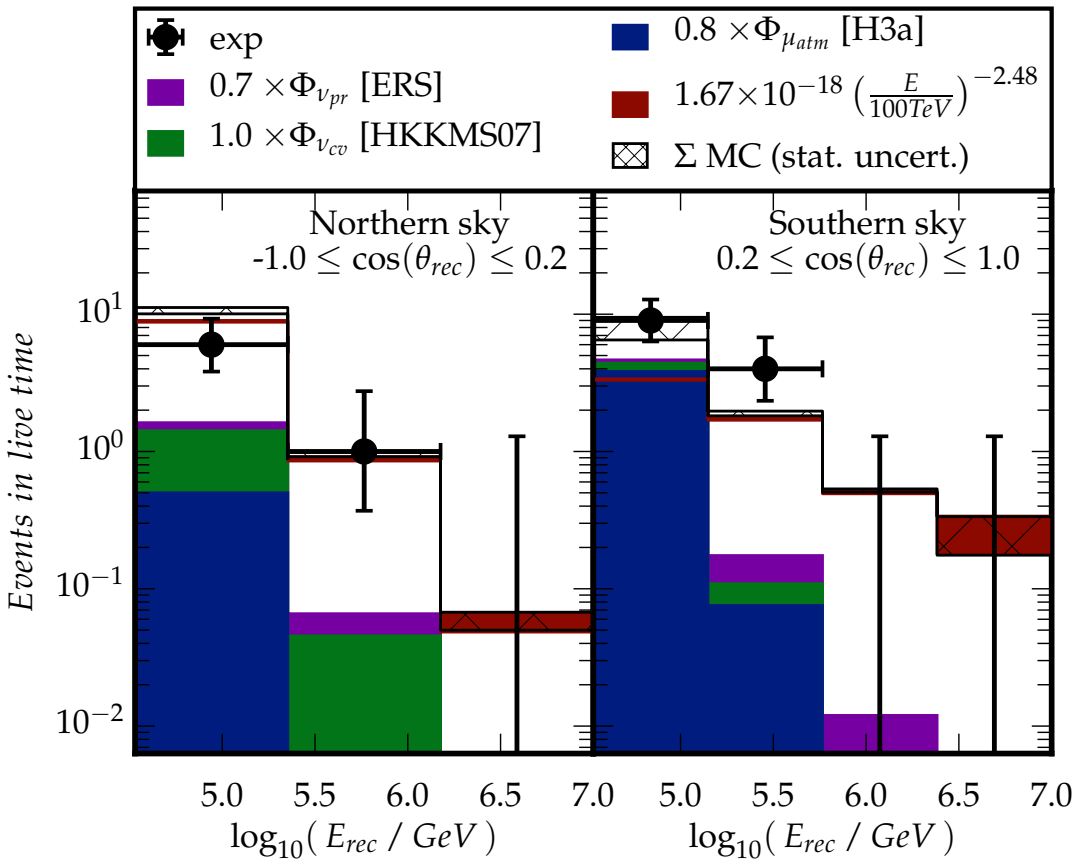

Figure 5.5 – The best-fit distributions to a model with a free power law index γ. The distribution is split in an up going part on the left, and an down going part on the right. The atmospheric muon contribution in the Northern hemisphere can be explained by the large reconstruction error. The fluxes are given in $\mathrm{GeVcm^{-2}s^{-1}sr^{-1}}$.

the actual horizon was chosen, to be consistent with other IceCube analysis. The split sample however allows a more detailed study of the individual background components, which reveals the good agreement of data and prediction in the most populated and background dominated bin. The best-fit results for a free floating power law index deviate only marginally from the un-split measurement.

5.4 Discussion

As presented in the previous chapters, the here described data obtained by a search for particle shower events with vertices at the edge or outside the instru-

Table 5.5 – Fit results for the an astrophysical model with free power-law index. The fit is performed for two zenith bins, which correspond to the Northern and Southern sky. The results for the fit parameters deviate only slightly from those for the all-sky fit in Table 5.4. The flux $\Phi_{astr.\nu}$ is given in GeVcm^{-2}s^{-1}sr^{-1}.

parameter	value	systematic pull
$\Phi_{astr.\nu}$	$1.67^{+0.82}_{-0.82}$	-
$\gamma_{astr.\nu}$	$2.47^{+0.28}_{-0.24}$	-
$\zeta_{\theta_{\Phi_E}}$	-	$+0.50^{+0.39}_{-0.85}$
$\zeta_{\theta_{\Phi_{cv.\nu}}}$	-	$-0.1^{+0.98}_{-0.88}$
$\zeta_{\theta_{\Phi_{pr.\nu}}}$	-	$-0.11^{+1.00}_{-1.00}$
$\zeta_{\theta_{\Phi_\mu}}$	-	$-0.32^{+0.68}_{-0.68}$
$-2\,\mathrm{lnLlh} = 6.57$		

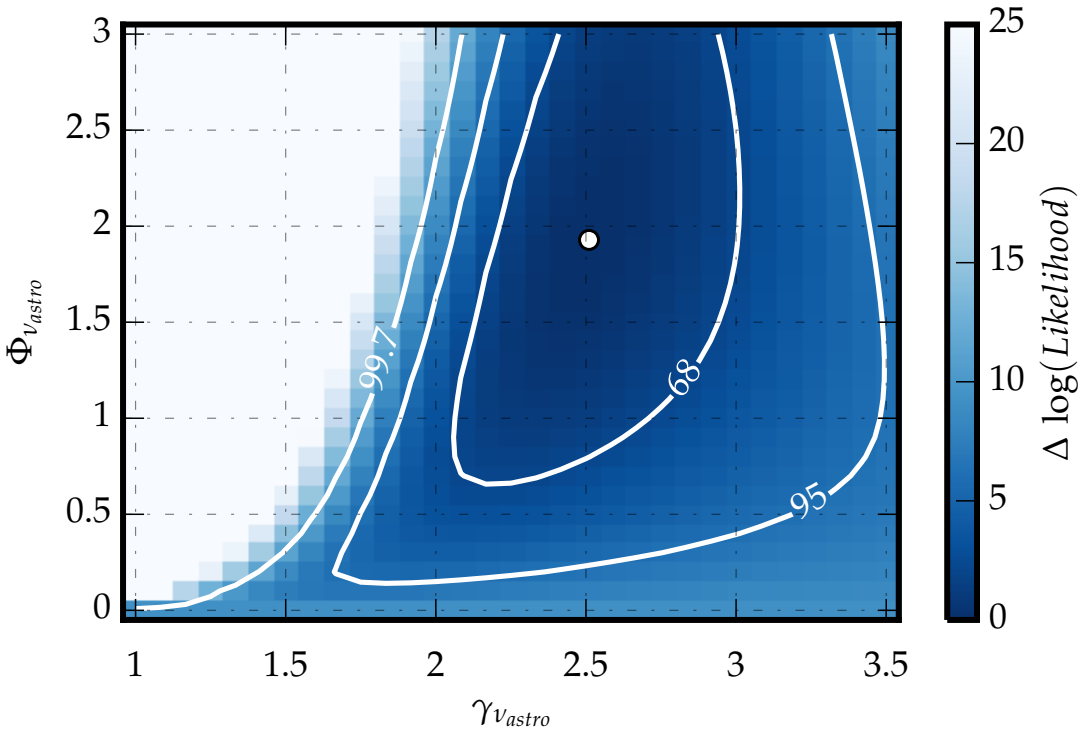

Figure 5.6 – Profile likelihood scan of the likelihood for the fit to an astrophysical model with a free spectral index, index and corresponding normalization are shown. 1,2 and 3-σ contours indicated. The flux $\Phi_{astr.\nu}$ is given in GeVcm^{-2}s^{-1}sr^{-1}.

mented volume of IceCube is able to contribute to IceCube's efforts to measure the diffuse astrophysical neutrino flux more precisely. For the first time, an event selection explicitly dedicated to such events was developed. A straight cut search was performed with a background estimate derived from Monte Carlo simulations. For two years of data, a MC livetime of larger than two years was simulated for primary protons with energy larger than about 165 TeV. The search yielded 18 events which were previously not observed. The highest energetic event found in this search is with 576 TeV reconstructed energy the fourth highest energetic observed and published cascade like event in IceCube.

The data clearly prefers an astrophysical signal over the pure background expectations at the 2.7 sigma level, a measurement of the power law index indicates a softer spectral index than the $\gamma = -2$ benchmark scenario, however with large errors. The measurement is within its errors in good agreement with previous analysis[59, 131, 139]. The vertex and energy resolutions of this analysis are only slightly worse than those of recent contained searches[138], and even better than previous searches with smaller detectors[127]. The effective area of this search compares well to contained searches and even overtakes at several 100 TeV. The systematic uncertainties in the energy estimate due to reconstruction uncertainty and ice model as well as DOM efficiency are included by a nuisance parameter in the final fit. Several other parameters describing systematic effects have been tested, although it was found that the data is not sensitive to these effects.

Comparing the found data with other analysis yields consistent results, an overview of the results of different analysis is shown in Figure 5.7. The data thus has been combined with its contained counterpart (see section 4.3). The combined analysis prefers a featureless power law, with no indications of different spectral indices when fitting only Northern or Southern hemispheres. The fitted index results in $\gamma = 2.67^{+0.12}_{-0.13}$ with a normalization of $\Phi_0 = 2.3^{+0.7}_{-0.6} \times$ GeVcm^{-2}s^{-1}sr^{-1}per flavor. The best-fit neutrino energy spectrum of the combined analysis is shown in Figure 5.8, where a simple unfolding technique has been applied: For each data bin an extraterrestrial neutrino flux of $\Phi_\nu \propto E^{-2}$ has been fitted separately. In combination with [23], a previously suspected "gap" in the spectrum vanishes. The spectrum is shown in Figure 5.9. Although anticipated as being statistically not significant, this gap has tempted the creation of

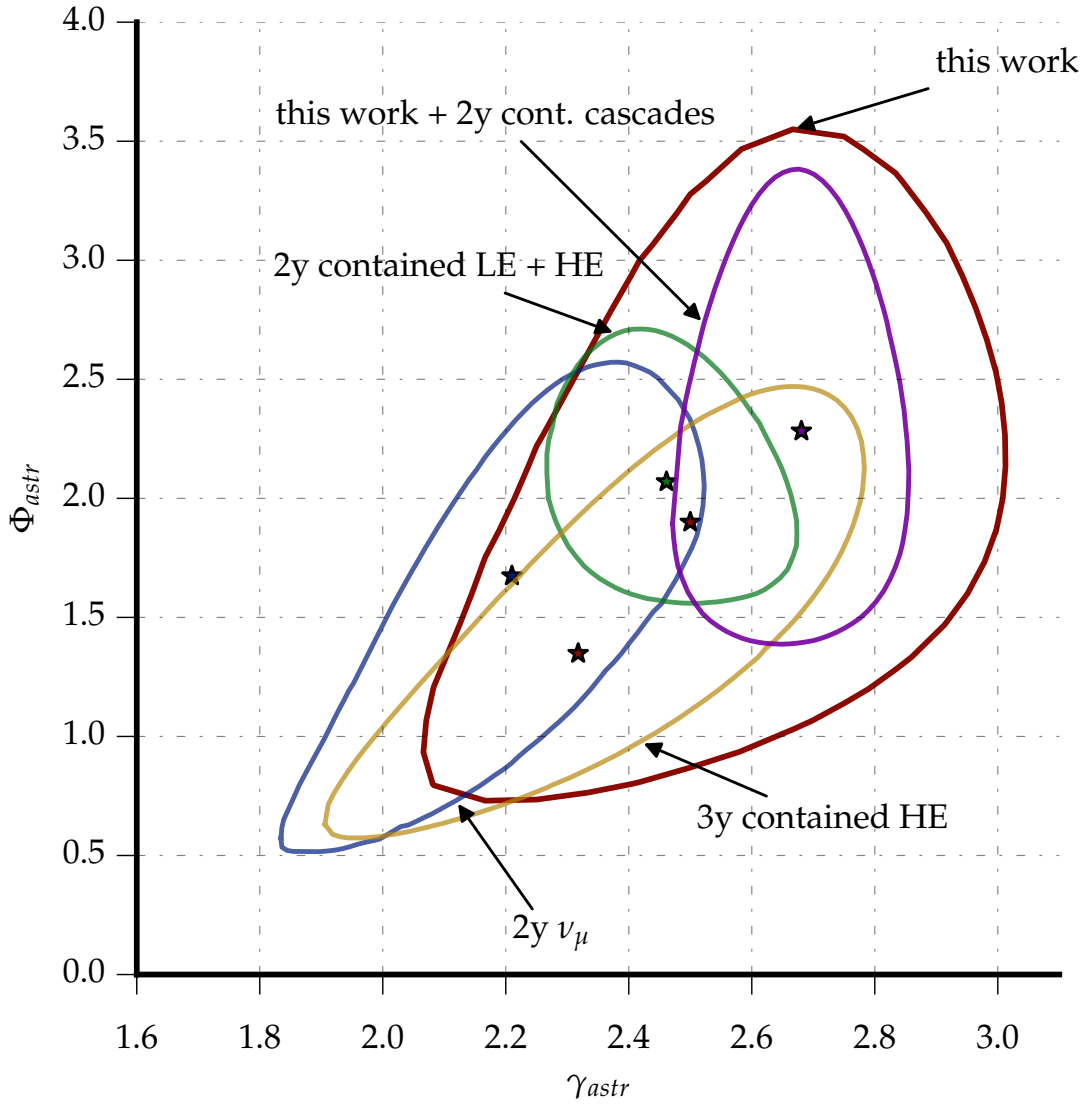

Figure 5.7 – The best-fit contours (as shown in Figure 5.6) in comparison with other results: 2-year low and high energy[139], 3-year high energy[131] and a 2-year search for ν_μ only[145]. The combination of this data with the data of its contained counterpart of 2-year contained low and high energy cascades (see section 4.3) is displayed as well.

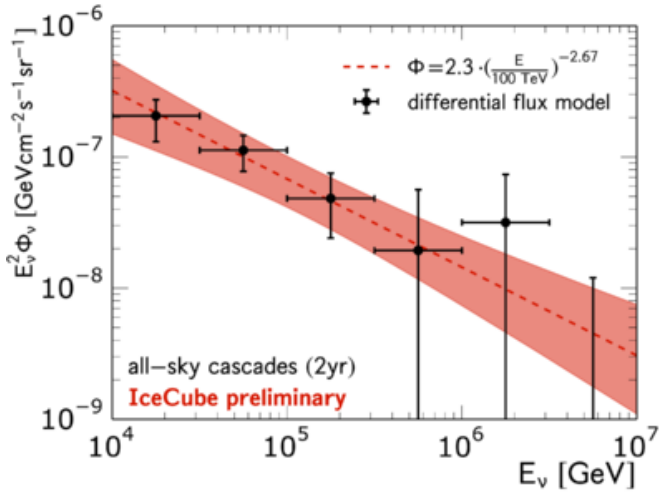

Figure 5.8 – The spectrum of the combined analysis of this work and the analysis described in section 4.3. A simple unfolding technique has been used, where in each energy bin an E^{-2} flux has been fitted. Figure kindly provided by [146].

models with a dip in the neutrino spectrum through the community, e.g. [56], which can be constrained by the help of the data presented here. The combined energy spectrum of both analysis is shown in Figure 5.10.

We finally conclude that the here presented sample contains a non-negligible contribution of neutrinos from non-terrestrial origin and thus can provide information about such a flux. The search for cascade-like events at the edge of the instrumented volume is promising, and it is capable to double the effective area of a factor of two at energies larger than 100 TeV compared to typical searches targeted at contained particle showers.

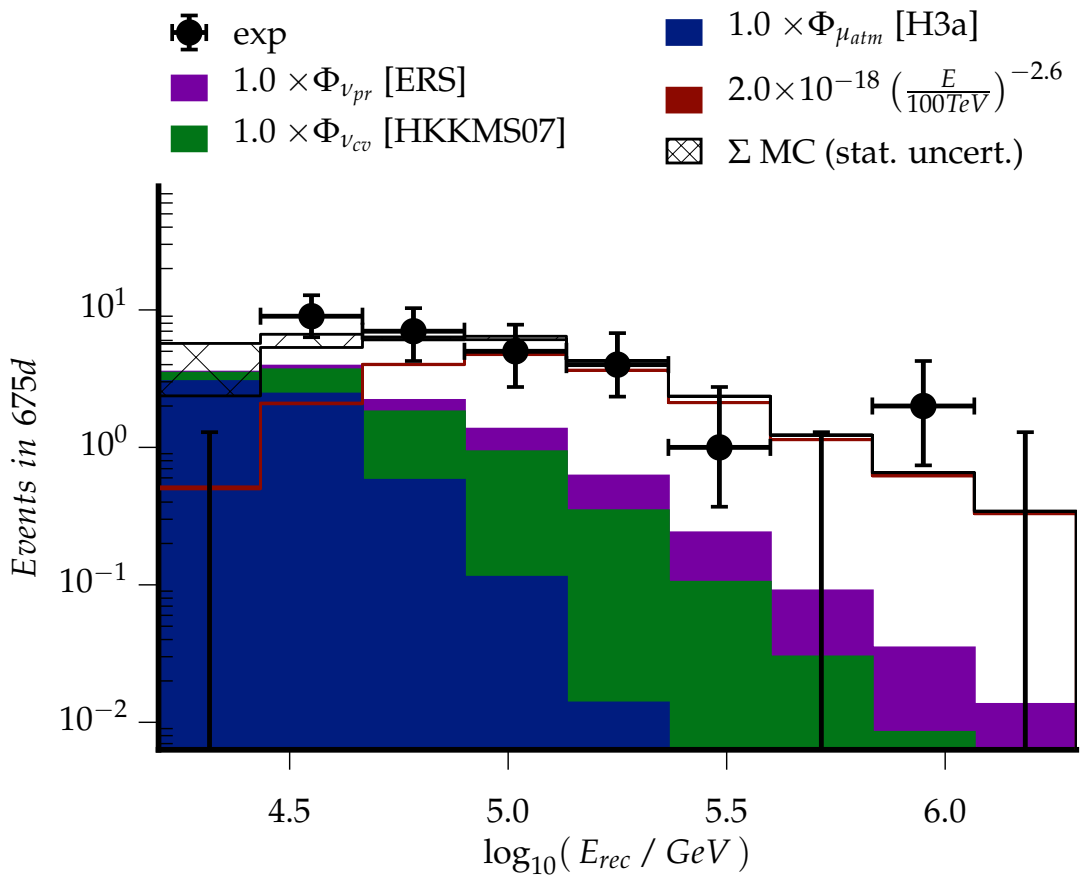

Figure 5.9 – The 2-year best-fit energy spectrum taken from [23]. The fluxes are given in GeVcm^{-2}s^{-1}sr^{-1}.

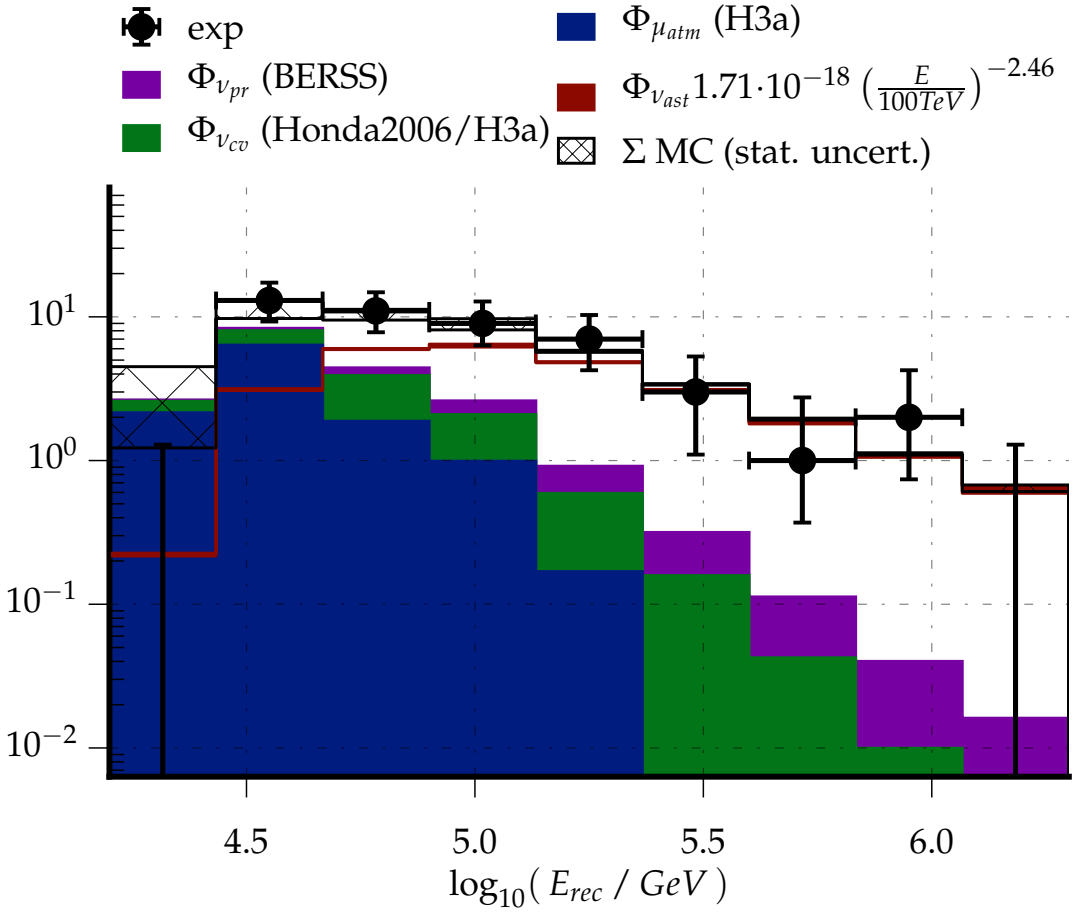

Figure 5.10 – Addition of this data to the data of [23], overlapping events removed. Shown is the combined best-fit spectrum. The fluxes are given in GeVcm^{-2}s^{-1}sr^{-1}.

6

Summary & Outlook

The here presented work was performed in the context of a search for a diffuse extraterrestrial neutrino flux. During the time this analysis was developed, IceCube discovered such a signal, and the desire of the community switched from the pure discovery of this signal to a precise measurement of the flux - questions of the steepness of the energy spectrum or a possible cut-off were raised. To answer these questions, large event samples are needed, as the event counts in IceCube merely exceed 10 - 20 events per year above $\approx$ 30 TeV. Thus individual analysis performed for different years or tailored for specific event signatures have to be combined. For the combination to be possible, the individual samples must be statistically independent.

This analysis provides such a sample: For the first time, a sample optimized for particle showers - or *cascades* - at the edge of the instrumented volume of IceCube was obtained, seconded by a solid background estimate derived from Monte Carlo simulations. Previously, this part of the detector had been used for cascade analysis only to reject background. The addition of this volume to other IceCube searches allows an increase in fiducial volume of about 350 MTon, which is an increase of about 80%. The analysis managed to combine 2 years of IceCube data with different pre-filter settings in a consistent way, one year of the data taken while IceCube was still under construction. The available background suppression techniques, which were designed for a contained

cascade signal have been investigated for their capability for uncontained cascades as well, and the most suitable have been chosen to isolate a sample of pure uncontained cascades for the first time. The available energy reconstruction techniques have been tested for their validity, and found to perform better than previous contained searches with less instrumentation[127], however poorer in performance than if used on a contained sample using the full IceCube array.

The techniques developed for this analysis are ready to be applied to future datasets, and as with this work the method of searching for uncontained cascades is established, future analysis can concentrate on optimizing the method. The found final sample exposes a high signal to noise ratio of 20 found events with energies in the range from 34 TeV to 576 TeV over an expectation from pure atmospheric background of ≈ 8 events. The obtained data sample was studied in detail and background-only hypothesis and signal hypothesis have been fit. Indications for an astrophysical signal with an index of about $\gamma = 2.5^{0.28}_{0.28}$ have been found, and the pure background hypothesis could be rejected at a 2.7 sigma level. We therefore conclude that the sample contains a non-negligible fraction of extraterrestrial neutrinos. The errors on the measurement itself are large, yet the measurement being statistically independent from any other sample found by IceCube, it reduces the errors on a combined analysis. A publication of such combined results is planned. The obtained data increases our knowledge about the extraterrestrial neutrino flux and thus allows to help the task of understanding the extraterrestrial neutrino flux and the nature of its possible source candidates, which will ultimately add another part to the puzzle of the origin of cosmic rays.

Appendix

Final sample - event displays and results of the likelihood scans

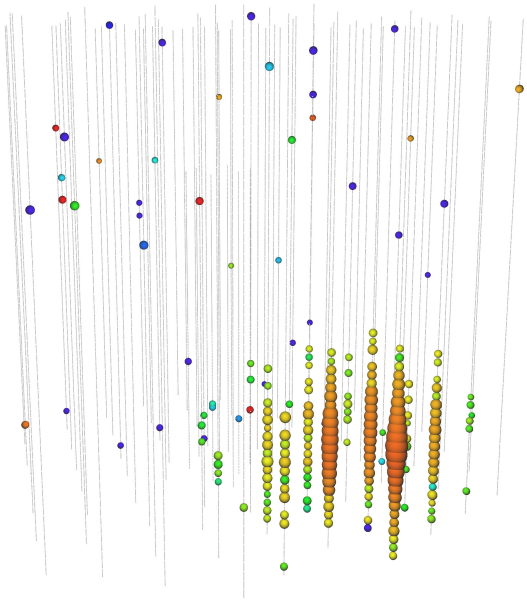

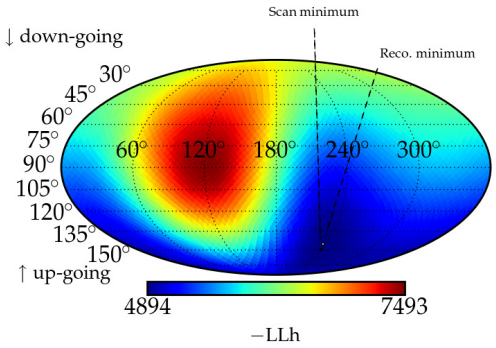

season	sample	run/event	E_{rec}	Θ_{rec}	x_{rec}	y_{rec}	z_{rec}
IC79	90	117744/54888465	34284	150	43	459	-305

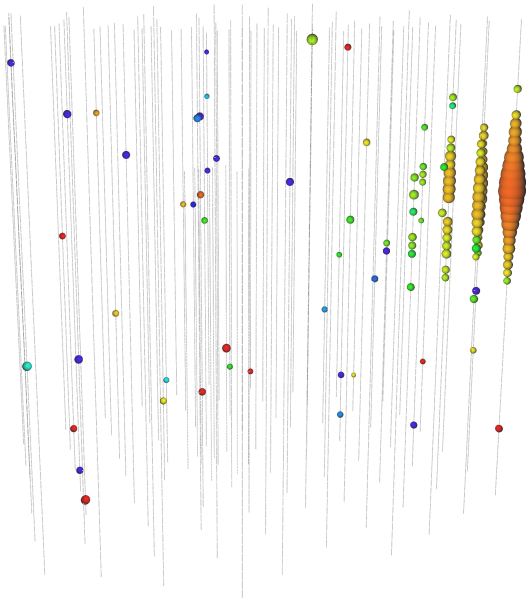

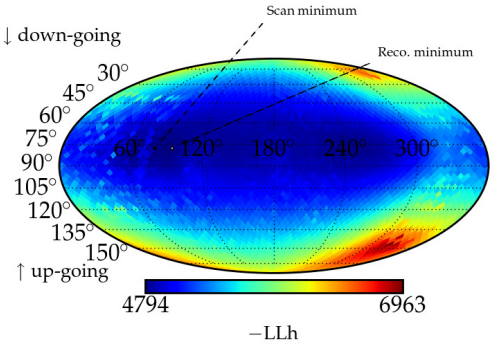

season	sample	run/event	E_{rec}	Θ_{rec}	x_{rec}	y_{rec}	z_{rec}
IC86	90	119507/35825553	98817	77	-312	460	162

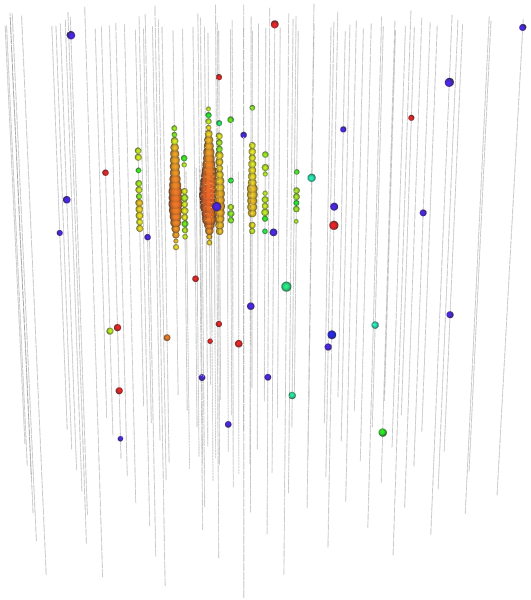

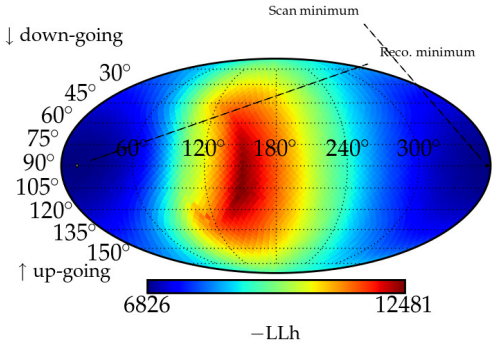

season	sample	run/event	E_{rec}	Θ_{rec}	x_{rec}	y_{rec}	z_{rec}
IC86	90	118466/21256734	384527	90	-202	-566	49

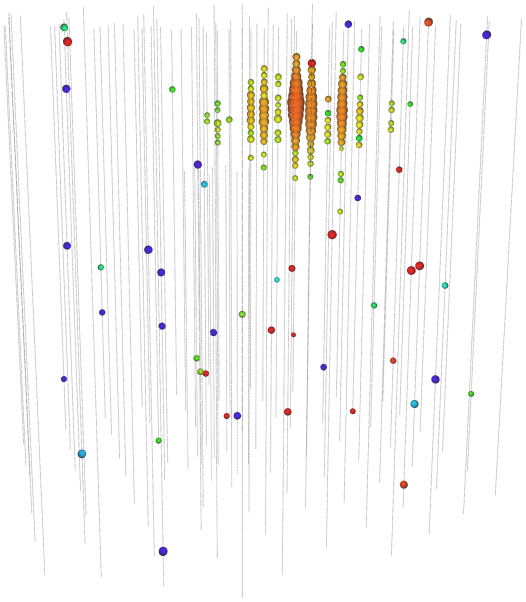

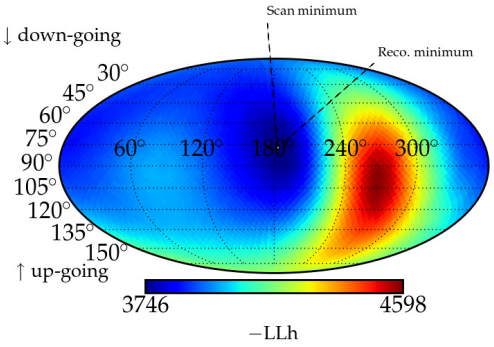

season	sample	run/event	E_{rec}	Θ_{rec}	x_{rec}	y_{rec}	z_{rec}
IC86	90	118692/5825484	62162	75	-424	-287	308

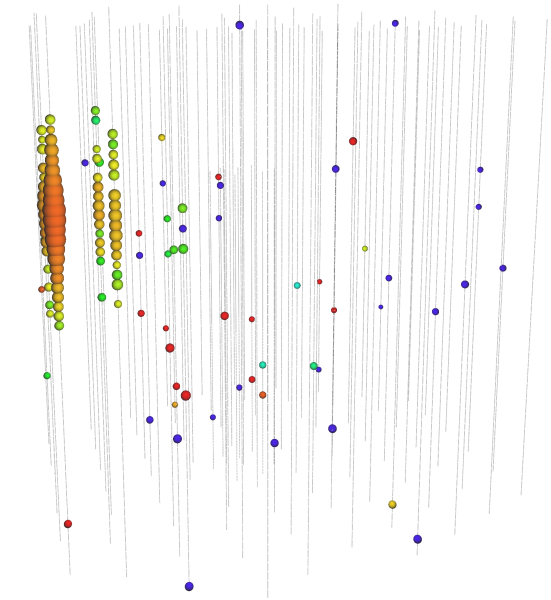

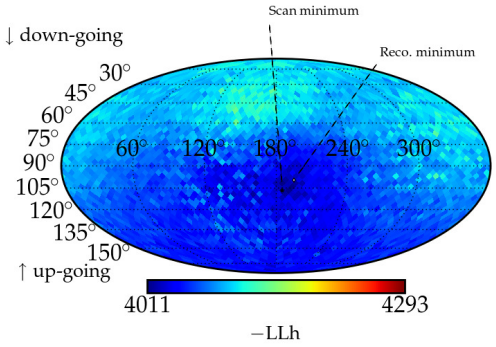

season	sample	run/event	E_{rec}	Θ_{rec}	x_{rec}	y_{rec}	z_{rec}
IC86	90	119736/73354228	148073	106	632	150	145

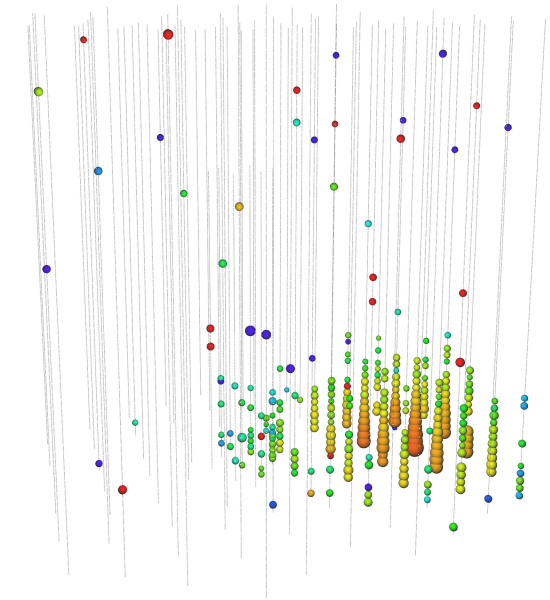

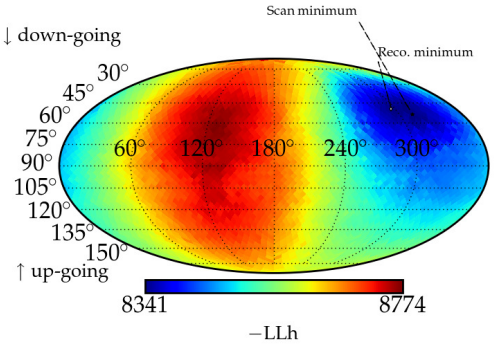

season	sample	run/event	E_{rec}	Θ_{rec}	x_{rec}	y_{rec}	z_{rec}
IC79	90	116522/17216576	395832	54	-338	92	-595

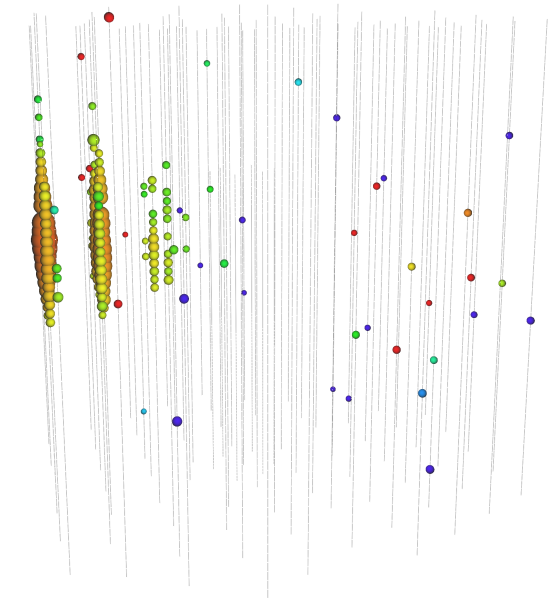

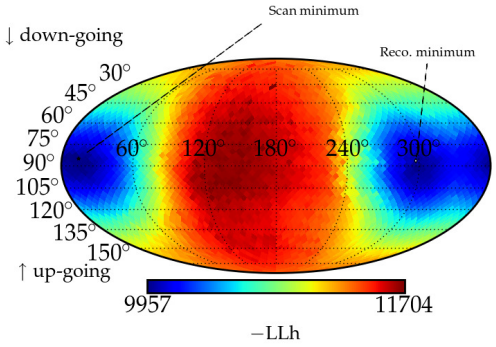

season	sample	run/event	E_{rec}	Θ_{rec}	x_{rec}	y_{rec}	z_{rec}
IC79	90	117721/55150085	152641	85	478	-47	67

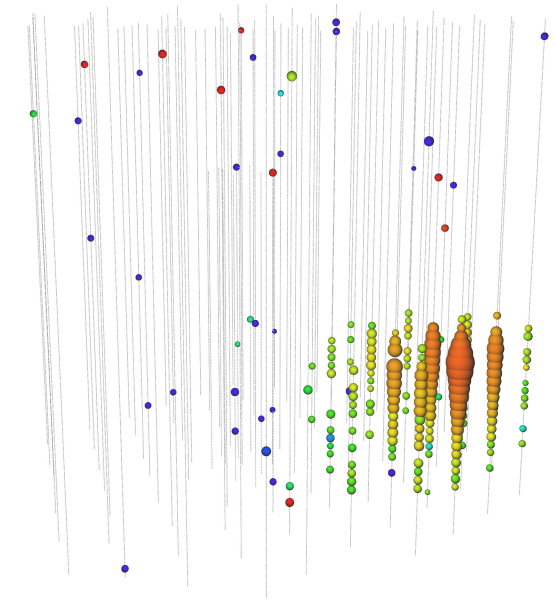

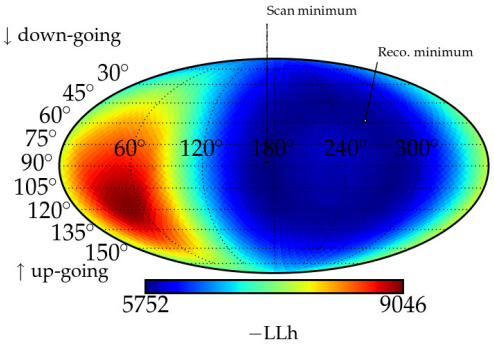

season	sample	run/event	E_{rec}	Θ_{rec}	x_{rec}	y_{rec}	z_{rec}
IC86	10	118420/72256529	140177	87	-138	464	-147

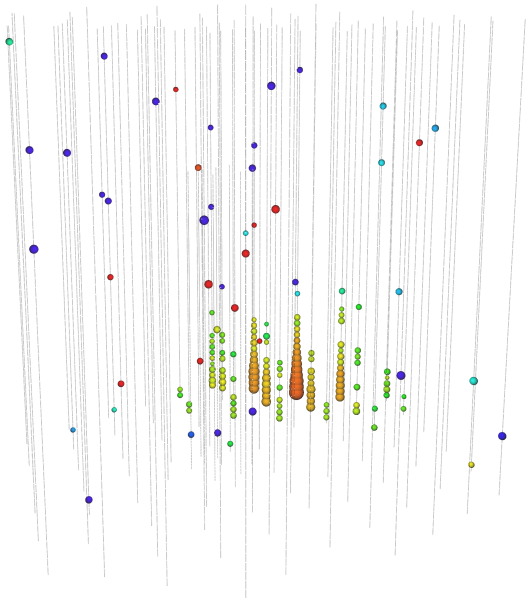

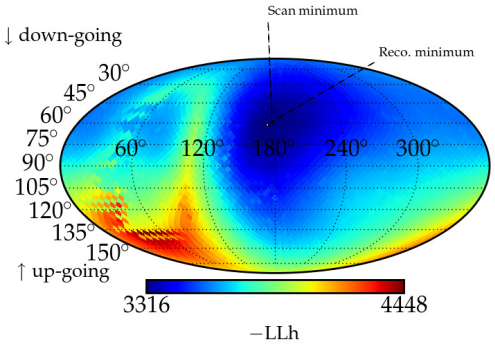

season	sample	run/event	E_{rec}	Θ_{rec}	x_{rec}	y_{rec}	z_{rec}
IC86	90	118178/6251579	25031	60	-425	-294	-497

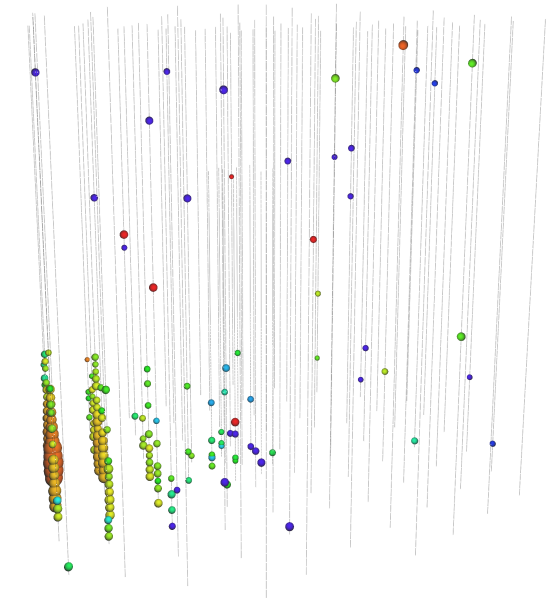

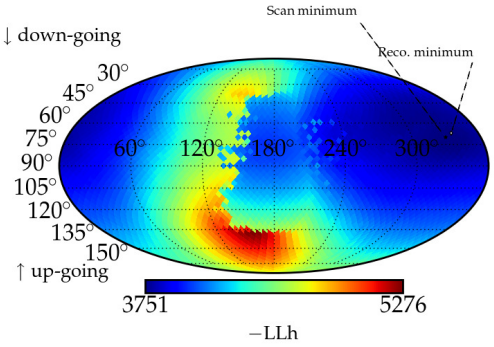

season	sample	run/event	E_{rec}	Θ_{rec}	x_{rec}	y_{rec}	z_{rec}
IC86	90	119651/30979523	32924	70	492	-217	-462

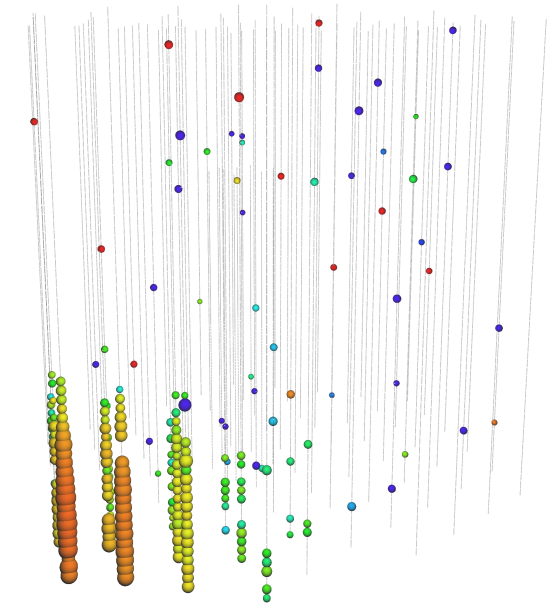

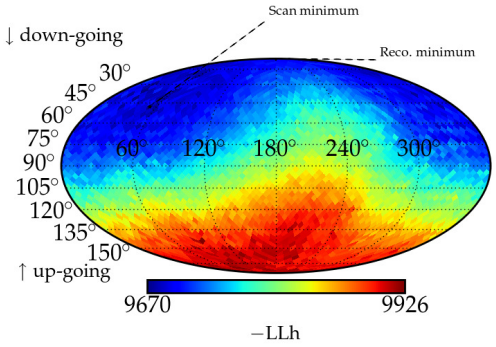

season	sample	run/event	E_{rec}	Θ_{rec}	x_{rec}	y_{rec}	z_{rec}
IC86	10	118670/58852406	543502	48	674	270	-410

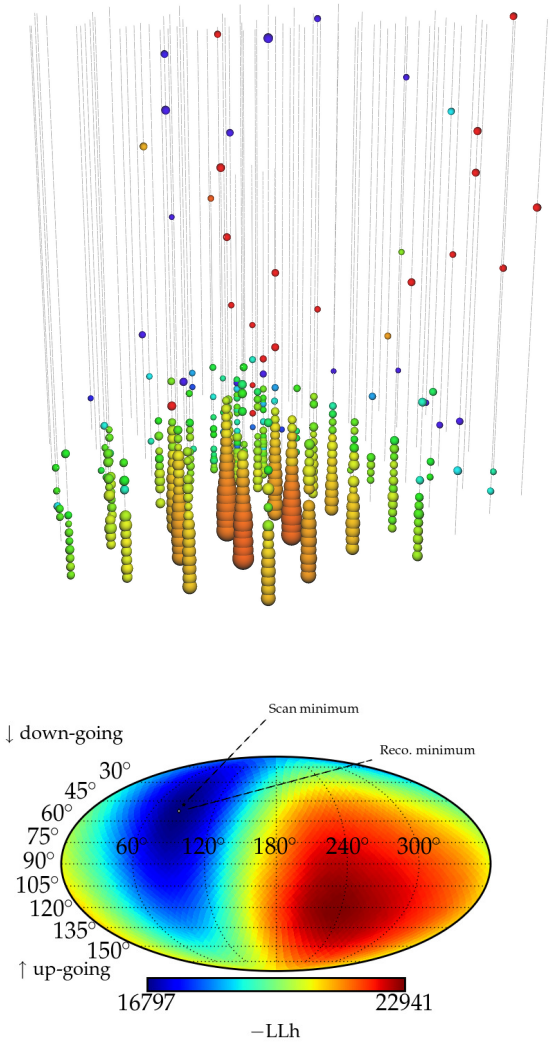

season	sample	run/event	E_{rec}	Θ_{rec}	x_{rec}	y_{rec}	z_{rec}
IC79	90	116698/10198436	169415	48	246	302	-469

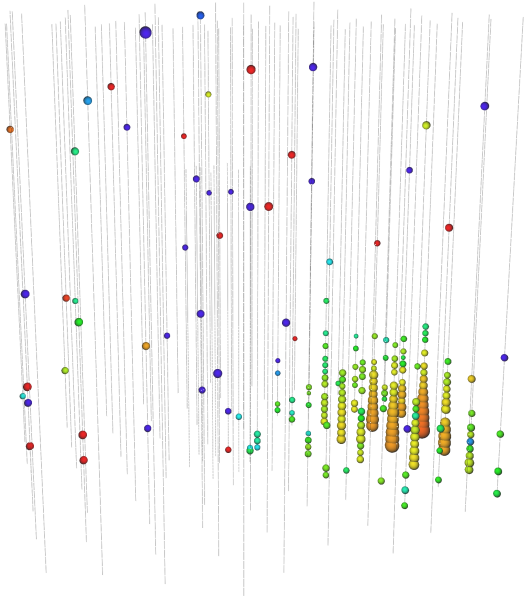

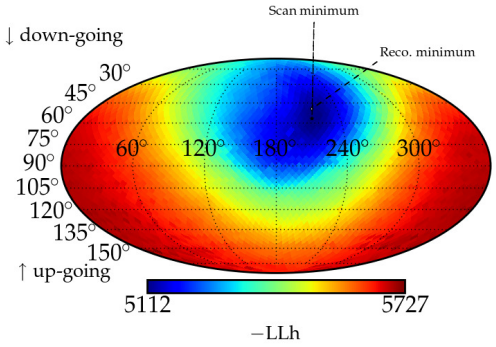

season	sample	run/event	E_{rec}	Θ_{rec}	x_{rec}	y_{rec}	z_{rec}
IC86	90	119962/11948966	62437	57	-467	87	-535

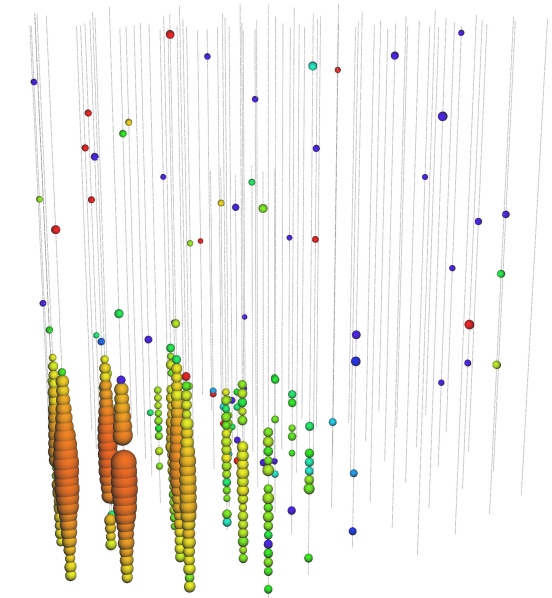

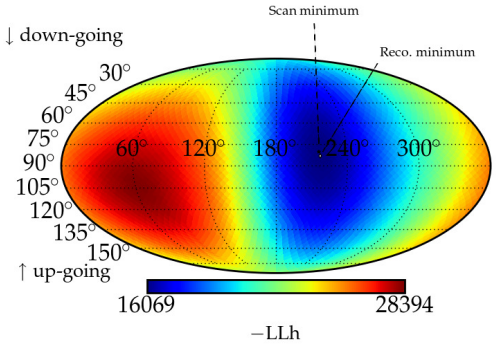

season	sample	run/event	E_{rec}	Θ_{rec}	x_{rec}	y_{rec}	z_{rec}
IC79	90	116457/702481	172767	80	497	188	-308

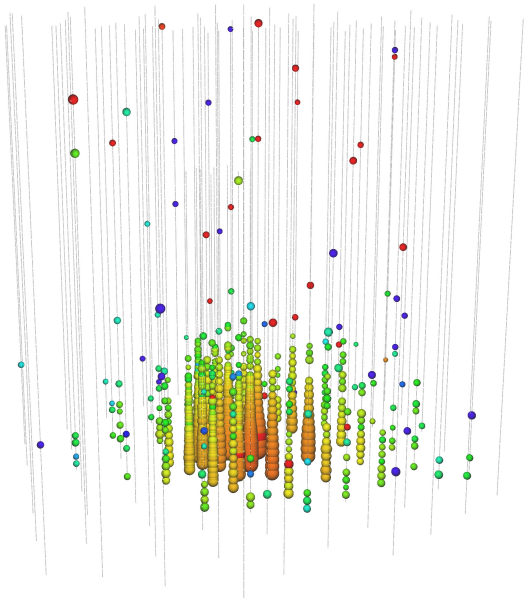

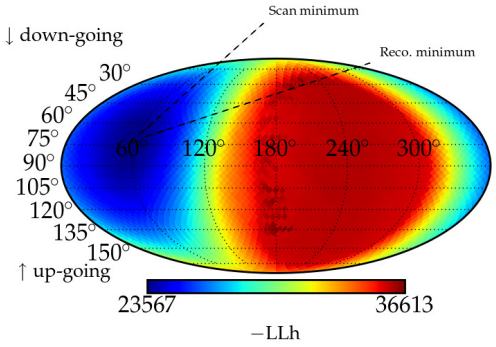

season	sample	run/event	E_{rec}	Θ_{rec}	x_{rec}	y_{rec}	z_{rec}
IC86	90	118178/66452255	90121	73	-60	3	-499

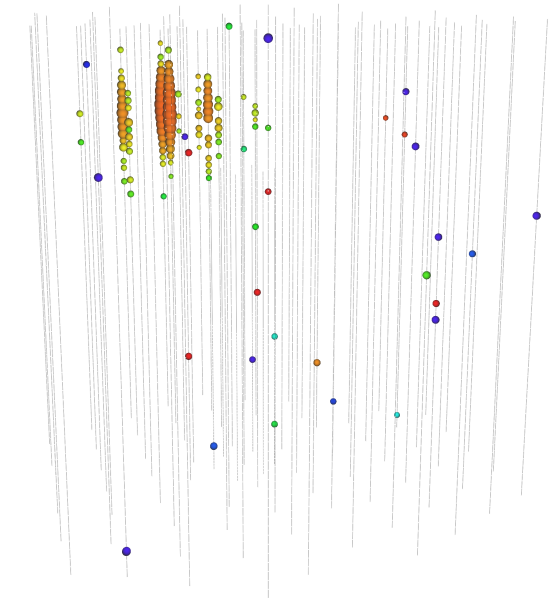

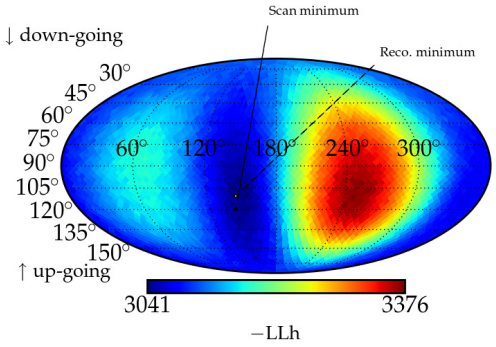

season	sample	run/event	E_{rec}	Θ_{rec}	x_{rec}	y_{rec}	z_{rec}
IC79	90	116351/5378257	53092	120	0	-419	305

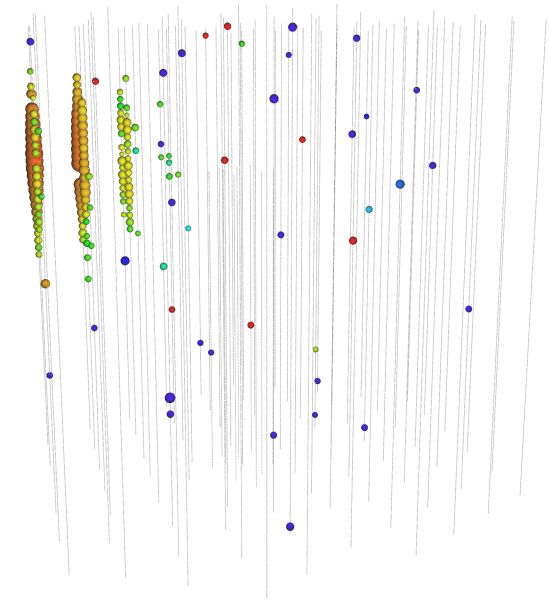

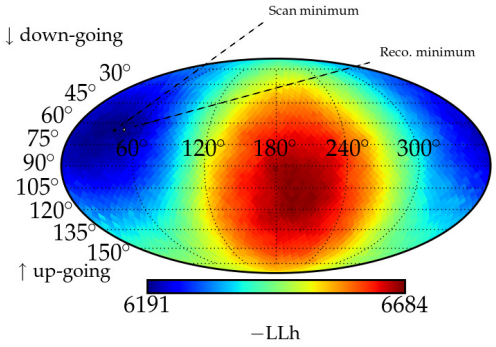

season	sample	run/event	E_{rec}	Θ_{rec}	x_{rec}	y_{rec}	z_{rec}
IC86	90	119117/23529568	659942	65	321	-487	207

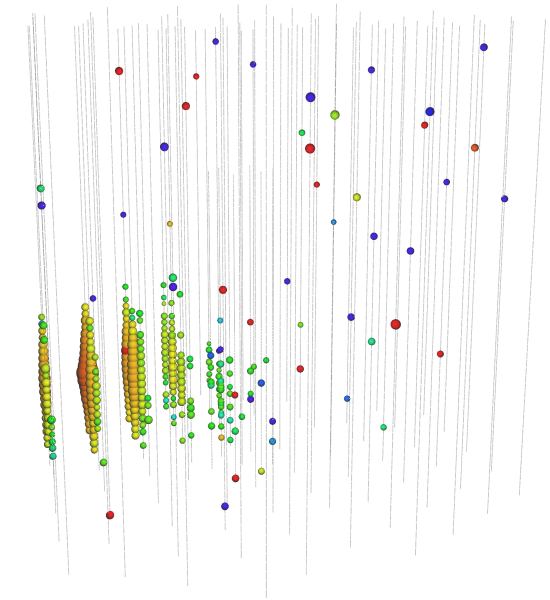

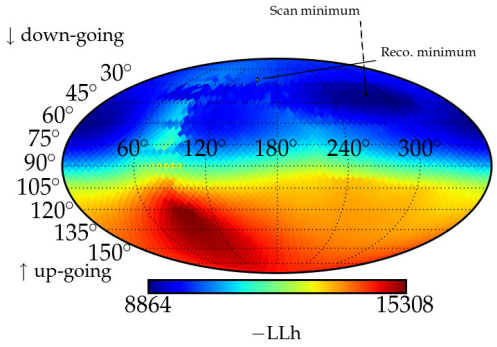

season	sample	run/event	E_{rec}	Θ_{rec}	x_{rec}	y_{rec}	z_{rec}
IC79	90	117273/15914878	66694	38	239	-469	-353

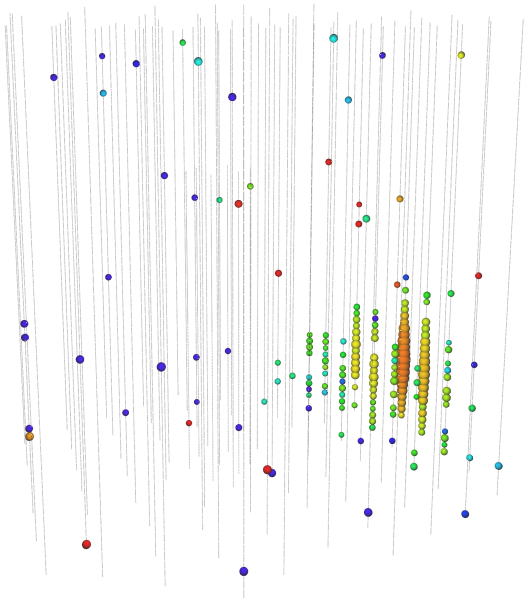

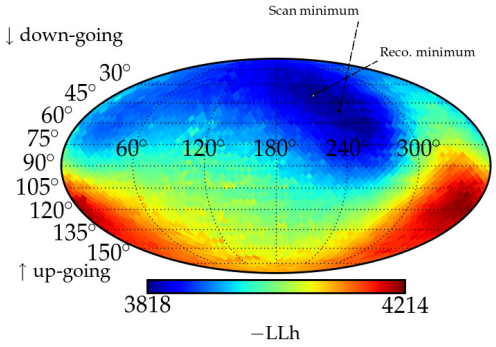

season	sample	run/event	E_{rec}	Θ_{rec}	x_{rec}	y_{rec}	z_{rec}
IC79	90	116532/28124500	69595	51	-616	0	-355

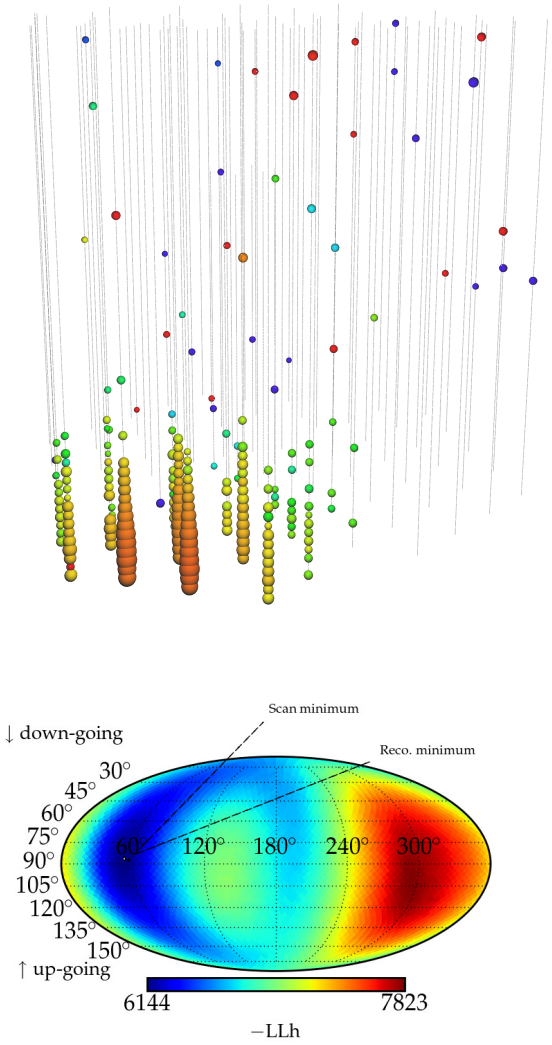

season	sample	run/event	E_{rec}	Θ_{rec}	x_{rec}	y_{rec}	z_{rec}
IC79	90	116794/31146792	40766	87	466	311	-459

Bibliography

[1] Pásztor, E. and Roslund, C. *An interpretation of the Nebra disc*. *Antiquity*, 81:267–278, 6 2007. doi:10.1017/S0003598X00095168

[2] Steele, J.M. *Greek influence on Babylonian astronomy? Mediterranean Archaeology and Archaeometry*, 6:153–160, 2006

[3] Masse, W.B. *The Celestial Basis of Civilization*. *Vistas in Astronomy*, 39:463–477, 1995. doi:10.1016/0083-6656(95)00025-9

[4] Theodossiou, E. and Manimanis, V.N. *The Eternal Role of Astronomy in History and Civilization*. In K. Tsinganos, D. Hatzidimitriou and T. Matsakos, editors, *9th International Conference of the Hellenic Astronomical Society*, volume 424 of *Astronomical Society of the Pacific Conference Series*, 475, July 2010

[5] Kelley, D., Aveni, A. and Milone, E. *Exploring Ancient Skies: A Survey of Ancient and Cultural Astronomy*. Springer, 2011. URL: http://books.google.de/books?id=ILBuYcGASxcC

[6] Curie, M., Curie, P. and G, B. *Sur une substance nouvelle radio-active, contenue dans la pechblende*. *Comptes rendus hebdomadaires des séances de l'Académie des sciences*, 127:1215–1217, 1898. URL: http://www.archive.org/details/surunesubstancen127curi

[7] F. Hess, V. *Über Beobachtungen der durchdringenden Strahlung bei sieben Freiballonfahrten*. *Physikalische Zeitschrift*, 13:1084–1091, November 1912

[8] Bird, D.J. et al. *Evidence for correlated changes in the spectrum and composition of cosmic rays at extremely high energies*. *Physical Review Letters*, 71:3401–3404, Nov 1993. doi:10.1103/PhysRevLett.71.3401

[9] Achterberg, A. et al. (IceCube Collaboration). *First Year Performance of The IceCube Neutrino Telescope*. *Astroparticle Physics*, 26:155–173, 2006. doi:10.1016/j.astropartphys.2006.06.007

[10] The Pierre Auger Collaboration. *The Pierre Auger Cosmic Ray Observatory*. *ArXiv e-prints*, February 2015. arXiv:1502.01323

[11] Kawai, H. et al. *Telescope Array Experiment*. *Nuclear Physics B - Proceedings Supplements*, 175–176(0):221–226, 2008. Proceedings of the XIV International Symposium on Very High Energy Cosmic Ray Interactions. doi:10.1016/j.nuclphysbps.2007.11.002

[12] Atwood, W.B. et al. *The Large Area Telescope on the Fermi Gamma-Ray Space Telescope Mission*. *The Astrophysical Journal*, 697(2):1071, 2009. URL: http://stacks.iop.org/0004-637X/697/i=2/a=1071

[13] Aharonian, F. et al. *First ground-based measurement of atmospheric Cherenkov light from cosmic rays*. *Physical Review D*, 75(4):042004, February 2007. doi:10.1103/PhysRevD.75.042004

[14] Zatsepin, G.T. and Kuz'min, V.A. *Upper Limit of the Spectrum of Cosmic Rays*. *Soviet Journal of Experimental and Theoretical Physics Letters*, 4:78, August 1966

[15] Ackermann, M. et al. (Fermi-LAT Collaboration). *Detection of the Characteristic Pion-Decay Signature in Supernova Remnants*. *Science*, 339:807, 2013. doi:10.1126/science.1231160

[16] Stecker, F.W. and de Jager, O.C. *On the Absorption of High-Energy Gamma-Rays by Intergalactic Infrared Radiation*. *The Astrophysical Journal*, 476(2):712, 1997. URL: http://stacks.iop.org/0004-637X/476/i=2/a=712

[17] Gould, R.J. and Schréder, G. *Opacity of the universe to high-energy photons*. *Physical Review Letters*, 16:252–254, Feb 1966. doi:10.1103/PhysRevLett.16.252

[18] Learned, J.G. and Mannheim, K. *High-energy neutrino astrophysics*. *Annual Review of Nuclear and Particle Science*, 50(1):679–749, 2000. doi:10.1146/annurev.nucl.50.1.679

[19] Fukuda, Y. et al. *Measurements of the Solar Neutrino Flux from Super-Kamiokande's First 300 Days*. *Physical Review Letters*, 81:1158–1162, Aug 1998. doi:10.1103/PhysRevLett.81.1158

[20] Velde, J.C.V.D. et al. (IMB). *Neutrinos from SN1987A in the IMB detector*. *Nuclear Instruments and Methods*, A264:28–31, 1988

[21] Alekseev, E.N. et al. *Detection of the neutrino signal from SN 1987A using the INR Baksan underground scintillation telescope*. In I.J. Danziger, editor, *European Southern Observatory Conference and Workshop Proceedings*, volume 26 of *European Southern Observatory Conference and Workshop Proceedings*, 237–247, 1987

[22] Hirata, K. et al. *Observation of a neutrino burst from the supernova SN1987A*. *Physical Review Letters*, 58:1490–1493, Apr 1987. doi:10.1103/PhysRevLett.58.1490

[23] Aartsen, M.G. et al. (IceCube Collaboration). *Evidence for High-Energy Extraterrestrial Neutrinos at the IceCube Detector*. *Science*, 342(6161):1242856, December 2013. doi:10.1126/science.1242856

[24] Aartsen, M.G. et al. (IceCube Collaboration). *First Observation of PeV-Energy Neutrinos with IceCube*. *Physical Review Letters*, 111(2):021103, July 2013. doi:10.1103/PhysRevLett.111.021103

[25] Richard, E. et al. (Super-Kamiokande Collaboration). *Measurements of the atmospheric neutrino flux by Super-Kamiokande: energy spectra, geomagnetic effects, and solar modulation*. *Physical Review D*, D94(5):052001, 2016. doi:10.1103/PhysRevD.94.052001

[26] Aartsen, M. et al. (IceCube Collaboration). *Measurement of the cosmic ray energy spectrum with IceTop-73*. *Physical Review*, D88(4):042004, 2013. doi:10.1103/PhysRevD.88.042004

[27] Abraham, J. et al. (Pierre Auger Collaboration). *Observation of the suppression of the flux of cosmic rays above* $4 \times 10^{19} eV$. *Physical Review Letters*, 101:061101, 2008. doi:10.1103/PhysRevLett.101.061101

[28] Gockel A., T.W. *Beobachtungen über die Radioaktivität der Atmosphäre im Hochgebirge*. *Physikalische Zeitung*, 9:907–911, 1908

[29] Walter, M. and Wolfendale, A. *Early history of cosmic particle physics*. *The European Physics Journal*, H37:323–358, 2012. doi:10.1140/epjh/e2012-30020-1

[30] Freedman, R. and Kaufmann, W. *Universe*. W. H. Freeman, 2007. URL: http://books.google.de/books?id=hfXHTJ6OK9oC

[31] Abraham, J. et al. *Measurement of the Depth of Maximum of Extensive Air Showers above $10^{18}eV$*. *Physical Review Letters*, 104(9):091101, March 2010. doi:10.1103/PhysRevLett.104.091101

[32] Abbasi, R.U. et al. *Study of Ultra-High Energy Cosmic Ray composition using Telescope Array's Middle Drum detector and surface array in hybrid mode*. *Astroparticle Physics*, 64:49–62, 2015. doi:10.1016/j.astropartphys.2014.11.004

[33] Gaisser, T. *Cosmic Rays and Particle Physics*. Cambridge University Press, 1991. URL: http://books.google.de/books?id=5JMmJI7Mm30C

[34] Berezinsky, V., Gazizov, A. and Grigorieva, S. *On astrophysical solution to ultrahigh energy cosmic rays*. *Physical Review D*, 74:043005, Aug 2006. doi:10.1103/PhysRevD.74.043005

[35] Greisen, K. *End to the Cosmic-Ray Spectrum?* *Physical Review Letters*, 16:748–750, Apr 1966. doi:10.1103/PhysRevLett.16.748

[36] Abbasi, R. et al. (IceCube Collaboration). *Constraints on the extremely-high energy cosmic neutrino flux with the icecube 2008-2009 data*. *Physical Review D*, 83:092003, May 2011. doi:10.1103/PhysRevD.83.092003

[37] Abdo, A.A. et al. *The large-scale cosmic-ray anisotropy as observed with milagro*. *The Astrophysical Journal*, 698(2):2121, 2009. URL: http://stacks.iop.org/0004-637X/698/i=2/a=2121

[38] Abbasi, R. et al. (IceCube Collaboration). *Measurement of the anisotropy of cosmic-ray arrival directions with icecube*. *The Astrophysical Journal Letters*, 718(2):L194, 2010. URL: http://stacks.iop.org/2041-8205/718/i=2/a=L194

[39] Hillas, A.M. *Cosmic Rays: Recent Progress and some Current Questions*, 2006. arXiv:astro-ph/0607109

[40] Gaisser, T.K. *Spectrum of cosmic-ray nucleons, kaon production, and the atmospheric muon charge ratio*. *Astroparticle Physics*, 35(12):801–806, 2012. doi:10.1016/j.astropartphys.2012.02.010

[41] Ahn, H.S. et al. *Discrepant Hardening Observed in Cosmic-ray Elemental Spectra*. *The Astrophysical Journal Letters*, 714(1):L89, 2010. URL: http://stacks.iop.org/2041-8205/714/i=1/a=L89

[42] Panov, A. et al. *Energy Spectra of Abundant Nuclei of Primary Cosmic Rays from the Data of ATIC-2 Experiment: Final Results*. *Bulletin of the Russian Academy of Sciences: Physics*, 73:564–567, 2009. doi:10.3103/S1062873809050098

[43] Olive, K. et al. (Particle Data Group). *Review of Particle Physics*. *Chinese Physics*, C38:090001, 2014. doi:10.1088/1674-1137/38/9/090001

[44] Fermi, E. *On the Origin of the Cosmic Radiation*. *Physical Review*, 75:1169–1174, April 1949. doi:10.1103/PhysRev.75.1169

[45] Graham, J.R. et al. *An X-ray and optical study of the interaction of the Cygnus Loop supernova remnant with an interstellar cloud*. *Astrophysical Journal*, 444:787–795, May 1995. doi:10.1086/175651

[46] Hillas, A.M. *The Origin of Ultra-High-Energy Cosmic Rays*. *Annual review of astronomy and astrophysics*, 22:425–444, 1984. doi:10.1146/annurev.aa.22.090184.002233

[47] Longair, M. *High Energy Astrophysics*. Cambridge University Press, 2011. URL: https://books.google.nl/books?id=KGe3FVbDNk4C

[48] Petschek, A. *Supernovae*. Astronomy and Astrophysics Library. Springer Verlag GmBH, 1990. URL: http://books.google.de/books?id=xZ3vAAAAMAAJ

[49] Bethe, H.A. *Supernova mechanisms*. *Review of Modenr Physics*, 62:801–866, Oct 1990. doi:10.1103/RevModPhys.62.801

[50] Acero, F. et al. *Detection of Gamma Rays from a Starburst Galaxy*. *Science*, 326:1080–, November 2009. doi:10.1126/science.1178826

[51] Stecker, F.W. *Upper limits to fluxes of neutrinos and gamma-rays from starburst galaxies*. *Journal of Physics: Conference Series*, 60(1):215, 2007. URL: http://stacks.iop.org/1742-6596/60/i=1/a=045

[52] Kowalski, M. *Status of High-Energy Neutrino Astronomy*. *ArXiv e-prints*, November 2014. arXiv:1411.4385

[53] Wang, B., Zhao, X. and Li, Z. *Implications of fermi -lat observations on the origin of icecube neutrinos*. *Journal of Cosmology and Astroparticle Physics*, 2014(11):028, 2014. URL: http://stacks.iop.org/1475-7516/2014/i=11/a=028

[54] Yuan, Q. et al. *Gamma rays and neutrinos from dark matter annihilation in galaxy clusters*. *Physical Review D*, 82(2):023506, July 2010. doi:10.1103/PhysRevD.82.023506

[55] Peter, A.H.G. *Dark matter in the Solar System. II. WIMP annihilation rates in the Sun*. *Physical Review D*, 79(10):103532, May 2009. doi:10.1103/PhysRevD.79.103532

[56] Esmaili, A., Kang, S.K. and Dario Serpico, P. *IceCube events and decaying dark matter: hints and constraints*. *Journal of Cosmology and Astroparticle Physics*, 12:054, December 2014. doi:10.1088/1475-7516/2014/12/054

[57] Honda, M. et al. *Calculation of atmospheric neutrino flux using the interaction model calibrated with atmospheric muon data*. *Physical Review D*, D75:043006, 2007. doi:10.1103/PhysRevD.75.043006

[58] Schmitz, N. *Neutrinophysik*. Teubner-Studienbücher : Physik. Vieweg+Teubner Verlag, 1997

[59] Aartsen, M.G. et al. (IceCube Collaboration). *A combined maximum-likelihood analysis of the high-energy astrophysical neutrino flux measured with IceCube*. *The Astrophysical Journal*, 809(1):98, 2015. doi:10.1088/0004-637X/809/1/98

[60] Aartsen, M.G. et al. (IceCube Collaboration). *Measurement of the Atmospheric ν_e Spectrum with IceCube*. *Physical Review D*, D91(12):122004, 2015. doi:10.1103/PhysRevD.91.122004

[61] Aartsen, M. et al. (IceCube Collaboration). *Development of a General Analysis and Unfolding Scheme and its Application to Measure the Energy Spectrum of Atmospheric Neutrinos with IceCube*. *The European Physics Journal*, C75(3):116, 2015. doi:10.1140/epjc/s10052-015-3330-z

[62] Abbasi, R. et al. (IceCube Collaboration). *IceTop: The surface component of IceCube*. *Nuclear Instruments and Methods*, A700:188–220, 2013. doi:10.1016/j.nima.2012.10.067

[63] Aartsen, M.G. et al. (IceCube Collaboration). *The IceCube Neutrino Observatory Part II: Atmospheric and Diffuse UHE Neutrino Searches of All Flavors*. In *Proceedings, 33rd International Cosmic Ray Conference (ICRC2013): Rio de Janeiro, Brazil, July 2-9, 2013*, 2013. arXiv:1309.7003

[64] Aamodt, K. et al. (ALICE). *Production of pions, kaons and protons in pp collisions at $\sqrt{s} = 900$ GeV with ALICE at the LHC*. *The European Physics Journal*, C71:1655, 2011. doi:10.1140/epjc/s10052-011-1655-9

[65] Schukraft, A. *Search for a diffuse flux of extragalactic neutrinos with the IceCube Neutrino Observatory*. PhD thesis, Rheinisch-Westfälische Technische Hochschule (RWTH) Aachen, June 2013

[66] Gaisser, T. and Honda, M. *Flux of atmospheric neutrinos*. *Annual Review of Nuclear and Particle Science*, 52:153–199, 2002. doi:10.1146/annurev.nucl.52.050102.090645

[67] Aartsen, M. et al. (IceCube Collaboration). *Measurement of the Atmospheric ν_e flux in IceCube*. *Physical Review Letters*, 110(15):151105, 2013. doi:10.1103/PhysRevLett.110.151105

[68] Enberg, R., Reno, M.H. and Sarcevic, I. *Prompt neutrino fluxes from atmospheric charm*. *PRD*, 78(4):043005–+, August 2008. doi:10.1103/PhysRevD.78.043005

[69] Bhattacharya, A. et al. *Perturbative charm production and the prompt atmospheric neutrino flux in light of RHIC and LHC*. *Journal of High Energy Physics*, 06:110, 2015. doi:10.1007/JHEP06(2015)110

[70] Willenbrock, S. *Symmetries of the standard model*, 2004. arXiv:hep-ph/0410370

[71] Novaes, S.F. *Standard model: An Introduction*. In *Particles and fields. Proceedings, 10th Jorge Andre Swieca Summer School, Sao Paulo, Brazil, February 6-12, 1999*, 5–102, 1999. arXiv:hep-ph/0001283

[72] Aad, G. et al. (ATLAS Collaboration). *Observation of a new particle in the search for the Standard Model Higgs boson with the ATLAS detector at the LHC*. *Physics Letters*, B716:1–29, 2012. doi:10.1016/j.physletb.2012.08.020

[73] Olive, K.A. *TASI lectures on dark matter*, 2003. arXiv:astro-ph/0301505

[74] Fukuda, Y. et al. (Super-Kamiokande Collaboration). *Evidence for oscillation of atmospheric neutrinos*. *Physical Review Letters*, 81:1562–1567, 1998. doi:10.1103/PhysRevLett.81.1562

[75] Goldhaber, M., Grodzins, L. and Sunyar, A. *Helicity of Neutrinos*. *Physical Review*, 109:1015–1017, Feb 1958. doi:10.1103/PhysRev.109.1015

[76] Ng, K.C.Y. et al. *Improved Limits on Sterile Neutrino Dark Matter using Full-Sky Fermi Gamma-Ray Burst Monitor Data*. *Physical Review D*, D92(4):043503, 2015. doi:10.1103/PhysRevD.92.043503

[77] Agostini, M. et al. (GERDA Collaboration). *Results on Neutrinoless Double-β Decay of ^{76}Ge from Phase I of the GERDA Experiment*. *Physical Review Letters*, 111(12):122503, 2013. doi:10.1103/PhysRevLett.111.122503

[78] Gribov, V. and Pontecorvo, B. *Neutrino astronomy and lepton charge*. *Physics Letters B*, 28(7):493 – 496, 1969. doi:10.1016/0370-2693(69)90525-5

[79] Bahcall, J. *Neutrino Astrophysics*. Cambridge University Press, 1989. URL: http://books.google.de/books?id=8GIP7uNMhlsC

[80] Aartsen, M.G. et al. (IceCube Collaboration). *Flavor Ratio of Astrophysical Neutrinos above 35 TeV in IceCube*. *Physical Review Letters*, 114(17):171102, 2015. doi:10.1103/PhysRevLett.114.171102

[81] Athar, H., Kim, C. and Lee, J. *The Intrinsic and oscillated astrophysical neutrino flavor ratios*. *Modern Physics Letters*, A21:1049–1066, 2006. doi:10.1142/S021773230602038X

[82] Waxman, E. and Bahcall, J.N. *High-energy neutrinos from astrophysical sources: An Upper bound*. *Physical Review D*, D59:023002, 1999. doi:10.1103/PhysRevD.59.023002

[83] Bird, D.J. et al. *The cosmic-ray energy spectrum observed by the Fly's Eye*. *Astrophysical Journal*, 424:491–502, March 1994. doi:10.1086/173906

[84] Davies, R.I. et al. *The Impact of Nuclear Star Formation on Gas Inflow to AGN*. In B.M. Peterson, R.S. Somerville and T. Storchi-Bergmann, editors, *IAU Symposium*, volume 267 of *IAU Symposium*, 283–289, May 2010. doi:10.1017/S1743921310006496

[85] Waxman, E. *High energy cosmic ray and neutrino astronomy*. *ArXiv e-prints*, January 2011. arXiv:1101.1155

[86] Gazizov, A. and Kowalski, M. *ANIS: High energy neutrino generator for neutrino telescopes*. *Computer Physics Communications*, 172:203–213, November 2005. doi:10.1016/j.cpc.2005.03.113

[87] Gandhi, R. et al. *Neutrino interactions at ultrahigh energies*. *Physical Review D*, 58(9):093009, November 1998. doi:10.1103/PhysRevD.58.093009

[88] Reno, M.H. *High energy neutrino cross sections*. *Nuclear Physics B Proceedings Supplement*, 143:407–413, 2005. doi:10.1016/j.nuclphysbps.2005.01.137

[89] Glashow, S. *Resonant Scattering of Antineutrinos*. *Physical Review*, 118:316–317, Apr 1960. doi:10.1103/PhysRev.118.316

[90] Bethe, H. *Zur Theorie des Durchgangs schneller Korpuskularstrahlen durch Materie*. *Annalen der Physik*, 397:325–400, 1930. doi:10.1002/andp.19303970303

[91] Fermi, E. *The Ionization Loss of Energy in Gases and in Condensed Materials*. *Physical Review*, 57:485–493, Mar 1940. doi:10.1103/PhysRev.57.485

[92] Jackson, J.D. *Classical electrodynamics*. Wiley, New York, NY, 3rd ed. edition, 1999. URL: http://cdsweb.cern.ch/record/490457

[93] Bolotovskii, B.M. *Vavilov – Cherenkov radiation: its discovery and application*. *Physics-Uspekhi*, 52(11):1099, 2009. URL: http://stacks.iop.org/1063-7869/52/i=11/a=R03

[94] Tsai, Y.S. *Pair production and bremsstrahlung of charged leptons*. *Review of Modern Physics*, 46:815–851, Oct 1974. doi:10.1103/RevModPhys.46.815

[95] Wheeler, J.A. *High-Energy Particles. Bruno Rossi. New York: Prentice-Hall, 1952*. *Science*, 117(3042):417–419, 1953. doi:10.1126/science.117.3042.417-a

[96] Amsler, C. *Kern- und Teilchenphysik*. vdf Hochschulverlag, 2007

[97] Longo, E. and Sestili, I. *Monte Carlo calculation of photon-initiated electromagnetic showers in lead glass*. *Nuclear Instruments and Methods*, 128(2):283–307, 1975. doi:10.1016/0029-554X(75)90679-5

[98] Wiebusch, C.H.V. *The Detection of Faint Light in Deep Underwater Neutrino Telescopes*. PhD thesis, Technische Hochschule Aachen, 1995

[99] Klein, S. *Suppression of bremsstrahlung and pair production due to environmental factors*. *Reviews of Modern Physics*, 71:1501–1538, Oct 1999. doi:10.1103/RevModPhys.71.1501

[100] Gerhardt, L. and Klein, S.R. *Electron and photon interactions in the regime of strong Landau-Pomeranchuk-Migdal suppression*. *Physical Review D*, 82(7):074017–+, October 2010. doi:10.1103/PhysRevD.82.074017

[101] Kowalski, M.P. *Search for Neutrino-Induced Cascades with the AMANDA-II Detector*. PhD thesis, Humboldt-Universität zu Berlin, 2003

[102] Spiering, C. *Towards high-energy neutrino astronomy. A historical review*. *European Physical Journal H*, 37:515–565, August 2012. doi:10.1140/epjh/e2012-30014-2

[103] Greisen, K. *Cosmic ray showers*. *Annual Review of Nuclear and Particle Science*, 10:63–108, 1960

[104] Babson, J. et al. *Cosmic-ray muons in the deep ocean*. *Physical Review D*, 42:3613–3620, Dec 1990. doi:10.1103/PhysRevD.42.3613

[105] Abbasi, R. et al. (IceCube Collaboration). *An absence of neutrinos associated with cosmic-ray acceleration in γ-ray bursts*. *Nature*, 484:351–354, April 2012. doi:10.1038/nature11068

[106] Aartsen, M.G. et al. (IceCube Collaboration). *Search for a diffuse flux of astrophysical muon neutrinos with the IceCube 59-string configuration*. *Physical Review D*, D89(6):062007, 2014. doi:10.1103/PhysRevD.89.062007

[107] Aartsen, M.G. et al. (IceCube Collaboration). *Evidence for Astrophysical Muon Neutrinos from the Northern Sky with IceCube*. *Physical Review Letters*, 115(8):081102, 2015. doi:10.1103/PhysRevLett.115.081102

[108] Folger, F. *Search for a diffuse cosmic neutrino flux using shower events in the ANTARES neutrino telescope*. PhD thesis, Friedrich-Alexander-Universität Erlangen-Nürnberg, 2014

[109] Ackermann, M. et al. (IceCube Collaboration). *Optical properties of deep glacial ice at the South Pole*. *Journal of Geophysical Research (Atmospheres)*, 111:D13203, July 2006. doi:10.1029/2005JD006687

[110] Abbasi, R. et al. (IceCube Collaboration). *The IceCube Data Acquisition System: Signal Capture, Digitization, and Timestamping*. *Nuclear Instruments and Methods*, A601:294–316, 2009. doi:10.1016/j.nima.2009.01.001

[111] IceCube Collaboration. *gallery*, 2015. URL: http://icecube.wisc.edu/gallery/

[112] Bretz, H.P. *personal communications*, 2015

[113] Abbasi, R. et al. *Calibration and characterization of the IceCube photomultiplier tube*. *Nuclear Instruments and Methods in Physics Research A*, 618:139–152, June 2010. doi:10.1016/j.nima.2010.03.102

[114] Hanson, K. and Tarasova, O. *Design and production of the icecube digital optical module*. *Nuclear Instruments and Methods in Physics Research Section A: Accelerators, Spectrometers, Detectors and Associated Equipment*, 567(1):214 – 217, 2006. Proceedings of the 4th International Conference

on New Developments in Photodetection BEAUNE 2005Fourth International Conference on New Developments in Photodetection. doi:http://dx.doi.org/10.1016/j.nima.2006.05.091

[115] Pandel, D. *Bestimmung von Wasser- und Detektorparametern und Rekonstruktion von Myonen bis 100 TeV mit dem Baikal-Neutrinoteleskop NT-72*. Diplomarbeit, Humboldt-Universit"at zu Berlin, 1996

[116] Aartsen, M.G. et al. (IceCube Collaboration). *Measurement of South Pole ice transparency with the IceCube LED calibration system*. *Nuclear Instruments and Methods*, A711:73–89, 2013. doi:10.1016/j.nima.2013.01.054

[117] Aartsen, M.G. et al. (IceCube Collaboration). *The IceCube Neutrino Observatory Part VI: Ice Properties, Reconstruction and Future Developments*. In *Proceedings, 33rd International Cosmic Ray Conference (ICRC2013): Rio de Janeiro, Brazil, July 2-9, 2013*, 2013. arXiv:1309.7010

[118] Panknin, S. *Search for neutrino-induced cascade events in the IceCube detector*. PhD thesis, Humboldt-Universität zu Berlin, 2011

[119] Heck, D. et al. *CORSIKA: a Monte Carlo code to simulate extensive air showers.* February 1998

[120] Dziewonski, A.M. and Anderson, D.L. *Preliminary reference earth model*. *Physics of the Earth and Planetary Interiors*, 25(4):297 – 356, 1981. doi:10.1016/0031-9201(81)90046-7

[121] Whitehorn, N., van Santen, J. and Lafebre, S. *Penalized Splines for Smooth Representation of High-dimensional Monte Carlo Datasets*. *Computer Physics Communications*, 184:2214–2220, 2013. doi:10.1016/j.cpc.2013.04.008

[122] Usner, M. *private communications*, 2015

[123] Bohm, G. and Zech, G. *Introduction to statistics and data analysis for physicists*. DESY, 2010. URL: https://books.google.co.jp/books?id=aQBHcgAACAAJ

[124] D'Agostino, M. *Effective Livetimes in Weighted CORSIKA*. http://internal.icecube.wisc.edu/reports/data/icecube/2009/02/001/icecube_200902001_v2.pdf, February 2009. Retrieved 2014-03-29

[125] van Santen, J. *Markov-Chain Monte-Carlo Reconstruction for cascade-like events in IceCube*. Diplomarbeit, Humboldt-Universität zu Berlin, January 2010

[126] Lawson, C.L. and Hanson, R.J. *Solving Least Squares Problems*. Series in Automatic Computation. Prentice-Hall, Englewood Cliffs, NJ 07632, USA, 1974

[127] Aartsen, M.G. et al. (IceCube Collaboration). *Search for neutrino-induced particle showers with icecube-40*. *Physical Review D*, 89:102001, May 2014. doi:10.1103/PhysRevD.89.102001

[128] Ahrens, J. et al. (AMANDA Collaboration). *Muon track reconstruction and data selection techniques in AMANDA*. *Nuclear Instruments and Methods*, A524:169–194, 2004. doi:10.1016/j.nima.2004.01.065

[129] Stenger, V. *Track fitting for DUMAND-II Octagon Array*. External Report HDC-1-90, 1990

[130] Aartsen, M. et al. *Improvement in Fast Particle Track Reconstruction with Robust Statistics*. *Nuclear Instruments and Methods*, A736:143–149, 2014. doi:10.1016/j.nima.2013.10.074

[131] Aartsen, M.G. et al. (IceCube Collaboration). *Observation of High-Energy Astrophysical Neutrinos in Three Years of IceCube Data*. *Physical Review Letters*, 113:101101, Sep 2014. doi:10.1103/PhysRevLett.113.101101

[132] D'Agostino, M.V. *First evidence for atmospheric neutrino-induced cascades with the IceCube detector*. PhD thesis, University of California, Berkeley, 2009

[133] Lauer, R.J. *Extending the search for cosmic point sources of neutrinos with IceCube beyond PeV energies and above the horizon*. PhD thesis, Humboldt-Universität zu Berlin, 2010

[134] Abbasi, R. et al. *Search for neutrino-induced cascades with five years of AMANDA data*. *Astroparticle Physics*, 34:420–430, January 2011. doi:10.1016/j.astropartphys.2010.10.007

[135] Powell, M.J.D. *An efficient method for finding the minimum of a function of several variables without calculating derivatives*. *The Computer Journal*, 7(2):155–162, 1964. doi:10.1093/comjnl/7.2.155

[136] Middell, E. *Reconstruction of Cascade-Like Events in IceCube*. Diplomarbeit, Humboldt-Universität zu Berlin, 2008

[137] Aartsen, M.G. et al. *Energy reconstruction methods in the IceCube neutrino telescope*. *Journal of Instrumentation*, 9(03):P03009, 2014. URL: http://stacks.iop.org/1748-0221/9/i=03/a=P03009

[138] van Santen, J. *Neutrino Interactions in IceCube above 1 TeV Constraints on Atmospheric Charmed-Meson Production and Investigation of the Astrophysical Neutrino Flux with 2 Years of IceCube Data taken 2010–2012*. PhD thesis, UW Madison, 2015

[139] Aartsen, M. et al. (IceCube Collaboration). *Atmospheric and astrophysical neutrinos above 1 TeV interacting in IceCube*. *Physical Review D*, D91(2):022001, 2015. doi:10.1103/PhysRevD.91.022001

[140] Seunarine, S. *2010 Request for Online Cascade Filter*. https://docushare.icecube.wisc.edu/dsweb/Get/Document-52559/2010_TFT_CascadeFilter.pdf, 12 2009. IceCube internal report

[141] Seunarine, S. *2011 Request for Online Cascade Filter*. https://docushare.icecube.wisc.edu/dsweb/Get/Document-56859/TFT_Filter_2010_11_Cascade.pdf, 3 2011. IceCube internal report

[142] Edwards, A. *Likelihood*. Cambridge science classics. Cambridge University Press, 1984. URL: https://books.google.de/books?id=LL08AAAAIAAJ

[143] Heinrich, J. *Pitfalls of Goodness-of-Fit from Likelihood*. In L. Lyons, R. Mount and R. Reitmeyer, editors, *Statistical Problems in Particle Physics, Astrophysics, and Cosmology*, 52, 2003. arXiv:physics/0310167

[144] Fedynitch, A., Becker Tjus, J. and Desiati, P. *Influence of hadronic interaction models and the cosmic ray spectrum on the high energy atmospheric muon and neutrino flux*. *Physical Review D*, 86:114024, Dec 2012. doi:10.1103/PhysRevD.86.114024

[145] Aartsen, M.G. et al. (IceCube Collaboration). *Evidence for Astrophysical Muon Neutrinos from the Northern Sky with IceCube*. *Physical Review Letters*, 115(8):081102, 2015. doi:10.1103/PhysRevLett.115.081102

[146] Niederhausen, H. *personal communications*, 2015

[147] Penzias, A.A. and Wilson, R.W. *A Measurement of Excess Antenna Temperature at 4080 Mc/s*. *Astrophysical Journal*, 142:419–421, July 1965. doi:10.1086/148307

List of Figures

List of Tables

Glossary

AGN *Active galactic nuclei* - A galaxy with an active black hole in its center accreting material and emiting jets of hot gas. 28, 29, 46

ATWD *Analog transient waveform digitizer* - A custom designed digitizer for the use in DOMs. 50

CC charged current interaction. 31

CMB *Cosmic microwave background* - A (mostly) isotropic cosmic background radiation at 3 Kelvin, created when electrons and photons decoupled in the early universe. Discovered by Penzias and Wilson[147]. 2, 7, 9, 29

COG *center of gravity*. 73

DIS *Deep inelastic neutrino nucleon scattering*. 3, 31–34, 43, 62, 68

DOM *Digital optical module* - The basic detection unit of IceCube, containing a 10 inch photomultiplier tube. 48, 50–57, 62, 70–76, 78, 80–84, 89, 94, 96, 100, 102, 115, 120, 134, 145

FADC *Flash analog to digital converter* - Used for digitization in IceCube DOMs. 51

FPGA *Field programmable gate array* - A programmable integrated circuit. 50

GRB *Gamma ray burst* - A short outburst of massive gamma radiation at high redshifts. 29, 46

HLC *Hard local coincidence* - Coincidence criterion required for IceCube triggering. Two adjacent DOMs must record signal over threshold within 1μs to form a HLC pair. 51, 89

ISM *Interstellar medium* - The ambient medium in galaxies. 9

LPM *Landau Pomeranchuk Migdal effect* - For high energetic cascades $\geqslant$ 10 PeV a reduction in crosssection results in elongated cascades. 41, 53, 62

NC neutral current interaction. 31

p.d.f. *probability density function*. 55, 56, 60–63, 82, 83

PMT *Photo multiplier tube* - A device capable of measuring individual photons. Commonly used in particle detectors. 46, 50, 51, 53–55, 68

SNR *Supernova remnant* - The remainder nebula of a supernova. 2, 3, 10, 13, 45

WIMP *Weakly interacting massive particle* - A not yet discovered candidate particle for dark matter. 16

Danksagung

Doktorarbeiten im Bereich der Experimentellen Astroteilchenphysik entstehen nur sehr selten ohne die Unterstützung Anderer. In meinem Falle, als Teil einer großen Kollaboration und Doktorand bei einer der größten Arbeitsgruppen für Experimentelle Astroteilchenphysik in Deutschland sind es sehr viele Menschen, deren Wege ich kreuzte und die das Gelingen dieser Arbeit in direkter oder indirekter Weise positiv beeinflussten und denen ich gerne danken möchte. Außerhalb des Instituts oder der Kollaboration wurde ich weiterhin von Familie und Freunden tatkräftig unterstützt, wobei ich mich glücklich schätzen kann dass diese Grenze fließend ist und ich viele meiner damaligen Mitstreiter heute zu meinen Freunden zählen kann.

Zuallererst möchte ich denjenigen danken, ohne die diese Arbeit schlicht gar nicht machbar gewesen wäre: Meinen Doktorvätern Alexander Kappes und Marek Kowalski, die mir den Rücken freihielten, mir die nötige Zeit verschafften die Arbeit zu beenden und mich mit dem Wunsch der Südpolüberwinterung unterstützten und dafür bereit waren die zeitlichen Abläufe anzupassen. Ebenso Markus Ackermann, der mich als Tutor betreut hat und stets die Zeit für den wissenschaftlichen Diskurs fand.

In der Zeit die ich als Doktorand verbrachte, kreuzte ich die Wege vieler Menschen, von denen ich leider nur Einigen hier in etwaiger chronologischer Reihenfolge unseres Kennenlernen danken kann: Meinen langjährigen Bürokollegen Arne Schönwald und Eike Middell, die beide eine große Hilfe bei Software und Physik Problemen aller Art waren. Eike betreute mich bereits während meiner Diplomarbeit und hat mich vom ersten Tag an für das Projekt begeistert und entscheidend zum Gelingen dieser Arbeit vom Anfang bis zum Ende beigetragen. Mike Walter, der mir über weite Strecken mit gutem Rat zur Seite stand und darüber hinaus die Mitarbeit in physik.begreifen angeregt hat, was ich schlussendlich mit zwei Polarsternfahrten krönen durfte. Sebastian Panknin,

der mich an die Magie der Computersprachen und des Designs herangeführt hat. Christian Spiering, der mich in seiner Arbeitsgruppe gut aufgenommen hat und mich unterstützt hat.
Ich bin den folgenden Personen sehr dankbar für viele anregende Diskussionen, Hilfe bei Software Problemen aller Art, gemeinsames Fussball spielen, Hilfe beim Fertigstellen der Arbeit und Vorbereiten auf die Verteidigung: Thorsten Glüsenkamp, David Altmann, Juan-Pablo Yáñez, Hans-Peter Bretz, Emanuel Jacobi, Meike de With, Angel Cruz, Lars Mohrmann und Daniella Kai. Des weiteren gebührt mein Dank Joanna Kiryluk der Stony Brook University die mir mehrmals ermöglicht hat, einige Zeit in Stony Brook zu verbringen, was mir stets geholfen hat, meine Arbeit in den größeren Kontext einzubetten. Ganz besonders gebührt mein Dank Hans Niederhausen, der mich während meiner Aufenthalte in Stony Brook unzählige Male bei sich untergebracht hat und mit dem es stets eine Freude ist, zusammenarbeiten zu können. Zu guter Letzt möchte ich denjenigen danken, die mich im Privaten begleitet haben und mich immer wieder aufgerichtet haben, dies sind meine Eltern Gisela und Hans-Joachim, meine Schwester Gisa, und insbesondere Tini, die stets an meiner Seite war, selbst wenn der Weg manchmal schwierig wurde. Abschliessend möchte ich Dank sagen an Dr. Bernd Epperlein, der mir damals in Klasse 9 in Chemie einen “Think ING” Aufkleber auf mein Chemieheft verpasst hat, und insgesamt einiges dazu beigetragen hat, damit alles seinen Anfang nahm. Ganz herzlichen Dank euch allen!